Transition-metal-based composite and hybrid nanomaterials for catalytic applications

Dissertation
zur Erlangung des akademischen Grades

doctor rerum naturalium
(Dr. rer. nat.)

im Fach Chemie
Anorganische und Allgemeine Chemie

eingereicht an der
Mathematisch-Naturwissenschaftlichen Fakultät
der Humboldt-Universität zu Berlin

von

M.Sc. Rui Zhang

Präsidentin der Humboldt-Universität zu Berlin:
Prof. Dr.-Ing. habil Dr. Sabine Kunst

Dekan der Mathematisch-Naturwissenschaftlichen Fakultät:
Prof. Dr. Elmar Kulke

Gutachter/innen:

1. Prof. Dr. Nicola Pinna
2. Prof. Dr. Yan Lu

Tag der mündlichen Prüfung: 16. April 2018

Abstract

High-performance catalysts play a key role in the development of technologies for sustainable production, storage, and conversion of energy. In this thesis, transition-metal-based catalysts, including TiO_2/carbon composites, hybrid organic-inorganic NiFe phosphonates, and Ni and Co phosphides are synthesized, characterized, and investigated in photocatalytic or electrocatalytic reactions.

TiO_2 is frequently combined with carbon materials, such as reduced graphene oxide (rGO), to produce composites with improved properties, for example for photocatalytic applications. It is shown that heating conditions significantly affect the interface and photocatalytic properties of TiO_2@C, and that microwave irradiation can be advantageous for the synthesis of carbon-based materials. During the synthesis of the TiO_2 nanoparticles, the carbon is involved in reactions that lead to the covalent attachment of the oxide, the extent of which depends on the carbon characteristics, heating rate, and mechanism. TiO_2 is more efficiently stabilized at the surface of rGO than amorphous carbon. Rapid heating of the reaction mixture results in a stronger coupling between the nanoparticles and carbon, more uniform coatings, and smaller particles with narrower size distributions. The more efficient attachment of the oxide leads to better photocatalytic performance.

Efficient water oxidation catalysts are required for the development of water splitting technologies. Layered hybrid NiFe-phenylphosphonate compounds are synthesized from metal acetylacetonate precursors and phenylphosphonic acid in benzyl alcohol, and their oxygen evolution reaction (OER) performance in alkaline medium is investigated. The hybrid particles transformed in situ into NiFe hydroxide nanosheets. X-ray absorption spectroscopy measurements suggest the metal sites in the active catalyst inherited partly the distorted coordination. Optimum electrocatalytic activity is achieved with the hybrid compound with a Fe content of 16 %. The combination of the synergistic effect between Ni and Fe with the structural properties of the hybrid results in an efficient catalyst that generates a current density of 10 mA cm^{-2} at an overpotential of 240 mV.

The synthesis of nanostructured transition metal phosphide (TMPs) often involves highly reactive and hazardous phosphorous-containing compounds. Herein, nickel phosphides are synthesized through thermal treatment under H_2(5%)/Ar of layered nickel phenyl- or methylphosphonates that act as single-source precursors. $Ni_{12}P_5$, $Ni_{12}P_5$-Ni_2P and Ni_2P nanoparticles with sizes of *ca.* 15-45 nm coated with a thin shell of carbonaceous material are produced. Thermogravimetric analysis coupled with mass spectrometry (TG-MS) shows that H_2, H_2O, P_2 and $–C_6H_5$ are the main compounds formed during the transformation of the precursor under argon, while no hazard phosphorous-containing compounds are created. $Ni_{12}P_5$-Ni_2P and Ni_2P NPs efficiently catalyze the hydrogen evolution reaction (HER) in acidic medium, with Ni_2P showing the best performance and generating a current density of -10 mA cm^{-2} at an overpotential of -87 mV and exhibiting long-term stability. Co_2P and CoP NPs are also synthesized following this method. The materials also showed high activity for the OER in alkaline solution.

Zusammenfassung

In der Entwicklung von Technologien für die nachhaltige Erzeugung, Speicherung und Umwandlung von Energie werden Hochleistungskatalysatoren benötigt. Im Rahmen dieser Arbeit werden verschiedene Übergangsmetall-basierte Katalysatoren, namentlich TiO_2/Kohlenstoff-Komposite, anorganisch-organische Hybridsysteme auf Basis von NiFe Phosphonaten sowie Ni- und Co-Phosphide, synthetisiert, charakterisiert und hinsichtlich ihrer photo- und elektrokatalytischen Eigenschaften untersucht.

Es wird gezeigt, dass die Grenzflächeneigenschaften und die photokatalytischen Eigenschaften der TiO_2/C-Komposite signifikant durch die Gestaltung des Heizvorgangs während der Synthese beeinflusst werden. Insbesondere der Einsatz von Mikrowellenstrahlung vermag die Synthese von Kohlenstoff-basierten Materialien positiv zu beeinflussen. Auf der Oberfläche von rGO wird TiO_2 effizienter stabilisiert als auf amorphem Kohlenstoff. Schnelles Erwärmen führt zu stärkeren Wechselwirkungen zwischen Nanopartikeln und Kohlenstoff, einheitlicheren Beschichtungen und kleineren Partikeln mit schmaleren Partikelgrößenverteilungen, wodurch die photokatalytische Aktivität verbessert wird.

Für die Entwicklung von wasserspaltenden Technologien werden leistungsfähige Katalysatoren für die Sauerstoffentwicklungsreaktion (OER) benötigt. Schichtartige, hybride NiFe-Phenylphosphonat-Materialien werden ausgehend von Metallacetylacetonaten und Phenylphosphonsäure in Benzylalkohol dargestellt und ihre Aktivität in der OER im basischen Milieu untersucht. Die Hybridpartikel werden in-situ in NiFe-Hydroxid Nanoschichten umgewandelt. Röntgenspektroskopische Untersuchungen deuten auf eine induzierte, teilweise verzerrte Koordinationsumgebung der Metallzentren im Katalysator hin. Die besten elektrokatalytischen Ergebnisse wurden mit Hybridmaterialien mit 16 % Eisen erzielt. Die Kombination der synergistischen Effekte zwischen Ni und Fe mit den strukturellen Eigenschaften des Hybridmaterials ermöglicht einen effizienten Katalysator, der eine Stromdichte von 10 mA cm^{-2} bei einer Überspannung von 240 mV generiert.

Weiterhin werden Nickel-Phosphide durch die thermische Behandlung der Phenyl- oder Methylphosphonate des Nickels, welche Schichtstrukturen aufweisen, in H_2(5%)/Ar-Atmosphäre synthetisiert. $Ni_{12}P_5$, $Ni_{12}P_5$-Ni_2P und Ni_2P Nanopartikel, die mit einer dünnen Schicht aus Kohlenstoffmaterial beschichtet sind, werden erhalten. $Ni_{12}P_5$-Ni_2P und Ni_2P Nanopartikel katalysieren die Wasserstoffentwicklungsreaktion (HER) im Sauren effektiv, wobei Ni_2P mit Stromdichten von -10 mA cm^{-2} bei einer Überspannung von -87 mV die besten katalytischen Ergebnisse mit einer guten Langzeitstabilität aufweist. Auf identischem Weg werden Co_2P und CoP Nanopartikel synthetisiert, die große Aktivität in der OER im Basischen aufweisen.

Table of Contents

List of abbreviations

γ_D, γ_G	Widths of D- and G- bands, respectively
η	Overpotential
ω_D, ω_G	Wavenumber positions of D- and G- bands, respectively
AC	Amorphous carbon
CV	Cyclic voltammetry
C_{dl}	Double-layer capacitance
EDX	Energy dispersive X-ray spectroscopy
EIS	Electrochemical impedance spectroscopy
ESR	Electron spin resonance
EXAFS	Extended X-ray absorption fine structure
FTIR	Fourier transform infrared spectroscopy
HER	Hydrogen evolution reaction
ICP-MS	Inductively coupled plasma mass spectrometry
j	Current density
LDH	Layered double hydroxide
LSV	Linear sweep voltammetry
MW	Microwave
NMR	Nuclear magnetic resonance
OER	Oxygen evolution reaction
rGO	Reduced graphene oxide
RDE	Rotating disk electrode
RhB	Rhodamine B
SEM	Scanning electron microscopy
TEM	Transmission electron microscopy
TGA-MS	Thermogravimetric analysis coupled with mass spectrometry
TOF	Turnover frequency
XAS	X-ray absorption spectroscopy
XANES	X-ray absorption near edge structure
XPS	X-ray photoelectron spectroscopy
XRD	X-ray powder diffraction

1. Introduction

The continuous growth of the world population and industries will require the production of large amounts of energy in the future. Currently, the energetic needs are mostly supplied by fossil fuels, such as petroleum, coal and nature gas[1]. However, relying exclusively on fossil fuels to meet the future energetic demands may have dramatic environmental consequences due to their association with greenhouse gases emission and climate change[2]. Therefore, the development of technology for the sustainable production of energy based on renewable energy sources such as wind, solar, or biomass, is crucial and is becoming the focus of intensive research worldwide[2,3,4]. Solar and wind energy are considered the best clean resources to meet both the industrial demands and environmental requirements. Solar cells are the most common technology used to convert the solar energy into electricity[5]. However, these intermittent renewable sources cannot provide the continuous and steady energy necessary for daily life and industrial production. This creates the need to develop technology to store the excess of solar or wind energy harvested into another form, for example, as chemical energy in fuels such as H_2 that can be later converted again to electrical energy using fuel cells. Water splitting, driven by renewable energy sources, is considered a promising method for the large-scale production of H_2.[6] However, there are still many challenges, from system efficiency to costs, hindering the widespread application of this process. The overall water electrolysis process comprises two redox half-cell reactions: the hydrogen evolution reaction (HER) and the oxygen evolution reaction (OER). Both reactions require catalysts.

Highly active and low-cost catalysts (photocatalysts and electrocatalysts) are thus essential for the development of efficient and inexpensive energy conversion and storage systems. Consequently, in the past decades, considerable efforts have been devoted to the design of nanostructured catalysts, in order to meet the ever-increasing demands (e.g. high activity, selectivity, and stability depending on structural and compositional complexity). The interest in nanoscale catalysts stems from the fact that their properties (optical, electronic, mechanical, chemical, etc.) are a function of their size, composition, and structural order[7]. Generally, the decrease in size of the catalyst particles leads to the promotion of catalytic activities, which is caused by the increase of exposed active surface and to the increase in surface defects. Different synthesis routes can lead to products with different physical and chemical properties arising from different surface areas, exposed crystal faces, lattice defects, local electronic environments, or surface functional groups[8].

Titanium dioxide is a well-known photocatalyst with important applications in, for example, environmental remediation[9,10,11], solar energy conversion[12], and other fields[13,14], due to its low toxicity, low cost, corrosion resistance, abundance, and high photocatalytic efficiency. The combination of TiO_2 nanoparticles with graphene or carbon nanotubes (CNTs) was found to increase the lifetimes of reactive charge carriers and extend the light absorption into the visible region of the spectrum[11]. It has been found that the performance of TiO_2/carbon composites depends on the interfacial properties between carbon and metal oxide. Strong coupling and maximum interfacial contact between the TiO_2 and the carbon promote the photocatalytic activity. Furthermore, TiO_2/rGO and TiO_2/AC synthesized through a microwave-assisted synthesis in benzyl alcohol were found to exhibit high stability under harsh catalytic conditions without significant detachment of oxide nanoparticles from the carbon surface, which suggests the existence of strong interactions between the carbon and TiO_2 in the composites prepared under microwave irradiation[15]. Chapter 2 of this thesis describes the study of the influence of the heating mechanism and heating rate on the physical-chemical, stability and photocatalytic properties of TiO_2/rGO and TiO_2/AC composites. For this purpose, composites were prepared by using MW-transparent glass vials, MW-shield SiC vials, and other two conventional heating methods (Teflon lined stainless steel autoclave, and autoclave reactor with internal temperature and pressure monitoring). This work was made in collaboration with Prof. Dr. Saveria Santangelo (Università "Mediterranea", Italy) who performed the Raman spectroscopy measurements, Dr. Massimiliano D'Arienzo and Prof. Dr. Franca Morazzoni (Università di Milano-Bicocca, Italy) who performed the electron spin resonance (ESR) measurements, and Dr. Enza Fazio and Prof. Dr. Fortunato Neri (Università di Messina, Italy) who performed the X-ray photoelectron spectroscopy (XPS) measurements.

Ir- and Ru-based materials are the benchmark electrocatalysts for the oxygen evolution reaction but are scarce and expensive. Consequently, catalysts based on earth-abundant and inexpensive transition-metals have been investigated as an alternative. Among those, electrocatalysts comprising simultaneously Ni and Fe have shown promising performances. Moreover, recent experimental and computational results suggest that the location of the metals in distorted coordination environments can promote the oxidation of water[16-19]. This behavior is attributed to the influence of the metal sites geometry on the binding energies of water molecules and OER intermediate species, facilitating the OER. Due to the coordination characteristics between the phenylphosphonate ligand and divalent metals such as Ni^{2+} or Fe^{2+}, in Ni or Fe phenylphosphonates materials the metals have distorted octahedral coordination. Chapter 3 of

this thesis describes the synthesis of mixed NiFe phenylphosphonate compounds, their characterization and performance as OER catalysts in alkaline medium. A detailed structural characterization of the hybrid material with optimized composition was carried out before and after the OER measurements to understand the relationship between its high electrocatalytic activity and the unique structural properties. This work was made in collaboration with Dr. Taeyeol Jeon who performed the X-ray absorption spectroscopy (XAS) measurements, Dr. Ana G. Buzanich who performed the XAS data fittings.

Platinum is the most active catalyst for the cathodic half-reaction of the electrocatalytic water splitting[22]. Transition-metal phosphides, such as nickel phosphides (Ni_2P and $Ni_{12}P_5$)[20,21], show competitive activities in this reaction. However, the syntheses of nanosized metal phosphides often involve highly reactive and toxic phosphorous compounds, such as PH_3[23]. Chapter 4 of this thesis describes a mild and non-hazardous synthesis route for producing nickel and cobalt phosphides nanoparticles coated with carbon, by thermal decomposition of hybrid organic-inorganic metal phosphonates, that act as a single source of metal and P, under H_2(5%)/Ar atmosphere. The reaction mechanism of the formation of phosphide nanoparticles from the decomposition of the hybrid precursor was investigated, and the electrocatalytic performances of the materials in the HER and OER were evaluated. This work was made in collaboration with Dr. Michael Feist who performed the thermogravimetric analysis coupled with mass spectrometry (TG−MS) measurements, and Prof. Dr. Norbert Koch and Dr. Patrick Amsalem who performed the X-ray photoelectron spectroscopy (XPS) measurements.

1.1 Bibliography

1. Zou, X.; Zhang, Y., Noble metal-free hydrogen evolution catalysts for water splitting. *Chemical Society Reviews* 2015, 44 (15), 5148-5180.
2. Cook, T. R.; Dogutan, D. K.; Reece, S. Y.; Surendranath, Y.; Teets, T. S.; Nocera, D. G., Solar Energy Supply and Storage for the Legacy and Nonlegacy Worlds. *Chemical Reviews* 2010, 110 (11), 6474-6502.
3. Kanan, M. W.; Nocera, D. G., In Situ Formation of an Oxygen-Evolving Catalyst in Neutral Water Containing Phosphate and Co^{2+}. *Science* 2008, 321 (5892), 1072-1075.
4. Reier, T.; Nong, H. N.; Teschner, D.; Schlögl, R.; Strasser, P., Electrocatalytic Oxygen Evolution Reaction in Acidic Environments - Reaction Mechanisms and Catalysts. *Advanced Energy Materials* 2017, 7 (1), 1601275.
5. Kärkäs, M. D.; Verho, O.; Johnston, E. V.; Åkermark, B., Artificial Photosynthesis: Molecular Systems for Catalytic Water Oxidation. *Chemical Reviews* 2014, 114 (24), 11863-12001.
6. Han, L.; Dong, S.; Wang, E., Transition-Metal (Co, Ni, and Fe)-Based Electrocatalysts for the Water Oxidation Reaction. *Advanced Materials* 2016, 28 (42), 9266-9291.

7. Chouhan, N.; Liu, R.-S., Electrochemical Technologies for Energy Storage and Conversion. In *Electrochemical Technologies for Energy Storage and Conversion*, Wiley-VCH Verlag GmbH & Co. 2011, 1-43.
8. Newsome, D. S., The Water-Gas Shift Reaction. *Catalysis Reviews* 1980, 21 (2), 275-318.
9. Hoffmann, M. R.; Martin, S. T.; Choi, W.; Bahnemann, D. W., Environmental Applications of Semiconductor Photocatalysis. *Chemical Reviews* 1995, 95 (1), 69-96.
10. Zhang, Y.; Tang, Z.-R.; Fu, X.; Xu, Y.-J., TiO_2−Graphene Nanocomposites for Gas-Phase Photocatalytic Degradation of Volatile Aromatic Pollutant: Is TiO_2−Graphene Truly Different from Other TiO_2-Carbon Composite Materials? *ACS Nano* 2010, 4 (12), 7303-7314.
11. Woan, K.; Pyrgiotakis, G.; Sigmund, W., Photocatalytic Carbon-Nanotube-TiO_2 Composites. *Advanced Materials* 2009, 21 (21), 2233-2239.
12. Toyoda, T.; Shen, Q., Quantum-Dot-Sensitized Solar Cells: Effect of Nanostructured TiO_2 Morphologies on Photovoltaic Properties. *The Journal of Physical Chemistry Letters* 2012, 3 (14), 1885-1893.
13. Li, W.; Wu, Z.; Wang, J.; Elzatahry, A. A.; Zhao, D., A Perspective on Mesoporous TiO_2 Materials. *Chemistry of Materials* 2014, 26 (1), 287-298.
14. Kazuhito, H.; Hiroshi, I.; Akira, F., TiO_2 Photocatalysis: A Historical Overview and Future Prospects. *Japanese Journal of Applied Physics* 2005, 44 (12R), 8269.
15. Russo, P. A.; Lima, S.; Rebuttini, V.; Pillinger, M.; Willinger, M.-G.; Pinna, N.; Valente, A. A., Microwave-assisted coating of carbon nanostructures with titanium dioxide for the catalytic dehydration of d-xylose into furfural. *RSC Advances* 2013, 3 (8), 2595-2603.
16. Bajdich, M.; García-Mota, M.; Vojvodic, A.; Nørskov, J. K.; Bell, A. T., Theoretical Investigation of the Activity of Cobalt Oxides for the Electrochemical Oxidation of Water. *Journal of the American Chemical Society* 2013, 135 (36), 13521-13530.
17. Friebel, D.; Louie, M. W.; Bajdich, M.; Sanwald, K. E.; Cai, Y.; Wise, A. M.; Cheng, M.-J.; Sokaras, D.; Weng, T.-C.; Alonso-Mori, R.; Davis, R. C.; Bargar, J. R.; Nørskov, J. K.; Nilsson, A.; Bell, A. T., Identification of Highly Active Fe Sites in (Ni,Fe)OOH for Electrocatalytic Water Splitting. *Journal of the American Chemical Society* 2015, 137 (3), 1305-1313.
18. Kim, H.; Park, J.; Park, I.; Jin, K.; Jerng, S. E.; Kim, S. H.; Nam, K. T.; Kang, K., Coordination tuning of cobalt phosphates towards efficient water oxidation catalyst. *Nature Communications* 2015, 6, 8253.
19. Grimaud, A.; Carlton, C. E.; Risch, M.; Hong, W. T.; May, K. J.; Shao-Horn, Y., Oxygen Evolution Activity and Stability of $Ba_6Mn_5O_{16}$, $Sr_4Mn_2CoO_9$, and $Sr_6Co_5O_{15}$: The Influence of Transition Metal Coordination. *The Journal of Physical Chemistry C* 2013, 117 (49), 25926-25932.
20. McCrory, C. C. L.; Jung, S.; Ferrer, I. M.; Chatman, S. M.; Peters, J. C.; Jaramillo, T. F., Benchmarking Hydrogen Evolving Reaction and Oxygen Evolving Reaction Electrocatalysts for Solar Water Splitting Devices. *Journal of the American Chemical Society* 2015, 137 (13), 4347-4357.
21. Popczun, E. J.; McKone, J. R.; Read, C. G.; Biacchi, A. J.; Wiltrout, A. M.; Lewis, N. S.; Schaak, R. E., Nanostructured Nickel Phosphide as an Electrocatalyst for the Hydrogen Evolution Reaction. *Journal of the American Chemical Society* 2013, 135 (25), 9267-9270.
22. Huang, Z.; Chen, Z.; Chen, Z.; Lv, C.; Meng, H.; Zhang, C., $Ni_{12}P_5$ Nanoparticles as an Efficient Catalyst for Hydrogen Generation via Electrolysis and Photoelectrolysis. *ACS Nano* 2014, 8 (8), 8121-8129.

23. d'Aquino, A. I.; Danforth, S. J.; Clinkingbeard, T. R.; Ilic, B.; Pullan, L.; Reynolds, M. A.; Murray, B. D.; Bussell, M. E., Highly-active nickel phosphide hydrotreating catalysts prepared in situ using nickel hypophosphite precursors. *Journal of Catalysis* 2016, 335, 204-214.

2. Microwave-assisted and conventional synthesis of TiO_2/carbon nanomaterials: effect of the heating conditions on the properties and catalytic activity

2.1 Introduction

2.1.1 Microwave heating

Microwaves are a type of electromagnetic radiation with frequency within the range 0.3 to 300 GHz and wavelength in the range of 1 mm to 1 m. The prefix "micro" indicates the wavelength of microwaves is "smaller" than the waves of typical radio broadcasting. Microwaves are extensively used in long-distance communication, radar technology, and heating devices in the form of microwave ovens. Radar equipment use wavelengths in the range of 1 to 25 cm whereas the rest of the range is generally used for telecommunications. To avoid interferences, the frequency at which commercialized domestic and industrial microwave devices are allowed to operate is regulated (915 MHz to 5.8 GHz), and the normally used frequency is 2.45 GHz[1,2]. The energy of this microwave radiation is low compared to the energies of chemical bonds and thus the absorption of microwave energy cannot directly break or create chemical bonds, i.e. does not directly lead to chemical reactions.

The potential of microwave irradiation for heating and cooking food was discovered by accident in 1945 by Percy LeBaron Spencer at the Raytheon Company while performing experiments with radar waves, after noticing that a candy bar in his pocket melted when he stood in front of an active radar set. Further research resulted in the commercialization of the first domestic microwave oven in 1954. However, it was only in the middle of the 1980's that microwave heating was applied to chemical synthesis. In 1985, Komarneni and Roy[3] reported the microwave-assisted synthesis of titania gel spheres in liquid phase. In 1986, Gedye *et al.*[4] and Giguere *et al.*[5] were the first to publish the application of microwave heating in the field of organic synthesis. The finding that organic reactions were significantly accelerated by microwave irradiation led first to a more intensive use of microwave heating in organic chemistry, and only late in the 1990's its use became more generalized in the field of inorganic chemistry[3]. One of the most famous examples of the benefits of microwave heating in organic chemistry reactions is the Suzuki-Miyaura cross coupling reaction[6], which requires several hours of heating treatment by conventional methods, but only about 50 s under microwave irradiation.

2.1.1.1 Microwave heating mechanisms

The heating of a substance under microwave irradiation is directly related with the physical properties of the substance, in particular its microwave absorption capacity and ability to convert it into heat[7]. The conversion of microwave energy into heat upon the interaction of the substance with the electric and/or magnetic components of the microwave electromagnetic radiation can occur through various mechanisms.

Dipolar polarization (dielectric heating or dielectric loss) mechanism: involves species that have a dipole moment[8,9]. When exposed to microwave radiation the dipoles try to align themselves with the electric field. As the electrical field alternates (at 2.45 GHz, the electric field alternates 2450 million times in a second), the constant attempt to realign causes dipole rotation, which results in the conversion of the energy into heat due to friction and collisions.

Ionic conduction mechanism: occurs when the substance contains charged species (usually ions)[8,9]. The alternating electric field generates motion of the charged species that move back and forth trying to couple with the electric field. Heat is generated through collisions of the moving species.

Joule heating (or ohmic or resistive heating) mechanism: occurs with conducting or many semiconducting substances through their interaction with the microwave electric and magnetic components[8,9]. An alternating magnetic field induces currents on the surface of conducting and semiconducting materials (called eddy or parasitic currents). The passage of current through the material generated heat (Joule heating), whose magnitude is proportional to the current and resistance of the material.

Magnetic hysteresis, domain-wall resonance and electron-spin resonance mechanisms: occur with magnetic materials[8,9]. The oscillating magnetic field causes rotation of the magnetic moments of the substance, displacements in the magnetic domain walls of the material (for multi domain materials), hysteresis of the process of creating, displace or extinguish a magnetic domain. All these processes dissipate energy in the form of heat.

Several mechanisms may operate simultaneously to heat a material under microwave irradiation, depending on the nature of the material. The most relevant mechanisms in organic synthesis are those involving interactions with the electric component of the radiation (most commonly dielectric heating). In the case of inorganic synthesis, a higher number of mechanisms may be

active simultaneously, as conduction and Joule heating are more frequent, to which magnetic loss mechanisms are added if magnetic materials are present.

The efficiency with which a substance transforms the electromagnetic energy into heat, i.e. how efficiently the substance is heated under microwave irradiation is determined by its loss tangent (tan δ). tan δ = ε´´/ ε´, where ε´´ is the dielectric loss or complexed permittivity (related to the amount of microwave energy that is dissipated as heat) and ε´ is the dielectric constant or relative permittivity (related to the polarizability of the substance in an electric field)[8,9]. For magnetic materials where heat is also generated by interaction with the magnetic component, the homologous parameters are the magnetic loss (μ´´) and magnetic permeability (μ´). Substances with high tan δ are strong microwave absorbers and are heated fast under microwave irradiation.

2.1.1.2 Differences between conventional and microwave heating

Conventional heating methods make use of external heat sources such as oil baths, heating mantles or furnaces to heat reaction systems through convection (heat transfer through the movement of fluids) and/or thermal conduction (energy transfer to the neighboring atoms and molecules of rotating/vibrating species) mechanisms. Heat transfer occurs first with the walls of the vessel to reach the solvent and reactants; the reaction mixture in contact with the vessel is heated first. The efficiency of the process depends on the thermal conductivity of the various substances involved. This heating process results in temperature gradients, with the walls of the vessel being hotter than the reaction mixture inside until thermal equilibrium is reached (Figure 2.1). Contrarily, microwave irradiation heats the entire volume of the reaction mixture at the same time because it is a consequence of the interaction of the species present in the reaction mixture with the radiation. Furthermore, because microwave-transparent microwave reaction vials (e.g. glass or Teflon) are normally used, the temperature of the vial walls is generally lower than that of the substances inside (Figure 2.1).

In general, microwave heating significantly decreases the time necessary to complete a chemical reaction compared to conventional heating, because it affects the kinetics of the system and can cause drastic increases in reaction rates. The rapid volumetric heating affects the temperature term (RT) in the exponential factor of the Arrhenius equation ($k = Ae^{-E_a/RT}$). The high amount of energy being introduced to the system per unit of time and consequent fast

temperature rise increases the number of reactant collisions and the fraction of those with the necessary energy to overcome the reaction activation barrier.

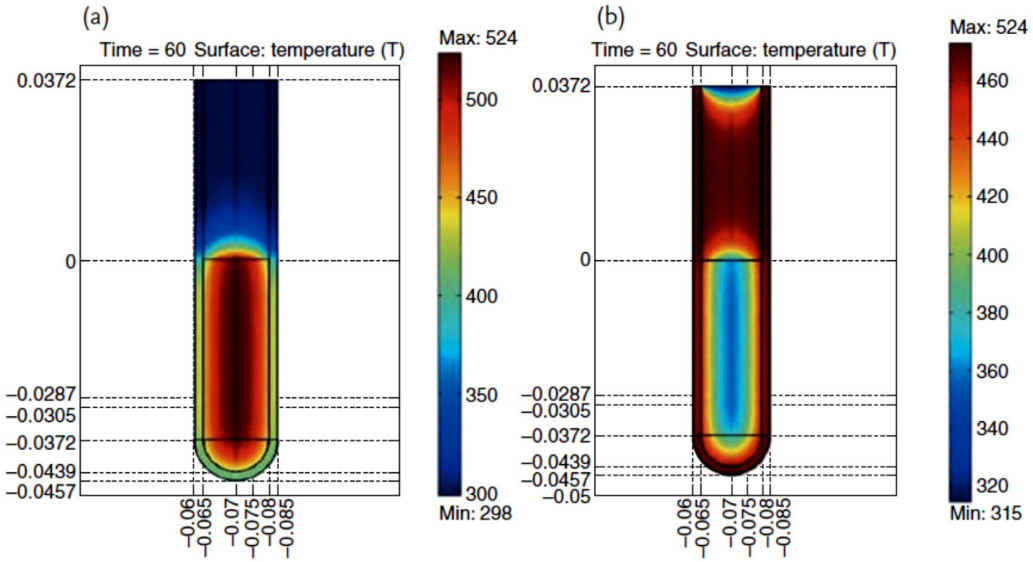

Figure 2.1 Temperature profile after 60 s as affected by microwave irradiation (a) compared to treatment in an oil-bath (b). Microwave irradiation raises the temperature of the whole reaction volume simultaneously, whereas in the oil heated tube, the reaction mixture in contact with the vessel wall is heated first. Temperature scale is given in K. '0' on the vertical scale indicates the position of the meniscus. Reproduced with permission from Ref. 10. Copyright 2003 Springer.

2.1.1.3 Microwave effects

Microwave heating can drastically increase reaction rates and decrease to minutes the time of reactions that take hours or days using conventional heating. In addition to the time reduction, many researchers reported different product outcomes for microwave-assisted reactions compared to those performed with conventional heating at the same apparent temperature. In some cases, reactions that occurred under microwave irradiation were not observed when conventional heating was used. These types of results apparently could not be explained by the simple kinetic microwave effects and, in the early days of microwave-assisted chemistry, led to the hypothesis that "specific" and "non-thermal" microwave effects could be responsible for the different results as well as the rate enhancements observed under microwave irradiation. Many of the cases reported involved organic reactions, and the differences between microwave and conventionally heated reactions were later attributed to misinterpretation of experimental data, especially errors in the measurement of reaction temperatures.

The possible effects involved in a chemical transformation performed under microwave irradiation are divided into three categories: "thermal/kinetic", "specific", and "non-thermal".

"Thermal/kinetic" effects are the high heating rates and high temperatures that can be quickly achieved by microwave irradiation of reaction mixtures. "Specific microwave effects" are defined as *accelerations of chemical transformations that cannot be achieved or duplicated by conventional heating, but are essentially still thermal effects*.[7,11,12] These effects are due to the specific mechanisms involved in the conversion of the microwave energy into heat and include: the superheating effect, the selective heating of strongly microwave absorbing species located in a less absorbing medium, the formation of "molecular radiators" by the coupling of specific reagents in solution with the microwave electromagnetic field (microscopic hot spots), and the elimination of wall effects caused by inverted temperature gradients[7,12,13]. For example, the generation of electric currents at the surface of conducting materials such as conductive carbons and consequent production of heat is a specific microwave effect that cannot be reproduced by conventional heating. "Non-thermal microwave effects" are *accelerations of chemical transformations that cannot be rationalized by either purely thermal/kinetic or specific microwave effects*.[7,11,12] These are proposed effects caused by interactions of reactant species with the electromagnetic field that affect the pre-exponential factor (A) or the activation energy (E_a) of the reaction in the Arrhenius equation.

It is now generally accepted that in most cases the reaction rate enhancements in microwave-assisted synthesis are exclusively the result of thermal/kinetic effects. The existence of "specific microwave effects" is also well-established in the field. Contrarily, the existence of "non-thermal microwave effects" is very controversial.

For a given reaction, the comparison between microwave and conventional heating (e.g. in an oil bath or autoclave) is challenging because it is difficult to reproduce exactly the same temperature, heating and cooling ramps, and accurately measure the internal temperature of the reaction mixtures. These factors contributed to the existence of many claims in the literature about the existence of specific and non-thermal microwave effects. Many of those were disproved by performing carefully designed comparative experiments. An important contribution to this field was given by the group of Kappe. Since 2009, Kappe and co-workers have used microwave SiC vials otherwise similar to the glass vials to investigate the existence of specific and non-thermal microwave effects[14-21]. SiC is a strong MW absorbing material that heats very efficiently through Joule heating mechanisms under MW irradiation. Therefore, the reaction mixture inside the SiC vial is essentially shielded from the MW radiation and heated through conventional mechanisms. By using a fiber-optic temperature probe inserted into the vials the MW temperature profile of a glass vial can be accurately reproduced inside a SiC vial.

The authors used this protocol to investigate a large number of organic reactions and found that specific or non-thermal MW effects were not involved.

2.1.2 Microwave-assisted synthesis of inorganic nanomaterials

Conventional synthesis methods of inorganic nanomaterials generally involve high temperatures and are time-consuming procedures. The microwave heating drastically decreases the synthesis time of inorganic materials. In addition to the rapid and uniform heating, higher yields, higher phase purity and narrower size distributions are also frequent outcomes of microwave-assisted synthesis of nanostructures compared with conventional heating methods. Smaller nanoparticles are obtained also often through MW-assisted synthesis compared to conventional synthesis. More importantly, because the physical and chemical properties depend not only on composition, but also on the particle size and shape[22], nanomaterials with enhanced performances can be obtained through microwave-assisted synthesis approaches. For example, Dahal *et al.*[23] reported the superior catalytic activity of microwave-prepared Rh nanoparticles in the hydrogenation of cyclohexene compared to those conventionally prepared. These results revealed that microwave heating exhibited a remarkable effect on both nucleation and growth processes, and selectively produced Rh particles with a majority of tetrahedra or cube morphology upon further crystal growth. García *et al.*[24] were able to synthesize classically immiscible RhAg and RhAu alloy nanoparticles with great potential in heterogeneous catalysis through a novel MW-assisted route.

Differences in the size/morphology of nanoparticles, higher monodispersity or higher yields can, in most cases, be attributed to the high and uniform temperatures that are quickly achieved under microwave irradiation. This results in a rapid and more homogeneous distribution of the nucleation and growth processes of the nanostructures. The production of smaller particles under MW irradiation can be attributed to the high nucleation rates that produces a comparatively larger amount of small nuclei.

In addition to the advantages discussed above, specific interactions of species present in the reaction mixture with the microwave electromagnetic field ("specific microwave effects") can also affect the synthesis of inorganic nanomaterials.[25-28] For example, Hu *et al.*[26,27] synthesized α-Fe_2O_3 nanorings by a MW-assisted hydrothermal reaction that could not be prepared with conventional heating. The authors proposed that α-Fe_2O_3 nanodisks were first formed, which, due to a "specific MW effect" were overheated compared to the mixture. The high surface temperatures reached caused a partial dissolution and consequent formation of the nanorings.

Another example is the merging of Ag nanowires in ethylene glycol to form a network under microwave irradiation, which was ascribed to the "superheating" of the metal surface due to the specific interaction of the metal with the MW electromagnetic field [25].

Carbon materials have an outstanding ability of absorbing microwave energy and converting it into heat. Menéndez and co-workers[29] treated activated carbon in a multimode microwave at 1000 watt and found that the temperature reached 1000 °C in about 1 minute. Under microwave irradiation, the alternating electromagnetic field induces a current of the delocalized π electrons on the graphitic regions of the carbon, and the energy is dissipated through a resistive heating mechanism. Microwave irradiation has been applied for the synthesis of carbon-based nanocomposites. Preferential dispersion of metal or metal oxide nanostructures on the surface of carbon materials such as graphene oxide (GO) or carbon nanotubes (CNT) has been efficiently carried out with MW heating.

A wide range of metal oxide nanoparticles with high crystallinity, purity and controlled size can be synthesized by non-aqueous sol-gel method in benzyl alcohol at relatively low reaction temperatures. Benzyl alcohol has the function of oxygen supplier, solvent and surfactant.[30-35] The application of microwave technology to the "benzyl alcohol route" allowed the synthesis of highly crystalline nanoparticles of many metal oxides in just minutes[36-45].

In addition, the selective and homogeneous coating of carbon nanostructures with metal oxide nanoparticles can be achieved in benzyl alcohol. In particular, dense coatings of metal oxide NPs on reduced graphene oxide (rGO) can be produced in a one-pot reaction in benzyl alcohol, starting from the metal precursors and GO[46,47,48]. This is because, in addition to acting as the metal oxide oxygen source, benzyl alcohol at the same time partly reduces the graphene oxide[46,47,48]. Fe_2O_3/rGO, SnO_2/rGO and TiO_2/rGO were easily synthesized in this way[46-50].

2.1.3 TiO_2@carbon nanomaterials

TiO_2 is a semiconductor material with band gap of 3.0 and 3.2 eV for rutile and anatase phases, respectively[51]. Owing to its long-term stability, including thermodynamic stability and chemical resistance, efficient photocatalytic activity, non-toxicity and low cost, TiO_2 is used for many commercial, environmental, energy and industrial applications, such as photodegration of organic pollution in liquid and gas phases, water photolysis for hydrogen production and dye-sensitized solar cells, or as photo-induced self-cleaning coating which is already widely used in vehicle's windshields and external glass walls[52].

TiO_2 is a well-known photocatalyst. The mechanism of the photocatalytic reaction is complicated and distinct for each application, but is generally based on the photogenerated electron-hole pairs under UV irradiation (reaction 2.1). In aqueous solution, photons excite electrons from valence band to the conduction band, leading to charge separation. The positive holes react with adsorbed water and/or oxygen forming hydroxyl radicals and/or oxygen radicals. These radicals are highly oxidizing agents that are able to oxidize most organic molecules to carbon dioxide and water (reaction 1.2-1.5) [52].

$$TiO_2 + hv \rightarrow e^- + h^+ \quad (2.1)$$

$$e^- + O_2 \rightarrow O_2^- \quad (2.2)$$

$$O_2^-(ad) + H^+ \rightarrow HO_2^\bullet(ad) \quad (2.3)$$

$$h^+ + H_2O \rightarrow {}^\bullet OH\ (ad) + H^+ \quad (2.4)$$

$$h^+ + O_2^-\ (ad) \rightarrow 2{}^\bullet O\ (ad) \quad (2.5)$$

However, the lifetime of these electron-hole pairs is very short due as they rapidly recombine[52]. Researchers have been investigating several ways to delay of suppress the recombination process and extend the photocatalytic activity to the visible range of the spectrum, which include transition-metal or anion doping, or coating with noble metals, semiconductors or dyes. Another approach is the combination of TiO_2 with conductive carbon materials such as rGO or carbon nanotubes (CNTs) to fabricate highly active photocatalysts.[53-57] The carbon material acts as an electron scavenger. The unique properties of graphene and related materials (graphene oxide and reduced graphene oxide) such as the high electronic conductivity provided by the large sp^2 hybridized carbon network that facilitates the delocalization of π electrons, high surface area, low thickness and high transparency[58]. Charge transfer at the interface between TiO_2 and carbon, attributed to the difference in the work functions of the two materials[59,60], results in efficient separation of photogenerated electron–hole pairs, which delays or hinders charge recombination and promotes redox activity.

Basically, TiO_2/carbon nanocomposites (and metal oxide/carbon nanocomposites in general) can be produced by two main strategies named ex situ hybridization and in situ hybridization[61]. The latter consists in the formation of the metal oxide from the precursors in the presence of the carbon material. The former involves mixing the carbon substrate and the pre-synthesized metal oxide particles for example in solution or with a ball mill[62]. This method allows the large scale production of composites, but may lead to poor metal oxide-carbon binding and non-

uniform covering on the carbon substrate[61]. On the contrary, the in situ process facilitates the metal oxide nanocrystals grow on the carbon surface, resulting in a more uniform coating of metal oxide and likely to stronger attachment[63].

It has been found that the performance of TiO_2/carbon composites depends on the interfacial properties between carbon and metal oxide. Zhang *et al.*[64] systematically compared the photocatalytic performances of in situ and ex situ hybridized TiO_2/graphene composites. Commercial TiO_2 particles (P25) were simply integrated with graphene to prepare ex situ hybridized P25/graphene, while a hydrothermal method was applied to produce in situ hybridized TiO_2/graphene. Photocurrent transient responses for these samples in the same experimental conditions indicated that the transport of photogenerated electrons from titanium oxide to the graphene plane was more effective in TiO_2/graphene than in P25/graphene. Electron spin resonance (ESR) data showed that a decay and lower superoxide radical species intensity was observed for the P25/graphene sample. Similar results were found for P25/CNTs and TiO_2/CNTs composites. Their findings suggest that the sufficient and intimate interfacial interactions between carbon and TiO_2 particles can prolong the lifetime of photogenerated electron-hole pairs and consequently promote photocatalytic activity. Moreover, strong interfacial interactions and the formation of covalent bonds can promote the extension of the photocatalytic activity into the visible range of the spectrum.[65] The crucial role of the TiO_2-graphene interface in mediating the performance of the composites has also been demonstrated in theoretical work.[60,66,67] It is therefore recognized that synthetic approaches leading to high loadings of semiconducting particles, strong coupling, and maximum interfacial contact are essential to fully exploit the carbon beneficial effects.

TiO_2@carbon composites with metal oxide loadings up to 70 wt. % can be rapidly (*ca.* 20 min) synthesized by reaction of titanium (IV) isopropoxide with benzyl alcohol under microwave irradiation, a reaction usually carried out in autoclave for 24-72 h due to the high autogenic pressures reached[68]. A uniform coating of anatase nanoparticles of *ca.* 8 nm on rGO and amorphous carbon black (AC) was produced. The materials showed high activity and stability in the liquid phase catalytic conversion of xylose to furfural. Interestingly, the microwave-prepared composites were able to resist the harsh catalytic conditions without significant detachment of nanoparticles from the carbon surface, which suggests the existence of strong interactions between the carbon and the oxide. Therefore, in this chapter TiO_2/rGO and TiO_2/AC were synthesized through the "benzyl alcohol route" by microwave-assisted and conventional methods. The materials were characterized, the stability of the particles at the

carbon surface was investigated, and the photocatalytic activity in a model test reaction was determined for understanding the effects of microwave heating on the properties, stability and catalytic performance of the composites.

2.2 Results and discussion

2.2.1 Synthesis of TiO_2@Carbon and reaction mechanism

TiO_2/carbon nanomaterials were prepared *via* the "benzyl alcohol route" using titanium (IV) isopropoxide as precursor[46] and graphene oxide (denoted TrGO) or amorphous carbon (denoted TAC) as support. The microwave-assisted syntheses were carried out in two types of MW vials: MW-transparent glass vials (TrGO-G, TAC-G), and silicon carbide vials (TrGO-S, TAC-S), which absorb the microwave radiation and heat the mixture by thermal conduction/convection. The temperature and pressure profiles of the microwave reactions are shown in Figure 2.2. The temperature in both the glass and SiC vials was monitored using a fiber-optic temperature probe inserted into the reaction mixture. Except the slight fluctuations of temperature and pressure in the heating profile of sample synthesis in SiC vials, which due to the lag of thermal transmission, no other distinct difference was observed between two kinds of vials. In both cases, the first rise in pressure was observed when the temperature of the mixture went to around 150 °C and continued until reaching the holding temperature, 245 °C, most likely because of the formation of isopropanol as a product of ligand exchange reaction and the presence of benzyl alcohol which had a boiling point of about 205 °C under one bar pressure. After keeping the temperature at 245 °C and overpressure at around 7 bars for 6 minutes, the second and more sharply rise in pressure was observed hitting at 10 bars in less than two minutes. The instantaneously increment of pressure was caused by the evolution of water as a byproduct of Ti center catalytic condensation reaction of benzyl alcohol to dibenzyl ether[68], as shown in equation 2.8. Meanwhile, the nucleation and nanoparticle growth occurred concurrently by the hydrolysis of titanium precursors. Materials were also synthesized using an autoclave reactor (TrGO-R, TAC-R) with internal temperature and pressure monitoring. The reaction mixture was heated as fast as possible to 245 °C (~11 °C/min) and held at this temperature for 10 min. However, it was not possible to achieve the high heating rates attained with microwave reactors. The temperature and pressure profiles of this reaction are shown in Figure 2.3. A similar step-type increase in pressure was also observed in the heating profile of samples produced by micro reactor (Figure 2.3), in which the overpressure went to 6 bars at 245 °C, then suddenly increased

to 7 bars after holding this temperature for around 8 minutes. For comparison, samples were also prepared in a Teflon-lined stainless-steel autoclave (TrGO-A, TAC-A), which is normally used to carry out these reactions. In this case, the reaction mixture is heated slowly, as it takes several hours to reach the target temperature and attain thermal equilibrium. All the experiments used the same TIP/carbon ratio.

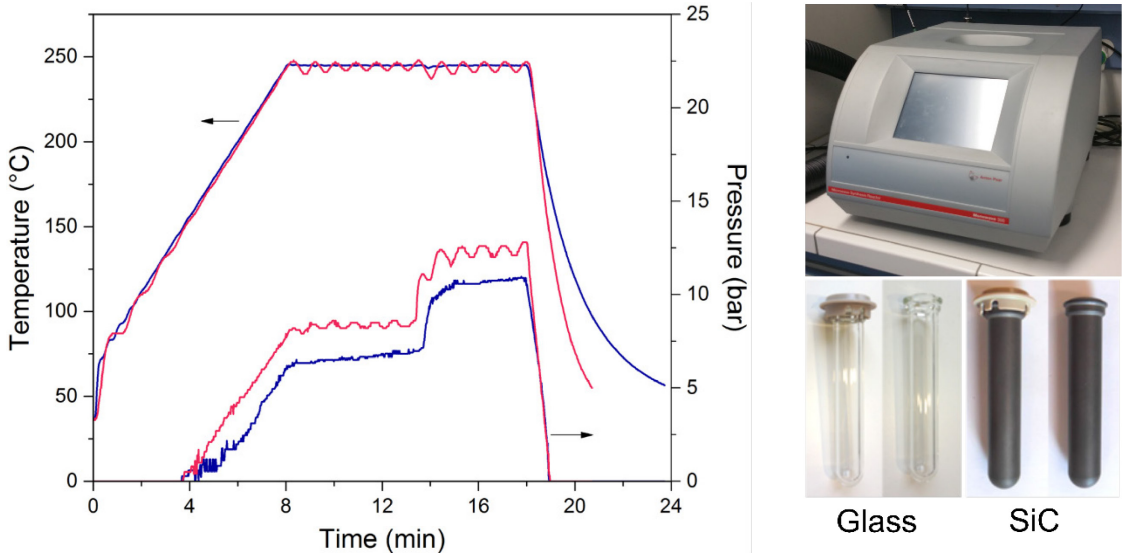

Figure 2.2 Temperature and pressure profiles (left) of the syntheses performed in the MW-glass(blue) and MW-SiC (red) vials. The temperature was measured with a fiber-opticprobe inserted into the reaction mixtures. The photographs of microwave synthesis reactor, glass vials and SiC vials (right).

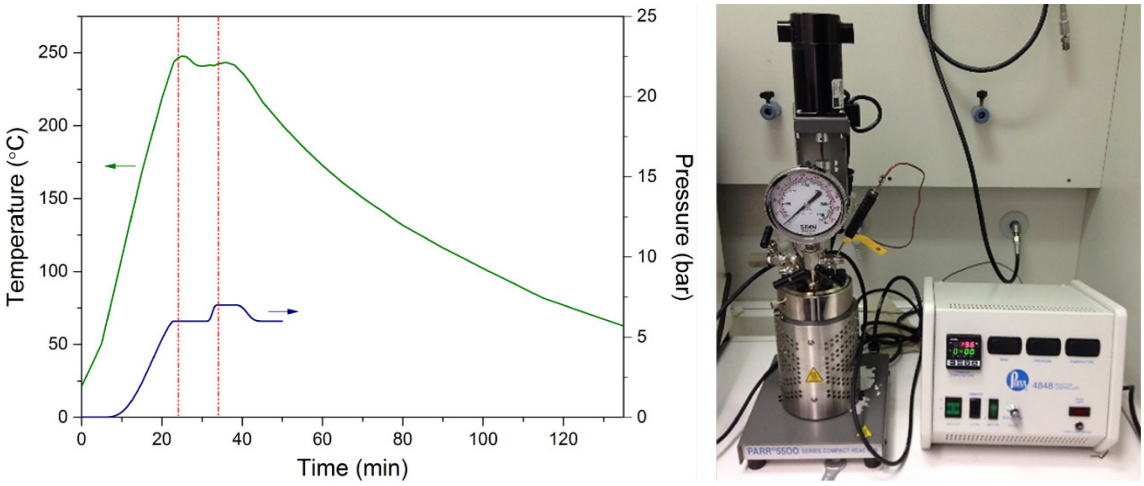

Figure 2.3 Temperature and pressure profiles (left) of the syntheses performed in the micro reactor. The temperature and pressure was measured by internal monitors. The photograph of micro reactor (right).

After the microwave synthesis carried out in the glass and SiC vials, the solid product was separated and the solution was analyzed by ^{1}H NMR spectroscopy. The ^{1}H NMR spectra of the

reaction solutions after the microwave-assisted synthesis of TrGO-G and TrGO-S are displayed in Figure 2.4. The chemical shifts at 4.54, 3.66 and 1.19 ppm are assigned to the CH_2 group of dibenzyl ether, CH group of benzyl isopropyl ether and CH_3 group of isopropanol, respectively. The signals at 4.64 and 2.53 ppm are attributed to the CH_2 group of benzyl alcohol and CH_3group of toluene, respectively. The presence of ethers in the solution at the end of the syntheses indicates that the formation of the TiO_2 in benzyl alcohol occurs through an ether elimination mechanism (equation 2.6). The reaction involves first the exchange of the isopropoxy ligand of the titanium isopropoxide precursor by benzyloxy groups from the solvent with formation of isopropyl alcohol (equation 2.7), that is detected in the solution. The metal oxide monomers and particles are then formed through condensation reactions with the elimination of ethers (equation 2.8). Toluene is produced by thermal decomposition of benzyl alcohol molecules. The reaction of titanium isopropoxide with benzyl alcohol has been thoroughly investigated by other authors. It was found that water is generated during the reaction, likely as a byproduct of the condensation reaction between benzyl alcohol molecules that produce dibenzyl ether, catalyzed by titanium. The formation of water is the cause of the sudden increase of pressure seen after *ca.* 12 minutes of the start of the synthesis (Figure 2.2). Nucleation and growth of the nanoparticles were found to proceed very fast during this pressure increment. Therefore, hydrolysis is also involved in the formation of the TiO_2 nanoparticles. Actually, there was no additional signal detected in the spectra of solution obtained from SiC vial (figure 2.2 red curves), indicating a same reaction process occurs in similar heating profiles regardless the heating mechanism.

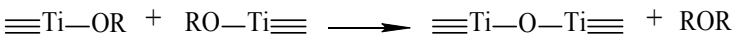

(2.6)

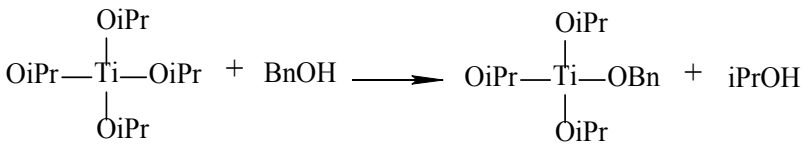

(2.7)

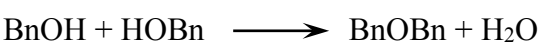

(2.8)

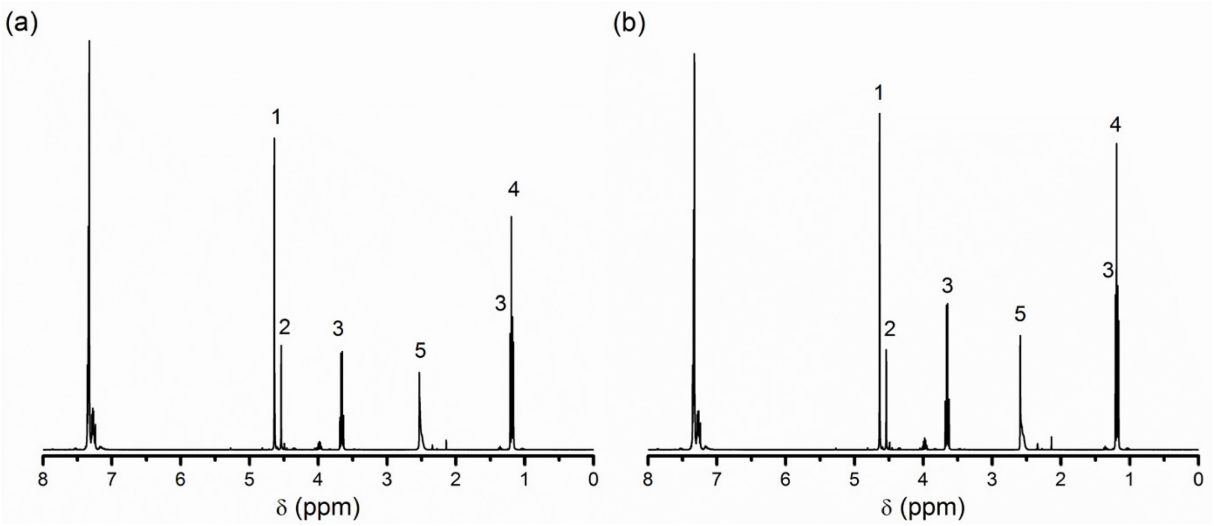

Figure 2.4 [1]H NMR spectra of the reaction solutions recovered at the end of the syntheses of TrGO-G (a) and TrGO-S (b) (1 benzyl alcohol, 2 dibenzylether, 3 benzyl isopropyl ether, 4 isopropanol, 5 toluene).

2.2.2 Structural properties of theTiO_2@Carbon nanostructures

Figure 1.5 shows the X-ray diffractograms of the TiO_2@rGO composites. $TiO_2$with tetragonal anatase phase (JCPDS file NO. 21-1272) was obtained with all of the synthesis methods.The TrGO-A sample exhibits the narrowest reflection peaks compared to the others, indicating bigger crystallite sizes than the other samples. The crystallite sizes of each sample were calculated from XRD patterns with the Scherrer equation using the (101) reflection. They are 9.4, 9.9, 19.9 and 8.0 nm for TrGO-G, TrGO-S, TrGO-A and TrGO-R, respectively, and are confirmed by the analysis of TEM images as shown in table 2.1.

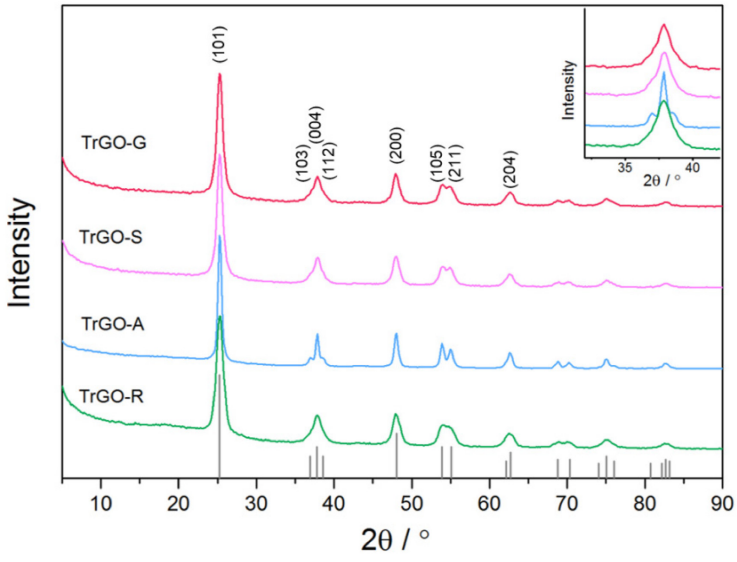

Figure 2.5 Powder X-ray diffraction patterns of the TrGO nanocomposites. Vertical gray bars represent the reference reflections of anatase (JCPDS file no. 21-1272).

Table 2.1 TiO_2 particle size and polydispersity of the TiO_2@rGO composites.

	XRD[a] / nm	TEM[b]/ nm	Polydispersity[b] / %
TrGO-G	9.4	9.0 ± 0.4	22.4
TrGO-S	9.9	9.1 ± 0.3	20.9
TrGO-A	19.9	20.5 ± 1.3	34.4
TrGO-R	8.0	8.0 ± 0.3	20.7

a. Crystallite size calculated from the XRD patterns by using the Scherrer equation and the (101) reflection.
b. Determined from analysis of the TEM images.

Transmission electron microscopy (TEM) images reveal that a homogeneous and dense coating of TiO_2 nanoparticles on the rGO sheets is obtained for the microwave-assisted syntheses in the glass and SiC vials (Figure 2.6a, b). The metal oxide particles have average sizes of 9.0 and 9.1 nm, and relatively low polydispersity of 22.4% and 20.9 %, respectively. Almost all are deposited on the surface of the rGO sheets and very few are separated from the carbon. Therefore, the differences in heating mechanism in the glass and SiC vials seem to have no effect on the morphology and crystallinity of theTiO_2 nanocrystals. For the synthesis performed in the autoclave reactor a less homogeneous coating was achieved and metal oxide nanoparticles of smaller size were produced (Figure 2.6d, Table 2.1). The composite was also prepared with a Teflon-lined stainless steel autoclave at 245 °C for 48 hours. The TEM image (Figure 2.6c) shows that a large portion of the rGO sheets are uncoated and a large amount of titanium oxide nanoparticles are not deposited on the carbon. The average size of the nanoparticles is 20.5 nm, which is much larger than those prepared by the other methods and the polydispersity is comparatively high (34.4%).

Additionally, the nanomaterials were prepared by using amorphous carbon spheres as carbon support (TAC), and similar results and trends were observed. Anatase was obtained from all the experiments (Figure 2.7). The TEM images and size analysis are displayed in Figure 2.8 and Table 2.2. For the samples prepared by microwave-assisted syntheses in glass and SiC vials, the amorphous carbon spheres were almost fully covered with titanium oxide nanoparticles with average diameter of around 9 nm. The composites prepared in the reactor and microwave-assisted synthesis shown similar morphologies, indicating an analogous process occurred under those conditions. The coatings of TiO_2 on amorphous carbon seemed condense compare to those on rGO sheets, mainly because of the smaller surface area of amorphous carbon.

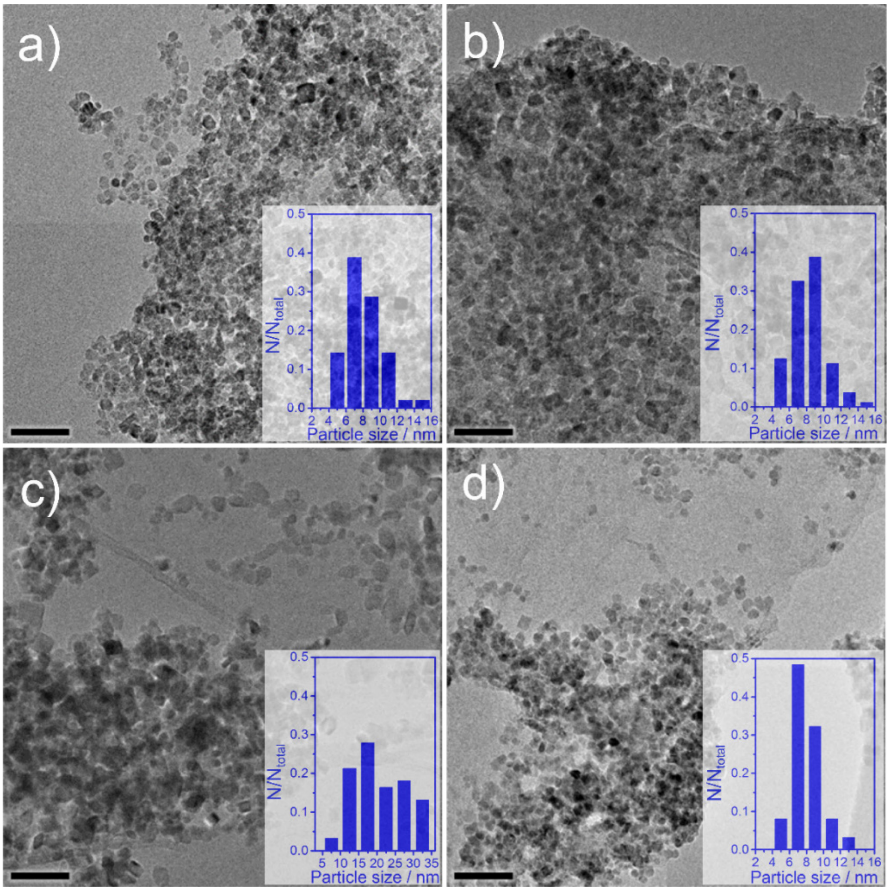

Figure 2.6 TEM images of a) TrGO-G, b) TrGO-S, c) TrGO-A, d) TrGO-R. Scale bars: 50 nm.

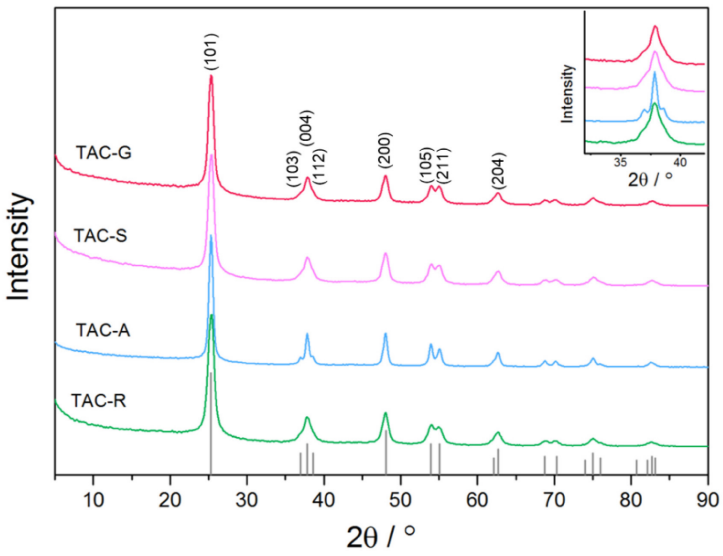

Figure 2.7 Powder X-ray diffraction patterns of the TAC nanocomposites. Vertical gray bars represent the reference reflections of anatase (JCPDS file no. 21-1272).

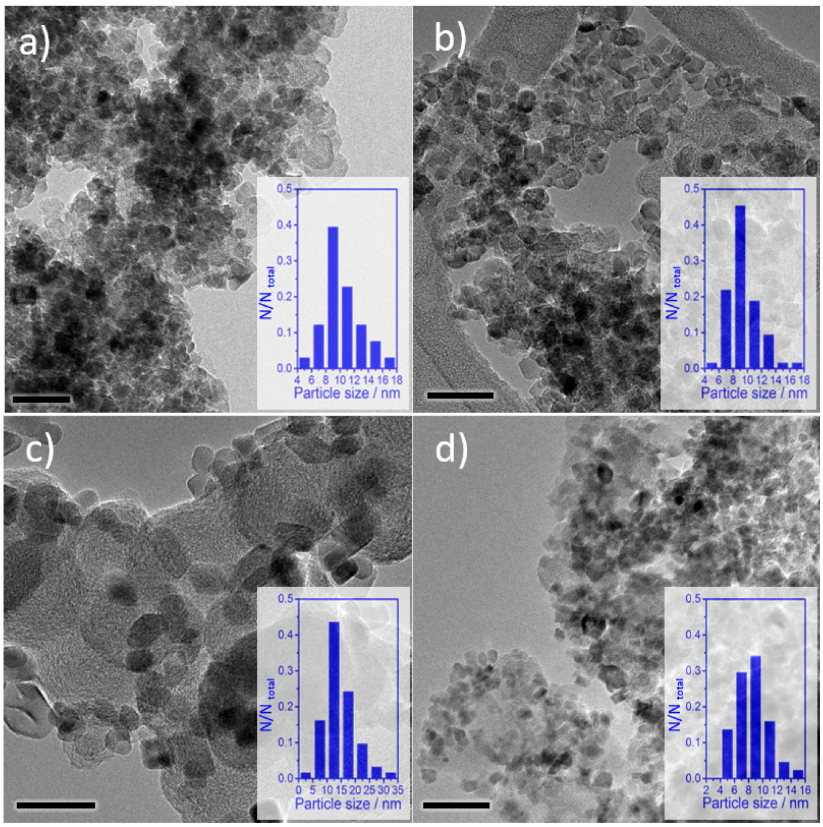

Figure 2.8 TEM images of a) TAC-G, b) TAC-S, c) TAC-A, d) TAC-R. Scale bars: 50 nm.

Table 2.2 TiO_2 particle sizes and polydispersity of TiO_2@AC composites.

	XRD[a] / nm	TEM[b]/ nm	Polydispersity[2] / %
TAC-G	9.3	9.4 ± 0.4	21.8
TAC-S	9.0	9.3 ± 0.4	21.4
TAC-A	17.3	16.4 ± 1.3	41.5
TAC-R	9.0	8.5 ± 0.4	28.0

a. Crystallite size calculated from the XRD patterns by using the Scherrer equation and the (101) reflection.
b. Determined from analysis of TEM images.

In a control experiment, titanium oxide was prepared in the same conditions as TrGO-G without the graphene oxide. The heating profile is shown in figure 2.9. Longer reaction time was necessary for obtain the oxide product. Larger power is required to reach the final temperature as well as to hold that temperature, which can be because GO absorbs microwave radiation more efficiently than benzyl alcohol. Moreover, the second step in pressure is observed after the system is maintained at 245 °C for 30 min, much longer than what occurs in the profile of TrGO-G. TEM images and SAED pattern of the TiO_2 nanoparticles are shown in Figure 2.10.

Anatase phase TiO_2 nanoparticles with mean size of 10.5 nm were produced and the polydispersity of those oxide particles is 22.3 %.

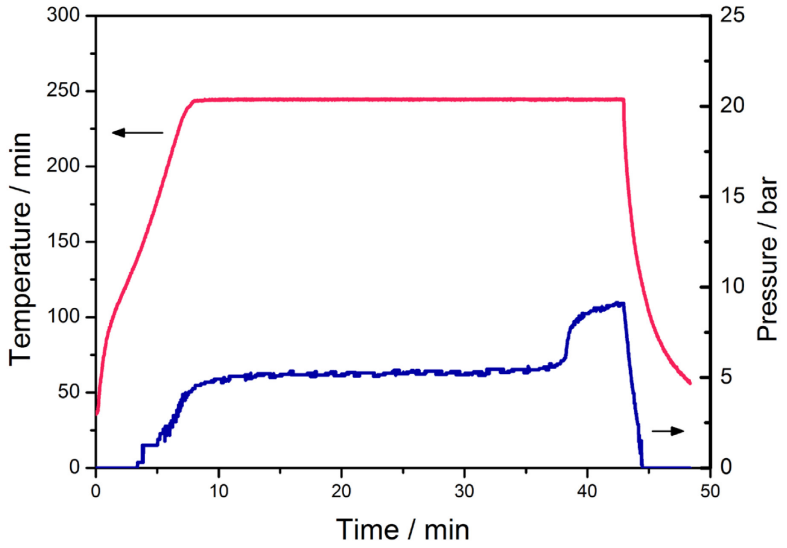

Figure 2.9 Temperature, pressure and power profiles of the synthesis of titanium oxide in glass vial under microwave irradiation without adding carbon substrates.

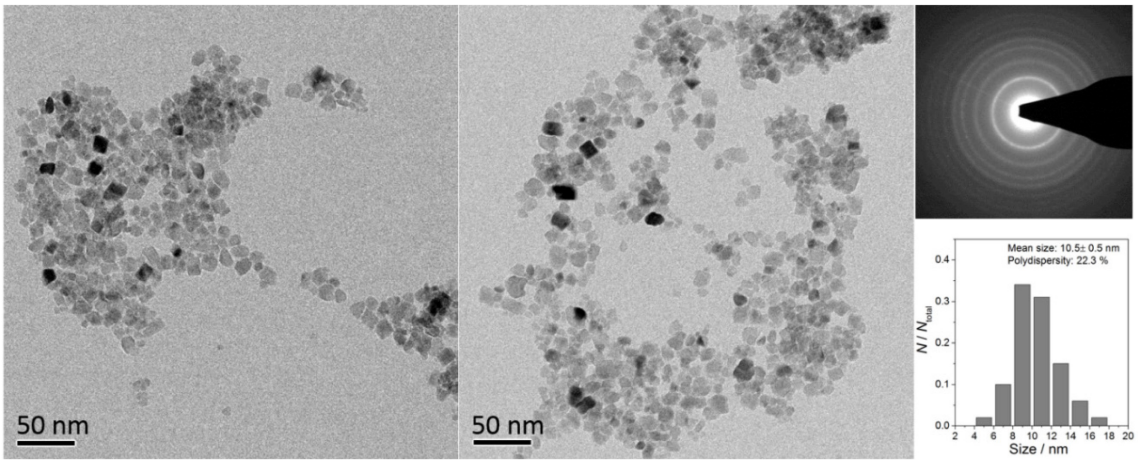

Figure 2.10 TEM images of TiO_2 nanoparticles prepared in glass vial under microwave irradiation without adding carbon substrates. Inserted is the selected area electron diffraction (SAED) pattern and particle size distribution.

Raman spectroscopy was used to confirm the crystal phases and structural details of the products. As shown in Figure 2.11, for TrGO-A, four Raman signals at 144, 200, 396, 510 and 634 cm^{-1} can be assigned to the E_g, E_g, B_{1g}, A_{1g} or B_{1g}, and E_g modes of anatase TiO_2, respectively[70,71]. The Raman spectra of the other samples show similar signals, indicating that all the TiO_2@rGO and TiO_2@AC composites consist of anatase phase nanocrystals. Raman scattering is a sensitive probe to characterize the short-range order and microstructure of

materials. In polycrystalline nanomaterials, the grain boundary breaks the translational symmetry and generates new phases between neighboring grains[72]. Due to phonon confinement effects, the Raman signals become broad and blue-shifted when the sample have local disorder or low crystallinity, exhibiting a large linewidth (FWHM) and increased frequency. Figure 2.11c illustrates the relationship between grain size obtained from XRD analysis and both Raman shift and linewidth for the strongest E_g. Compared to TrGO-A, a blue-shift of 4 cm^{-1} was observed for the TrGO-G, TrGO-S and TrGO-R samples. That is mainly due to the decrease in grain size, as discussed above. The linewidth of TrGO-R is 24 cm^{-1}, which is much larger than for the samples prepared under microwave irradiation. The larger linewidth of TrGO-R may result from the smaller grain size and lower crystallinity of the corresponding TiO_2 nanoparticles. An analogous trend in the Raman spectra results is found for the TiO_2@AC composites (Figure 2.11b, c).

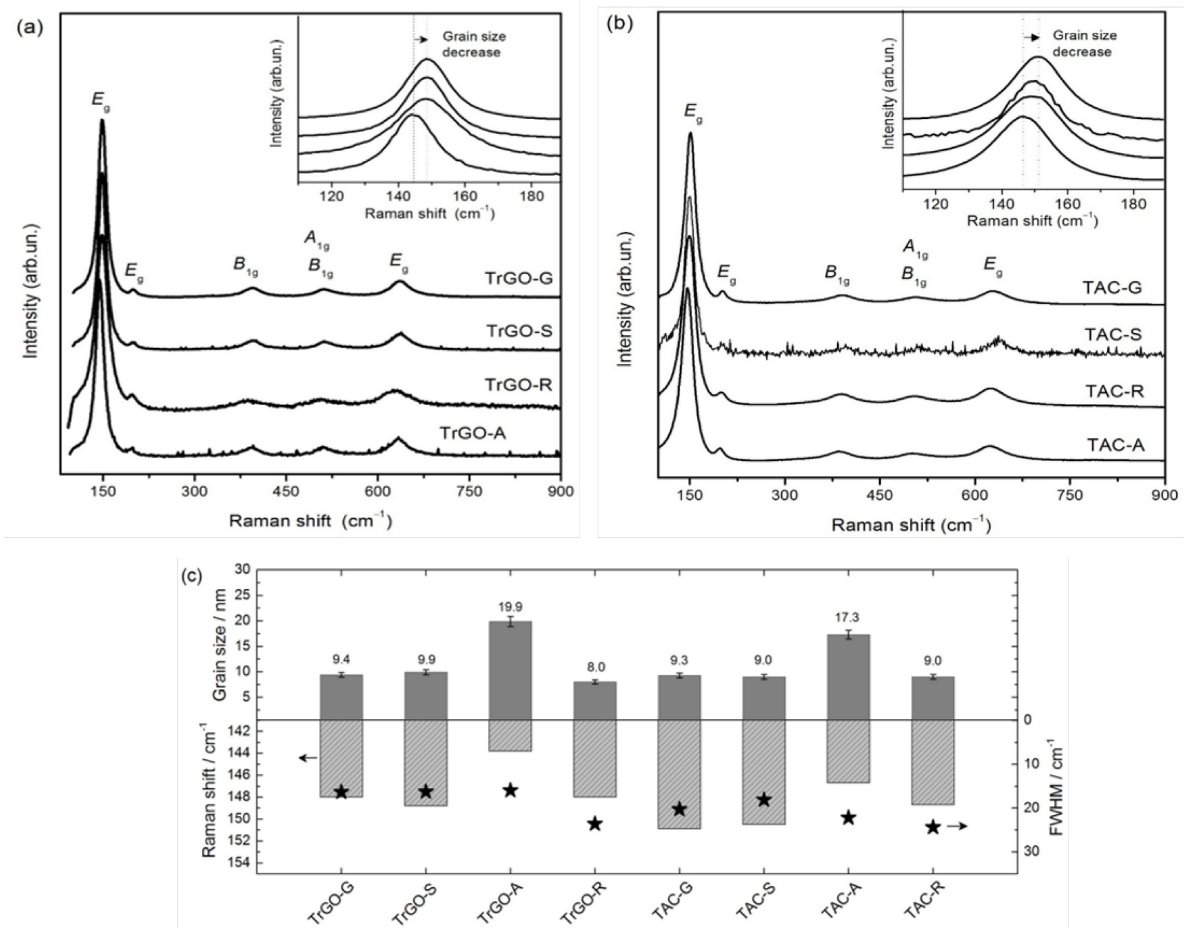

Figure 2.11 (a) TiO_2 vibration modes region of the Raman spectra of the TiO_2@rGO and (b) TiO_2@AC composites. Insets show the region of the most intense E_g vibration mode, sensitive to phonon confinement effects. (c) relationship between grain size and phonon frequencies and linewidths. Grain sizes were calculated from the XRD patterns.

To investigate the chemical oxidation state of Ti in the composites, X-ray photoelectron spectra (XPS) were measured. The Ti 2p core level XPS spectra, as shown in Figure 2.12. The binding energies of Ti $2p_{3/2}$ and Ti $2P_{1/2}$ are equal to 459.0 eV and 464.9 eV, respectively, which confirm the oxidation state of titanium is 4+ and agrees with other XPS analysis of anatase titanium oxide reported in the literatures[73]. Furthermore, the symmetric peaks of Ti 2p indicate that stoichiometric TiO_2 with a low concentration of defects was produced in all the syntheses. It is worth noting that formation of C-O-Ti bonds does not cause alterations in the Ti 2p XPS spectra, which would be expected in the case of C-Ti bond formation[74].

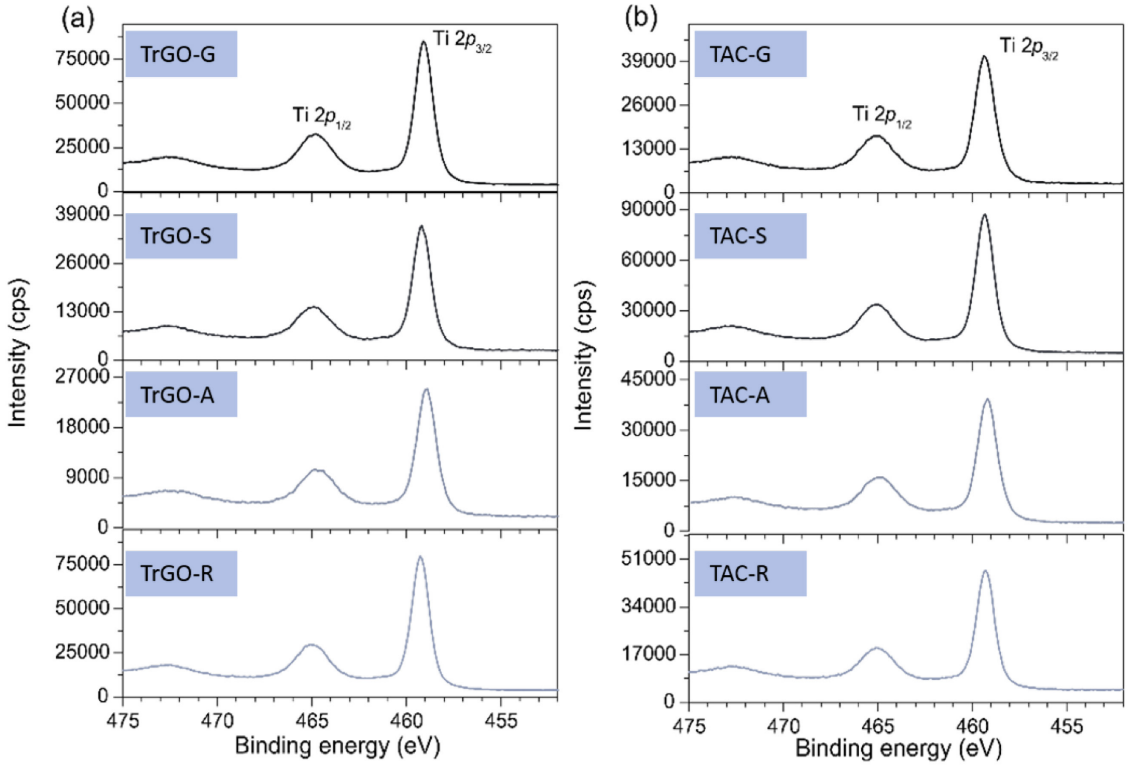

Figure 2.12 Ti 2p core level X-ray photoelectron spectra (XPS) of the TiO_2@rGO (a) and TiO_2@AC (b) composites.

The results discussed above show that rapid heating of the reaction mixture leads to the formation of TiO_2 nanoparticles with smaller size, smaller crystallite size, narrower particle size distribution, and more uniform morphology compared to low heating rates, which explains why the characteristics of the oxide in the TrGO-R and TAC-R materials are closer to those produced in the microwave reactor than those of TrGO-A and TAC-A. The size and morphology of the TiO_2 nanoparticles, as well as the carbon coating, are the same for the samples synthesized in the MW-glass and MW-SiC vials, that is, when the microwave temperature profile is reproduced through conventional heating mechanisms a similar outcome

is obtained. This means that the structural and morphological characteristics of the titanium dioxide are not affected by the heating mechanism or microwave electromagnetic field.

These results match those reported for various oxides and metal nanoparticles, in which the high heating rates achieved under MW irradiation resulted in smaller particles with improved monodispersity, compared to slower conventional heating.[36,75-78] MW heating was found to accelerate both the nucleation and growth stages of particle formation, although in several works it seems to have a more pronounced effect on the nucleation kinetics. [36,78] For example, MW irradiation appeared to affect more the nucleation stage of Silicalite-1 and VSB-5 oxides formation than their growth.[78] Similarly, Bilecka *et al.*[36] reported almost 1 order of magnitude increase in the rate constant of the reaction generating the monomers during the synthesis of ZnO nanoparticles in benzyl alcohol, while the increment in the rate constant of crystal growth was lower. Accordingly, high heating rates enhance the kinetics of TiO_2 nucleation resulting in a higher amount of uniform small nuclei for subsequent growth. Increasing the heating rate of the synthesis also improves the coating process of the carbons. A more homogeneous coating was accomplished with the MW syntheses, possibly because the MW temperature profile could not be reproduced outside the MW reactor. These results highlight some of the benefits of performing inorganic syntheses in a MW reactor, regardless of the heating mechanism. Not only it allows the precise control of the ramping, holding and cooling steps, which enhances synthesis reproducibility, but more importantly it allows performing reactions in times so short that are sometimes difficult or impossible to reproduce with an oil bath or autoclave.

2.2.3 Interface characteristic of TiO_2 nanoparticles and carbon

Figure 2.13a shows the C 1s core level X-ray photoelectron spectra of the TiO_2@rGO composites and reduced graphene oxide. The reference sample (rGO-G) was prepared in a glass vials in the same conditions used for the synthesis of composites but without adding metal oxide precursor. The main signal of binding energy at 284.6 eV is assigned to the C-C or C=C bonds, and three minor peaks at 286.3 eV, 287.5 eV and 289.3 eV are originated from C-O, C=O and O-C=O bonds, respectively. The relative area percentages of the three latter contributions are shown in Figure 2.13b for the rGO and TiO_2@rGO materials. The atomic percentages of carbon, oxygen and titanium were calculated from spectral deconvolution and are summarized in Table 2.3. The C/O atomic ratio represents the extent of the reduction of the carbon materials, and is around 2.7 for graphene oxide prepared through strong oxidation processes[79]. It is known that benzyl alcohol is a mild reduction agent of carbon materials, decreasing their oxygen content.

Therefore, the C/O ratio of rGO-G is 7.16, which is for example higher than that of reduced graphene oxide prepared using sodium borohydride ($NaBH_4$) as reducing agent (5.3)[80], but lower than that reduced by hydrazine hydrate (10.3) [81].

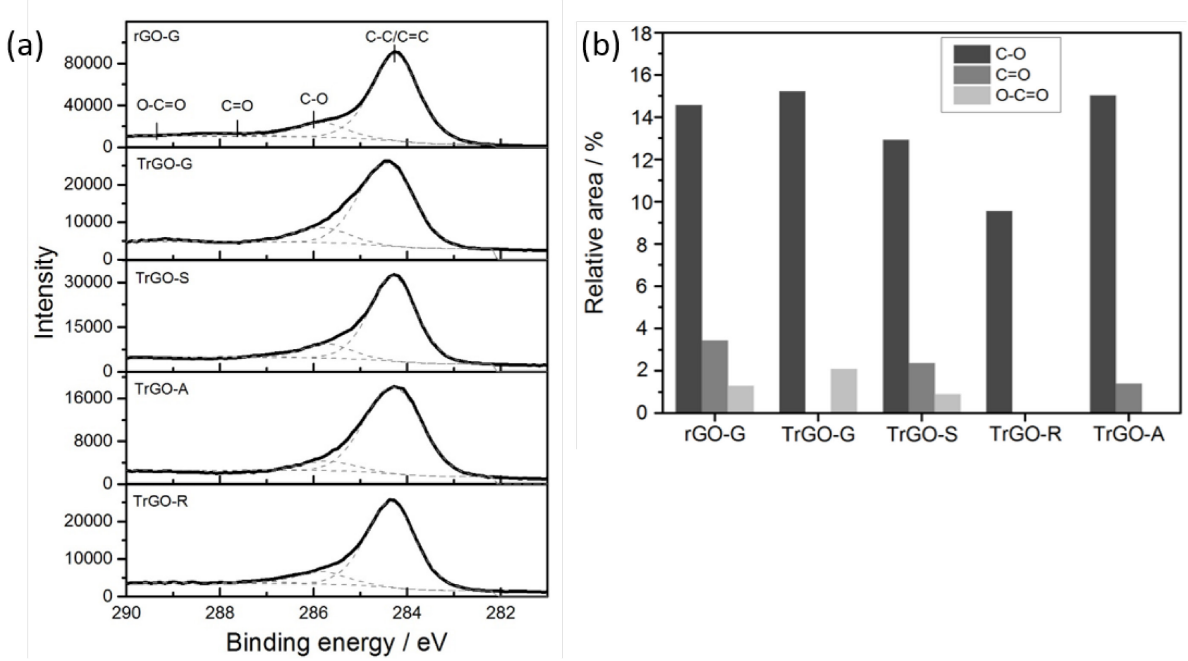

Figure 2.13 a) C 1s core-level X-ray photoelectron spectra of the rGO-G and TrGO composites, and b) the relative area percentages estimated from deconvolution of the C 1s spectra.

Table 2.3 Composition of the prepared TiO_2@rGO and TiO_2@AC structures and reference carbons determined by XPS analysis.

Sample	C (at%)	Ti (at%)	O (at%)	TiO_2 (wt%)
rGO-G	87.75	0	12.25	0
TrGO-G	41.83	16.58	41.59	68.42
TrGO-S	60.35	10.66	28.99	50.11
TrGO-R	59.07	10.54	35.36	47.30
TrGO-A	46.77	15.27	37.96	64.19
AC-G	97.86	0	2.15	0
TAC-G	55.28	12.91	31.81	57.58
TAC-S	50.44	14.59	34.97	62.52
TAC-R	52.60	14.01	33.39	60.93
TAC-A	66.09	10.02	23.89	48.34

The C 1s core level XPS spectra of the reference AC-G and TiO_2@AC composites, and their relative area percentages are shown in Figure 2.14. The relative surface composition of the carbon in the TrGO-G and TAC-G composites is different from those of the respective reference carbons rGO-G and AC-G. The differences are much more pronounced for the amorphous carbon, for which the C-O, C=O and O-C=O percentages are 50% or more above those of AC-G. These results suggest that the carbon surface is involved in reactions during the formation of the TiO_2 nanoparticles. It is possible that reactive intermediate species, generated in the vicinity of the carbon during the TiO_2 synthesis, react with the carbon surface, leading to the covalent attachment of the metal oxide. The formation of C-O-Ti bonds has been reported before for composites of TiO_2 with carbon nanotubes and reduced graphene oxide.[60,63,82,83] Covalent bonding may involve reactions of the oxide with oxygen-containing moieties of the carbon such as carboxyl and carbonyl groups. Zhang *et al.*[82] reported that the chemical attachment of preformed TiO_2 particles to reduced graphene oxide under hydrothermal treatment occurred by reaction of the carboxyl functionalities with the TiO_2 surface. TEM images of the composites showed that the particles were preferentially deposited along the wrinkles and edges of the rGO sheets, where carboxyl and carbonyl groups are located, supporting their hypothesis. Reaction of TiO_2 intermediates with these groups can account for the low O-C=O/C=O relative percentages found for some of the composite samples in this work (*e.g.* for the materials prepared in the autoclaves). However, for sample TAC-G there is an increase of the C-O, O-C=O and C=O percentages compared to AC-G. These results resemble those obtained for carbon-doped TiO_2 materials, in which C-O-Ti bonds were created.[84] The C 1s spectra of those materials showed contributions in the carbon-oxygen bonding region ascribed to O-C=O and C=O, which were considered indicative of the formation of C-O-Ti bonds in the materials. Therefore, the generation of O-containing functionalities upon reaction that was found for some of the composites suggests the chemical attachment of TiO_2 to the carbon.

The difference between the surface composition of the carbon in the TrGO composite and rGO-G is much less pronounced than observed for TAC-G, which could be considered an indication that less extensive chemical bonding occurred in TrGO-G. However, the different behavior may simply be due to the different structure and chemistry between rGO and AC, as reports in the literature suggest that chemical attachment of TiO_2 to reduced graphene oxide may occur without additional increase or even with decrease of the relative oxygen content. Perera *et al.* [63] reported the covalent attachment of titania nanotubes to reduced graphene oxide in

composites prepared by hydrothermal treatment. Graphene oxide was simultaneously reduced during the synthesis of the composites, which resulted in considerable decreases of the C-O bonding and O/C ratio of the carbon component.

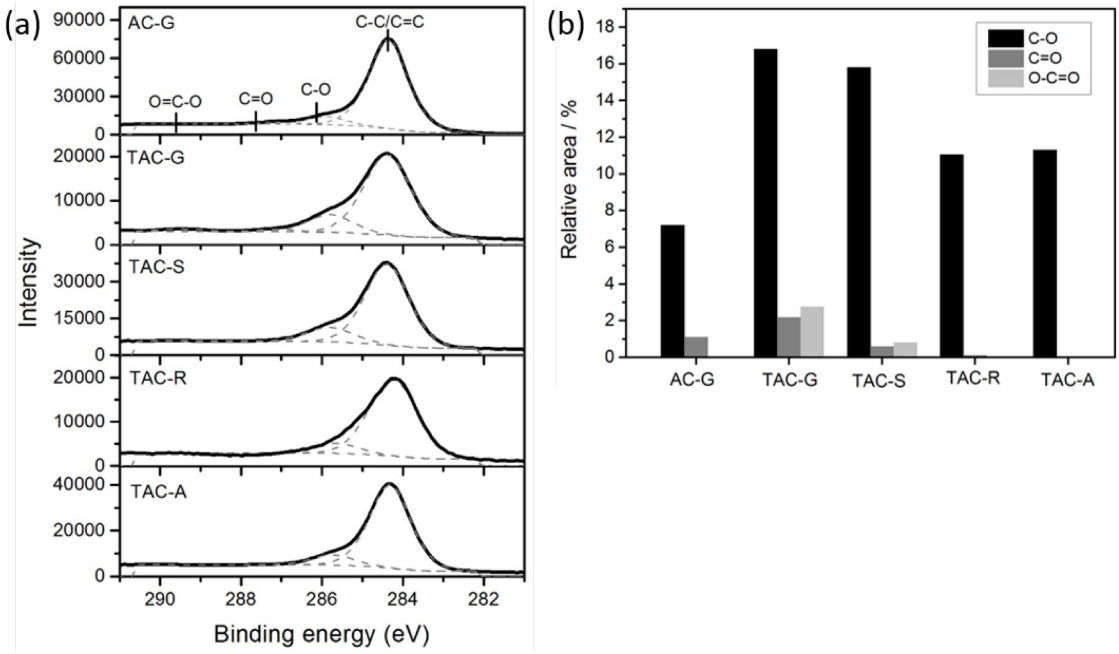

Figure 2.14 a) C 1s core-level X-ray photoelectron spectra of the AC-G and TAC composites and, b) he relative area percentages estimated from deconvolution of the C 1s spectra.

Fourier transform infrared spectra (FT-IR) have been used before to demonstrate the formation of chemical bonds between TiO_2 and carbon[63,82,84]. Therefore, the FT-IR spectra of TiO_2@rGO and TiO_2@AC composites were recorded to confirm the presence of C-O-Ti bonds (Figure 2.15). The spectra of reference reduced graphene oxide (GO) and amorphous carbon (AC) were measured for comparison. For graphene oxide, the strong FT-IR signal between 1000 and 1220 cm^{-1} originates from the vibration of C-O bonds in the O-containing groups. The band at 1575 cm^{-1} is assigned to C=C skeleton vibrations and the band at 1733 cm^{-1} is assigned to the C=O stretching vibration from carbonyl groups[85]. Other two bands at 692 cm^{-1} and 735 cm^{-1} are attributed to C-H stretching in aromatic group. The intense signals indicate that graphene oxide is effectively functionalized with a variety of O-groups on both the edges and basal plane. The vibration of Ti-O-Ti bonds produces bands at 480 cm^{-1} and 690 cm^{-1}. A broad and intense band ranging from 1000 cm^{-1} to 400 cm^{-1} was detected in the spectra of the composites, which is considered as a combination of the Ti-O-Ti vibration bands with a band at *ca.* 798 cm^{-1} ascribed to the vibration of C-O-Ti bonds.[63,82]

For amorphous carbon (and all the other samples), the strong signal centered at 3400 cm^{-1} is assigned to the O-H stretching vibration of adsorbed H_2O. The band assigned to the carbon skeleton vibrations is also found in this material at 1637 cm^{-1}. Several small bands in the range 1000-1400 cm^{-1} indicate the presence of C-O containing groups on the surface of AC. Broad band at 500-700 cm^{-1} overlapped with a band at 798 $cm^{-1}$are found in the spectra of TiO_2@AC as in the spectra of TiO_2@rGO, which are attributed to Ti-O-Ti and C-O-Ti vibrations, respectively. Excluding this low wavenumber region, the spectrum of TAC-A is very similar with that of amorphous carbon, suggesting that the surface environment did not changed so much after the TiO_2 loading. This is consistent with the analysis of the TAC-A TEM images where large portions of carbon spheres are uncoated and big amounts of nanoparticles are distributed separately.

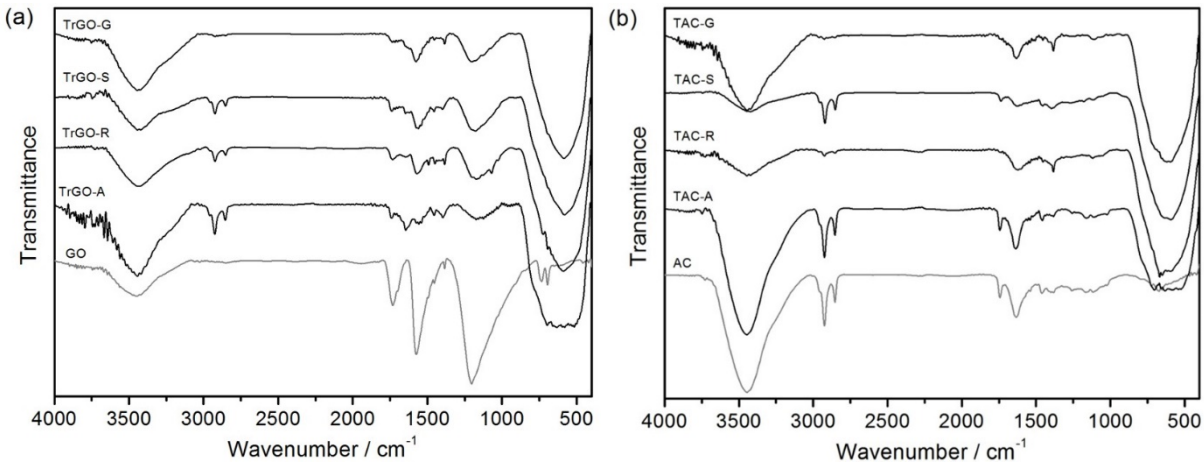

Figure 2.15 FT-IR spectra of TiO_2@rGO and TiO_2@AC composites.

Additional information on the interface between TiO_2 and carbon materials was obtained from the electron spin resonance (ESR) spectra and analysis of the sp^2 region of the Raman spectra. ESR is a highly sensitive technique for detecting and studying paramagnetic species. In particular, it provides valuable information on the π electrons and paramagnetic species of carbon materials such as free radicals, which affect their chemical, electronic, and optical properties.[86-92] This technique is also useful for detecting spin density changes in functionalized carbon materials and carbon composites, and can contribute to the understanding of coupling effects.[89]

Figure 2.16 shows the ESR spectra of the composites and reference carbon materials rGO-G and AC-G. The spectra of the materials prepared in the MW-glass vials are very different from the corresponding reference carbon materials. No signals are detected on the spectrum of AC-

G while the spectrum of rGO-G presents a broad, weak, and anisotropic signal. On the contrary the spectra of TrGO-G and TAC-G show a very intense signal, which is slightly anisotropic for the latter. The measured g factor is very close to the value for free electrons (g_e=2.0023) and typical of localized states on carbon. The absence of other resonances, such as at g=1.98 typical of Ti^{3+} defects and indicative of oxygen vacancies in TiO_2,[93,94] is in agreement with the XPS results and confirms that the ESR features of our composites are attributable to electrons localized on carbon species (carbon radicals).

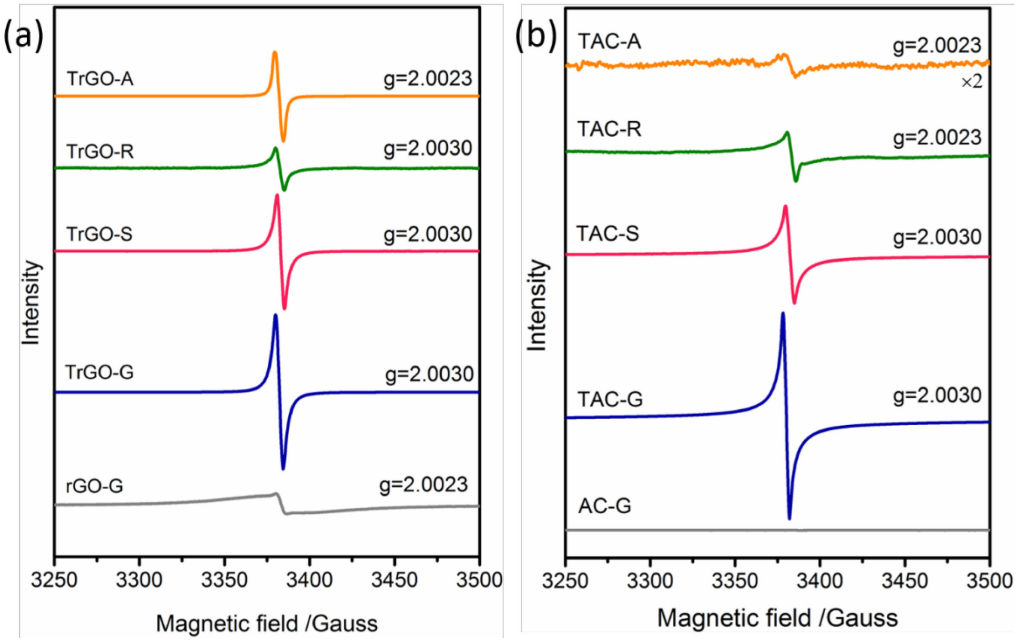

Figure 2.16 Electron spin resonance spectra of the (a) TrGO and (b) TAC composites and corresponding reference carbon materials.

The interpretation of the ESR spectra of graphene-related carbon materials is controversial. Su *et al.*[88] suggested that the signal detected in porous graphene oxide comprised two contributions: a narrower component with g=2.002, assigned to sigma dangling bonds, and a broader component attributed to localized spins at the graphene edges. Conversely, Barbon *et al.*[95] highlight that in pure, single layer graphene the isotropic signal with g-value of 2.003 is due to unpaired electrons localized on edge states. Moreover, they reported that radicals with low-anisotropic g-tensors with typical values of 2.003~2.004 are likely to be delocalized systems constituted by carbon, hydrogen, and adventitious oxygen. Recently, Yang *et al.*[90] detected a sharp and intense signal in the spectrum of GO, very similar to that of TrGO-G, originating from the addition of hydroxyl groups to the graphene layer upon reaction with hydrogen

peroxide. The signal was ascribed to carbon radicals located on the GO basal plane that are stabilized by the neighboring π conjugated double bonds.

ESR active species have been also detected on carbon materials as a result of the introduction of heteroatoms, such as the incorporation of oxygen upon reaction of the carbon with oxidizing agents.[89,90] Similarly, the paramagnetic defects detected on the composite samples most likely originate from the reactions that lead to the chemical attachment of TiO_2 to the carbon matrix. The intensity of the signal varies among the composites (Table 2.4). The composites synthesized with the MW-SiC vials show resonances slightly less intense than the corresponding TrGO-G or TAC-G samples, and the signal anisotropy also increases for TAC-S as compared to TAC-G. In general, the spectra of the materials produced using the autoclave and reactor display weak and anisotropic signals.

Table 2.4 Spin density of rGO and amorphous carbon references and their composites.

Sample	Spin density / 10^{17} cm^{-3}
rGO-G	0.74
TrGO-G	108.00
TrGO-S	41.70
TrGO-R	0.47
TrGO-A	39.50
AC-G	0.00
TAC-G	3.93
TAC-S	2.93
TAC-R	0.11
TAC-A	0.05

The amount of paramagnetic defects (spin density) detected by ESR is likely associated with the formation of TiO_2 at the carbon surface, and therefore provides indirect indication of the extent of chemical bonding occurring between the oxide particles and carbon. The results (Table 2.4) suggest that chemical bonding is more extensive for TrGO composites compared to the TAC homologues. To support this hypothesis the ESR spectra of TrGO-G and TAC-G during and after UV/Vis irradiation were measured. For TrGO-G, the concentration of paramagnetic defects sharply decreases (-23%) upon UV/Vis irradiation (500 s), suggesting the occurrence of an efficient electron transfer between the conduction band of anatase and the rGO layer.

More significantly, the signal depletion is considerably larger than that observed for TAC-G (-13 %). This indicates the existence of stronger oxide-carbon interactions in TrGO composites.

The fact that no significant increase of the relative C-O, C=O, or O-C=O percentages was observed for TrGO compared to rGO-G indicates that chemical attachment to rGO involves mostly reactions with oxygen surface groups already present on the carbon. Since carboxyl functionalities are located only at the edges of the rGO holes and sheets in limited quantity, and our samples have high amount of nanoparticles covering the rGO sheets and not only along the edges, we conclude that chemical attachment of the TiO_2 particles to rGO involves mostly breaking of C-O-C bonds, for example in epoxides. These type of groups are located on the basal plane of GO, which could generate π-conjugated carbon radicals on the basal plane, as reported by Yang *et al*.[90]

The shape of the Raman spectra is known to be sensitive to the changes introduced into the graphitic network and was employed here to get more information of the chemical attachment of TiO_2 nanoparticles to rGO and amorphous carbon. Figure 2.17a shows the C sp^2 vibration mode region in the Raman spectra of the reference carbons and composites. The G band located at around 1590 cm^{-1} has E_{2g} symmetry. It is associated with the in-plane bond stretching vibration of pairs of C sp^2 atoms, thus it occurs at all sp^2 sites but not only in hexatomic rings[96]. The D band at 1346 cm^{-1} is a breathing mode with A_{1g} symmetry, which requires the presence of disorder or defects within the hexagonal graphitic structure for its activation. Activated by disorder, the D-band progressively broadens and becomes more intense with respect to the G-band with increasing deviation from perfect hexagonal carbon structure. The intensity ratio of D-band and G-band is indicative of the extent of disorder or defects in graphitic structure. The Raman results are summarized in Table 2.5. Compared with the spectrum of rGO-G, the G-band slightly shift to higher wavenumbers and ω_G (FWHM of G-band) are narrower in TrGO-G and TrGO-S, both of these effects are caused by the introduction of structural imperfections in graphene[27,97]. However, it is difficult to infer any chemically intrinsic change in the graphitic substrate or any specific interaction of the oxide nanoparticles with the graphene oxide only from these small variations in G-band blueshift and linewidth.

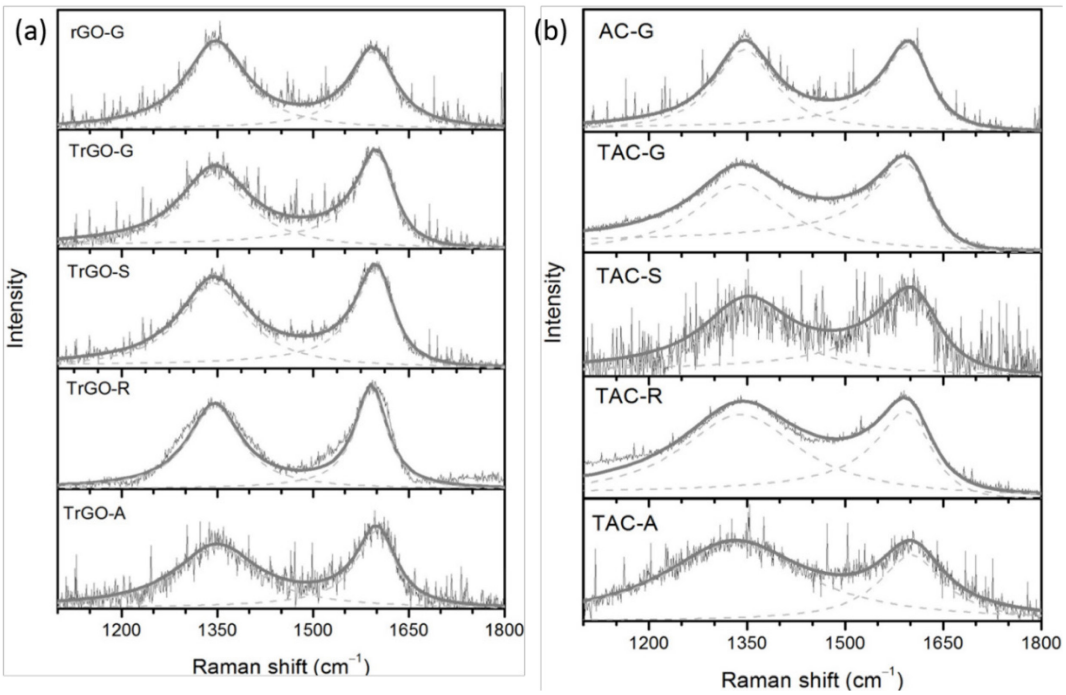

Figure 2.17 Raman spectra of TrGO and TAC composites, and references (rGO-G, AC-G).

The analysis of the I_D/I_G is believed to be a more efficient way to unveil the modification effect of TiO_2 nanoparticles over graphene oxide. The decrease in I_D/I_G is observed for all of the TrGO composites, suggesting a reduction of the sp^2 defects in the hexagonal rings. F. Inoue *et al.*[98] reported a similar trend in TiO_2-functionalized multiwalled carbon nanotubes (f-MWNTs/TiO_2) composite. In the presence of TiO_2 nanostructure, the D/G intensity ratio of the f-MWNTs decreased from 1.46 to 0.92, which was regarded as an evidence of the interaction between TiO_2 nanostructure and f-MWNTs. The decline of D/G intensity ratio was explained as the nanostructured TiO_2 attached to the outer wall of carbon nanotubes decreased the characteristic Raman signals of these functionalized outer tubes and resembled the spectra of the pristine inner carbon nanotubes. In the case of TiO_2@rGO composites, one explanation for the shielding effect on the Raman spectra is that the TiO_2 nanoparticles prefer to attach on the area that has more O-groups and the interfacial bonding between nanoparticles and rGO nanosheets transforms sp^2 defects into sp^3 defects which would not contribute to the D-band intensity, consequently diminishes the I_D/I_G.

Table 2.5 Results of the spectral deconvolution of the Csp^2 vibration modes region of the Raman spectra of the TiO_2@rGO and TiO_2@AC composites and reference carbons.

Sample	γ_D (cm^{-1})	ω_D (cm^{-1})	γ_G (cm^{-1})	ω_G (cm^{-1})	I_D/I_G
rGO-G	1347.5	114.3	1593.5	85.3	1.09
TrGO-G	1345.7	130.5	1599.0	72.5	0.81
TrGO-S	1344.9	128.4	1597.8	71.8	0.86
TrGO-A	1348.7	156.4	1599.6	76.0	0.78
TrGO-R	1342.0	127.9	1589.8	94.1	0.82
AC-G	1345.9	111.7	1596.4	87.3	0.97
TAC-G	1349.6	172.0	1591.3	100.3	0.84
TAC-S	1350.0	160.0	1599.1	115.0	0.84
TAC-A	1330.0	264.7	1602.3	120.6	1.17
TAC-R	1340.0	220.0	1592.5	102.2	1.00

Considering that the diameter of amorphous carbon spheres is around 30-50 nm, the shielding effects may be stronger in the presence of TiO_2. The spectra of TAC-G and TAC-S exhibit lower I_D/I_G ratios than AC-G, while the spectra of those prepared in autoclave and micro reactor, TAC-A and TAC-R, have similar I_D/I_G ratios compared with the AC reference. That means the TiO_2@AC composites prepared under microwave irradiation have an intense chemical attachment of the oxide coating, and shielded the Raman spectra of the amorphous carbon from oxidized surface. But for the samples prepared in autoclave and micro reactor, the interaction of the two phases is not sufficient to affect the spectra of the carbon or there is not enough sp^2 defects to sp^3 defects transformation to diminish the D-band intensity.

2.2.4 Stability test of TiO_2 nanoparticles on carbon supports

The stronger the interaction between the oxide nanoparticles and the carbon surface the more stabilized the nanoparticles will be under harsh experimental conditions. To evaluate the strength of TiO_2-carbon interactions in the composites, a stability test was performed as follows: first, the samples were dispersed in ethanol and vigorously stirred for 48 hours, and then the suspension was sonicated for 2 hours; after, the supernatants were collected for inductively coupled plasma mass spectrometry (ICP-MS) analysis. During the first step, weakly bonded nanoparticles detached from the carbon surface and dispersed into the ethanol. Thus the higher

amount of TiO_2 detected by ICP-MS analysis the less stabilized were the nanoparticles in the composites and the weaker were the interactions between oxide and carbon.

The results of the tests are shown in Figure 2.18a. The TiO_2 nanoparticles in TrGO-G are very stable and less than 0.05 μg of TiO_2 per mg of sample was detected and thus detached from the surface. The stability trend of TiO_2 nanoparticles on rGO surface among the TrGO composites is TrGO-G >TrGO-S >TrGO-R >TrGO-A. This trend is consistent with the interface characterization results, as they suggest that more covalent bonding is found in the samples prepared under microwave irradiation and in the micro reactor compared with the one prepared in the autoclave. This confirms that a stronger interfacial interaction results in a better stabilization of the oxide nanoparticles on rGO nanosheets. Although no significant difference is found in TrGO-G and TrGO-S samples from the structural and morphological investigation, TrGO-G exhibits slightly better stability in this test, which means the stability of the composites is also affected by the heating mechanism. A similar trend is observed for the TAC composites (Figure 2.18b). Compared to reduced graphene oxide, more titanium oxide detaches from the amorphous carbon spheres, which is likely caused by the high surface area of the rGO nanosheets as well as the abundant and O-groups on the GO surface.

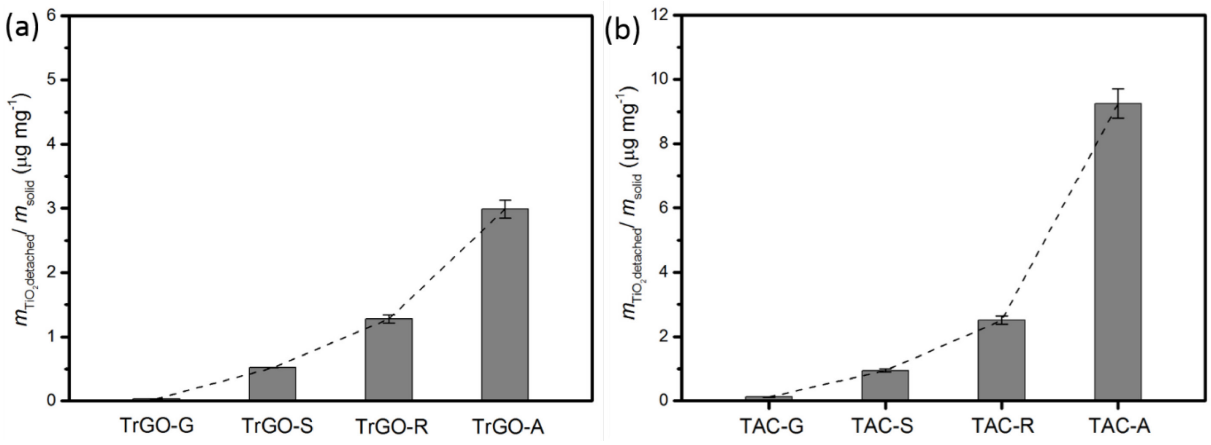

Figure 2.18 Amount of TiO_2 detached from the (a) rGO and (b) AC surface after stirring/sonication.

2.2.5 Photocatalytic performance

The effect of the strength of the TiO_2 and carbon interactions on the catalytic performance of the composites was evaluated using a test model photocatalytic reaction, specifically the photocatalytic degradation reaction of rhodamine B (RhB). Figure 2.19 illustrates the time-resolved absorption spectra of RhB for the TrGO-G sample. Since the photocatalytic activity of TiO_2 is influenced by the crystallinity of the oxide particles, only the samples containing

TiO_2 particles with similar characteristics are compared to determine the effect of the heating rate and mechanism on the photocatalytic performance.

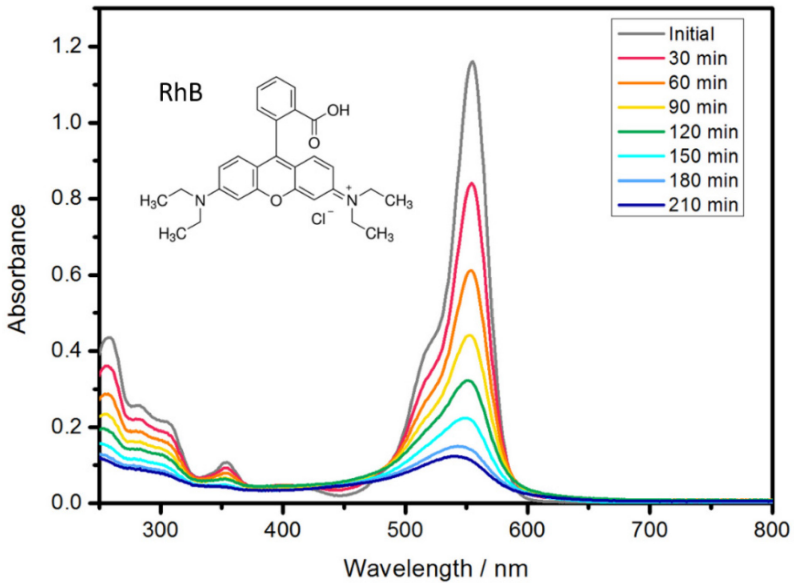

Figure 2.19 Time-resolved absorption spectrum of RhB for TrGO-G.

Figure 2.20 shows the photodegradation curves of RhB under UV irradiation of the TiO_2/carbon composites. The results show that for both carbon substrates, the samples prepared in microwave glass vials have the best photocatalytic activity, while the performance of those prepared in the micro reactor is worse than others. In TiO_2/carbon materials, the carbon acts as an electron scavenger during the UV irradiation and prolongs the lifetime of the photo-generated holes for efficiently oxidizing the organic molecules. Graphene is considered a promising electron acceptor due to its 2D π-conjuncted structure. A strong interaction between TiO_2 and rGO benefits the formation of a Schottky barrier where the photo-generated electron-hole pairs are separated from each other[99]. This formation of Schottky barrier results in the rGO sheet having an excess of electrons and the n-type TiO_2 an excess of positive charge and suppresses the recombination of electron-hole pairs, leaving more charge carriers to produce active radicals and promote the photodegradation reaction. Due to the excellent charge carrier conductivity, an effective photo-generate charge separation can be achieved and simultaneously electrons can be distributed rapidly in the graphitic plane. Thus, the presence of graphene sheets or carbon nanotubes enhances the photocatalytic activity of TiO_2 materials[82,100]. The photodegradation mechanism is illustrated in Figure 2.21. With an intensive contact of TiO_2 on the carbon surface, such as chemical attachment formed by covalent bonding, the photo-generate electrons may easily sink in the carbon substrates. Moreover, due to the extraordinary

features of reduced graphene oxide in terms of structure and morphology such as high surface area, high electronic conductivity and light transparency, TiO_2@rGO composites perform better than TiO_2@AC composites.

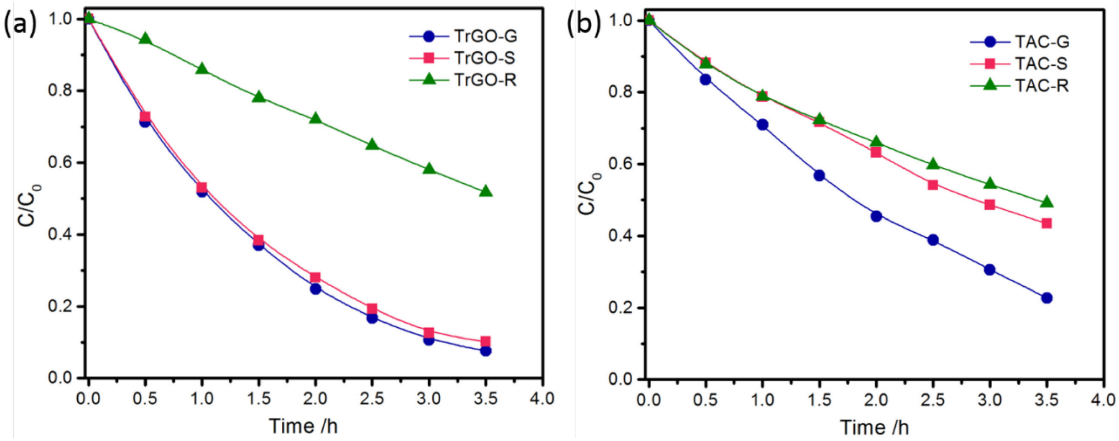

Figure 2.20 Photocatalytic degradation curves of RhB with TiO_2@rGO (a) and TiO_2@AC (b).

The reactions taking place during the TiO_2 formation that lead to covalent binding of the metal oxide with generation of C radicals, and consequent stabilization of the nanoparticles, are promoted by the fast heating of the reaction mixture. Therefore, the samples synthesized in the MW-glass and MW-SiC vials are the most stable, since the fast heating achieved in the MW reactor could not be reproduced in the autoclave synthesis. The rapid heating of the synthesis likely increases the kinetics of the reactions with the carbon surface in the same way it increases the kinetics of nanoparticle nucleation and growth. However, even when the temperature profile of the synthesis performed in the MW-glass vials is reproduced through conventional heating mechanisms using the SiC vials, nanostructures with slightly different stability and interfacial characteristics are obtained. The materials prepared under MW irradiation show improved stability, and slightly more extensive changes on the carbon component after synthesis than the MW-SiC materials. This suggests that chemical attachment and stabilization of the nanoparticles is further promoted by the MW heating mechanisms.

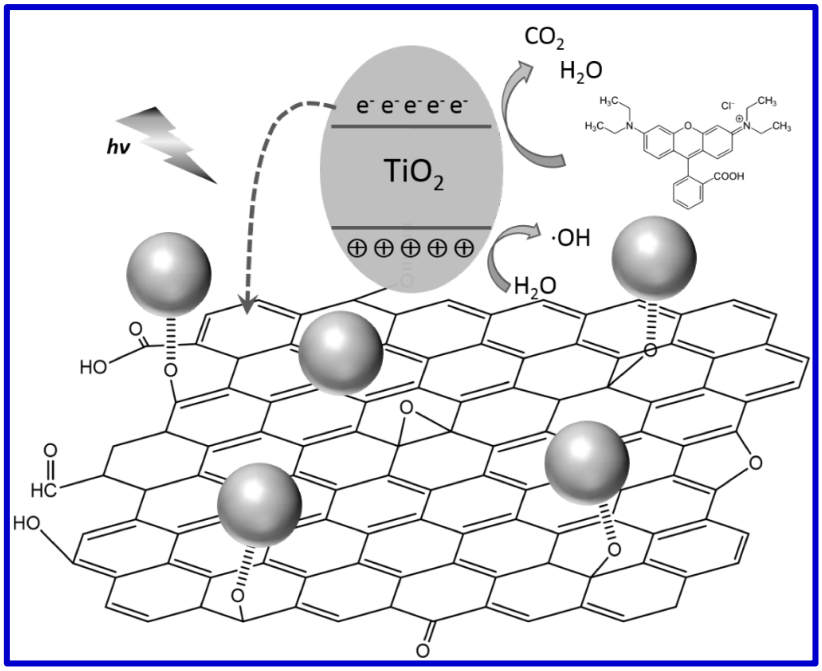

Figure 2.21 TiO_2@rGO composite photodegrades RhB dye molecules under the irradiation.

Very different from the conventional heating mechanisms (convection/thermal conduction), heating of a substance under MW irradiation occurs through loss mechanisms resulting from the direct coupling of the MW radiation to the substances.[7,22] Dipolar polarization and ionic conduction are the main loss mechanisms occurring in solution, and are associated with the coupling of molecular dipoles or charged species, respectively, to the alternating electric field. On the other hand, MW heating of inorganic solids is a much more complex process that can involve several electric and magnetic loss mechanisms simultaneously, depending on the characteristics of the material (insulator, conductor, semiconductor, magnetic, etc.).[7] Carbons have a high ability for absorbing MW energy and convert it into heat.[101,102] The alternating electric field of the MW radiation induces a current of the delocalized π electrons of the graphitic regions of the carbon, and as the electrons try to couple with the alternating electric field, energy is dissipated through a resistive heating mechanism. The higher MW absorption ability of the carbon compared to the solvent (benzyl alcohol) can result in the average temperature of the carbon being slightly higher than the macroscopic temperature measured. It has been recently demonstrated that selective heating of an absorbing molecule in a less absorbing medium, and the consequent higher effective temperature of the absorbing species, can result, in certain conditions, in a MW-specific acceleration of a homogeneous chemical reaction.[103] The effective temperature of the absorbing substance will depend on the system and rate of heat transfer from the domains surrounding the adsorbing substance to the bulk, a process

that can be slower for MW heating compared to conventional heating.[103-105] On the other hand, the MW-specific selective heating of carbons and other strong MW absorbers is well-known and has been exploited for performing MW reactions involving weakly absorbing species[101].

The strong MW absorbing characteristics of the carbon further promotes the reactions of the carbon surface during the synthesis of TiO_2, which leads to the formation of more covalent bonding and improved stabilization of the particles. Since this effect occurs specifically under MW irradiation and cannot be reproduced with the SiC vial, the composites prepared with the MW-glass and MW-SiC vials have slightly different properties.

The materials with higher stability show better catalytic performance, which confirms the influence of the strength of the TiO_2-carbon interactions, and thus of the heating conditions and mechanism, on the properties of the materials.

2.3 Conclusion

TiO_2/carbon composites were synthesized in benzyl alcohol in four different ways. Compared to the conventional autoclave synthesis, fast heating methods carried out in a microwave reactor lead to a homogeneous and uniform coating of TiO_2 nanoparticles on carbon surfaces and the formation of oxide nanoparticles with smaller size and narrower particle size distribution. The syntheses carried out in microwave-transparent glass vials and microwave-shielded SiC vials had similar heating profiles and lead to materials with similar and structural morphological characteristics. A variety of characterization methods were employed to investigate the interface interaction between TiO_2 nanoparticles and carbon substrates. It was found that during the formation of anatase TiO_2 nanoparticles, the carbon substrates are involved in reactions resulting in the attachment through covalent bonding between oxide particles and carbon surface, with simultaneously generation of stable carbon radicals. The stabilization of the oxide nanoparticles on reduced graphene oxide is more efficient than on amorphous carbon spheres due to the distinct chemical nature of the former 2D nanosheets. The extent of those interactions are promoted by the fast heating rate and further enhanced by microwave irradiation. Particularly, the microwave-assisted synthesis of TiO_2/carbon nanostructures, accelerate the etherification reactions leading to the formation of monomers. On the other hand, microwave irradiation generates local hot spots on the carbon surface due to the high microwave absorption ability of carbon materials compared to benzyl alcohol. Consequently, the selective heated carbon initiates the reactions of nucleation and the growth of TiO_2 nanocrystals at its surface and produces more covalent bonds between oxide and carbon surface. Therefore, the samples

prepared in microwave transparent glass vials show the stronger interactions between TiO_2 and carbon substrates, subsequently leading to the strongest stabilization of oxide nanoparticles on carbon surface and the highest photocatalytic activity towards the photodegradation of a dye. Additionally, the rapid heating process achieved in the microwave reactor cannot be reproduced in any other way, which involves the precise control of the temperature, pressure, input power, ramping and cooling. This work shows that the specificity of the microwave heating mechanisms can be advantageous for the fabrication of carbon-based or other strong microwave-absorbing nanomaterials with enhanced interface interactions and promoted stability.

2.4 Experimental section

2.4.1 Materials

Titanium (IV) isopropoxide (99.999 %) and benzyl alcohol (99%) were purchased from Sigma Aldrich and. Graphene oxide was synthesized from synthetic graphite powder (Aldrich). The amorphous carbon (carbon black Vulcan XC72R) was purchased from Cabot. Before use, the carbon black (AC) was treated in a 5M nitric acid solution at 80°C for 4h, and subsequently washed with deionized water.

2.4.2 Synthesis method

Preparation of graphene oxide. Graphene oxide (GO) was prepared by a modified Hummers method[69]. Graphite (graphite powder, < 20 μm, Aldrich) was first pre-oxidized: 3 g of $K_2S_2O_8$ followed by 3 g of P_2O_5 were added slowly and under stirring to a suspension of 2 g of graphite powder in 40 mL of concentrated H_2SO_4. The suspension was heated at 80 °C for 5 h, after which the solid was recovered by centrifugation, repeatedly washed with water and dried. Oxidation: 2 g of pre-oxidized graphite was added to 90 mL of concentrated H_2SO_4 and stirred in an ice bath. Then, 2 g of $NaNO_3$ followed by 12 g of $KMnO_4$ were added slowly under vigorous stirring. During the addition of $KMnO_4$ the temperature was not allowed to rise above 10 °C. After stirring for 1 h in the ice bath followed by 5 days at room temperature, 250 mL of water were added slowly under vigorous stirring. The suspension was heated at 98 °C for 1 h, after which 20 mL of H_2O_2 (30 wt. %) was added slowly. The warm suspension was filtered, washed with 300 mL of 2 M HCl solution, repeatedly washed with water until pH=7 and dried at 65 °C.

Preparation of TiO_2@carbon composite. The composites were prepared through the reaction of titanium (IV) isopropoxide (TIP) with benzyl alcohol in the presence of the carbon material. The syntheses in the microwave reactor were performed using 10 mL borosilicate glass (MW-glass) or silicon carbide (MW-SiC) reactions vials. Briefly, 50 mg of GO (or AC), 1.5 mmol of TIP and 5 mL of benzyl alcohol were mixed in a glass or SiC vial in a glovebox under Ar (O_2 and H_2O < 1 ppm) and sealed with a silicone cap. The mixture was sonicated for several hours until the carbon was completely dispersed and a homogeneous suspension was obtained. The suspension was then heated in a single mode microwave reactor (Anton Parr Monowave 300), using a ramping of 8 min to reach the target temperature of 245 °C, holding time of 10 min, and subsequent quenching with compressed air. The mixture was stirred with a magnetic stir bar at 1000 rpm during all steps of the reaction. The reaction temperature was controlled with a fiber-optic temperature probe inserted into the vial. The products were separated from the liquid phase by centrifugation, washed with ethanol, and dried at 65 °C. The solutions were kept for NMR analysis.

Composites were also synthesized in a Teflon-lined stainless steel autoclave. Briefly, 50 mg of GO (or AC) and 1.5 mmol of TIP were added to 20 mL of benzyl alcohol under Ar, and sonicated to disperse the carbon. The suspensions were then transferred to the autoclave under Ar, and then heated at 245 °C for 48 h. Similar suspensions were prepared and transferred to a Parr 5500 micro reactor. The mixtures were heated as fast as possible to the target temperature (*ca.* 25 min), under stirring, maintained at 245 °C for 10 min, and then allowed to cool down to room temperature. The composites synthesized in the autoclaves were recovered by centrifugation, washed with ethanol, and dried at 65 °C.

2.4.3 Characterization

X-ray powder diffraction patterns were recorded with a STOE MP diffractometer in transmission configuration using CuKα radiation (λ=0.1541 nm). Transmission electron microscopy (TEM) images were acquired on a Philips CM 200 microscope at 200 kV. Fourier transformed infrared spectra of the samples were measured on a Thermo Scientific Nicolet iS50 spectrometer in the wavelength range of 4000-400 cm^{-1} (4 cm^{-1} resolution), using pellets of the solid diluted in KBr. Carbon elemental analyses were performed on a HEKAtech Euro EA CHNSO Elemental analyzer. The liquid phase collected after separation of the solid products were analyzed by ^1H nuclear magnetic resonance (NMR) on a Bruker AVANCE 400 spectrometer (400 MHz, $CDCl_3$, TMS).

To evaluate the stability of the composites, *ca.* 5 mg of composite was added to 3 mL of ethanol. The suspensions were stirred at 1400 rpm for 48h and sonicated for 2h. The solid was separated with a syringe filter, and the detached TiO_2 suspended in ethanol was collected. The ethanol was subsequently evaporated and the amount of Ti remaining was quantified. Titanium quantification was done by inductively coupled plasma mass spectrometry (ICP-MS) on a Thermo Scientific Element ICP-MS. All solutions were prepared using high purity HNO_3 69% (Rotipuran Supra, Carl Roth) and Milli-Q water with resistivity of 18.2 MΩ cm^{-1} at 25 °C.

X-ray photoelectron spectroscopy analyses were carried out on a K-Alpha system from Thermo Scientific, equipped with a monochromatic Al Kα source (1486.6 eV), and operating in constant analyzer energy mode with a pass energy of 200 and 50 eV for survey and high resolution spectra, respectively. A spot size diameter of 400 μm was adopted.

Electron spin resonance (ESR) spectra were recorder on a Bruker EMX spectrometer operating at the X-band frequency and equipped with an Oxford cryostat. The samples were placed into quartz glass tubes connected both to a high vacuum pumping system and to a controlled gas feed (O_2). Irradiation was performed by a UV-Vis 150 W Xe lamp (Oriel) through an optical fiber (50 cm length, 0.3 cm diameter). Samples were irradiated at 130 K in vacuum ($p < 10^{-5}$ mbar) before, during and after 30 min-long irradiation, using a modulation frequency of 100 kHz, modulation amplitudes of 2-5 gauss and a microwave power of10 mW. The *g* values were calculated by standardization with α,α-diphenyl-β-picrylhydrazyl. The spin concentration was obtained by double integration of the resonance lines, referring to the area of the standard Bruker weak pitch (9.7×10^{12} ± 5% spins cm^{-1}). Accuracy on double integration was ± 15%. Care was taken to always keep the most sensitive part of the ESR cavity (1 cm length) filled.

Raman scattering (excitation energy: 2.33 eV) was measured at room temperature using a Horiba Jobin Yvon spectrometer (objective: 100X). The use of a low laser power density (below $1x10^5$ W/cm^2) prevented excessive heating of the samples and annealing effects. Spectra from several random positions on each specimen were collected on account of the possible spatial non-homogeneity of the samples. The features arising from the oxide vibrations modes were fitted to Lorentzian lines superimposed to a constant background. The spectral profile in the region of the Csp^2 vibration modes was reproduced by the use of a Lorentzian line for the D-band and a Breit-Wigner-Fano line for the G-band.

Photocatalytic performance was evaluated by degradation reaction of rhodamine B (RhB) under UV irradiation. 10 mg of sample was dispersed in 100 mL of 20 μmol L^{-1} aqueous solution of

RhB. Prior to irradiation, the suspensions were stirred in the dark for 30 min to achieve adsorption equilibrium. After irradiating the mixture at 365 nm for the desired time, 2 mL of suspension was extracted and centrifuged to recover the supernatant. The amount of RhB in the supernatant was obtained by measuring the absorption at the peak around 550 nm with a ThermoScientific Evolution 220 UV-vis spectrophotometer. Afterwards, the extracted subsample was remixed into the suspension.

2.5 Bibliography

1. Galema, S. A., Microwave chemistry. *Chemical Society Reviews* 1997, 26 (3), 233-238.
2. *Microwave in Nanoparticle Synthesis: Fundamentals and Applications*. (Eds.: Horikoshi, S.; Serpone, N.), Wiley-VCH: Weinheim, 2013.
3. Komarneni, S.; Roy, R., Titania gel spheres by a new sol-gel process. *Materials Letters* 1985, 3 (4), 165-167.
4. Gedye, R.; Smith, F.; Westaway, K.; Ali, H.; Baldisera, L.; Laberge, L.; Rousell, J., The use of microwave ovens for rapid organic synthesis. *Tetrahedron Letters* 1986, 27 (3), 279-282.
5. Giguere, R. J.; Bray, T. L.; Duncan, S. M.; Majetich, G., Application of commercial microwave ovens to organic synthesis. *Tetrahedron Letters* 1986, 27 (41), 4945-4948.
6. Namboodiri, V. V.; Varma, R. S., Microwave-accelerated Suzuki cross-coupling reaction in polyethylene glycol (PEG). *Green Chemistry* 2001, 3 (3), 146-148.
7. Baghbanzadeh, M.; Carbone, L.; Cozzoli, P. D.; Kappe, C. O., Microwave-Assisted Synthesis of Colloidal Inorganic Nanocrystals. *Angewandte Chemie International Edition* 2011, 50 (48), 11312-11359.
8. Gabriel, C.; Gabriel, S.; H. Grant, E.; H. Grant, E.; S. J. Halstead, B.; Michael P. Mingos, D., Dielectric parameters relevant to microwave dielectric heating. C*hemical Society Reviews* 1998, 27 (3), 213-224.
9. Kappe, C. O., Controlled Microwave Heating in Modern Organic Synthesis. *Angewandte Chemie International Edition* 2004, 43 (46), 6250-6284.
10. Schanche, J.-S., Microwave synthesis solutions from personal chemistry. *Molecular Diversity* 2003, 7 (2), 291-298.
11. Kappe, C. O.; Dallinger, D.; Murphree, S. S., *Practical Microwave Synthesis for Organic Chemists- Strategies, Instruments, and Protocols.* Wiley-VCH: Weinheim, 2009.
12. Kappe, C. O., Microwave dielectric heating in synthetic organic chemistry. *Chemical Society Reviews* 2008, 37 (6), 1127-1139.
13. Dallinger, D.; Irfan, M.; Suljanovic, A.; Kappe, C. O., An Investigation of Wall Effects in Microwave-Assisted Ring-Closing Metathesis and Cyclotrimerization Reactions. *The Journal of Organic Chemistry* 2010, 75 (15), 5278-5288.
14. Baghbanzadeh, M.; Carbone, L.; Cozzoli, P. D.; Kappe, C. O., Mikrowellen-unterstützte Synthese von kolloidalen anorganischen Nanokristallen. *Angewandte Chemie* 2011, 123 (48), 11510-11561.
15. Kappe, C. O., Unraveling the Mysteries of Microwave Chemistry Using Silicon Carbide Reactor Technology. *Accounts of Chemical Research* 2013, 46 (7), 1579-1587.
16. Obermayer, D.; Gutmann, B.; Kappe, C. O., Microwave Chemistry in Silicon Carbide Reaction Vials: Separating Thermal from Nonthermal Effects. *Angewandte Chemie International Edition* 2009, 48 (44), 8321-8324.

17. Moghaddam, M. M.; Baghbanzadeh, M.; Keilbach, A.; Kappe, C. O., Microwave-assisted synthesis of CdSe quantum dots: can the electromagnetic field influence the formation and quality of the resulting nanocrystals? *Nanoscale* 2012, 4 (23), 7435-7442.
18. Kappe, C. O.; Pieber, B.; Dallinger, D., Microwave Effects in Organic Synthesis: Myth or Reality? *Angewandte Chemie International Edition* 2013, 52 (4), 1088-1094.
19. Obermayer, D.; Gutmann, B.; Kappe, C. O., Microwave Chemistry in Silicon Carbide Reaction Vials: Separating Thermal from Nonthermal Effects. *Angewandte Chemie* 2009, 121 (44), 8471-8474.
20. Gutmann, B.; Obermayer, D.; Reichart, B.; Prekodravac, B.; Irfan, M.; Kremsner, J. M.; Kappe, C. O., Sintered Silicon Carbide: A New Ceramic Vessel Material for Microwave Chemistry in Single-Mode Reactors. *Chemistry – A European Journal* 2010, 16 (40), 12182-12194.
21. Pein, A.; Baghbanzadeh, M.; Rath, T.; Haas, W.; Maier, E.; Amenitsch, H.; Hofer, F.; Kappe, C. O.; Trimmel, G., Investigation of the Formation of $CuInS_2$ Nanoparticles by the Oleylamine Route: Comparison of Microwave-Assisted and Conventional Syntheses. *Inorganic Chemistry* 2011, 50 (1), 193-200.
22. Wang, L.; Sasaki, T., Titanium Oxide Nanosheets: Graphene Analogues with Versatile Functionalities. *Chemical Review*, 2014, 114 (19), 9455–9486
23. Dahal, N.; García, S.; Zhou, J.; Humphrey, S. M., Beneficial Effects of Microwave-Assisted Heating versus Conventional Heating in Noble Metal Nanoparticle Synthesis. *ACS Nano* 2012, 6 (11), 9433-9446.
24. García, S.; Zhang, L.; Piburn, G. W.; Henkelman, G.; Humphrey, S. M., Microwave Synthesis of Classically Immiscible Rhodium–Silver and Rhodium–Gold Alloy Nanoparticles: Highly Active Hydrogenation Catalysts. *ACS Nano* 2014, 8 (11), 11512-11521.
25. Gou, L.; Chipara, M.; Zaleski, J. M., Convenient, Rapid Synthesis of Ag Nanowires. *Chemistry of Materials* 2007, 19 (7), 1755-1760.
26. Hu, X.; Yu, J. C.; Gong, J.; Li, Q.; Li, G., α-Fe_2O_3 Nanorings Prepared by a Microwave-Assisted Hydrothermal Process and Their Sensing Properties. *Advanced Materials* 2007, 19 (17), 2324-2329.
27. Hu, X.; Yu, J. C., Continuous Aspect-Ratio Tuning and Fine Shape Control of Monodisperse α-Fe_2O_3 Nanocrystals by a Programmed Microwave–Hydrothermal Method. *Advanced Functional Materials* 2008, 18 (6), 880-887.
28. Druzhinina, T.; Weltjens, W.; Hoeppener, S.; Schubert, U. S., The Selective Heating of Iron Nanoparticles in a Single-Mode Microwave for the Patterned Growths of Carbon Nanofibers and Nanotubes. *Advanced Functional Materials* 2009, 19 (8), 1287-1292.
29. Menéndez, J. A.; Menéndez, E. M.; García, A.; Parra, J. B.; Pis, J. J., Thermal Treatment of Active Carbons: a Comparison Between Microwave and Electrical Hating. *Journal of Microwave Power and Electromagnetic Energy* 1999, 34 (3), 137-143.
30. Pinna, N.; Niederberger, M., Surfactant-Free Nonaqueous Synthesis of Metal Oxide Nanostructures. *Angewandte Chemie International Edition* 2008, 47 (29), 5292-5304.
31. *Metal Oxide Nanoparticles in Organic Solvents-Synthesis, Formation, Assembly and Application.* (Eds.: Niederberger, M.; Pinna, N.), Springer-Verlag London: 2009.
32. Niederberger, M.; Pinna, N.; Polleux, J.; Antonietti, M., A General Soft-Chemistry Route to Perovskites and Related Materials: Synthesis of $BaTiO_3$, $BaZrO_3$, and $LiNbO_3$ Nanoparticles. *Angewandte Chemie International Edition* 2004, 43 (17), 2270-2273.
33. Pinna, N.; Neri, G.; Antonietti, M.; Niederberger, M., Nonaqueous Synthesis of Nanocrystalline Semiconducting Metal Oxides for Gas Sensing. *Angewandte Chemie International Edition* 2004, 43 (33), 4345-4349.

34. Pinna, N.; Garnweitner, G.; Antonietti, M.; Niederberger, M., Non-Aqueous Synthesis of High-Purity Metal Oxide Nanopowders Using an Ether Elimination Process. *Advanced Materials* 2004, 16 (23-24), 2196-2200.
35. Pinna, N.; Grancharov, S.; Beato, P.; Bonville, P.; Antonietti, M.; Niederberger, M., Magnetite Nanocrystals: Nonaqueous Synthesis, Characterization, and Solubility. *Chemistry of Materials* 2005, 17 (11), 3044-3049.
36. Bilecka, I.; Elser, P.; Niederberger, M., Kinetic and Thermodynamic Aspects in the Microwave-Assisted Synthesis of ZnO Nanoparticles in Benzyl Alcohol. *ACS Nano* 2009, 3 (2), 467-477.
37. Hilaire, S.; Suess, M. J.; Kranzlin, N.; Bienkowski, K.; Solarska, R.; Augustynski, J.; Niederberger, M., Microwave-assisted nonaqueous synthesis of WO_3 nanoparticles for crystallographically oriented photoanodes for water splitting. *Journal of Materials Chemistry A* 2014, 2 (48), 20530-20537.
38. Zeng, G.; Caputo, R.; Carriazo, D.; Luo, L.; Niederberger, M., Tailoring Two Polymorphs of $LiFePO_4$ by Efficient Microwave-Assisted Synthesis: A Combined Experimental and Theoretical Study. *Chemistry of Materials* 2013, 25 (17), 3399-3407.
39. Luo, L.; Rossell, M. D.; Xie, D.; Erni, R.; Niederberger, M., Microwave-Assisted Nonaqueous Sol–Gel Synthesis: From Al:ZnO Nanoparticles to Transparent Conducting Films. *ACS Sustainable Chemistry & Engineering* 2013, 1 (1), 152-160.
40. Carriazo, D.; Rossell, M. D.; Zeng, G.; Bilecka, I.; Erni, R.; Niederberger, M., Formation Mechanism of $LiFePO_4$ Sticks Grown by a Microwave-Assisted Liquid-Phase Process. *Small* 2012, 8 (14), 2231-2238.
41. Bilecka, I.; Kubli, M.; Amstad, E.; Niederberger, M., Simultaneous formation of ferrite nanocrystals and deposition of thin films via a microwave-assisted nonaqueous sol–gel process. *Journal of Sol-Gel Science and Technology* 2011, 57 (3), 313-322.
42. Bilecka, I.; Luo, L.; Djerdj, I.; Rossell, M. D.; Jagodič, M.; Jagličić, Z.; Masubuchi, Y.; Kikkawa, S.; Niederberger, M., Microwave-Assisted Nonaqueous Sol−Gel Chemistry for Highly Concentrated ZnO-Based Magnetic Semiconductor Nanocrystals. *The Journal of Physical Chemistry C* 2011, 115 (5), 1484-1495.
43. Bilecka, I.; Hintennach, A.; Rossell, M. D.; Xie, D.; Novak, P.; Niederberger, M., Microwave-assisted solution synthesis of doped LiFePO4 with high specific charge and outstanding cycling performance. *Journal of Materials Chemistry* 2011, 21 (16), 5881-5890.
44. Bilecka, I.; Niederberger, M., Microwave chemistry for inorganic nanomaterials synthesis. *Nanoscale* 2010, 2 (8), 1358-1374.
45. Bilecka, I.; Djerdj, I.; Niederberger, M., One-minute synthesis of crystalline binary and ternary metal oxide nanoparticles. *Chemical Communications* 2008, (7), 886-888.
46. Russo, P. A.; Lima, S.; Rebuttini, V.; Pillinger, M.; Willinger, M.-G.; Pinna, N.; Valente, A. A., Microwave-assisted coating of carbon nanostructures with titanium dioxide for the catalytic dehydration of d-xylose into furfural. *RSC Advances* 2013, 3 (8), 2595-2603.
47. Russo, P. A.; Ahn, M.; Sung, Y.-E.; Pinna, N., Improved electrocatalytic stability in ethanol oxidation by microwave-assisted selective deposition of SnO_2 and Pt onto carbon. *RSC Advances* 2013, 3 (19), 7001-7008.
48. Yu, S.-H.; Conte, D. E.; Baek, S.; Lee, D.-C.; Park, S.-K.; Lee, K. J.; Piao, Y.; Sung, Y.-E.; Pinna, N., Structure-Properties Relationship in Iron Oxide-Reduced Graphene Oxide Nanostructures for Li-Ion Batteries. *Advanced Functional Materials* 2013, 23 (35), 4293-4305.
49. Neri, G.; Leonardi, S. G.; Latino, M.; Donato, N.; Baek, S.; Conte, D. E.; Russo, P. A.; Pinna, N., Sensing behavior of SnO_2/reduced graphene oxide nanocomposites toward NO_2. *Sensors and Actuators B: Chemical* 2013, 179, 61-68.

50. Marichy, C.; Russo, P. A.; Latino, M.; Tessonnier, J.-P.; Willinger, M.-G.; Donato, N.; Neri, G.; Pinna, N., Tin Dioxide–Carbon Heterostructures Applied to Gas Sensing: Structure-Dependent Properties and General Sensing Mechanism. *The Journal of Physical Chemistry C* 2013, 117 (38), 19729-19739.
51. Dahl, M.; Liu, Y.; Yin, Y., Composite Titanium Dioxide Nanomaterials. *Chemical Reviews* 2014, 114 (19), 9853-9889.
52. Kazuhito, H.; Hiroshi, I.; Akira, F., TiO 2 Photocatalysis: A Historical Overview and Future Prospects. *Japanese Journal of Applied Physics* 2005, 44 (12R), 8269.
53. Yamaguchi, S.; Kobayashi, H.; Narita, T.; Kanehira, K.; Sonezaki, S.; Kubota, Y.; Terasaka, S.; Iwasaki, Y., Novel Photodynamic Therapy Using Water-dispersed TiO_2–Polyethylene Glycol Compound: Evaluation of Antitumor Effect on Glioma Cells and Spheroids In Vitro. *Photochemistry and Photobiology* 2010, 86 (4), 964-971.
54. Chen, C.-T.; Chen, Y.-C., Fe_3O_4/TiO_2 Core/Shell Nanoparticles as Affinity Probes for the Analysis of Phosphopeptides Using TiO_2 Surface-Assisted Laser Desorption/Ionization Mass Spectrometry. *Analytical Chemistry* 2005, 77 (18), 5912-5919.
55. Jones, B. J.; Vergne, M. J.; Bunk, D. M.; Locascio, L. E.; Hayes, M. A., Cleavage of Peptides and Proteins Using Light-Generated Radicals from Titanium Dioxide. *Analytical Chemistry* 2007, 79 (4), 1327-1332.
56. Leitner, A., Phosphopeptide enrichment using metal oxide affinity chromatography. *TrAC Trends in Analytical Chemistry* 2010, 29 (2), 177-185.
57. Li, Y.; Xu, X.; Qi, D.; Deng, C.; Yang, P.; Zhang, X., Novel Fe_3O_4@TiO_2 Core-Shell Microspheres for Selective Enrichment of Phosphopeptides in Phosphoproteome Analysis. *Journal of Proteome Research* 2008, 7 (6), 2526-2538.
58. Wang, X.; Zhi, L.; Müllen, K., Transparent, Conductive Graphene Electrodes for Dye-Sensitized Solar Cells. *Nano Letters* 2008, 8 (1), 323-327.
59. Du, A.; Ng, Y. H.; Bell, N. J.; Zhu, Z.; Amal, R.; Smith, S. C., Hybrid Graphene/Titania Nanocomposite: Interface Charge Transfer, Hole Doping, and Sensitization for Visible Light Response. *The Journal of Physical Chemistry Letters* 2011, 2 (8), 894-899.
60. Woan, K.; Pyrgiotakis, G.; Sigmund, W., Photocatalytic Carbon-Nanotube–TiO_2 Composites. *Advanced Materials* 2009, 21 (21), 2233-2239.
61. Khan, M.; Tahir, M. N.; Adil, S. F.; Khan, H. U.; Siddiqui, M. R. H.; Al-warthan, A. A.; Tremel, W., Graphene based metal and metal oxide nanocomposites: synthesis, properties and their applications. *Journal of Materials Chemistry A* 2015, 3 (37), 18753-18808.
62. Fan, Y.; Wang, L.; Li, J.; Li, J.; Sun, S.; Chen, F.; Chen, L.; Jiang, W., Preparation and electrical properties of graphene nanosheet/Al_2O_3 composites. *Carbon* 2010, 48 (6), 1743-1749.
63. Perera, S. D.; Mariano, R. G.; Vu, K.; Nour, N.; Seitz, O.; Chabal, Y.; Balkus, K. J., Hydrothermal Synthesis of Graphene-TiO_2 Nanotube Composites with Enhanced Photocatalytic Activity. *ACS Catalysis* 2012, 2 (6), 949-956.
64. Zhang, Y.; Tang, Z.-R.; Fu, X.; Xu, Y.-J., Engineering the Unique 2D Mat of Graphene to Achieve Graphene-TiO_2 Nanocomposite for Photocatalytic Selective Transformation: What Advantage does Graphene Have over Its Forebear Carbon Nanotube? *ACS Nano* 2011, 5 (9), 7426-7435.
65. Grobert, N.; Hsu, W. K.; Zhu, Y. Q.; Hare, J. P.; Kroto, H. W.; Walton, D. R. M.; Terrones, M.; Terrones, H.; Redlich, P.; Rühle, M.; Escudero, R.; Morales, F., Enhanced magnetic coercivities in Fe nanowires. *Applied Physics Letters* 1999, 75 (21), 3363-3365.
66. Long, R.; English, N. J.; Prezhdo, O. V., Photo-induced Charge Separation across the Graphene–TiO_2 Interface Is Faster than Energy Losses: A Time-Domain ab Initio Analysis. *Journal of the American Chemical Society* 2012, 134 (34), 14238-14248.

67. Zhang, L.; Diao, S.; Nie, Y.; Yan, K.; Liu, N.; Dai, B.; Xie, Q.; Reina, A.; Kong, J.; Liu, Z., Photocatalytic Patterning and Modification of Graphene. *Journal of the American Chemical Society* 2011, 133 (8), 2706-2713.
68. Zimmermann, M.; Garnweitner, G., Spontaneous water release inducing nucleation during the nonaqueous synthesis of TiO_2 nanoparticles. *CrystEngComm* 2012, 14 (24), 8562-8568.
69. Hummers, W. S.; Offeman, R. E., Preparation of Graphitic Oxide. *Journal of the American Chemical Society* 1958, 80 (6), 1339-1339.
70. Santangelo, S.; Messina, G.; Faggio, G.; Donato, A.; De Luca, L.; Donato, N.; Bonavita, A.; Neri, G., Micro-Raman analysis of titanium oxide/carbon nanotubes-based nanocomposites for hydrogen sensing applications. *Journal of Solid State Chemistry* 2010, 183 (10), 2451-2455.
71. Naldoni, A.; Allieta, M.; Santangelo, S.; Marelli, M.; Fabbri, F.; Cappelli, S.; Bianchi, C. L.; Psaro, R.; Dal Santo, V., Effect of Nature and Location of Defects on Bandgap Narrowing in Black TiO_2 Nanoparticles. *Journal of the American Chemical Society* 2012, 134 (18), 7600-7603.
72. Gouadec, G.; Colomban, P., Raman Spectroscopy of nanomaterials: How spectra relate to disorder, particle size and mechanical properties. *Progress in Crystal Growth and Characterization of Materials* 2007, 53 (1), 1-56.
73. Yang, H. G.; Zeng, H. C., Preparation of Hollow Anatase TiO_2 Nanospheres via Ostwald Ripening. *The Journal of Physical Chemistry B* 2004, 108 (11), 3492-3495.
74. Ren, W.; Ai, Z.; Jia, F.; Zhang, L.; Fan, X.; Zou, Z., Low temperature preparation and visible light photocatalytic activity of mesoporous carbon-doped crystalline TiO_2. *Applied Catalysis B: Environmental* 2007, 69 (3), 138-144.
75. Horikoshi, S.; Abe, H.; Torigoe, K.; Abe, M.; Serpone, N., Access to small size distributions of nanoparticles by microwave-assisted synthesis. Formation of Ag nanoparticles in aqueous carboxymethylcellulose solutions in batch and continuous-flow reactors. *Nanoscale* 2010, 2 (8), 1441-1447.
76. Zhu, J.-F.; Zhu, Y.-J., Microwave-Assisted One-Step Synthesis of Polyacrylamide−Metal (M = Ag, Pt, Cu) Nanocomposites in Ethylene Glycol. *The Journal of Physical Chemistry B* 2006, 110 (17), 8593-8597.
77. Campelo, J. M.; Conesa, T. D.; Gracia, M. J.; Jurado, M. J.; Luque, R.; Marinas, J. M.; Romero, A. A., Microwave facile preparation of highly active and dispersed SBA-12 supported metal nanoparticles. *Green Chemistry* 2008, 10 (8), 853-858.
78. Jhung, S. H.; Jin, T.; Hwang, Y. K.; Chang, J.-S., Microwave Effect in the Fast Synthesis of Microporous Materials: Which Stage Between Nucleation and Crystal Growth is Accelerated by Microwave Irradiation? *Chemistry – A European Journal* 2007, 13 (16), 4410-4417.
79. Stankovich, S.; Piner, R. D.; Chen, X.; Wu, N.; Nguyen, S. T.; Ruoff, R. S., Stable aqueous dispersions of graphitic nanoplatelets via the reduction of exfoliated graphite oxide in the presence of poly(sodium 4-styrenesulfonate). *Journal of Materials Chemistry* 2006, 16 (2), 155-158.
80. Shin, H.-J.; Kim, K. K.; Benayad, A.; Yoon, S.-M.; Park, H. K.; Jung, I.-S.; Jin, M. H.; Jeong, H.-K.; Kim, J. M.; Choi, J.-Y.; Lee, Y. H., Efficient Reduction of Graphite Oxide by Sodium Borohydride and Its Effect on Electrical Conductance. *Advanced Functional Materials* 2009, 19 (12), 1987-1992.
81. Stankovich, S.; Dikin, D. A.; Piner, R. D.; Kohlhaas, K. A.; Kleinhammes, A.; Jia, Y.; Wu, Y.; Nguyen, S. T.; Ruoff, R. S., Synthesis of graphene-based nanosheets via chemical reduction of exfoliated graphite oxide. *Carbon* 2007, 45 (7), 1558-1565.
82. Zhang, H.; Lv, X.; Li, Y.; Wang, Y.; Li, J., P25-Graphene Composite as a High Performance Photocatalyst. *ACS Nano* 2010, 4 (1), 380-386.

83. Wang, Q.; Yang, D.; Chen, D.; Wang, Y.; Jiang, Z., Synthesis of anatase titania-carbon nanotubes nanocomposites with enhanced photocatalytic activity through a nanocoating-hydrothermal process. *Journal of Nanoparticle Research* 2007, 9 (6), 1087-1096.
84. Sakthivel, S.; Kisch, H., Tageslicht-Photokatalyse durch Kohlenstoff-modifiziertes Titandioxid. *Angewandte Chemie* 2003, 115 (40), 5057-5060.
85. Long, M.; Qin, Y.; Chen, C.; Guo, X.; Tan, B.; Cai, W., Origin of Visible Light Photoactivity of Reduced Graphene Oxide/TiO_2 by in Situ Hydrothermal Growth of Undergrown TiO_2 with Graphene Oxide. *The Journal of Physical Chemistry C* 2013, 117 (32), 16734-16741.
86. Barklie, R. C., Characterisation of defects in amorphous carbon by electron paramagnetic resonance. *Diamond and Related Materials* 2001, 10 (2), 174-181.
87. Zaka, M.; Ito, Y.; Wang, H.; Yan, W.; Robertson, A.; Wu, Y. A.; Rümmeli, M. H.; Staunton, D.; Hashimoto, T.; Morton, J. J. L.; Ardavan, A.; Briggs, G. A. D.; Warner, J. H., Electron Paramagnetic Resonance Investigation of Purified Catalyst-free Single-Walled Carbon Nanotubes. *ACS Nano* 2010, 4 (12), 7708-7716.
88. Su, C.; Acik, M.; Takai, K.; Lu, J.; Hao, S.-j.; Zheng, Y.; Wu, P.; Bao, Q.; Enoki, T.; Chabal, Y. J.; Ping Loh, K., Probing the catalytic activity of porous graphene oxide and the origin of this behaviour. *Nature Communication* 2012, 3, 1298.
89. Pham, C. V.; Krueger, M.; Eck, M.; Weber, S.; Erdem, E., Comparative electron paramagnetic resonance investigation of reduced graphene oxide and carbon nanotubes with different chemical functionalities for quantum dot attachment. *Applied Physics Letters* 2014, 104 (13), 132102.
90. Yang, L.; Zhang, R.; Liu, B.; Wang, J.; Wang, S.; Han, M.-Y.; Zhang, Z., π-Conjugated Carbon Radicals at Graphene Oxide to Initiate Ultrastrong Chemiluminescence. *Angewandte Chemie* 2014, 126 (38), 10273-10277.
91. Tommasini, M.; Castiglioni, C.; Zerbi, G.; Barbon, A.; Brustolon, M., A joint Raman and EPR spectroscopic study on ball-milled nanographites. *Chemical Physics Letters* 2011, 516 (4), 220-224.
92. *Carbon Based Magnetism: An Overview of the Magnetism of Metal Free Carbon-based Compounds and Materials.* (Eds.: Makarova, T.; Palacio, F.) Elsevier: Amsterdam, 2006.
93. Li, L.; Li, G.; Xu, J.; Zheng, J.; Tong, W.; Hu, W., Insights into the roles of organic coating in tuning the defect chemistry of monodisperse TiO_2 nanocrystals for tailored properties. *Physical Chemistry Chemical Physics* 2010, 12 (36), 10857-10864.
94. Berger, T.; Sterrer, M.; Diwald, O.; Knözinger, E.; Panayotov, D.; Thompson, T. L.; Yates, J. T., Light-Induced Charge Separation in Anatase TiO_2 Particles. *The Journal of Physical Chemistry B* 2005, 109 (13), 6061-6068.
95. Tampieri, F.; Silvestrini, S.; Ricco, R.; Maggini, M.; Barbon, A., A comparative electron paramagnetic resonance study of expanded graphites and graphene. *Journal of Materials Chemistry C* 2014, 2 (38), 8105-8112.
96. Ferrari, A. C.; Robertson, J., Interpretation of Raman spectra of disordered and amorphous carbon. *Physical Review B* 2000, 61 (20), 14095-14107.
97. Yang; Xu; Tomita, A.; Kyotani, T., Double Coaxial Structure and Dual Physicochemical Properties of Carbon Nanotubes Composed of Stacked Nitrogen-Doped and Undoped Multiwalls. *Chemistry of Materials* 2005, 17 (11), 2940-2945.
98. Inoue, F.; Ando, R. A.; Corio, P., Raman evidence of the interaction between multiwalled carbon nanotubes and nanostructured TiO_2. *Journal of Raman Spectroscopy* 2011, 42 (6), 1379-1383.
99. Liu, B.; Huang, Y.; Wen, Y.; Du, L.; Zeng, W.; Shi, Y.; Zhang, F.; Zhu, G.; Xu, X.; Wang, Y., Highly dispersive {001} facets-exposed nanocrystalline TiO_2 on high quality graphene

as a high performance photocatalyst. *Journal of Materials Chemistry* 2012, 22 (15), 7484-7491.
100. Zhang, Y.; Tang, Z.-R.; Fu, X.; Xu, Y.-J., TiO_2−Graphene Nanocomposites for Gas-Phase Photocatalytic Degradation of Volatile Aromatic Pollutant: Is TiO_2−Graphene Truly Different from Other TiO_2−Carbon Composite Materials? *ACS Nano* 2010, 4 (12), 7303-7314.
101. Menéndez, J. A.; Arenillas, A.; Fidalgo, B.; Fernández, Y.; Zubizarreta, L.; Calvo, E. G.; Bermúdez, J. M., Microwave heating processes involving carbon materials. *Fuel Processing Technology* 2010, 91 (1), 1-8.
102. Horikoshi, S.; Osawa, A.; Abe, M.; Serpone, N., On the Generation of Hot-Spots by Microwave Electric and Magnetic Fields and Their Impact on a Microwave-Assisted Heterogeneous Reaction in the Presence of Metallic Pd Nanoparticles on an Activated Carbon Support. *The Journal of Physical Chemistry C* 2011, 115 (46), 23030-23035.
103. Chen, P.-K.; Rosana, M. R.; Dudley, G. B.; Stiegman, A. E., Parameters Affecting the Microwave-Specific Acceleration of a Chemical Reaction. *The Journal of Organic Chemistry* 2014, 79 (16), 7425-7436.
104. Huang, W.; Richert, R., The Physics of Heating by Time-Dependent Fields: Microwaves and Water Revisited. *The Journal of Physical Chemistry B* 2008, 112 (32), 9909-9913.
105. Huang, W.; Richert, R., Dynamics of glass-forming liquids. XIII. Microwave heating in slow motion. *The Journal of Chemical Physics* 2009, 130 (19), 194509.

3. Microwave-assisted synthesis of hybrid organic-inorganic transition-metal phosphonates for the electrocatalytic oxygen evolution reaction

3.1 Introduction

3.1.1 Oxygen evolution reaction

Electrochemical water splitting is the splitting of water into gaseous O_2 and gaseous H_2 driven by electrical energy. In combination with renewable energy sources, it is a promising sustainable method for the large-scale production of hydrogen, which is a fuel for environmentally friendly energy conversion technologies such as fuel cells.[1] The overall water electrolysis process comprises two half-cell reactions: the hydrogen evolution reaction (HER) at the cathodic electrode and the oxygen evolution reaction (OER) at the anodic electrode (equations 3.1, 3.2, 3.3). Water splitting is an endothermic reaction with $\Delta G = 237.2$ kJ/mol and the equilibrium potential = 1.23 V at 25 ˚C and 1 atm[2].

Overall water splitting reaction:

$$H_2O \rightarrow H_2(g) + \tfrac{1}{2}O_2(g) \quad (3.1)$$

OER half-reaction:

$$2H_2O \rightarrow O_2(g) + 4H^+ + 4e^- \text{ (in acidic media)} \quad (3.2)$$

$$4OH^- \rightarrow O_2(g) + 2H_2O + 4e^- \text{ (in alkaline media)} \quad (3.3)$$

The OER is a complex multistep reaction involving the transfer of four electrons making it kinetically sluggish and thus decreasing the efficiency of the overall water splitting process. The mechanisms of OER in both acidic and alkaline conditions are not clear yet and several mechanisms have been proposed. Nevertheless, there are similarities among the proposed mechanisms according to experimental observations and computational simulations[3,4]. Most of these mechanisms involve the formation similar intermediates such as M-O and M-OH (where M is a metal active site)[3,4]. The major difference is in the reactions to produce oxygen. O_2 can be produced by the combination of two M-O intermediates (equations 3.7, 3.14) or through the formation of a MOOH intermediate that decomposes into O_2 (equations 3.9, 3.10, 3.16, and/or 3.17). Despite the absence of complete knowledge about the OER mechanisms, it is generally

accepted that the bonding in the reaction intermediates (M-O, M-OH, MOOH) plays a key role in the electrocatalytic activity of the catalyst.[5-9]

Proposed pathway reactions in acidic electrolyte:

$$M + H_2O(l) \rightarrow M\text{-}OH + H^+ + e^- \quad (3.4)$$

$$2M\text{-}OH \rightarrow M\text{-}O + M + H_2O(l) \quad (3.5)$$

$$M\text{-}OH \rightarrow M\text{-}O + H^+ + e^- \quad (3.6)$$

$$2M\text{-}O \rightarrow 2M + O_2(g) \quad (3.7)$$

$$M\text{-}O + H_2O(l) \rightarrow M\text{-}OOH + H^+ + e^- \quad (3.8)$$

$$2M\text{-}OOH \rightarrow M\text{-}O + M + H_2O(l) + O_2(g) \quad (3.9)$$

$$M\text{-}OOH \rightarrow M + O_2(g) + H^+ + e^- \quad (3.10)$$

Proposed pathway reactions in alkaline electrolyte:

$$M + OH^- \rightarrow MOH \quad (3.11)$$

$$M\text{-}OH + OH^- \rightarrow M\text{-}O + H_2O(l) \quad (3.12)$$

$$2M\text{-}OH \rightarrow M\text{-}O + M + H_2O(l) \quad (3.13)$$

$$2M\text{-}O \rightarrow 2M + O_2(g) \quad (3.14)$$

$$M\text{-}O + OH^- \rightarrow M\text{-}OOH + e^- \quad (3.15)$$

$$2M\text{-}OOH \rightarrow M\text{-}O + M + H_2O(l) + O_2(g) \quad (3.16)$$

$$M\text{-}OOH + OH^- \rightarrow M + O_2(g) + H_2O(l) \quad (3.17)$$

The complexity of this multi-step reaction, involving various high-energy intermediates, makes water oxidation difficult to achieve without the application of a significant extra potential, also known as overpotential (η). The overpotential is the potential above the thermodynamic potential necessary to overcome the reactions activation barriers. In practice, the applied potential at which the OER occurs is

$$E_{ap} = E^0 + iR + \eta \quad (3.18)$$

where the E^0 is the equilibrium potential, η is the overpotential, and iR is the ohmic drop which represents the excess potential applied because of the system resistance, including ion and gas

diffusion resistance, interface resistance, and uncompensated series resistance of the solution and wires[10].

The reduction of the system resistance can be achieved by suitable cell engineering and by employing strong electrolytes that have high ionic conductivities, while to decrease the overpotential requires catalysts with fast kinetics to catalyze the reaction at a high rate[10].

There are various parameters useful for evaluating the performance of an electrocatalyst. The main figure of merit used to compare the OER (and HER) performance is the overpotential necessary to achieve a current density per geometric area of 10 mA cm^{-2}. This is the approximated current density expected for an integrated solar water-splitting device under 1 sun illumination operating at 10% solar-to-fuels efficiency[6].

The kinetics of electrocatalytic reactions are described by the Butler-Volmer equation (equation 3.19) that relates the current density (j) and the overpotential:

$$j = j_0[-e^{-\alpha nF\eta/RT} + e^{(1-\alpha)nF\eta/RT}] \quad (3.19)$$

where j is the current density, j_0 is the exchange current density, α is the charge transfer coefficient, n is the constant, and T is the temperature.

The exchange current density describes the rate of reaction at the equilibrium potential. It is associated with the intrinsic charge transfer ability between electrocatalyst and reactant.

At high overpotentials (η > 0.05 V), the Butler-Volmer equation can be simplified into the Tafel equation:

$$\eta = a + b\log j = \frac{-2.3RT}{\alpha nF}\log j_0 + \frac{2.3RT}{\alpha nF}\log j \quad (3.20)$$

This equation describes a linear relationship between the overpotential and log j, with a slope $b = \frac{2.303RT}{\alpha F}$ named the Tafel slope[11,12]. The Tafel slope is an important figure of merit used for comparing catalysts, as it reflects the increment of the overpotential that is necessary to increase the current density by ten-fold. The smaller the Tafel slope the steepest is the rise of the electrocatalytic current density generated and the more efficient is the catalyst at enhancing the reaction kinetics. The Tafel slope also can provide mechanistic insights into the reactions.

An important parameter is the turnover frequency (TOF) of the catalyst, defined as the number of O_2 molecules evolved per second per metal site, which provides insight into the intrinsic

activity of the catalysts. However, there are difficulties associated with the evaluation of TOF values of catalysts including the determination of the number of active sites. Ideal catalysts should have small overpotentials at j=10 mA cm^{-2}, low Tafel slopes and high TOF values.

3.1.2 Catalysts for the oxygen evolution reaction

The benchmark catalysts for electrocatalytic OER are based on ruthenium and iridium, which show high activity in both acidic and alkaline electrolytes[4,13,14]. However, the scarcity and high cost of these metals hinder the widespread application of water splitting devices. Therefore, intensive research has been focused on the study of earth-abundant transition-metal-based catalysts. In particular those containing Mn, Co, Ni or Fe in the form of metal alloys[15], oxides[16], hydroxides[17], phosphides[18], phosphates[19], sulfides[20], and selenides[21], have been investigated and found to be active for OER in alkaline conditions. Among them, Co-based and especially NiFe-based catalysts are considered very promising for water oxidation in alkaline conditions.

Boettcher and co-workers[22] compared the activity of NiO_x, CoO_x, FeO_x, MnO_x, and mixed metal oxides ($Ni_{0.9}Fe_{0.1}O_x$, $Ni_yCo_{1-y}O_x$) prepared by electrodeposition. The results showed that $Ni_{0.9}Fe_{0.1}O_x$ exhibited the best activity in 1 M KOH, followed by NiO_x, $Ni_yCo_{1-y}O_x$, CoO_x, FeO_x, and MnO_x. The $Ni_{0.9}Fe_{0.1}O_x$ film electrode reached 10 mA cm^{-2} at an overpotential of 336 mV with a Tafel slope of 30 mV dec^{-1}, which outperformed the IrO_x electrode prepared by the same method. They found that the excellent performance for this material in OER was attributed to the formation in situ of a layered oxyhydroxide ($Ni_{0.9}Fe_{0.1}OOH$), similarly to previous works on Ni oxides[16].

Trotochaud *et al.*[22] prepared electrodes by depositing thin films of Ni hydroxide and NiFe hydroxide and investigated their activity in purified (Fe-free) and non-purified KOH electrolytes. Grazing-incidence XRD patterns indicated that the $Ni(OH)_2$ electrodes in a purified alkaline medium were converted from α-$Ni(OH)_2$ to the more crystalline β-$Ni(OH)_2$ after potential cycling or just by aging in the electrolyte. On the contrary, the as-deposited NiFe hydroxide showed weak reflections belonging to β-$Ni(OH)_2$, which subsequently diminished after aging. The authors argued that the incorporated Fe^{3+} is compensated by anions in between the layers, leading to the formation of a stable hydrated Ni-Fe layered double hydroxide (LDH) structure.

Ni-Fe layered double hydroxides (LDHs) have also been extensively investigated as water oxidation catalysts in basic solution. The structure of these materials can be represented by the

formula $[Ni^{II}_{1-x}Fe^{III}_{x}(OH)_2]^{x+}[x/n\ A^{n-}]^{x-}\cdot zH_2O$, where A are anions, n is the charge of the anions, and z is the amount of intercalated water molecules[3]. As shown in Figure 3.1, NiFe LDHs are composed of metal hydroxide layers in which a fraction of the divalent nickel cations coordinated octahedrally by hydroxyl groups have been replaced by trivalent iron cations, leading to positively charged layers. The value of x equals the molar ratio of Fe that is incorporated in the structure and is generally below 0.33, as after above this value the agglomeration of neighboring Fe(III) octahedra may lead to the formation of FeO_xH_y phases[3]. Inorganic or organic anions are present in the interlayer space to compensate the positive charges. The hydroxyl groups are located on both sides of the Ni-Fe layers and usually interact with the interlayer water molecules and anions. The interlayer bonding is relatively weak and can be expanded or exfoliated by anion exchange or mechanical methods [20-22]. NiFe LDHs are commonly synthesized through co-precipitation of Ni^{2+} and Fe^{3+} precursors in alkaline solution[23]. These materials are efficient and fairly stable OER electrocatalysts in basic solutions[24-28].

Exfoliation of LDHs can significantly increase the surface area and consequently expose more active sites [25,29,30]. Song and Hu[25] proposed an approach for the exfoliation of NiFe LDH in colloidal suspension. First, LDHs with CO_3^{2-} as counter anions were obtained by a precipitation method. The interlayer distance was increased by anion exchange in a ClO_4^- solution. Finally, the bulk LDH was dispersed in degassed formamide under stirring for 24 h to obtain the single-layered nanosheets. The enhanced OER activity of the exfoliated materials compared to the bulk counterparts was attributed to the presence of a higher amount of edge sites on the former. Apart from the liquid exfoliation, dry methods, such as argon plasma etching[29] and electrostatic repulsion[30], have also been successfully applied for producing single layered LDH nanosheets.

Many mixed NiFe oxides have been also investigated in the oxidation of water. These can be prepared by various methods, but most commonly are synthesized by sol-gel methods[17,22,31,32]. Amorphous $Ni_yFe_{1-y}O_x$ nanoparticles can be synthesized by a solvothermal method in benzyl alcohol[31,32].

Mixed NiFe oxides and hydroxides catalysts have been studied for several decades as electrocatalysts for the oxidation of water in alkaline media. It has been shown that the actual catalyst is a NiFe hydroxide formed in situ under OER conditions, regardless of the nature of the starting material. Nevertheless, the many reports available in the literature show significant variations on the electrocatalytic performance, which indicates the strong effect of the starting

materials characteristics including morphology, surface area, and crystalline structure on the catalytic activity. Recent studies suggest that the catalytic activity of NiFe-based catalysts is also correlated with distortion around the metal cations, with higher activity being associated with higher local structural disorder [31,33].

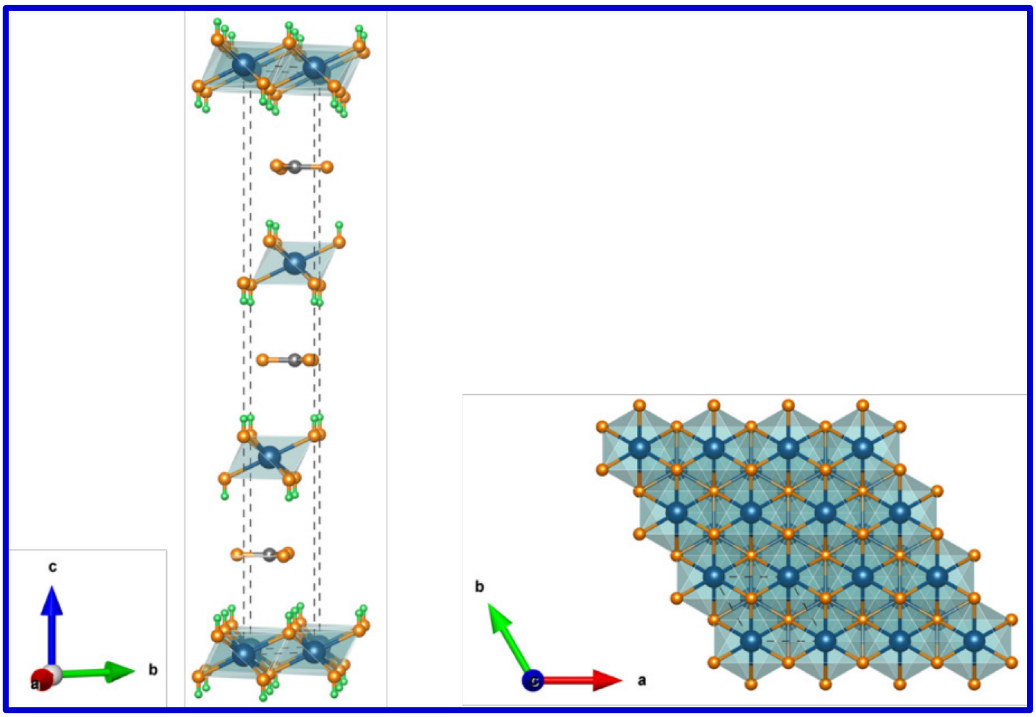

Figure 3.1 Crystal structure of NiFe LDHs. Left image shows the unite-cell packing viewed along *a*-axis; right image shows the structure viewed along *c*-axis. Carbonate ions randomly incorporated between layers. All the crystal structure models in this thesis are produce by the software of VESTA[34]. (Blue-Ni/Fe, orange-oxygen, green-hydrogen, gray-carbon)

From the numerous studies available in the literature, it is clear that the Fe plays a critical role in promoting the OER activity of the NiFe catalysts. However, the nature and structure of the actual active sites have not been completely clarified yet. 30 years ago, Corrigan[35] found that Fe impurities in thin film nickel oxide electrodes dramatically enhanced the electrocatalytic OER performance. The trace iron impurities were introduced from the KOH electrolyte, and as little as 0.1 % Fe would strongly affect the oxygen evolution reaction activity and the cyclic voltammetric behavior of the electrode, with an observed anodic shift of the oxidation Ni2+/Ni3+ peak. Corrigan proposed that the dramatic increase in OER activity was caused by a partial electron transfer from NiOOH to Fe^{3+} leading to the oxidation of Ni^{3+} to Ni^{4+}, which was observed by in situ Mössbauer spectroscopy. Trotochaud *et al.*[33] examined the activity of pure $Ni(OH)_2$ and NiFe oxyhydroxide films in purified (Fe-free) and non-purified KOH

electrolyte. They found that the $Ni(OH)_2$/NiOOH electrode exhibited very poor activity in the purified alkaline medium, even after aging. A good performance of the $Ni(OH)_2$ electrode was only achieved after Fe incorporation. This work demonstrated that the presence of Fe is crucial for achieving high catalytic activity with Ni-based electrodes. The authors suggested that the Fe modified the Ni^{3+} electronic environment by partial electron transfer. This partial charge-transfer process has also been suggested by other groups[31,36] to enhance the activity of the nickel active sites. It should be noted that the presence of nickel in the electrode is also crucial, as pure Fe oxyhydroxides show poor OER activity. Therefore, the OER activity enhancement arises from the synergy between Ni and Fe.

More recently, in situ characterization studies and computational works suggest that the Fe sites in NiFe hydroxides and oxyhydroxides have higher activity for OER than the Ni sites, i.e. that Fe is the active site[9,22,37]. Bell and co-workers[9] prepared Fe doped NiO_x and investigated the surface properties and energetics of the catalysts by DFT+U calculations. They found that the Fe^{3+} cations in oxyhydroxides, which are formed under OER conditions, exhibited higher activity compared to the Ni^{3+} cations, and predicted that for all other materials containing edge-sharing $[FeO_6]$ and $[NiO_6]$, the Fe sites are the OER active sites. The conclusion was consisted with the operando X-ray absorption spectroscopy data, which indicated shorter Fe-O distances in Ni-Fe catalysts than in pure γ-FeOOH. Recently, Boettcher and co-workers[38] studied the active sites in NiFe oxyhydroxide films by comparing the electrochemical properties of a co-electrodeposited $NiFeO_xH_y$ electrode and a NiO_xH_y thin film electrode with Fe incorporated in situ from the electrolyte. They found that 11% Fe was incorporated into the Fe-free NiO_xH_y film within 2 potential cycles and the activity increased by ~150-fold. Moreover, although the Fe-incorporated NiO_xH_y and co-electrodeposited $NiFeO_xH_y$ had similar Fe content and activities, they observed large differences in the redox behavior, TOF, and e^- transferred per Ni. They suggested that the Fe cations are initially incorporated into the NiO_xH_y structure from the electrolyte at surface/edge sites. They proposed that the coordination environment of the metal sites play a key role on the activity, and that Fe cations at surface/edge sites with imcomplete coordination are responsible for the high activity of NiFe oxyhydroxide catalysts.

3.1.3 Hybrid organic-inorganic transition metal phosphonates

Metal phosphonates are a group of hybrid materials consisting of metal cations bonded to bridging organophosphonate ligands that results in the formation of extended structures[39,40]. Different structures can be produced such as 1D linear chains[41], 2D layers[42], and 3D pillared

structures or metal organic frameworks (MOFs) [43], depending on the precursors, synthesis conditions, and presence of additional coordinating moieties including those in the organic part of the phosphonate ligand (e.g. carboxylate, sulfonate, pyridine, hydroxyl or phosphonate). Zirconium phosphonates were the first metal phosphonates to be synthesized in 1978 by Alberti et al. and are the most extensively investigated[44-46]. In general, zirconium phosphonates can be prepared by the reaction between zirconium salts and phosphonic acids:

$$Zr^{4+} + 2RPO_3H_2 \rightarrow Zr(O_3PR)_2 + 2H^+ \quad (3.23)$$

where R is an alkyl or aryl group. However, only in 1993 the structure of Zr phenylphosphonate $Zr(O_3PC_6H_5)_2$ was solved by Poojary *et al.*[45]. This compound has a layered structure with an interlayer distance of 14.87 Å (Figure 3.2). The crystals belong to the space group *C*2/*c* with $a = 9.0985$, $b = 5.4154$, $c = 30.235$ Å and $\beta = 101.333°$. Zr atoms are coordinated with six oxygen connecting with six adjacent phosphonate ligands, thus the ZrO_6 octahedra are separated from each other by O-P-O bridges. The Zr atoms are situated in the same plane while the organic ligands P-C_6H_5 are located above and below the plane. The phenyl groups are oriented away from this plane and inclined by about 30° with respect to the *c* axis.

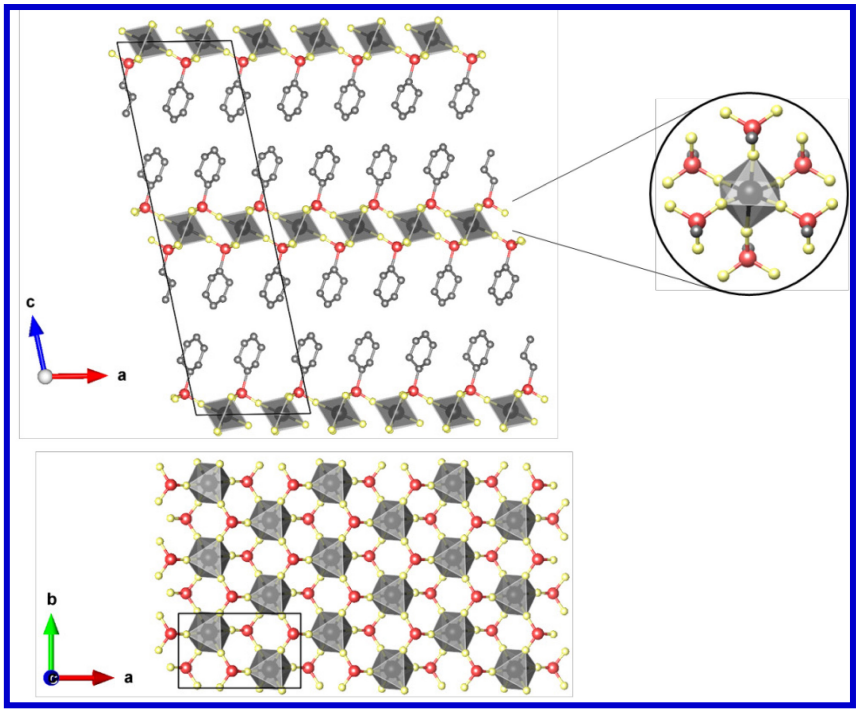

Figure 3.2 Structure of α-zirconium phosphonate viewed from *b*- (top) and *c*- (down) axis. Inserted image shows the coordination environment of a Zr atom. (Black-Zr, red-P, yellow-O, gray-C)

Simple divalent metal phosphonates have the general formula of $M(O_3PR)\cdot H_2O$, where M=Ni, Co, Fe, Mn or Cu, and R is an aryl or alkyl group[47]. These compounds have generally layered structure. The crystalline structure of single metal phosphonates has been studied by several research groups[45,47-50]. These materials have orthorhombic crystal structures (*Pmn*2_1 group), as shown in Figure 3.3a for nickel phenylphosphonate. The inorganic layers are made of corner-shared NiO6 octahedra. Each metal is coordinated by five oxygen atoms from the phosphonate ligands and one oxygen atom from a water molecule. In between the inorganic layers there are two organic layers interaction through London dispersion and van der Waals forces.

The structure of trivalent metal phosphonates can be more complicated. For example, Fe(III) phenylphosphonate can be prepared by the reaction between FeOCl and phenylphosphonic acid, but three phases of $FeH(O_3PC_6H_5)_2\cdot H_2O$ and the additional compound $FeH(O_3HPC_6H_5)_4$ were obtained, depending on the Fe to P ratio and the reaction time[51].

Although many metals tend to coordinate with phosphonate ligands to form layered structures, owing to the rich chemistry of the organophosphonic acid family various metal phosphonates with tri-dimensional structure can be synthesized also. By using a biphosphonic acid instead of a monophosphonic acid, pillared 3D metal phosphonates can be fabricated [52]. In some cases, pores are formed during crystal growth by the stacking of layers of unequal length[53]. Moreover, Chen *et al.* [54] synthesized a series of zeolite-type (gismondine) Zn phosphonate based on the reaction between zinc acetate [$Zn(AC)_2$)] and 4-phosphonobenzoic acid (PBC) in different solvents. In these structures, the sheets are composed of corner-shared ZnO_4 and CPO_3 tetrahedra that are cross-linked by the organic moieties of the PBC ligands.

3.1.4 Metal phosphonates in energy conversion and storage applications

The versatility of the coordination chemistry of metal phosphonates together with their relatively high chemical and thermal stability (compared for example with metal carboxylates) makes these compounds attractive for a variety of applications such as biological chemistry[55], catalysis[56,57], gas storage[58], magnetism[59], and fluorescent sensors[60], as well as for applications in energy conversion and storage.

Metal phosphonates, especially metal organic frameworks (MOFs), have been investigated as proton conductors for possible usage in fuel cells[61]. The ion conductor in proton exchange membrane fuel cells (PEMFCs) for hybrid vehicles needs to have high mechanical strength, high ion conduction, low cost, and the ability to operate under conditions of low humidity and

high temperature (exceeding the boiling point of water) [62]. Several advantages based on the structural features make metal phosphonates competitive candidates. The organophosphonate groups of a metal phosphonate can be readily designed with a desired size, shape and denticity, leading to a flexible structure and variable ion conduction [63,64]. Moreover, in porous phosphonate MOFs guest molecules acting as proton carriers can be placed[65]. Additionally, the 3D frameworks with crystalline structures can facilitate a deeper understanding of proton conduction pathways through both experimental and computational methods[66].

Some metal phosphonates have recently been investigated in charge storage devices due to their ordered porous structure and the synergy effects between organic and inorganic constituents[40,67]. Pramanik and co-workers published several works on the synthesis of mesoporous metal phosphonates for application in Li-ion batteries[67-70]. The synthesis involves the reaction between metal precursors and nitrilotris(methylene)triphosphonic acid (NMPA) in the presence of cetyltrimethylammonium bromide (CTAB) as a structure directing agent. The Fe phosphonate has high surface area (470 m^2/g) with the mesopore size of *ca.* 2.9 nm, which offered a large contact area with electrolyte and short transport paths for Li^+ ions[67]. The charge-discharge capacities reached maximum at 541 mA h g^{-1} and decreased to 355 mA h g^{-1} after 30 cycles, indicating the poor stability of this material. The vanadium phosphonate[70]. prepared in a similar way exhibited better Li-ion storage performance than the iron phosphonate material, especially at higher rate (10 C). They also use the mesoporous metal phosphonate as precursor or template to prepare porous metal phosphate[69]. Through this route, Ni phosphate, Al phosphate and Zr phosphate with porous structure are obtained. Zhang *et al.*[71] recently prepared a hierarchical nickel phenylphosphonate material with flower-like morphology by utilizing urea to control the deprotonation of the phosphonic acid. The material was tested as supercapacitor on Ni foam and showed good pseudo-capacitive performance owing to the large surface area and the reversible redox reaction of Ni^{2+}/Ni^{3+}.

This family of hybrid materials remains almost unexplored as water oxidation catalysts, as only a few promising reports are available in the literature concerning the application of cobalt phosphonates as photocatalytic or electrocatalytic water oxidation catalysts[72-75]. Zhou *et al.*[74] synthesized a series of layered cobalt phosphonates with different structures depending on the phosphonate ligands and tested them as catalysts for visible light driven water oxidation. They found that the hybrid catalysts with both corner- and edge-sharing Co octahedra, $Co_3(O_3PCH_2\text{-}NC_4H_7\text{-}CO_2)_2\cdot 4H_2O$ and $Co_3(O_3PCH_2\text{-}NC_4H_7\text{-}CO_2)_2\cdot 5H_2O$, displayed superior catalytic activity compare to the compounds with only one type of octahedral structure. Furthermore, the

presence of Co-N bonds resulted in distorted asymmetric coordination geometry around the metal that promoted the catalytic activity. Saha *et al.*[75] reported a cobalt phosphonate material as heterogeneous catalyst for electrocatalytic water oxidation. The material with porous structure was produced by reaction between $CoCl_2$ and nitrilotris(methylene)triphosphonic acid (NMPA) in the presence of the surfactants F127 and polyvinyl alcohol (PVA). The catalyst was characterized after electrolysis and no phosphorous was detected from the P 2p XPS spectrum, suggesting that the organic phosphonate groups dissolved in the electrolyte during water oxidation and the actual catalyst was cobalt oxide or hydroxide.

In this chapter, a series mixed Ni_xFe_{1-x} phenylphosphonates were synthesized in benzyl alcohol under the microwave irradiation, and tested as water oxidation electrocatalysts in alkaline electrolyte. The structure of the hybrid organic-inorganic was characterized in detail before and after the electrocatalytic tests to understand the relationship between the properties of the materials and the high electrocatalytic water oxidation activity displayed.

3.2 Structural characterization of the NiFe phenylphosphonates

3.2.1 Synthesis of NiFe phenylphosphonates with different Fe content

The NiFe phenylphosphonates were synthesized by the reaction of nickel acetylacetonate/ Fe acetylacetonate with phenylphosphonic acid in benzyl alcohol. Microwave irradiation was employed as the heating source due to the fast heating kinetics and specific heating mechanism, both of which dramatically reduce the reaction time from about one day to just 30 minutes[42]. After washing and drying, the products were then grounded into powder with the color range from yellow to olive-green corresponding to the Fe content from 0% to 100% in the compounds. The NiFe phenylphosphonates are denoted as NiFex-Ph, where x is the Fe atomic percentage of the as-prepared materials determined by energy dispersive X-ray spectroscopy (EDX); while pure Ni or pure Fe phenylphosphonate is denoted as Ni-Ph or Fe-Ph. NiFe phenylphosphonates with the chemical formula of $Ni_xFe_{1-x}(O_3PC_6H_5 \cdot H_2O)$ are isostructural with other layered divalent metal phenylphosphonates $M(II)(O_3PC_6H_5 \cdot H_2O)$ (M = Fe, Ni, Mn, Co)[47,76-78].

The structure of single metal phenylphosphonates has been previously solved by other researcher groups[48-52]. These materials have orthorhombic crystal structures ($Pmn2_1$ group), as shown in Figure 3.3a for nickel phenylphosphonate. The coordination environment around the metal atoms is distorted octahedral. Two of the six oxygen atoms in the NiO_6 octahedra come from one phosphonate group, while three oxygen atoms belong to three other different

neighboring phosphonate ligands. At the same time, these phosphonate ligands also bridge to adjacent nickel atoms forming the 2-dimensional network. The final coordinated oxygen is provided by a water molecule. The nickel atoms are almost coplanar in the inorganic layer and between the inorganic layers there are two layers of organic -C_6H_5 groups (Figure 3.3b) interacting with each other by van der Waals forces. There is disorder in the organic layers, as the aromatic ring has two different perpendicular to the inorganic layers orientations due to the rotation of C-P bonds and steric effects[47]. In one orientation, the phenyl planes are parallel to the *c* axis and perpendicular to the inorganic layer. In the other orientation, the phenyl planes are rotated by 90° with respect to the first orientation and are leaning at an angle different from 90° with respect to the plane of the Ni ions. The non-perpendicular C-P bonds to the layer arise from the distorted Ni octahedra with O-Ni-O angles ranging from 68° to 116°.[78] The top view of the organic-inorganic hybrid plane in Figure 3.3c shows the Ni-O-P networks and corner-shared NiO_6 octahedra. Fe(II) phenylphosphonate has the same structure as Ni(II) phenylphosphonate with small variations in unit-cell parameters [77].

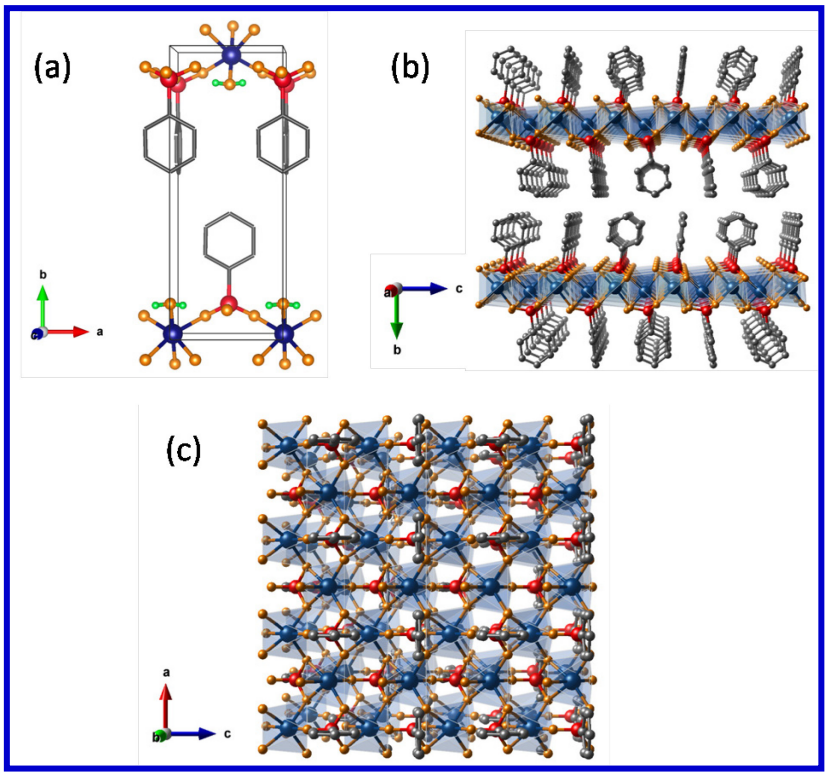

Figure 3.3 Crystal structure of nickel phenylphosphonate. a) Unit cell viewed along the *c*-axis; b) structure viewed along the *a*-axis; c) structure viewed along the *b*-axis. (Blue-Ni, red-phosphorus, orange-oxygen, green-hydrogen from water molecules, gray-aromatic carbon)

To investigate the effect of the concentration of the metal precursors on the final products, Ni-Ph compounds were prepared using three different concentrations of nickel acetylacetonate (0.03, 0.1 and 0.2 mmolmL^{-1}), and a fixed 1:1 molar ratio between P and Ni. Transmission electron microscopy (TEM) images of the Ni-Phs reveal the layered structure of these materials and variations in morphology. The sample synthesized with the lowest concentration (Figure 3.4a-c) have the shape of wires. With the increase of the Ni concentration in the reaction mixture, the particles become broader and thicker (Figure 3.4c-e). Some particles are assembled in structures with flower-like morphology. Irregular flakes are observed in the TEM images of the sample prepared with the highest Ni concentration, as shown in Figure 3.4g-i. The thickness of the flakes is 15 - 30 nm corresponding to 10 - 20 inorganic layers.

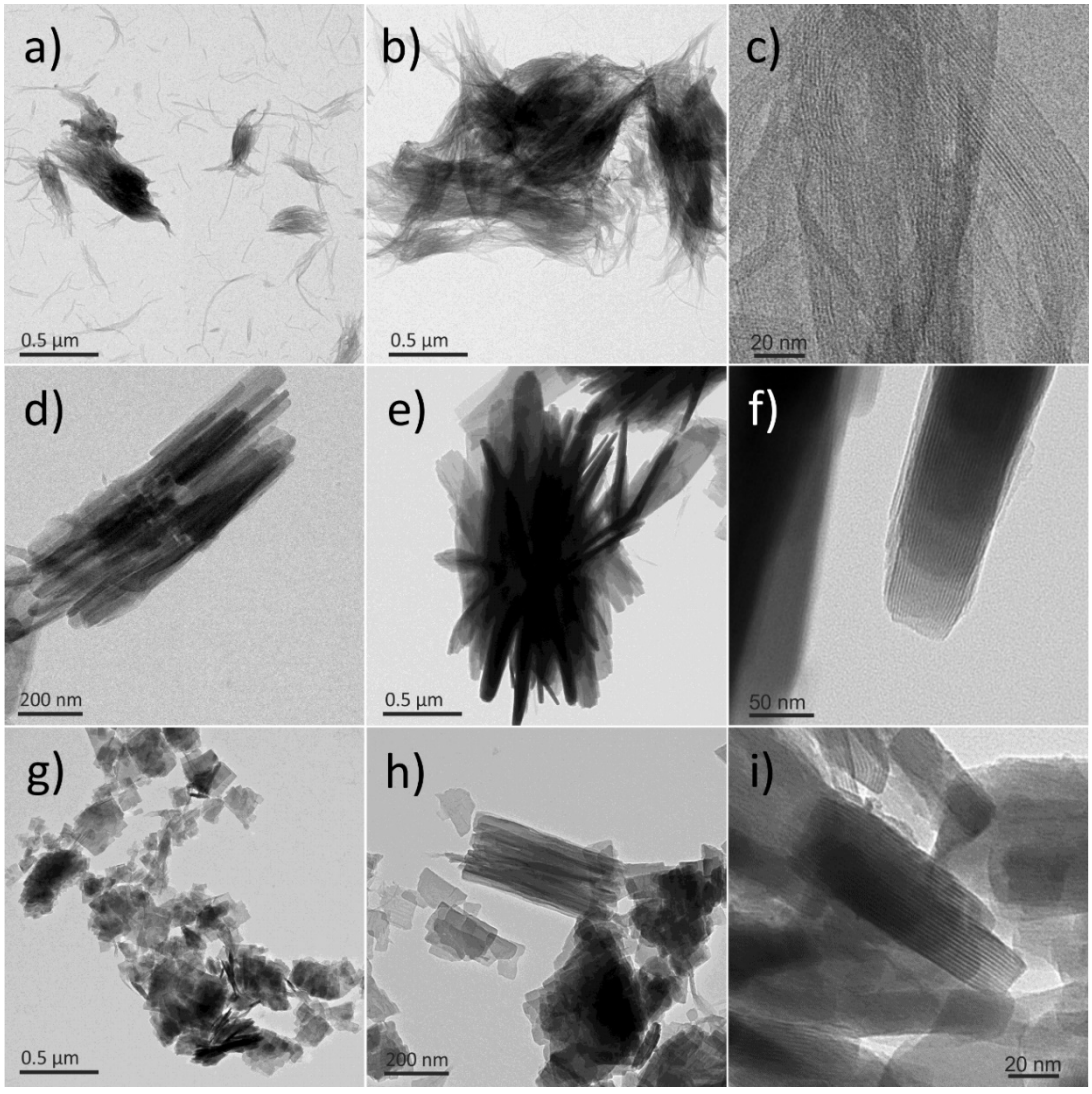

Figure 3.4 TEM images of NiPh compounds prepared with different Ni concentration: a-c, 0.03 mmol mL^{-1}; d-f, 0.1 mmol mL^{-1}; g-i, 0.2 mmol mL^{-1}.

The powder X-ray diffraction (XRD) patterns of the Ni-Ph compounds are shown in Figure 3.5, which confirm the layered structure of the materials. The well-defined reflections at 2θ = 2.80, 5.62 and 8.48 for the sample synthesized with a Ni concentration of 0.1 mmolmL^{-1}correspond to diffractions by the (010), (020) and (030) planes. While the Ni-Ph synthesized in less concentrated reaction mixtures exhibits broader reflections, indicating that the as-prepared compound has lower crystallinity which may arise from defects such as stacking faults or twinning along the stacking direction [77]. Moreover, the structural defects lead to a larger interlayer distance, as illustrated in Table 3.1.

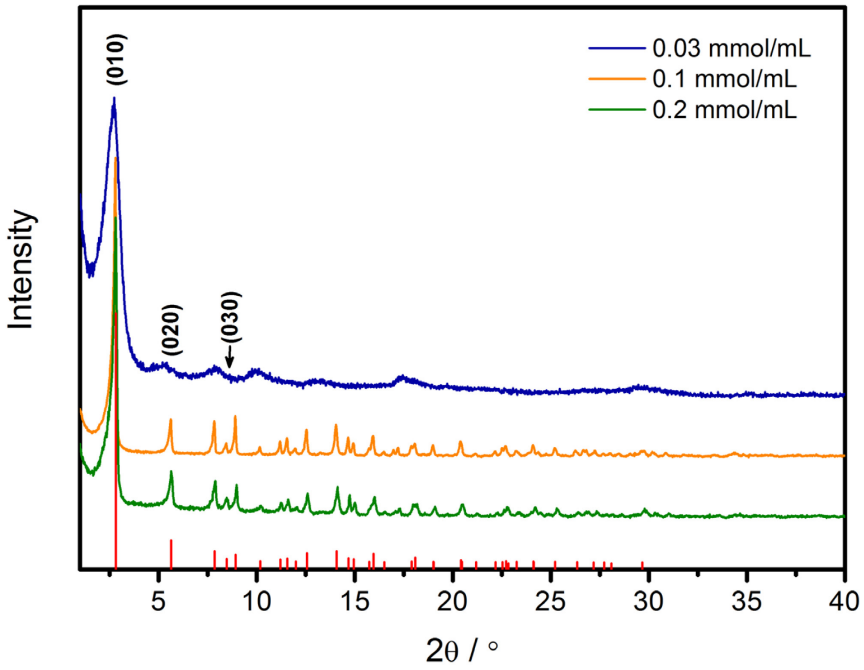

Figure 3.5 XRD patterns of NiPh-Ps prepared with different Ni concentrations. The vertical bars represent the calculated pattern of Ni phenylphosphonate.

Table 3.1 Interlayer distances calculated from the (010) reflections of the XRD patterns.

Ni conc. / mmol mL^{-1}	*d*-value / nm
0.03	1.53
0.1	1.45
0.2	1.44

The Ni-Ph synthesized in a less concentrated reaction mixture exhibits wire-like structure, larger interlayer distance and lower crystallinity. These features are expected to be

advantageous for the application of this material as heterogeneous catalyst in electrochemical water oxidation owing to: i) the wire-like structure with less stacked layers provides more surface area than the larger flakes comprising more inorganic layers; ii) the larger interlayer distance provides easier access of the electrolyte to the active sites and facilitates the release of the produced gas. Therefore, a total concentration of metal precursors of 0.03 mmol mL^{-1} (Ni and/or Fe) was employed for the preparation of the NiFe phenylphosphonates. TEM images of NiFe phenylphosphonates with various Fe contents (Figure 3.6) show that with the decrease of Ni:Fe ratio, the length of these elongated particles decrease. XRD patterns in Figure 3.7 suggest the lamellar structure of these samples. Moreover, the (010), (020), and (030) reflections become sharper when more Fe present in these structures, indicating the improved crystallinity of NiFex-Ph.

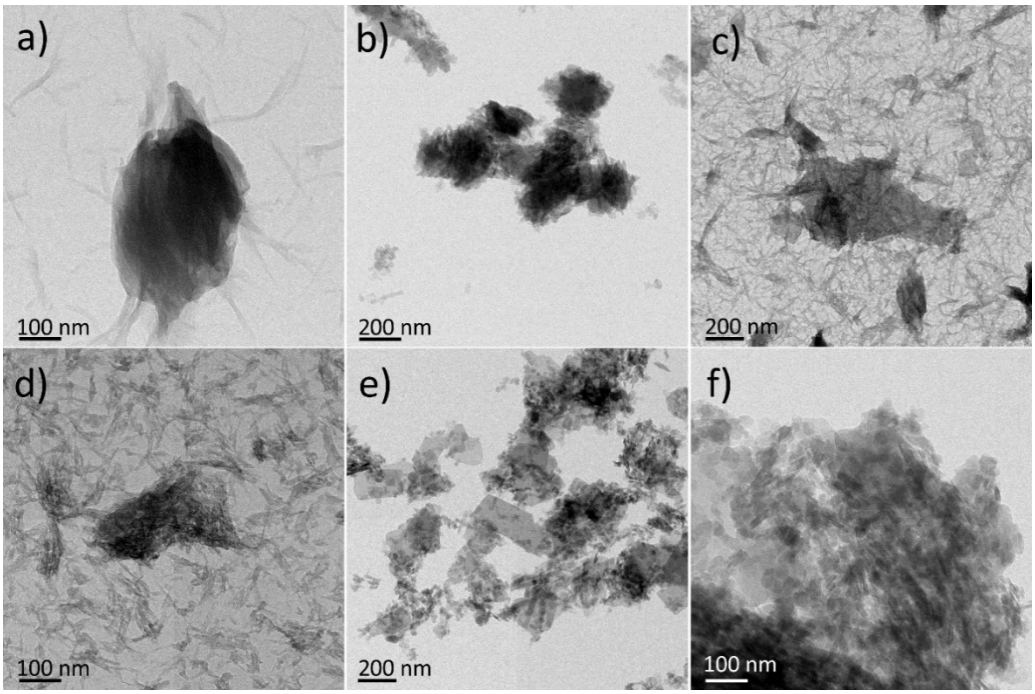

Figure 3.6 TEM images of NiFe phenylphosphonates and pure Fe phenylphosphonate. a) NiFe9-Ph; b) NiFe16-Ph; c) NiFe28-Ph; d) NiFe37-Ph; e,f) Fe-Ph.

3.2.2 X-ray absorption spectroscopy analysis

Information on the oxidation states of the metals and their local structure was obtained by X-ray absorption spectroscopy (XAS). NiFe16-Ph was selected for this measurement due to its high electrocatalytic activity, which will be discussed in the later sections. Figure 3.8 and Figure 3.9 show respectively the X-ray absorption near edge structure (XANES) and extended X-ray absorption fine structure (EXAFS) spectra of the hybrid NiFe16-Ph.

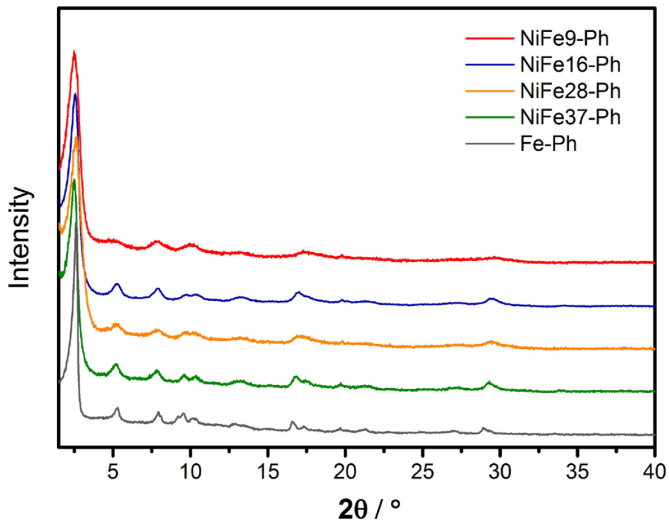

Figure 3.7 Powder XRD patterns of the NiFex-Ph and Fe-Ph.

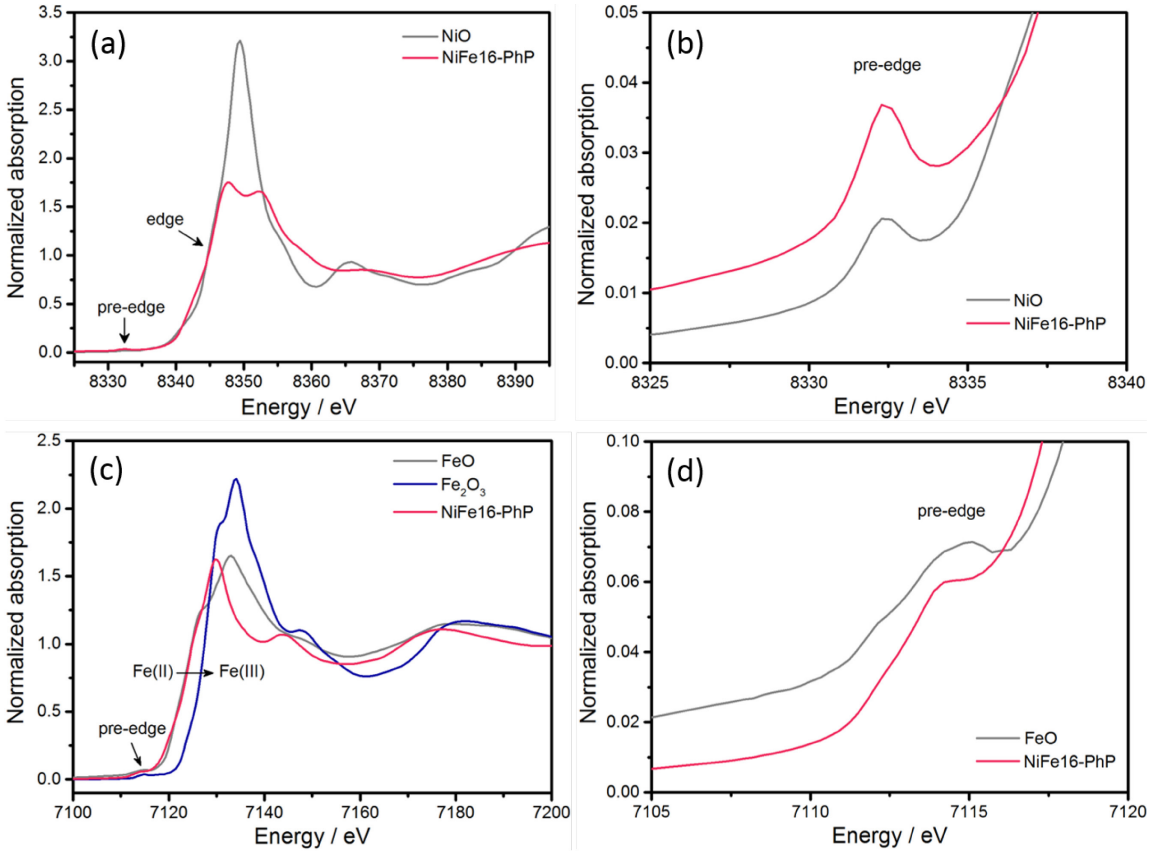

Figure 3.8 (a, b) Ni K-edge and (b, c) Fe K-edge XANES spectra of the NiFe16-Ph and reference compounds and corresponding expanded pre-edge regions.

The position of the edge in the XANES spectra is sensitive to the formal oxidation state of the monitored metal. Although the edge positions do not directly reflect the oxidation states, by carefully comparison of the edge position of the sample with those of reference compounds, one can easily estimate the oxidation state of the elements. For example, Wang *et al.*[79] found

that in the case of metal oxides, the position of the edge is linearly related to the oxidation states of metal, and a shift of ~ 2 eV was observed for a change of 1 in the valence. For NiFe16-Ph, the edge position in the Ni spectrum matches that of NiO (Ni^{2+}) and the one of Fe matches that of FeO (Fe^{2+}), indicating that both metals have oxidation state +2 in the hybrid material. As we discussed above, the inorganic layers consist of corner-shared MO_6 octahedra separated by bilayers of the organic groups. Because the metal: phosphorous ratio is 1:1 and there are coordinated water molecules, the structures contain strongly distorted octahedral. The Ni and Fe K-edge EXAFS spectra of NiFe16-Ph were fitted by modeling the structures of $Ni(II)O_3PC_6H_5 \cdot H_2O$ and $Fe(II)O_3PC_6H_5 \cdot H_2O$ using the crystallographic data given in. The bond lengths determined from the fittings (R_{fit}) are given in Table 3.2 and 3.3. The Fourier transform of EXAFS in Figure 3.9c show a direct view of the scattering of metal center in the hybrid materials, where the first shell is dominated by coordinated oxygen with the bond lengths between 2.04 - 2.18 Å for Ni-O bonds and 1.95 - 2.29 Å for Fe-O bonds.

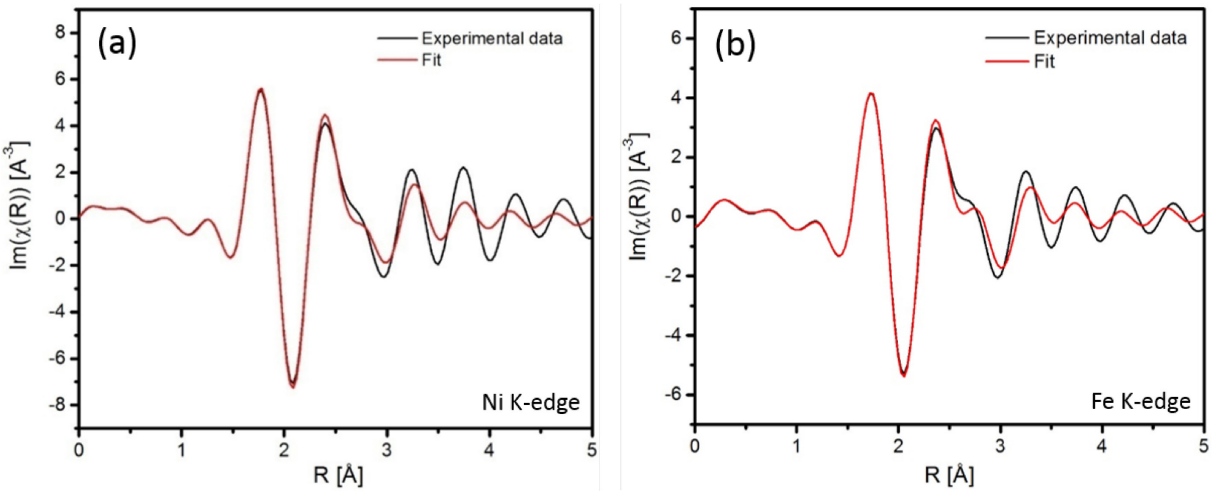

Figure 3.9 (a) Ni K-edge and (b) Fe K-edge experimental EXAFS spectra of NiFe16-Ph shown in real space and fitted data. The theoretical structure of $Ni(II)O_3PC_6H_5 \cdot H_2O$ and $Fe(II)O_3PC_6H_5 \cdot H_2O$ are used for the fitting.

The pre-edge features in the XANES spectra were also analyzed, as they are very sensitive to the coordination environment of the absorbing atom. The pre-edges are associated with electric quadrupole 1s→3d and electric dipole 1s→4p transitions [80,81]. For centrosymmetric geometries (e.g. octahedral), the intensity of the pre-edge peak is relatively low (1s→3d transitions). Deviation from centrosymmetry owing to a decrease of the coordination number (CN) or change in the arrangement of the ligands around the metal allows the occurrence of 1s→4P transitions (due to 3d and 4p molecular orbital hybridization), which enhance the pre-edge

intensity [80,81]. Thus, the increase of the intensity correlates directly with the extent of deviation from centrosymmetry. Plots correlating the pre-edge intensity with the coordination geometry have been constructed for Ni and Fe coordinated to O, based on the analysis of the pre-edge of a large number of reference compounds [82-85]. It has been shown that each geometry of the metal site and oxidation state of Ni and Fe corresponds to a defined region of pre-edge intensity[82-85]. These data were used as a guide for the analysis of our materials.

Table 3.2 Ni K-edge EXAFS fit parameters of NiFe16-Ph. The root mean square error (RMSE) is 0.108 Å.

Scattering path	R_{model} (Å)	R_{fit} (Å)	R_{diff}^2(Å^2)
Ni-O1	2.14745	2.0391	0.01174
Ni-O3	2.17315	2.0648	0.01174
Ni-O2	2.28745	2.1791	0.01174
Ni-P1	2.86165	2.7533	0.01174
Ni-O3-H1	2.87695	2.7686	0.01174
Ni-O3-H2	2.88645	2.7781	0.01174
Ni-P2	3.26055	3.1522	0.01174

The integrated intensities of the pre-edge peaks were calculated by modeling the background using a spline function[83]. The intensity of the pre-edge peaks in the spectra of the reference NiO is 0.02, which is in agreement with the values reported in the literature for this and other materials with Ni^{2+} in regular octahedral geometry[82,83]. The pre-edge feature in the spectrum of the reference FeO has two maxima due to the crystal field splitting and its intensity is 0.091, which is consistent with the results in the literature[82,85]. The pre-edge intensities in the Ni and Fe spectra of NiFe16-Ph are 0.036 and 0.14, respectively, which are high compared to those of the reference compounds and other materials in which Ni^{2+} and Fe^{2+} have regular octahedral coordination. In fact, these intensities are in the ranges normally observed for pentacoordinated Ni^{2+} and Fe^{2+}.[82-85] Although this type of hybrid materials generally contain incompletely coordinated sites at the edges of the layers, the average CN estimated from the EXAFS data is close to 6 for both metals and does not support the existence of exclusively pentacoordinated Ni and Fe. Therefore, the contribution of incompletely coordinated sites to the pre-edge intensity should be relatively small. The relatively high pre-edge intensity must be attributed to the presence of Ni and Fe in distorted octahedral sites, in agreement with the findings of other

authors[83,84]. Thus, the pre-edge analysis provides further confirmation that Ni and Fe are located in strongly distorted sites.

Table 3.3 Fe K-edge EXAFS fit parameters of NiFe16-Ph. The RMSE is 0.045 Å.

Scattering path	R_{model} (Å)	R_{fit} (Å)	R_{diff}^2(Å^2)
Fe-O1	1.99616	1.9509	0.002048
Fe-O2	2.08196	2.0367	0.002048
Fe-O3	2.33046	2.2852	0.002048
Fe-O2.2	2.45666	2.4114	0.002048
Fe-P1	3.14396	3.0987	0.002048
Fe-O3.2	3.20426	3.159	0.002048

3.2.3 Syntheses of NiFe hydroxide and oxides

For comparison, Ni hydroxide, NiFe LDH, and NiFe oxide were also synthesized according to the previous reports. The hydroxides are denoted as Ni-LDH and NiFe16-LDH representing the pure Ni hydroxide and the one containing 16 at. % Fe, respectively. Similarly, the oxide samples NiFe16-Ox and NiFe52-Ox represent the Fe contents are 16 and 52 at. % according to EDX. Figure 3.10 shows the TEM images, XRD patterns and EDX spectra of Ni-LDH and NiFe16-LDH. It can be observed that the NiFe16-LDH consists of platelets with widths between *ca.* 50-100 nm and thickness between *ca.* 20-30 nm (Figure 3.10c, d). These platelets are assembled by several layers as illustrated in the structure of NiFe LDH (Figure 3.2). The well-defined reflections at $2\theta = 5.1°$ and 10.3° are assigned to the diffractions by (003) and (006) planes, respectively. On the other hand, Ni-LDH consists of thin layers with winkles on the surface.

The TEM images (Figure 3.11 a, b) and XRD patterns of NiFe16-Ox and NiFe52-Ox (Figure 3,11c) reveal that the NiFe oxides synthesized are amorphous materials consisting of agglomerates of very small particles.

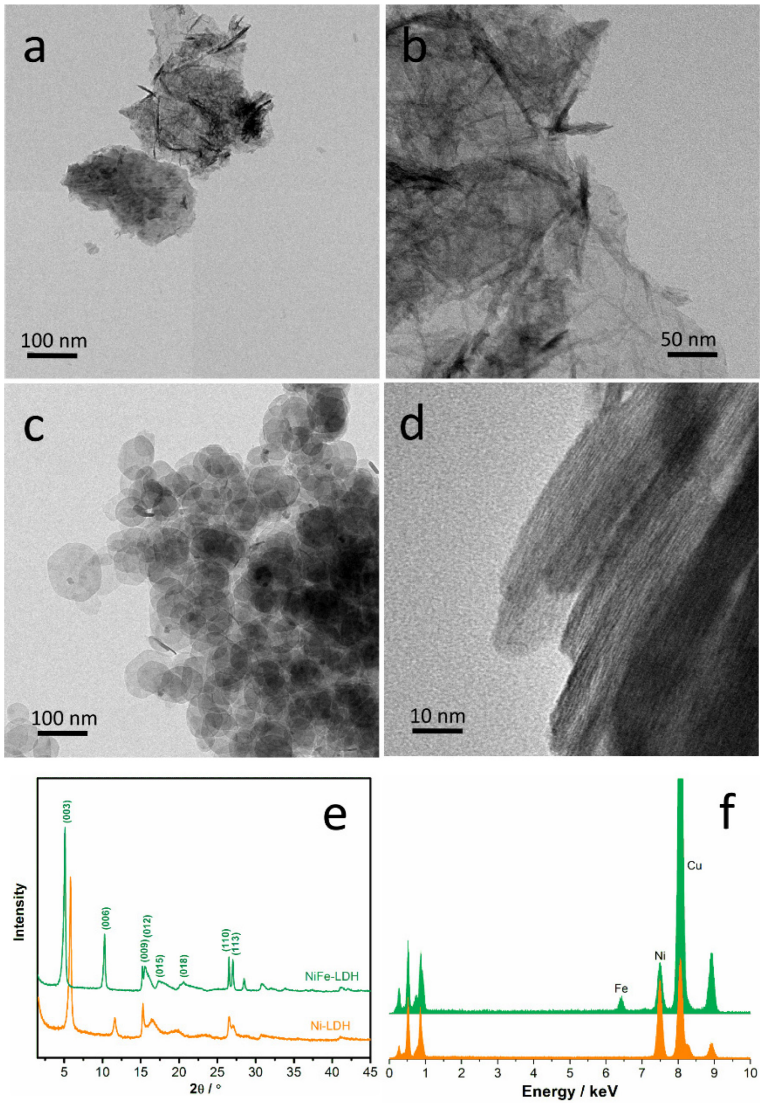

Figure 3.10 TEM images, XRD patterns and EDX spectrum of Ni-LDH (a, b, orange spectra) and NiFe16-LDH (c, d, green spectra).

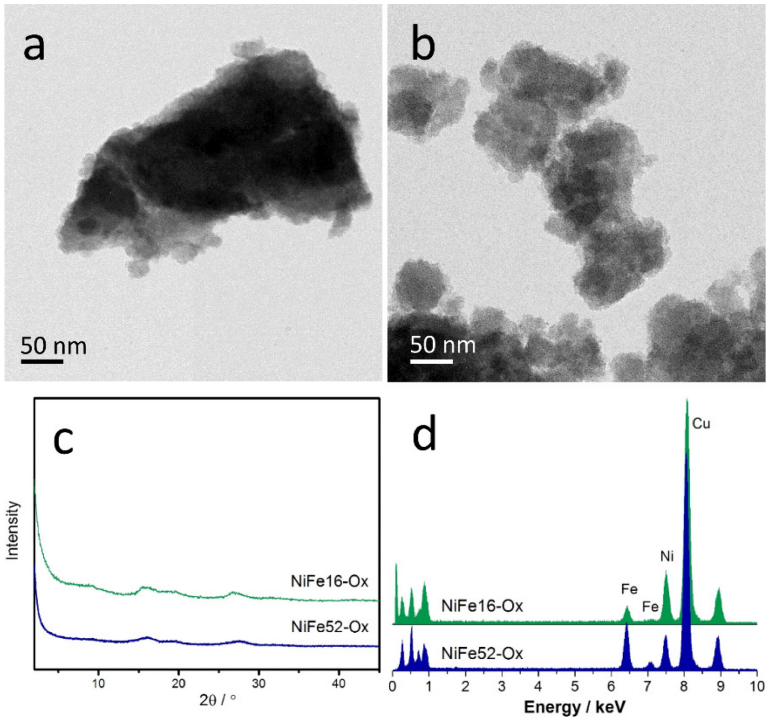

Figure 3.11 TEM images, XRD patterns and EDX spectrum of NiFe16-Ox (a, green spectra in c and d) and NiFe52-Ox (b, blue spectra in c and d).

3.3 Electrocatalytic water oxidation tests

3.3.1 Voltammetric analysis

The cyclic voltammetry (CV) and linear sweep voltammetry (LSV) techniques were applied to evaluate the electrochemical water oxidation activities in 1 M KOH, using a three-electrode rotating disc electrode (RDE) setup. Catalysts were drop-coated on a glassy carbon electrode with the addition of carbon black to improve the electronic conductivity. The catalyst mass loading is 0.42 mg cm^{-2}.

The CV curves and LSV curves of NiFex-Ph, Ni-Ph, Fe-Ph and pristine glassy carbon are shown in Figure 3.12 and Figure 3.13. It can be observed that pre-OER oxidation peaks appear in the region 1.3-1.5 V vs. RHE, which are due to the reversible redox reaction of Ni^{2+}/Ni^{3+}, [86-88] and indicate the occurrence of changes in situ in the hybrid catalysts. Several works show that the surface of different Ni- and NiFe-based OER catalysts is transformed into hydroxides or oxyhydroxides in alkaline medium[87,89,90]. The formation of a hydroxide phase during the reaction was also observed in this work, as it will be discussed in detail in Section 3.4. Moreover, the addition of Fe to the Ni phenylphosphonate structure enhances the OER activity and causes

anodic shifts of the Ni^{2+}/Ni^{3+} oxidation peaks. For the samples NiFe28-Ph and NiFe37-Ph, the Ni^{2+}/Ni^{3+}oxidation peaks overlap with the water oxidation wave (Figure 3.12 d, e).

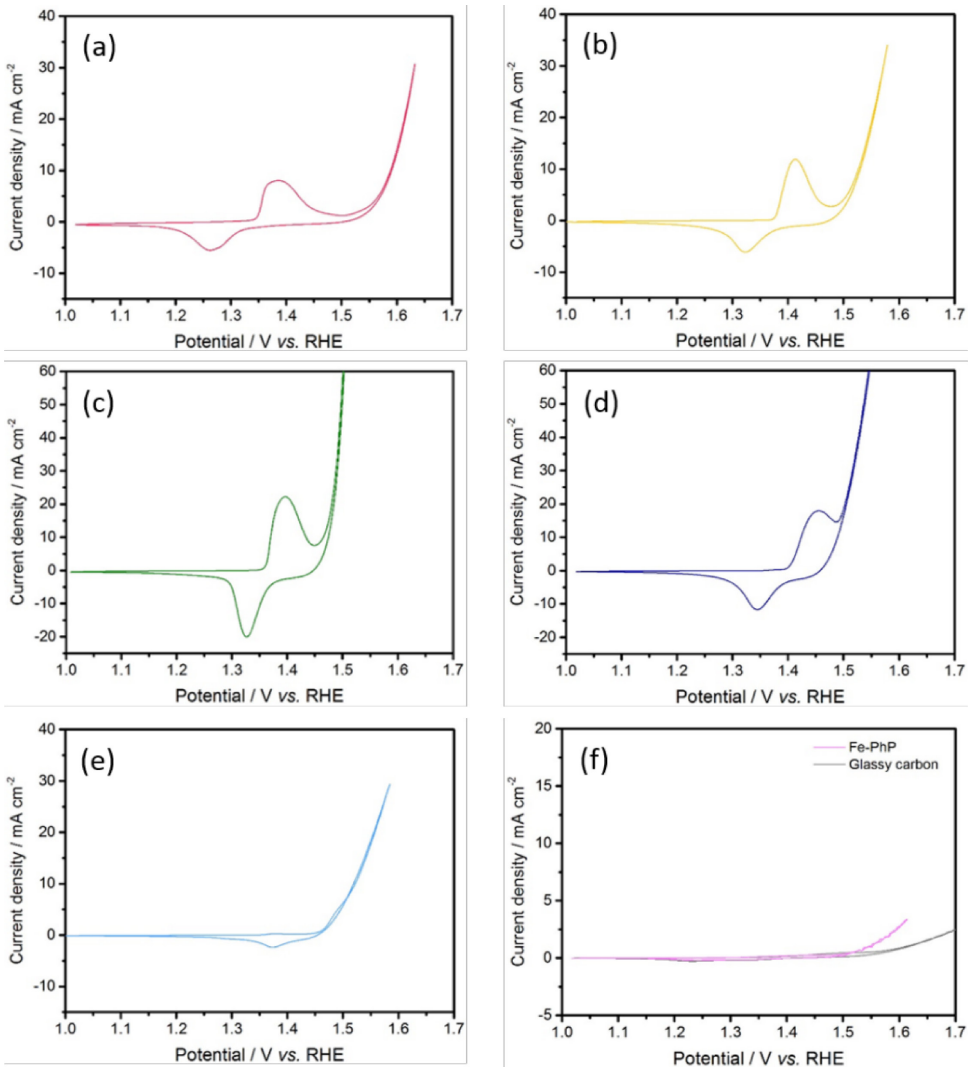

Figure 3.12 Cyclic voltammetry (CV) curves of (a) Ni-Ph, (b) NiFe9-Ph, (c) NiFe16-Ph, (d) NiFe28-Ph, (e) NiFe37-Ph, (f) Fe-Ph and pristine glassy carbon. Scan rate: 20 mV/s.

Normally, two potentials are extracted from the LSV or CV curves and used for determining the activities of the catalyst in the water oxidation reaction: one is the onset potential (E_{onset}), and the other is the overpotential at a specific current density (η). E_{onset} is the lowest potential at which a reaction product is formed at a given electrode and at defined conditions[91]. In this work, the onset potentials are difficult to obtain due to the peaks overlapping. The potential applied on the working electrode (E_{OER}) to reach a current density of 10 mA cm^{-2} was used to calculate the overpotential η (η = E_{OER} – 1.23 V).

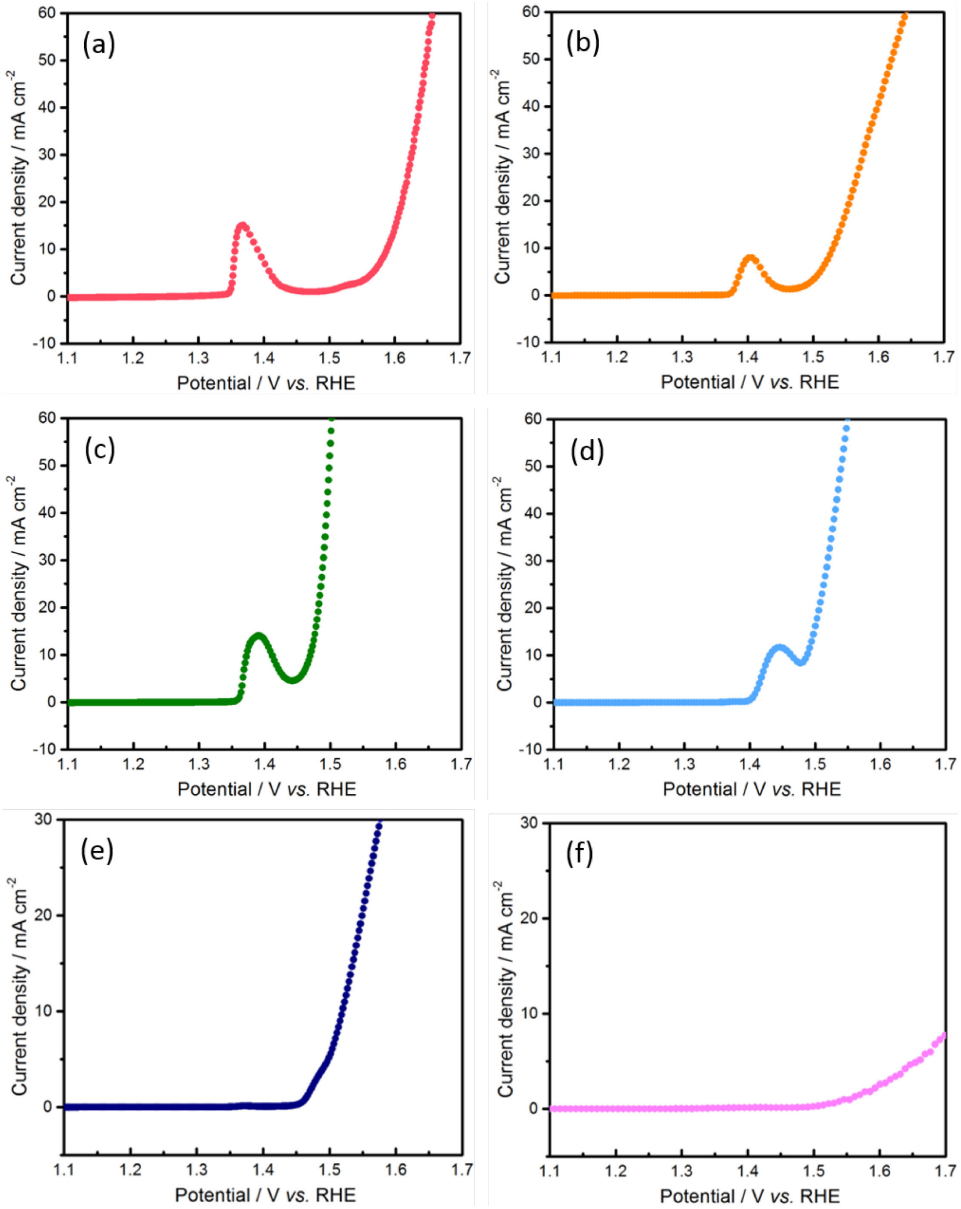

Figure 3.13 LSV curves of (a) Ni-Ph, (b) NiFe9-Ph, (c) NiFe16-Ph, (d) NiFe28-Ph, (e) NiFe37-Ph, (f) Fe-Ph. Scan rate: 10 mV/s.

Figure 3.14 displays the overpotentials η for the NiFex-Ph catalysts as a function of the Fe atomic percentage. The activity of the NiFex-Ph increases with the increase of the iron content until the overpotential reaches the optimal value of 240 mV at a Fe atomic percentage of 16, and subsequently decreases with further increase of the iron content. The pure Fe phenylphosphonate performs poorly and cannot even reach the current density of 10 mA cm^{-2} within the potential window. This result is similar to those reported for many Fe oxides and hydroxides and has been attributed partly to the low electrical conductivity of Fe oxyhydroxides[92,93]. The optimum Fe content, i.e. the amount of Fe introduced into the material

that maximizes the synergy between Fe and Ni, and thus maximizes the activity, varies significantly (between *ca.* 10 and 55 %) among the NiFe-based catalysts described in the literature. A possible explanation for the decrease in the activity above a certain Fe content is the formation of segregated iron oxyhydroxide phases[94,95], which are inactive and have a detrimental effect on the catalytic activity.

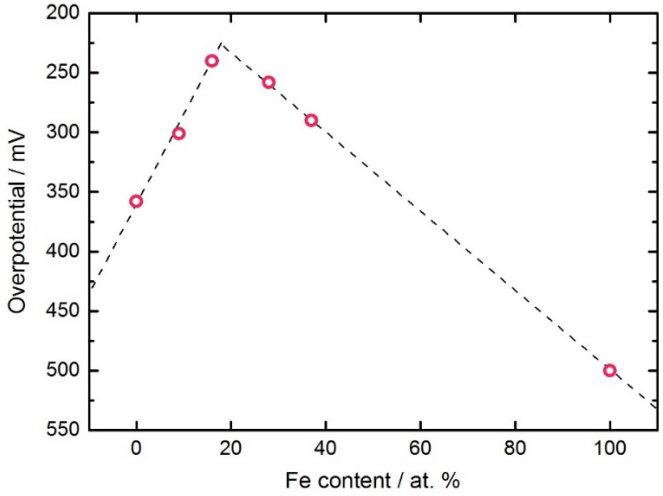

Figure 3.14 Overpotentials for NiFex-Ph catalysts as a function of iron atomic percentage.

The performance of the pure Ni catalyst (NiFe0) improved with potential cycling; the activity increased during the first 300 CV cycles and then remained constant after further 200 cycles (Figure 3.15). This behavior generally occurs with pure Ni oxide and hydroxide electrodes and has been attributed to the incorporation of Fe present as an impurity in the electrolyte[33]. Evidence of Fe incorporation is the anodic shift of the oxidation peaks which agrees with the reports that the oxidation peaks shift to more positive potential with the increase of Fe contents in NiFe oxides or hydroxides[7,33]. EDX analysis of the Ni-Ph catalyst after cycling further confirmed the incorporation of iron (8%) from the electrolyte. Similar observation was demonstrated by Trotochaud *et al.*[33] the iron impurities in the electrolyte were readily incorporated into pure Ni oxyhydroxide electrodes: a Fe content of 5 % was detected in the electrode after just 5 CV cycles in high purity KOH electrolyte. The activity and iron content of other catalysts, on the other hand, did not varied significantly during cycling.

The Tafel plots of the NiFe phenylphosphonate catalysts are shown in Figure 3.16, which consist on the variation of the overpotential as a function of the logarithm of the current density. A smaller Tafel slop suggests that a smaller overpotential rise is required for reaching a faster increase of the current density; in another word, the reaction occurs on the electrode having

faster kinetics. The NiFe16-Ph has a Tafel slope of 40 mV dec^{-1} implying a fast electrocatalytic kinetic in the experimental condition.

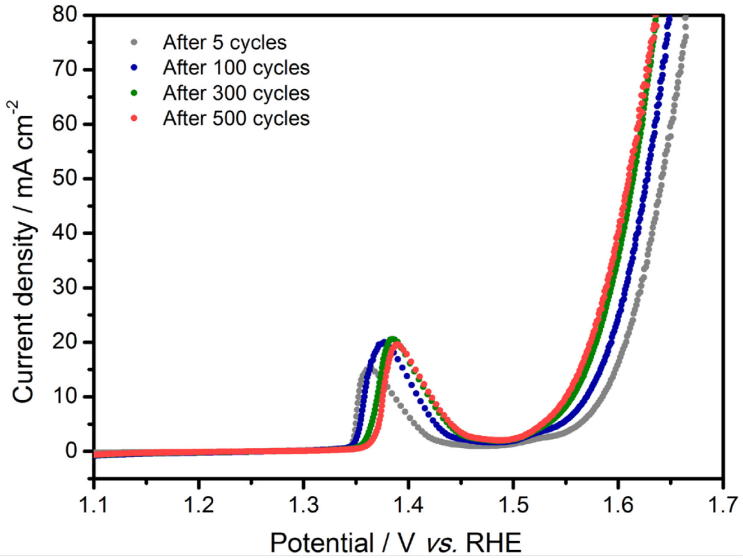

Figure 3.15 LSV curves of Ni-Ph after potential cycling. Scan rate: 10 mV/s.

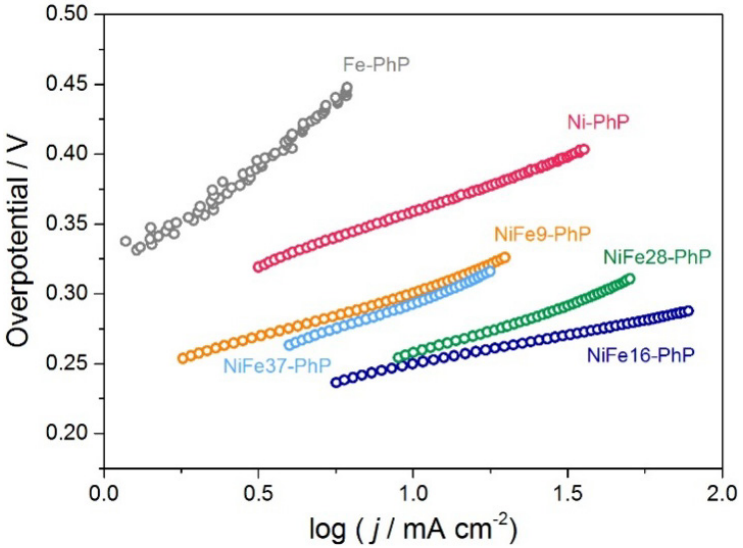

Figure 3.16 Tafel plots of the NiFe phenylphosphonates with different Fe content.

NiFe hydroxides and NiFe oxides were also tested as references in the same conditions as the NiFex-Ph catalysts and the LSV curves and Tafel plots were shown in Figure 3.17 and 3.18. Since the NiFe16-Ph catalyst exhibits the highest electrocatalytic activity among the NiFe phenylphosphonates, the reference samples were prepared with the same Fe content of 16 at. %. NiFe16-LDH performed better than Ni-LDH, exhibiting an overpotential at 10 mA cm^{-2} of 308 mV and Tafel slope of 85 mV dec^{-1}. For the NiFe oxides, the sample with Fe content of 52 at. % exhibits lower overpotential (η = 297 mV at 10 mA cm^{-2}) and smaller Tafel slope (64 mV dec-

[1]) compared to NiFe16-Ox. Therefore, for a better understanding of the structural effects on electrocatalytic activity, we choose NiFe16-Ph, NiFe16-LDH and NiFe16-Ox for the further studies.

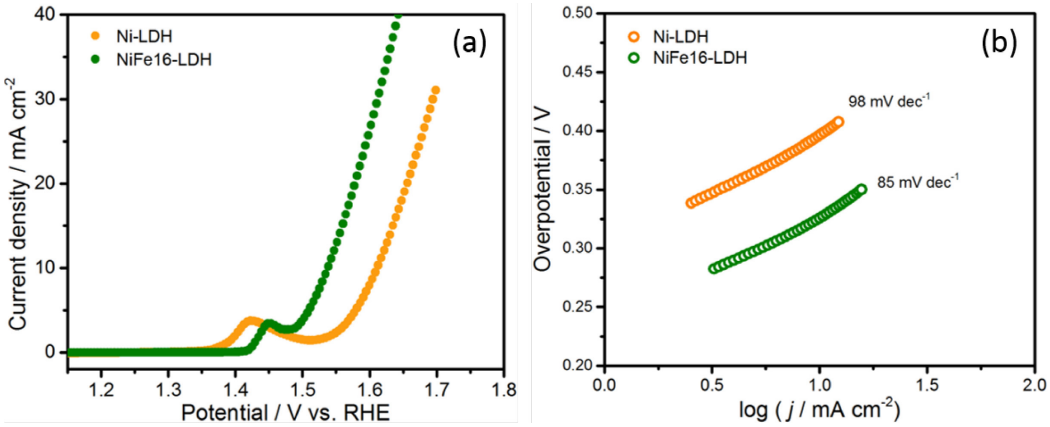

Figure 3.17 LSV curves and Tafel plots of Ni-LDH and NiFe16-LDH catalysts.

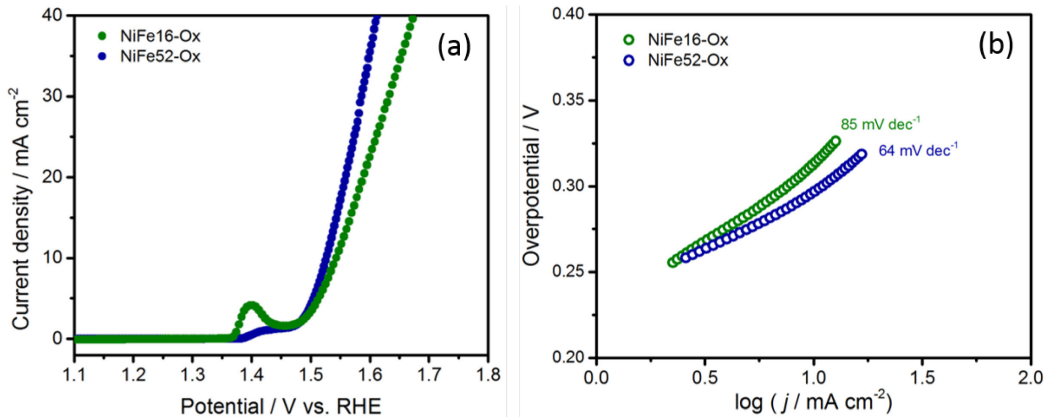

Figure 3.18 LSV curves and Tafel plots of NiFe16-Ox and NiFe52-Ox catalysts.

3.3.2 Double-layer capacitance and turnover frequency

The superior OER performance of NiFe16-Ph can be due to the inherent activity of this catalyst and/or to an increased electrochemically active surface area (ECSA). The surface area of an electrode affects the amount of active sites exposed to the electrolyte, and consequently influences the activity of a catalyst: higher electrode surface area leading to higher geometric current density at a given potential. The double-layer capacitance (C_{dl}) is proportional to the electrochemically active surface area of the electrode according to equation (3.24):

$$\mathrm{ESCA} = \frac{C_{dl}}{C_s} \tag{3.24}$$

where Cs is the specific capacitance of the material. However, capacitance measurements can be affected by large errors, especially in the case of poorly electronic conductive NiFe hydroxide phases[10,14,96,97]. For this reason, the C_{dl} cannot be used for calculating absolute values of ECSA but are considered suitable for evaluating trends among the materials.

The double-layer capacitance (C_{dl}) of the catalysts was determined by cyclic voltammetry. The potential window is determined by open circuit potential, i.e. between -0.1 V to 0 V vs. Ag/AgCl, where no faradaic processes are observed. The potential was swept in this potential window three times at each of six different scan rates (5, 10, 25, 50, 75 and 100 mV/s) and hold for 10s between sweeps. The capacitive current densities for each sample was recorded and are shown in Figure 3.19 a, b and c. The double-layer capacitances were extracted from the slope of the linear plots of Δj (taken at -0.05Vvs. Ag/AgCl) as a function of the scan rate. As shown in Figure 16 d, the C_{dl} of the NiFe16-Ph is 108 μF cm^{-2}, 12.5 % higher than that of NiFe16-LDH (96 μF cm^{-2}) and 21.3 % higher than that of NiFe16-Ox (89 μF cm^{-2}). The C_{dl} of the bare GC electrode is 36 μF cm^{-2}. Considering the differences in overpotential η among these electrodes, which for NiFe16-Ph is 28.3% lower than NiFe16-LDH and 30.4% lower than NiFe16-Ox, the differences of the C_{dl} are not sufficiently large for explaining the high activity of the NiFe16-Ph catalyst.

The turnover frequency (TOF) for each catalyst was calculated to obtain insights on the intrinsic electrochemical activity of the catalytic sites. TOF values reported here are defined as the moles of O_2 evolved per mole of Ni in the catalyst per second. The calculation was carried out according to equation (3.3) mentioned in the Experimental section. The overpotentials were extracted at the current density of 300 mA cm^{-2}, and the amount of active sites were calculated by integrating the Ni^{2+}/Ni^{3+} oxidation peaks. Ni was considered the active sites according to the discussion in the Section 3.1.2. The TOFs are 0.100, 0.027, 0.013 and 0.056 S^{-1} for NiFe16-Ph, NiFe16-LDH, NiFe16-Ox and NiFe52-Ox, respectively. This trend roughly agrees with the OER activity of these materials, especially for those with the same Fe content, as shown in Figure 3.20. And a similar trend is observed if the reduction peaks are used for calculating the number of active sites, although the TOF values are slightly different. Therefore, the superior OER activity of NiFe16-Ph can be attributed to the high intrinsic activity of this hybrid structure compared to the hydroxide and oxide reference catalysts.

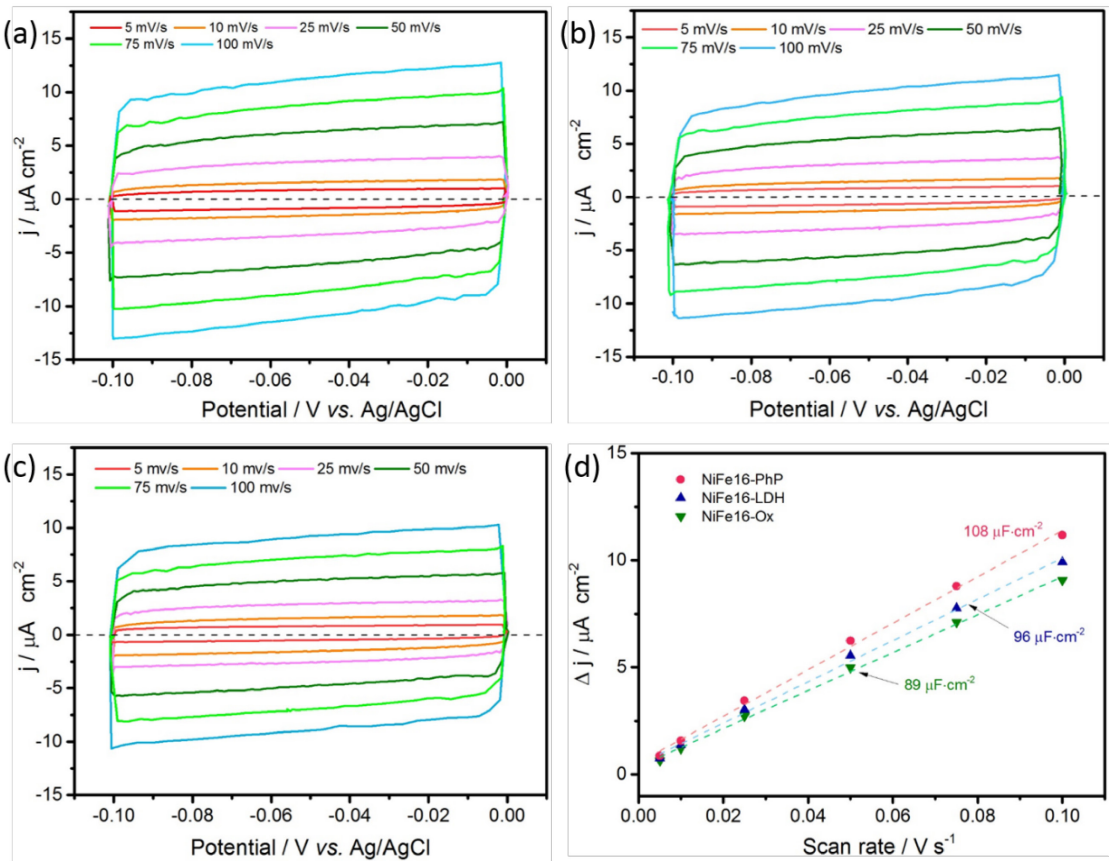

Figure 3.19 Double-layer current densities measured at different scan rates in the potential window -0.1 to 0 V vs Ag/AgCl (3.0 M) for (a) NiFe16-Ph, (b) NiFe16-LDH and (c) NiFe16-Ox. (d) Plots of the average of anodic current density and absolute cathodic current density (Δ j) at the -0.05 V vs Ag/AgCl as a function of scan rate for the three electrodes. The linear dependence of the current density on the scan rate is consistent with non-faradaic behavior in the potential region. The double-layer capacitance was extracted from the slope of linear fits.

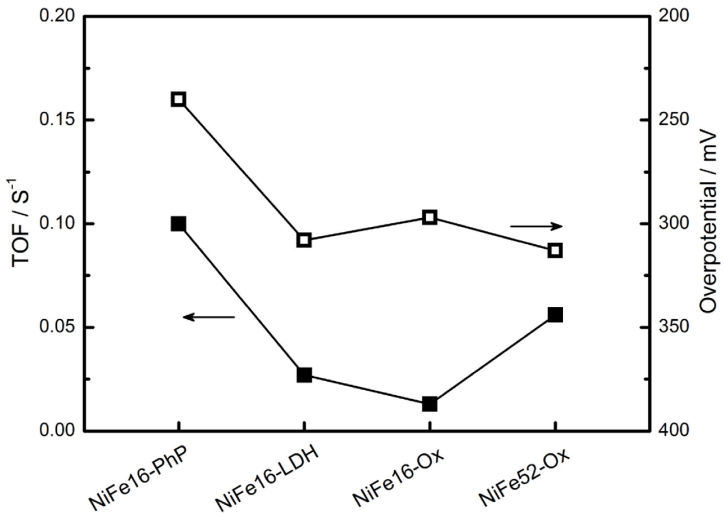

Figure 3.20 TOF and overpotentials for NiFe16-Ph, NiFe16-LDH, NiFe16-Ox and NiFe52-Ox catalysts.

3.3.3 Stability tests and Faradaic efficiency

The stability of a catalyst under the operating conditions is an essential requirement for practical applications. Therefore, two methods are applied to evaluate the NiFe16-Ph electrode in alkaline electrolyte: potential cycling test by cyclic voltammetry and long-term test by chronopotentiometry. The cycling performance was examined by using RDE set-up at the rotating speed of 1600 rpm and sweeping the potential between 0.1 and 0.6 V vs Ag/AgCl at a scan rate of 100 mV/s. Figure 3.21a shows the LSV curves recorded at a scan rate of 10 mV/s before and after 500, 1000 CV cycles. The overpotential required to achieve a current density of 10 mA cm^{-2} increased from 245 mV to 250 mV after 500 cycles and then 254 mV after 1000 cycles. The initial overpotential here (245 mV) is slightly higher than the one shown in Figure 3.12 (240 mV), that may cause by experimental errors within the acceptable range of ± 10 mV. Chronopotentiometry was carried out in other set-up where the catalyst was coated on a static nickel foil which is perpendicular to the liquid level. The potential was recorded over time during the continuous electrolysis at a fixed current density of 10 mA cm^{-2}. As shown in Figure 3.21c, the overpotential of the NiFe16-Ph electrode increases by less than 20 mV after 160 hours of continuous operation.

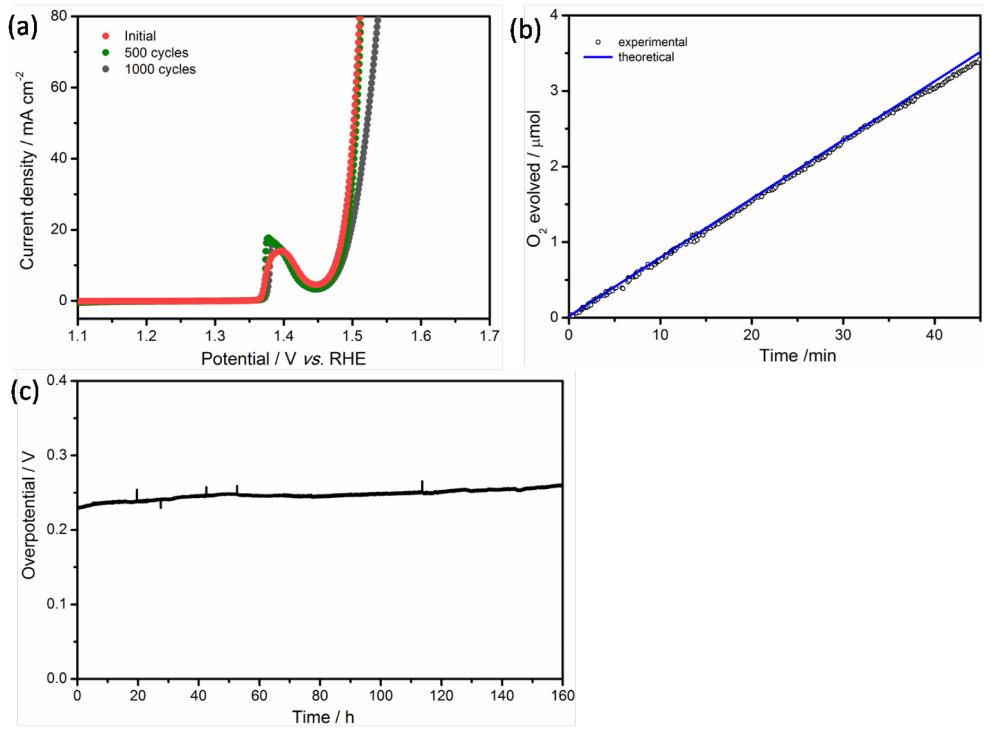

Figure 3.21 (a) LSV curves of NiFe16-Ph electrode measured before and after 500, 1000 CV cycles; (b) comparison between the amount of O_2 produced by the NiFe16-Ph electrode and the theoretical amount. (c) chronopotentiometric curve with a fixed current density of 10 mA cm^{-2}. Inserted is the overpotential record in the first 5 minutes.

To confirm that oxygen was being produced and determine the efficiency of the electrocatalytic process, the amount of O_2 evolved during electrolysis was quantified by using an O_2 sensor. As shown in Figure 3.21 b, the NiFe16-Ph catalyst was found to catalyze the water oxidation with a faradaic efficiency of 97 %, indicating the working electrode produced almost all of the current at such a low overpotential from the production of O_2, but not other reactions such as oxidation of the phosphonate groups.

3.4 Characterization of the NiFe16-Ph after OER measurement

3.4.1 In situ transformation of the metal phenylphosphonate

The NiFe16-Ph catalyst without the addition of carbon was characterized after the electrocatalytic OER measurements. The samples after catalysis were named as NiFe16-10CV or NiFe16-50CV corresponding to the samples collected after 10 or 50 potential cycles, respectively. Figure 3.22a, c, e show the scanning electron microscopy (SEM) images of the fresh NiFe16-Ph electrode on a nickel foil substrate. The catalyst coating is composed of elongated particles and the surface has some rugosity due to the randomly stacking of the particles. After 50 potential cycles, the color of the electrode changed from yellowish-green to black. Figure 3.22 b, d and f show that the elongated particles transform into smaller particles which cannot be identified separately in the magnification during measurement. The catalyst was also collected from the nickel foil after OER for element analysis. The carbon content of the material was initially 32 wt.%; after cycling, the carbon content was almost zero and phosphorous was no longer detected by EDX analysis (Figure 3.23), suggesting that the organophosphonate component was almost entirely transferred to the electrolyte. This indicates that not only the superficial region, as observed for other Ni- or NiFe-based catalysts[87], but the entire material was transformed in situ during the reaction, which may be attributed to the large spacing between the inorganic layers that allows the electrolyte to access the structure. The Fe content was 17% after catalysis, determined by EDX.

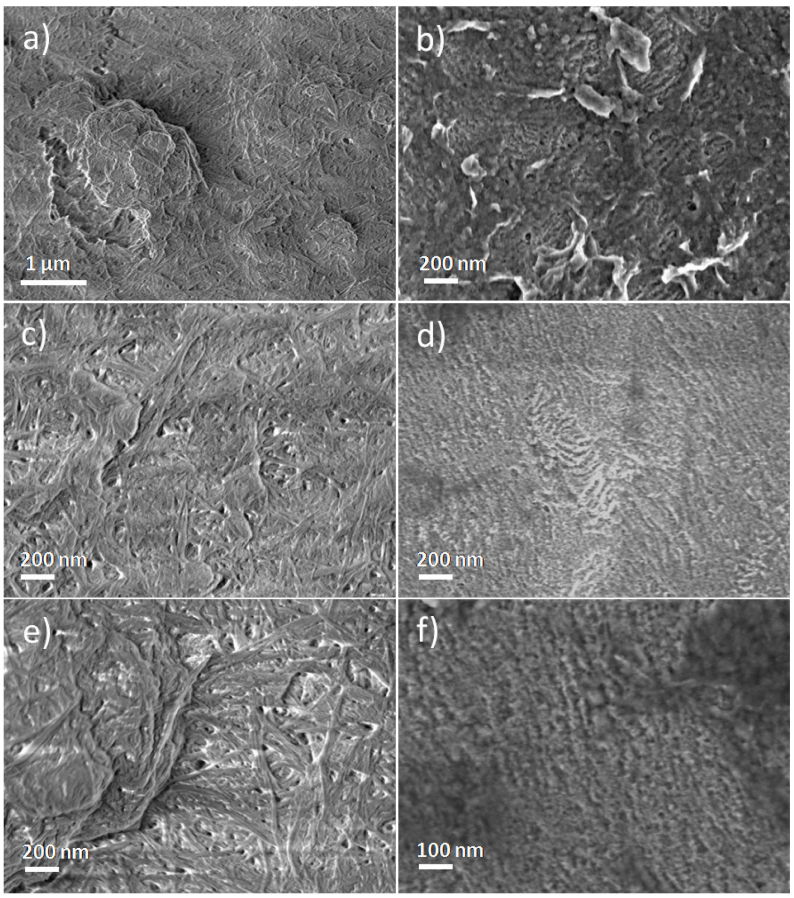

Figure 3.22 Scanning electron microscopy (SEM) images of the (a, c, e) fresh NiFe16-Ph electrode and (b, d, f) the electrode after 50 potential cycles in the potential window of 0 to 0.7 V vs Ag/AgCl. The electrodes were flashed three times by deionized water and dried at 65°C overnight before characterization.

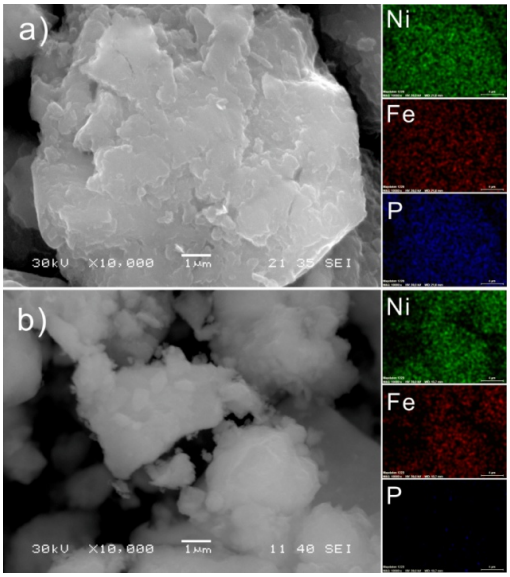

Figure 3.23 SEM images and corresponding EDX elemental mapping of the a) as-prepared NiFe16-Ph catalyst powder and b) the catalyst after 50 potential cycles (NiFe16-50CV) in the potential window of 0 to 0.7 V vs Ag/AgCl.

The powder XRD patterns of NiFe16-50CV only shows reflections indexed to a hydroxide (Figure 3.24), confirming the complete transformation of the hybrid. On the contrary, the (010) reflection of the hybrid is still very intense in the XRD pattern of the catalyst after 10 CV cycles (NiFe16-10CV). The transformation of the material occurs progressively during OER but is not accompanied by a significant variation in the performance of the catalyst. The activities in the beginning (when the material still contains the hybrid) and after 500 or 1000 cycles (when the catalyst is fully transformed) are similar, as shown in Figure 3.21 a. TEM analysis reveals that NiFe16-50CV consists of small and thin nanosheets with sizes around 5-25 nm and thicknesses between 3 and 10 nm (Figure 3.25). The thin nanosheets are made of a reduced number of layers that are not perfectly stacked because they were derived from the metal organophosphonate structure, which is consistent with the broad reflections in the XRD pattern indicative of disorder, as compared with those of NiFe-LDH (Figure 3.10 e). The selected area electron diffraction (SAED) patterns confirmed the crystal structure of a hydroxide after the electrocatalytic water oxidation reaction.

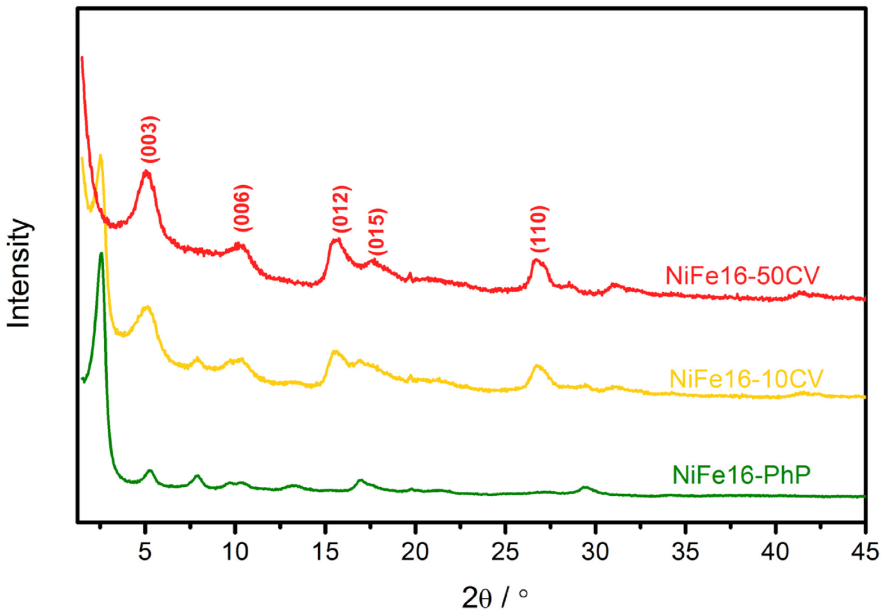

Figure 3.24 XRD patterns of the NiFe16 catalysts before and after 10 and 50 CV cycles.

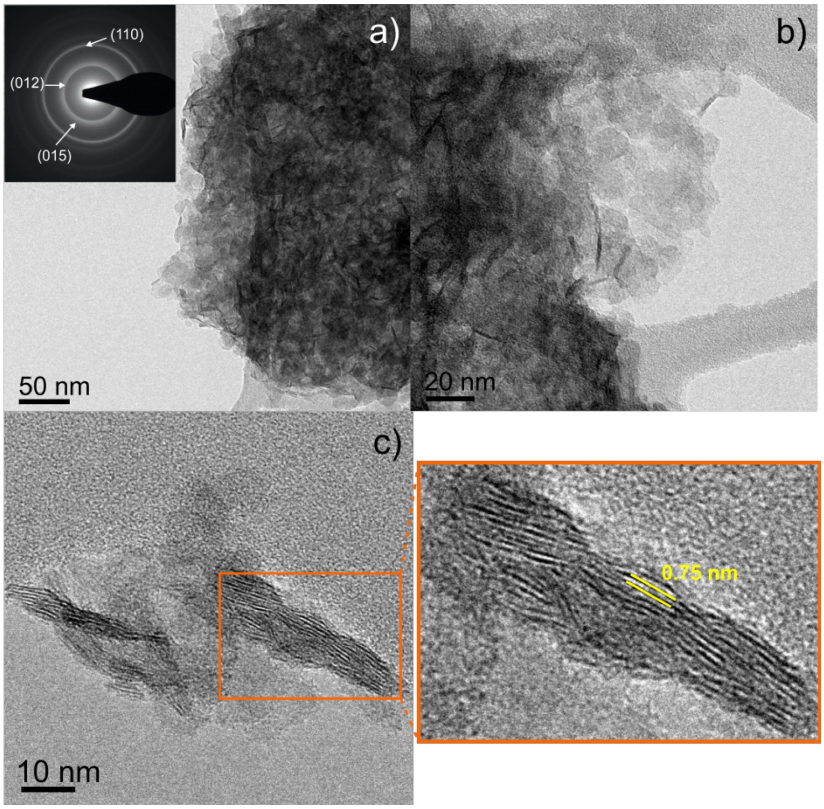

Figure 3.25 TEM images of the NiFe16 catalyst after 50 CV cycles (NiFe16-50CV) in 1M KOH in the potential window of 0 - 0.7 V vs. Ag/AgCl. The SAED pattern (inset in figure a) shows diffraction rings indexed to the hydroxide.

3.4.2 X-ray absorption spectroscopy (XAS) of the NiFe16-Ph catalyst after OER

To understand the local structure of the catalyst, X-ray absorption spectroscopy (XAS) characterization of the catalyst collected after 50 CV cycles (NiFe16-50CV) was done. Comparison of the edge position in the Ni and Fe K-edge XANES spectra with those of reference compounds NiO (Ni^{2+}) and Fe_2O_3 (Fe^{3+}) indicates that Ni and Fe are in oxidation state of +2 and +3 (Figure 3.26). The Ni and Fe EXAFS data of NiFe16-50CV were fitted by modeling the structures of the hydrated α-$Ni(OH)_2$ and γ-FeOOH, respectively, and confirm the transformation of the hybrid material during the electrocatalytic testing (Figure 3.27). A structural reorganization occurs, with the inorganic layers of the hybrid formed by corner-shared octahedra being transformed into edge-shared octahedra, and the average interlayer distance decreasing as the organic groups are removed. The EXAFS fitting data (Table 3.4 and 3.5) suggests that the distances of Ni-O and Fe-O reduce from 2.04 - 2.18 Å and 1.95 - 2.29 Å in NiFe phenylphosphonate to 1.92 Å and 1.98 - 2.07 Å after OER. The second peaks in Fourier transforms of EXAFS (Figure 3.27c, d) exhibit the oscillations of the Ni-Ni and Fe-Fe shells in

α-Ni(OH)$_2$ and γ-FeOOH, respectively. The distances are 3.03 Å for Ni-Ni and 3.05Å for Fe-Fe which are in agreement with the literatures in these materials[31,98].

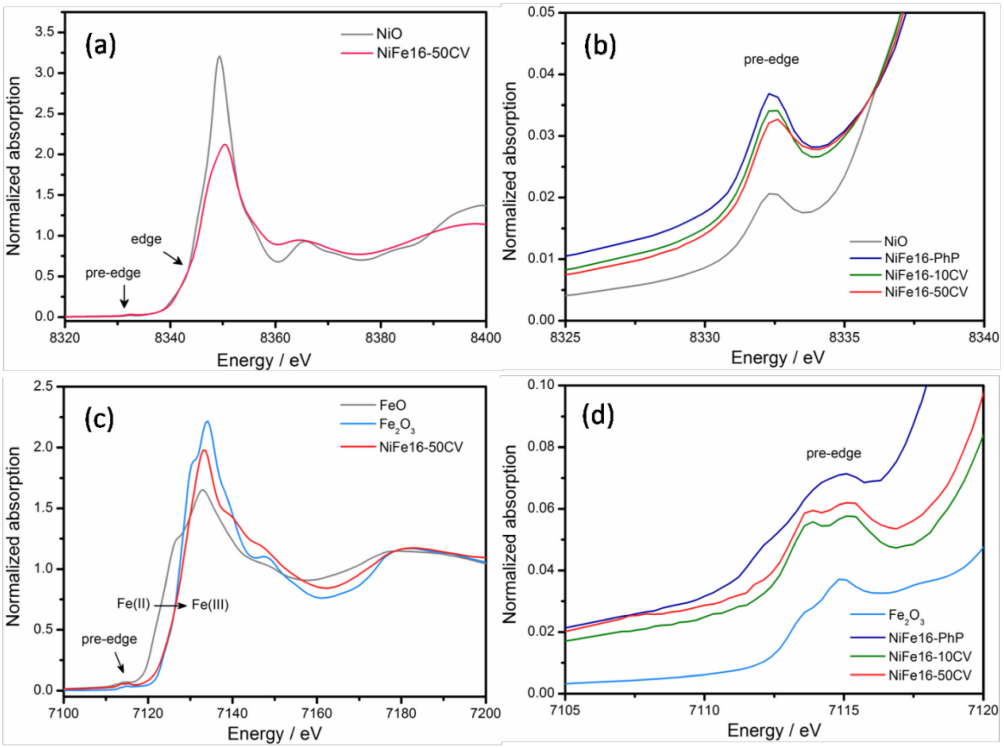

Figure 3.26 (a, b) Ni K-edge and (b, c) Fe K-edge XANES spectra of the NiFe16-Ph catalyst after OER and reference compounds and corresponding expanded pre-edge regions.

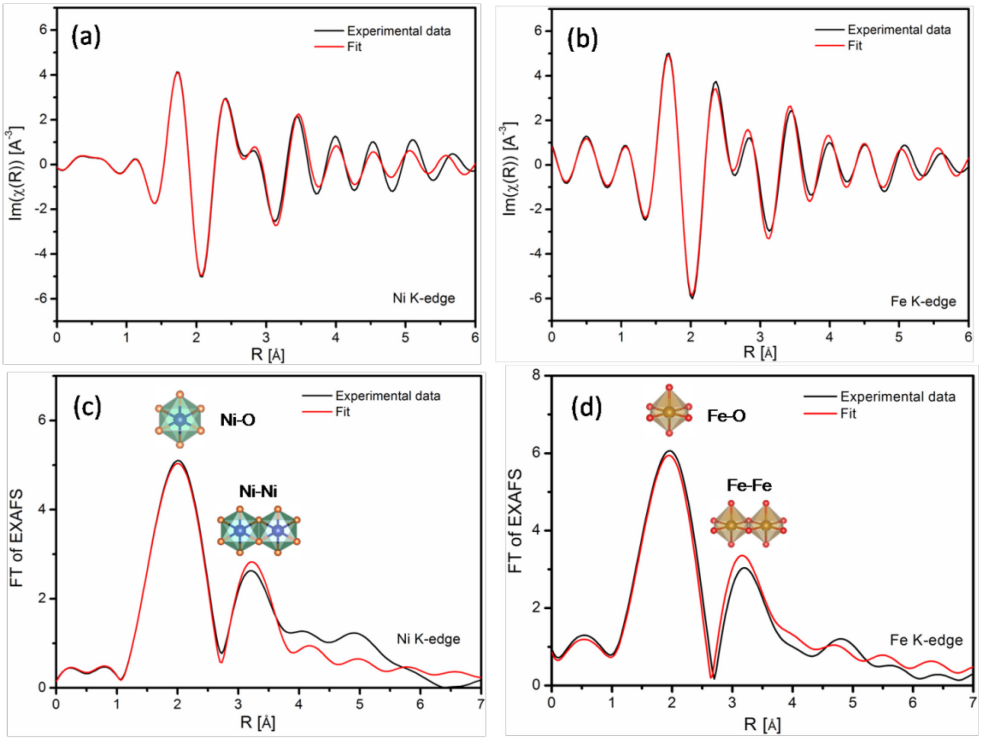

Figure 3.27 (a, c) Ni K-edge and (b, d) Fe K-edge EXAFS spectra of NiFe16-50CV shown in real space and after Fourier Transform. The theoretical structure of α-Ni(OH)$_2$ and γ-FeOOH are used for the fitting.

Table 3.4 Ni K-edge EXAFS fit parameters of NiFe16-50CV. The root mean square error (RMSE) is 0.042 Å. The theoretical structure of α-$Ni(OH)_2$ is used for the fitting.

Scattering path	R_{model} (Å)	R_{fit} (Å)	R_{diff}^2(Å^2)
Ni-O	1.966	1.92365	0.001794
Ni-Ni1	3.07	3.02765	0.001794
Ni-O1-H1	3.1945	3.15215	0.001794
Ni-O1-H1	3.501	3.45865	0.001794
O-H1-Ni1	3.501	3.45865	0.001794
Ni-O-H2	3.6456	3.60325	0.001794

Table 3.5 Fe K-edge EXAFS fit parameters of NiFe16-50CV. The RMSE is 0.161 Å. The theoretical structure of γ-FeOOH is used for the fitting.

Scattering path	R_{model} (Å)	R_{fit} (Å)	R_{diff}^2(Å^2)
Fe-O1	2.1447	1.9841	0.025792
Fe-O2	2.2269	2.0663	0.025792
Fe-Fe1	3.2108	3.0502	0.025792
Fe-O1-O2	3.5149	3.3543	0.025792
Fe-O1-O-H1	3.6353	3.4747	0.025792
Fe-O1-Fe2	3.6999	3.5393	0.025792
Fe-O2-H2	3.7963	3.6357	0.025792
Fe-Fe3	4.0306	3.87	0.025792
Fe-O1-O1	4.0709	3.9103	0.025792
Fe-O1-Fe3	4.0709	3.9103	0.025792
Fe-O1-O1	4.1111	3.9505	0.025792

In order to evaluate the changes occurring in the first coordination shell of the metals, the pre-edge features in the XANES spectra were analyzed. The analysis is facilitated for Ni because the oxidation state of this metal did not change. The pre-edge intensity decreases as the catalyst is transformed. Nevertheless, the decrease is not drastic as the intensity corresponding to the fully converted catalyst is 0.031 and consequently high for Ni^{2+} in regular octahedral geometry[82,83]. The centroid of the pre-edge feature in the Fe spectrum shifts to higher energy by 1.3 eV for the NiFe16-50CV. The magnitude of the shift is close to the value 1.4 eV reported in the literature for the increase in the oxidation state of Fe from 2+ to 3+. The intensity of the pre-edge decreases with increasing the number of cycles. However, as observed for Ni, the intensity is still high for NiFe16-50CV (0.12) compared to that of the reference Fe_2O_3 and other materials with Fe^{3+} in regular octahedral sites [82,83]. Although the presence of some incompletely coordinated metal sites at the edges of the nanosheets cannot be excluded, the average coordination number (CN) estimated from the EXAFS signals are close to 6, suggesting that the presence of distorted metal sites are the major contributor to the increased intensity observed. Furthermore, although the structural changes occurring in the materials in situ lead to a small loss of pre-edge intensity, the coordination environment of the metals in the hybrid seems to be transferred in some extent to the hydroxide. This means the hybrid material acts as a template for the structure of the metal sites, as well as a template for the formation of the small nanosheets, which is illustrated in Figure 3.28. The inorganic layers of the metal-organophosphonate are converted into the layers of the hydroxide as the large organic ligands are gradually replaced by the hydroxide ligands, decreasing also the interlayer spacing. The presence of only a small number of inorganic layers in each hybrid particles leads to the formation of thin hydroxide nanosheets. Moreover, the templating effect of the local structure by the phosphonate ligands possibly originates from the gradual replacement of the phosphonate by the hydroxyl groups. When an O atom from a hydroxyl ligand replaces an O atom from a phosphonate in a coordination site, the presence of other coordinating phosphonate ligands does not allow the complete relaxation of the local geometry and "forces" the hydroxyl group to coordinate in certain geometry. This effect successively occurs as the hydroxyls replace all the original ligands and the local coordination environment remains with some distortion when the transformation is complete. The transformation of the catalyst starts to occur in the first CV cycles prior to OER as indicated by the pre-OER Ni^{2+}/Ni^{3+} redox couple, whose magnitude does not change significantly with cycling, suggesting that the majority of the active sites are accessible to the electrolyte from the beginning. Therefore, replacement of O from the phosphonate by O from the hydroxyl groups at some coordination sites likely occurs for many

of the metal centers in the first cycles. Furthermore, although the composition of the catalyst changes during the first 50 cycles, the chemical environment to the metal does not vary drastically (the metals are bonded to six O atoms in both the metal-organophosphonate and metal hydroxide), as well as the structure of the sites as discussed above. These effects help explaining why the activity of the catalyst does not change significantly during the transformation.

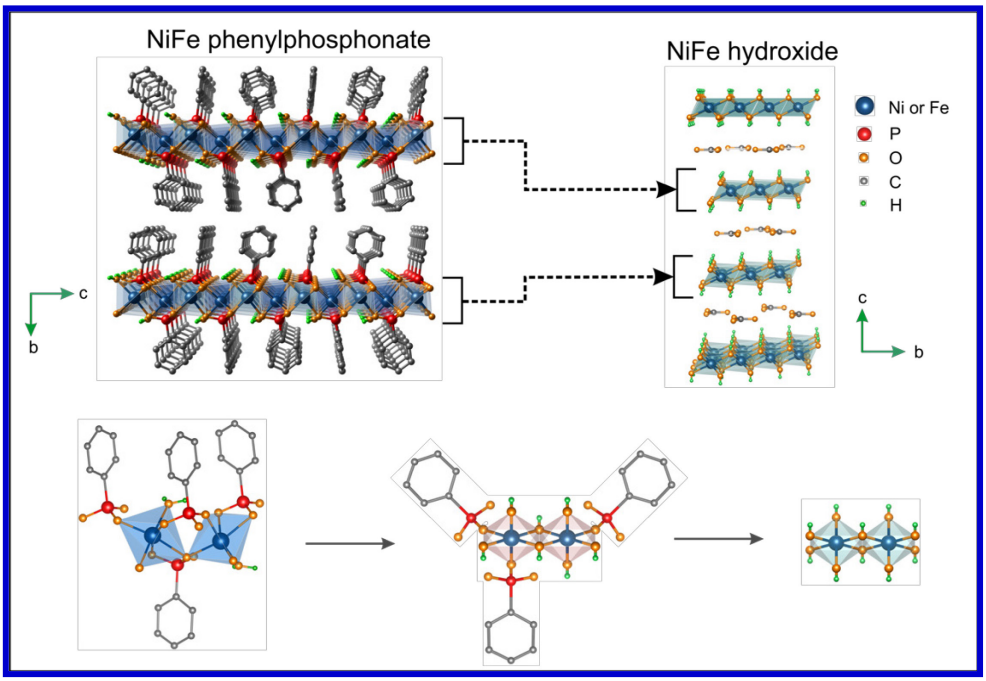

Figure 3.28 Transformation of the NiFex-Phenylphosphonate catalyst into a hydroxide: templating effect of the metal phosphonate on the formation of the hydroxide nanosheets and on the local structure of the metal sites.

The high activity of the NiFe16-Ph catalyst derives primarily from the synergistic effect between the Ni and Fe metals that has been extensively reported in the literature[9,31,90,95,99], which is maximized for the catalysts studied here at a Fe content of 16 %. However, NiFe16-Ph also exhibits higher intrinsic activity than the hydroxide and oxide reference catalysts, suggesting that the structural characteristics of the NiFe16-Ph materials, in particular the local environment around the metal centers, are favorable for electrocatalytic water oxidation. As described above, the local coordination environment of the metals, as well as the activity, are not drastically affected during the complete transformation of the material. The location of the metals in distorted sites of some Co- and Mn-based catalysts has been shown to promote the oxidation of water[100,101]. This behavior has been attributed to the influence of the metal sites

geometry on the binding energies of water molecules and OER intermediate species, with theoretical calculations suggesting these energies are optimized in distorted sites, facilitating the oxidation of water[99,101]. It has also been reported that the introduction Fe into Ni oxyhydroxide is accompanied by increase of structural disorder[31,90]. In a very recent work, Stevens *et al.* [38] reported that the incorporation of Fe into Ni oxyhydroxide would introduce defect sites at edges and further in the "bulk" of the nanosheets, and this changes in local environment played an important role in OER activity. Görlin *et al.* [31] recently demonstrated by using XAS measurements that the addition of Fe leads to distortion of the metal sites in NiFe oxyhydroxide catalysts and a correlation was found between OER activity and extent of distortion, with the highest OER activity being observed for the catalyst preserving the highest distortion in the active states. In the case of the NiFex catalysts, the metals are "forced" to be located in strongly distorted sites owing to the coordination characteristics of the phosphonate ligand, regardless of the Fe content (the sites in the pure Ni-phenylphosphonate are equally distorted, according to XAS measurements), and the distortion is partly transferred to the metal sites of the hydroxide derived from the hybrid. Therefore, the irregular geometry of the sites likely further enhances the activity, which explains the electrochemical behavior of the NiFe16-Ph discussed above.

3.5 Conclusion

Layered organic-inorganic hybrid NiFex-Phenylphosphonate compounds with general formula $Ni_xFe_{1-x}O_3PC_6H_5 \cdot H_2O$ and iron content from 0 to 100 % were synthesized based on the reaction between phenylphosphonic acid and Ni(II) and Fe(II) acetylacetonate in benzyl alcohol using microwave irradiation as the heating method, and investigated as water oxidation electrocatalysts. The hybrid particles comprise inorganic layers of distorted corner-shared NiO_6 and FeO_6 octahedra and act as an in situ template. They are converted into NiFe hydroxide nanosheets with sizes in the range 5-25 nm and thickness between 3 and 10 nm during OER in alkaline medium. Characterization of the local coordination structure through XAS indicates that the geometry of the metal sites in the hydroxide also deviates from regular octahedral geometry. The optimum performance was reached with the catalyst containing 16 % of Fe, which generates j=10 mA cm^{-2} at an overpotential of 240 mV, and exhibits high stability, performing continuous electrolysis efficiently for 160 h. This catalyst outperformed NiFe oxide and hydroxide catalysts used as references. The performance was attributed primarily to the

synergy between the Ni and Fe metals and additionally to the structural properties of the material, specifically the presence of distorted metal sites that further promote water oxidation.

3.6 Experimental section

3.6.1 Materials

Nickel(II) acetylacetonate (95 %), iron(II) acetylacetonate (99 %), iron(III) acetylacetonate (97 %), phenylphosphonic acid (98 %), nickel(II) nitrate hexahydrate (98.5 %), benzyl alcohol (99 %), potassium hydroxide (99.99 %), Nafion perfluorinated resin solution (5 wt.%) were purchased from Sigma Aldrich. Iron (III) nitrate nonahydrate (98%) and sodium hydroxide (98%) were purchased from abcr GmbH. Purified water with resistivity 18.2 MΩ cm^{-1} was used for ink preparation and electrochemical measurements.

3.6.2 Synthesis of the catalysts

3.6.2.1 Hybrid NiFe phenylphosphonates

The hybrid mixed NiFex-Phenylphosphonates with varying Ni/Fe molar ratios were synthesized as follows. 0.5 mmol of phenylphosphonic acid and a total of 0.5 mmol of Ni(II) acetylacetonate and/or Fe(II) acetylacetonate were added to 15 mL of benzyl alcohol in a 30 mL microwave glass vial to form a metal concentration of 0.03 mmol/mL. The mixture was sealed with a silicone cap under Ar (O_2 and H_2O < 1 ppm) and subsequently was stirred and sonicated at room temperature to disperse the precursors. Afterwards, the suspension was heated in a microwave reactor (Anton Paar Monowave 300) at 180 °C for 30 min (with a 5 min heating ramp to reach the final temperature). The hybrid compounds were collected by centrifugation, washed with ethanol and hexane, and dried at 70 °C. The samples are denoted NiFex-Ph, where x is the Fe atomic percentage determined by EDX. Pure Ni phenylphosphonate (Ni-Ph) and pure Fe phenylphosphonate (Fe-Ph) were synthesized for comparison.

3.6.2.2 NiFe hydroxide

A $Ni(OH)_2$ catalyst (Ni-LDH) was synthesized as follow: 0.291 g of $NiNO_3 \cdot 6H_2O$ and 0.300 g of urea were dissolved in 36 mL of DI water. The mixture was transferred to an autoclave and maintained at 120 °C for 24 h. The product was then separated by centrifugation, washed with DI water, and dried at 70 °C overnight.

A NiFe layered double hydroxide (NiFe16-LDH) material with iron atomic percentage of 16 was synthesized following a procedure reported in literature[102]. 1.5 g of $NiNO_3 \cdot 6H_2O$ and 0.521 g of $Fe(NO_3)_3 \cdot 9H_2O$ were dissolved in 30 mL of DI water. The pH of the solution was adjusted to 9.0 through the dropwise addition of a NaOH solution under stirring. The mixture was transferred to a 50 mL Teflon lined stainless steel autoclave and hydrothermally treated at 120 °C for 24 h. The solid was separated by centrifugation, washed with DI water, and dried at 70 °C overnight.

3.6.2.3 NiFe oxide

NiFe oxide catalysts were prepared via a microwave-assisted synthesis in benzyl alcohol. 0.11 g of $NiNO_3 \cdot 6H_2O$ and desired amount of Fe(III) acetylacetonate were dissolved in 15 mL of benzyl alcohol in a 30 mL MW glass vial. The mixture was heated under microwave irradiation at 190 °C for 10 min with a 5 min heating ramp to reach the final temperature. The product was collected by centrifugation, washed five times with ethanol, and dried at 70 °C overnight. Two samples are prepared and donated as NiFe16-Ox and NiFe52-Ox corresponding to the iron atomic percentages of 16 and 52 respectively.

3.6.3 Characterization

Powder X-ray diffraction patterns were recorded with a STOE MP diffractometer in transmission configuration using Mo Kα radiation (λ=0.07093 nm). The measurements were performed in the 2θ range 1-45 ° with a step size of 0.015°. Transmission electron microscopy (TEM) images were acquired on a Philips CM 200 microscope at 200 kV. Energy dispersive X-ray spectroscopy (EDX) analysis were performed using an EDAX SDD detector coupled to the TEM. Scanning electron microscopy (SEM) images were acquired on a JEOLJSM-6060 microscope. Carbon elemental analyses were performed on a HEKAtech Euro EA CHNSO Elemental analyzer. X-ray absorption fine structure (XAFS) was measured at 8C nano-probe XAFS beamline (BL8C) of Pohang Light Source (PLS-II) in the 3.0 GeV storage ring, with a ring current of 300 mA. The radiation source of BL8C is a tapered in-vacuum-undulator. The X-ray beam was monochromated by a Si(111) double crystal where the beam intensity was reduced by 30% to eliminate the higher-order harmonics. The x-ray beam was then delivered to a secondary source aperture where the beam size was adjusted to be 0.3 mm (v) × 1 mm (h). A high voltage (3000 V) was applied to ionization chambers which were filled with N_2/Ar mixture gases to detect x-ray intensity. XAFS spectra were collected in both transmission and

fluorescence modes. The data were processed by using ATHENA and ARTEMIS[103]. The structures were theoretically modelled and fitted to the experimental spectra using ARTEMIS.

3.6.4 Electrochemical experiments

All electrochemical measurements were performed with a Bio-Logic VMP3 Potentiostat-Galvanostat having a built-in electrochemical impedance spectroscopy analyzer. The electrochemical activity and stability of catalysts were measured in a three-electrode electrochemical cell using a 3 mm diameter glassy carbon rotating disc electrode (RDE). A platinum wire was used as the counter electrode and an Ag/AgCl (3 M KCl) electrode was used as the reference electrode. The catalysts inks were prepared as follows: 6 mg of the catalyst was added to 300 µL of purified H_2O, 290 µL of absolute ethanol, and 10µL of 5 wt. % Nafion solution. 20 wt. % of carbon black (TIMCAL Super C-65) was added to the ink to promote the adhesion of the catalyst to the electrode surface. The mixture was sonicated for at least 30 min to obtain a homogeneous ink. The electrodes were prepared by depositing 3 µL of catalyst ink onto the GC disc and drying at room temperature to achieve a catalyst loading of 0.42 mg cm^{-2}. The carbon improved the conductivity of the electrodes and slightly increased their activity. For example, the overpotential at current density of 10 mA cm^{-2} for the NiFe16 catalyst decreased by 20 mV with the addition of the carbon to the electrode. Prior to catalyst deposition, the GC electrode was polished with 1 µm alumina slurry followed by 0.05 µm alumina slurry, and then rinsed with purified water, sonicated for 3 min and dried in air. The oxygen evolution reaction measurements were conducted in 1 M KOH at 25 °C with the RDE rotated at 1600 rpm. Cyclic voltammetry (CV) experiments were performed in the potential window 0 V to 0.6 V vs Ag/AgCl with a scan rate of 20 mV s^{-1}. Linear sweep voltammetry (LSV) curves were measured in the potential window 0 V to 0.7 V with a scan rate of 10 mV s^{-1}. Potential cycling of the catalysts was performed between 0.1 and 0.6 V vs Ag/AgCl with a scan rate of 100 mV s^{-1}. The long term stability was assessed through chronopotentiometry experiments where the change in the potential with time was recorded at a fixed current density of 10 mA cm^{-2}. Prior to the measurements, the electrolyte solution was purged with argon for 30 min. All the data was corrected for the ohmic drop. The uncompensated resistance was determined by electrochemical impedance spectroscopy (EIS). EIS measurements were carried out in the frequency range of 10^5 - 0.1 Hz with 5 mV sinusoidal perturbations. Quantification of the amount of oxygen evolved and determination of the faradaic efficiency was done in a gas tight

cell completely filled with the electrolyte by using a Unisense Ox-500 oxygen sensor. The electrolyte solution was stirred during the measurements.

The turnover frequencies (TOF) were calculated with the equation:

$$TOF = \frac{j.A}{4.F.n} \tag{3.25}$$

where j is the geometric current density at an overpotential of 300 mV, A is the geometric area of the electrode, F is the Faraday constant, and n is the number of moles of metal active sites.

The TOF values were used for comparing catalysts with the same atomic % of Fe. The Ni atoms were considered as the active sites and the moles of Ni were estimated by integration of the Ni^{2+}/Ni^{3+} oxidation and reduction peaks in the CV curves (n of Ni was the average of the values obtained from the oxidation and reduction peaks).

For characterizing the catalysts after potential cycling, the catalysts were deposited on Ni foil. 42 µL of an ink consisting of 6 mg of catalyst, 300 µL of water and 300 µL of ethanol was deposited on Ni foil (1 cm x 1 cm) to achieve the same catalyst loading used for the RDE experiments. Prior to the deposition, the Ni foil was carefully cleaned with a 1 M HCl solution for 10 min followed by acetone for 30 min, in order to remove the surface oxide and organic impurities, and then rinsed with water and dried at 60 °C. The catalyst was subjected to 50 potential cycles in the potential range 0 to 0.6 V vs Ag/AgCl, and subsequently collected from the Ni foil, washed three times with water, and recovered by centrifugation.

3.7 Bibliography

1. Cook, T. R.; Dogutan, D. K.; Reece, S. Y.; Surendranath, Y.; Teets, T. S.; Nocera, D. G., Solar Energy Supply and Storage for the Legacy and Nonlegacy Worlds. *Chemical Reviews* 2010, 110 (11), 6474-6502.
2. Callejas, J. F.; Read, C. G.; Roske, C. W.; Lewis, N. S.; Schaak, R. E., Synthesis, Characterization, and Properties of Metal Phosphide Catalysts for the Hydrogen-Evolution Reaction. *Chemistry of Materials* 2016, 28 (17), 6017-6044.
3. Reier, T.; Nong, H. N.; Teschner, D.; Schlögl, R.; Strasser, P., Electrocatalytic Oxygen Evolution Reaction in Acidic Environments - Reaction Mechanisms and Catalysts. *Advanced Energy Materials* 2017, 7, 1601275.
4. Suen, N.-T.; Hung, S.-F.; Quan, Q.; Zhang, N.; Xu, Y.-J.; Chen, H. M., Electrocatalysis for the oxygen evolution reaction: recent development and future perspectives. *Chemical Society Reviews* 2017,46, 337-365.
5. Burke, M. S.; Zou, S.; Enman, L. J.; Kellon, J. E.; Gabor, C. A.; Pledger, E.; Boettcher, S. W., Revised Oxygen Evolution Reaction Activity Trends for First-Row Transition-Metal (Oxy)hydroxides in Alkaline Media. The *Journal of Physical Chemistry Letters* 2015, 6 (18), 3737-3742.

6. Seitz, L. C.; Dickens, C. F.; Nishio, K.; Hikita, Y.; Montoya, J.; Doyle, A.; Kirk, C.; Vojvodic, A.; Hwang, H. Y.; Norskov, J. K.; Jaramillo, T. F., A highly active and stable $IrO_x/SrIrO_3$ catalyst for the oxygen evolution reaction. *Science* 2016, 353 (6303), 1011-1014.
7. Oh, H.-S.; Nong, H. N.; Reier, T.; Bergmann, A.; Gliech, M.; Ferreira de Araújo, J.; Willinger, E.; Schlögl, R.; Teschner, D.; Strasser, P., Electrochemical Catalyst–Support Effects and Their Stabilizing Role for IrO_x Nanoparticle Catalysts during the Oxygen Evolution Reaction. *Journal of the American Chemical Society* 2016. 138 (38), 12552-12563
8. Lee, Y.; Suntivich, J.; May, K. J.; Perry, E. E.; Shao-Horn, Y., Synthesis and Activities of Rutile IrO_2 and RuO_2 Nanoparticles for Oxygen Evolution in Acid and Alkaline Solutions. *The Journal of Physical Chemistry Letters* 2012, 3 (3), 399-404.
9. Friebel, D.; Louie, M. W.; Bajdich, M.; Sanwald, K. E.; Cai, Y.; Wise, A. M.; Cheng, M.-J.; Sokaras, D.; Weng, T.-C.; Alonso-Mori, R.; Davis, R. C.; Bargar, J. R.; Nørskov, J. K.; Nilsson, A.; Bell, A. T., Identification of Highly Active Fe Sites in (Ni,Fe)OOH for Electrocatalytic Water Splitting. *Journal of the American Chemical Society* 2015, 137 (3), 1305-1313.
10. Batchellor, A. S.; Boettcher, S. W., Pulse-Electrodeposited Ni–Fe (Oxy)hydroxide Oxygen Evolution Electrocatalysts with High Geometric and Intrinsic Activities at Large Mass Loadings. *ACS Catalysis* 2015, 5 (11), 6680-6689.
11. Surendranath, Y.; Nocera, D. G., Oxygen Evolution Reaction Chemistry of Oxide-Based Electrodes. In *Progress in Inorganic Chemistry*, Karlin, K. D., Ed. John Wiley & Sons, Inc.: Hoboken, NJ, USA, 2011; Vol. 57.
12. Tafel, J., Über die Polarisation bei kathodischer Wasserstoffentwicklung. *Zeitschrift für Physikalische Chemie*, 1905, 50U, 641-712.
13. Reier, T.; Oezaslan, M.; Strasser, P., Electrocatalytic Oxygen Evolution Reaction (OER) on Ru, Ir, and Pt Catalysts: A Comparative Study of Nanoparticles and Bulk Materials. *ACS Catalysis* 2012, 2 (8), 1765-1772.
14. McCrory, C. C. L.; Jung, S.; Peters, J. C.; Jaramillo, T. F., Benchmarking Heterogeneous Electrocatalysts for the Oxygen Evolution Reaction. *Journal of the American Chemical Society* 2013, 135 (45), 16977-16987.
15. Li, X.; Hao, X.; Abudula, A.; Guan, G., Nanostructured catalysts for electrochemical water splitting: current state and prospects. *Journal of Materials Chemistry A* 2016, 4 (31), 11973-12000.
16. Giordano, L.; Han, B.; Risch, M.; Hong, W. T.; Rao, R. R.; Stoerzinger, K. A.; Shao-Horn, Y., pH dependence of OER activity of oxides: Current and future perspectives. *Catalysis Today* 2016, 262, 2-10.
17. Gong, M.; Dai, H., A mini review of NiFe-based materials as highly active oxygen evolution reaction electrocatalysts. *Nano Research* 2015, 8 (1), 23-39.
18. Zhang, W.; Zhou, K., Ultrathin Two-Dimensional Nanostructured Materials for Highly Efficient Water Oxidation. *Small* 2017, 13 (32), 1700806.
19. Kanan, M. W.; Surendranath, Y.; Nocera, D. G., Cobalt-phosphate oxygen-evolving compound. *Chemical Society Reviews* 2009, 38 (1), 109-114.
20. Benck, J. D.; Chen, Z.; Kuritzky, L. Y.; Forman, A. J.; Jaramillo, T. F., Amorphous Molybdenum Sulfide Catalysts for Electrochemical Hydrogen Production: Insights into the Origin of their Catalytic Activity. *ACS Catalysis* 2012, 2 (9), 1916-1923.
21. Xia, C.; Liang, H.; Zhu, J.; Schwingenschlögl, U.; Alshareef, H. N., Active Edge Sites Engineering in Nickel Cobalt Selenide Solid Solutions for Highly Efficient Hydrogen Evolution. *Advanced Energy Materials* 2017, 7 (9), 1602089.
22. Trotochaud, L.; Ranney, J. K.; Williams, K. N.; Boettcher, S. W., Solution-Cast Metal Oxide Thin Film Electrocatalysts for Oxygen Evolution. *Journal of the American Chemical Society* 2012, 134 (41), 17253-17261.

23. Wehrens-Dijksma, M.; Notten, P. H. L., Electrochemical Quartz Microbalance characterization of $Ni(OH)_2$-based thin film electrodes. *Electrochimica Acta* 2006, 51 (18), 3609-3621.
24. Fan, G.; Li, F.; Evans, D. G.; Duan, X., Catalytic applications of layered double hydroxides: recent advances and perspectives. *Chemical Society Reviews* 2014, 43 (20), 7040-7066.
25. Song, F.; Hu, X., Exfoliation of layered double hydroxides for enhanced oxygen evolution catalysis. *Nature Communications* 2014, 5, 4477.
26. Lu, Z.; Xu, W.; Zhu, W.; Yang, Q.; Lei, X.; Liu, J.; Li, Y.; Sun, X.; Duan, X., Three-dimensional NiFe layered double hydroxide film for high-efficiency oxygen evolution reaction. *Chemical Communications* 2014, 50 (49), 6479-6482.
27. Ma, W.; Ma, R.; Wang, C.; Liang, J.; Liu, X.; Zhou, K.; Sasaki, T., A Superlattice of Alternately Stacked Ni–Fe Hydroxide Nanosheets and Graphene for Efficient Splitting of Water. *ACS Nano* 2015, 9 (2), 1977-1984.
28. Han, N.; Zhao, F.; Li, Y., Ultrathin nickel-iron layered double hydroxide nanosheets intercalated with molybdate anions for electrocatalytic water oxidation. *Journal of Materials Chemistry A* 2015, 3 (31), 16348-16353.
29. Wang, Y.; Zhang, Y.; Liu, Z.; Xie, C.; Feng, S.; Liu, D.; Shao, M.; Wang, S., Layered Double Hydroxide Nanosheets with Multiple Vacancies Obtained by Dry Exfoliation as Highly Efficient Oxygen Evolution Electrocatalysts. *Angewandte Chemie* 2017, 129 (21), 5961-5965.
30. Yu, J.; Wang, Q.; O'Hare, D.; Sun, L., Preparation of two dimensional layered double hydroxide nanosheets and their applications. *Chemical Society Reviews* 2017, 46 (19), 5950-5974.
31. Görlin, M.; Chernev, P.; Ferreira de Araújo, J.; Reier, T.; Dresp, S.; Paul, B.; Krähnert, R.; Dau, H.; Strasser, P., Oxygen Evolution Reaction Dynamics, Faradaic Charge Efficiency, and the Active Metal Redox States of Ni–Fe Oxide Water Splitting Electrocatalysts. *Journal of the American Chemical Society* 2016, 138 (17), 5603-5614.
32. Pinna, N.; Niederberger, M., Surfactant-Free Nonaqueous Synthesis of Metal Oxide Nanostructures. *Angewandte Chemie International Edition* 2008, 47 (29), 5292-5304.
33. Trotochaud, L.; Young, S. L.; Ranney, J. K.; Boettcher, S. W., Nickel–Iron Oxyhydroxide Oxygen-Evolution Electrocatalysts: The Role of Intentional and Incidental Iron Incorporation. *Journal of the American Chemical Society* 2014, 136 (18), 6744-6753.
34. Momma, K.; Izumi, F., VESTA 3 for three-dimensional visualization of crystal, volumetric and morphology data. *Journal of Applied Crystallography* 2011, 44 (6), 1272-1276.
35. Corrigan, D. A., The Catalysis of the Oxygen Evolution Reaction by Iron Impurities in Thin Film Nickel Oxide Electrodes. *Journal of The Electrochemical Society* 1987, 134 (2), 377-384.
36. Dincă, M.; Surendranath, Y.; Nocera, D. G., Nickel-borate oxygen-evolving catalyst that functions under benign conditions. *Proceedings of the National Academy of Sciences* 2010, 107 (23), 10337-10341.
37. Burke, M. S.; Enman, L. J.; Batchellor, A. S.; Zou, S.; Boettcher, S. W., Oxygen Evolution Reaction Electrocatalysis on Transition Metal Oxides and (Oxy)hydroxides: Activity Trends and Design Principles. *Chemistry of Materials* 2015, 27 (22), 7549-7558.
38. Stevens, M. B.; Trang, C. D. M.; Enman, L. J.; Deng, J.; Boettcher, S. W., Reactive Fe-Sites in Ni/Fe (Oxy)hydroxide Are Responsible for Exceptional Oxygen Electrocatalysis Activity. *Journal of the American Chemical Society* 2017, 139 (33), 11361-11364.
39. Zhu, Y.-P.; Ma, T.-Y.; Liu, Y.-L.; Ren, T.-Z.; Yuan, Z.-Y., Metal phosphonate hybrid materials: from densely layered to hierarchically nanoporous structures. *Inorganic Chemistry Frontiers* 2014, 1 (5), 360-383.

40. Gagnon, K. J.; Perry, H. P.; Clearfield, A., Conventional and Unconventional Metal–Organic Frameworks Based on Phosphonate Ligands: MOFs and UMOFs. *Chemical Reviews* 2012, 112 (2), 1034-1054.
41. Zhang, B.; Poojary, D. M.; Clearfield, A., Synthesis and Crystal Structure of the Linear Chain Zirconium Organophosphonate $(NH4)Zr[F_2][H_3\{O_3PCH_2NH(CH_2CO_2)_2\}_2]\cdot 3H_2O\cdot NH_4Cl$. *Inorganic Chemistry* 1998, 37 (2), 249-254.
42. Di, W.; Ferreira, R. A. S.; Willinger, M.-G.; Ren, X.; Pinna, N., Enhanced Photoluminescence Features of Rare Earth Phenylphosphonate Hybrid Nanostructures Synthesized under Nonaqueous Conditions. *The Journal of Physical Chemistry C* 2010, 114 (14), 6290-6297.
43. Janiak, C., Functional Organic Analogues of Zeolites Based on Metal–Organic Coordination Frameworks. *Angewandte Chemie International Edition in English* 1997, 36 (13-14), 1431-1434.
44. Alberti, G.; Costantino, U.; Allulli, S.; Tomassini, N., Crystalline $Zr(R\text{-}PO_3)_2$ and $Zr(R\text{-}OPO_3)_2$ compounds (R = organic radical). *Journal of Inorganic and Nuclear Chemistry* 1978, 40 (6), 1113-1117.
45. Poojary, M. D.; Hu, H.-L.; Campbell III, F. L., Clearfield, A., Determination of crystal structures from limited powder data sets: crystal structure of zirconium phenylphosphonate. *Acta Crystallographica Section B* 1993, 49 (6), 996-1001.
46. Cabeza, A.; Aranda, M. A. G., Chapter 4 Metal Carboxyphosphonates. In *Metal Phosphonate Chemistry: From Synthesis to Applications*, Clearfield, A.; Demadis, K., Ed. The Royal Society of Chemistry: Cambridge, UK, 2012; 107-132.
47. Cao, G.; Lee, H.; Lynch, V. M.; Mallouk, T. E., Synthesis and structural characterization of a homologous series of divalent-metal phosphonates, $M^{II}(O_3PR)\cdot H_2O$ and $M^{II}(HO_3PR)_2$. *Inorganic Chemistry* 1988, 27 (16), 2781-2785.
48. Hix, G. B.; Harris, K. D. M., Synthesis of layered nickel phosphonate materials based on a topotactic approach. *Journal of Materials Chemistry* 1998, 8 (3), 579-584.
49. Poojary, D. M.; Zhang, Y.; Zhang, B.; Clearfield, A., Synthesis, X-ray Powder Structure, and Intercalation Behavior of Molybdenyl Phenylphosphonate, $MoO_2(O_3PC_6H_5)\cdot H_2O$. *Chemistry of Materials* 1995, 7 (5), 822-827.
50. Cabeza, A.; Aranda, M. A. G.; Bruque, S.; Poojary, D. M.; Clearfield, A.; Sanz, J., Aluminum Phenylphosphonates: A Fertile Family of Compounds. *Inorganic Chemistry* 1998, 37 (17), 4168-4178.
51. Bujoli, B.; Palvadeau, P.; Rouxel, J., Synthesis of new lamellar iron(III) phosphonates. *Chemistry of Materials* 1990, 2 (5), 582-589.
52. Kirumakki, S.; Huang, J.; Subbiah, A.; Yao, J.; Rowland, A.; Smith, B.; Mukherjee, A.; Samarajeewa, S.; Clearfield, A., Tin(IV) phosphonates: porous nanoparticles and pillared materials. *Journal of Materials Chemistry* 2009, 19 (17), 2593-2603.
53. Wang, Z.; Heising, J. M.; Clearfield, A., Sulfonated Microporous Organic-Inorganic Hybrids as Strong Bronsted Acids1. *Journal of the American Chemical Society* 2003, 125 (34), 10375-10383.
54. Chen, Z.; Zhou, Y.; Weng, L.; Zhao, D., Mixed-Solvothermal Syntheses and Structures of Six New Zinc Phosphonocarboxylates with Zeolite-type and Pillar-Layered Frameworks. *Crystal Growth & Design* 2008, 8 (11), 4045-4053.
55. Cai, Z.-S.; Ren, M.; Bao, S.-S.; Hoshino, N.; Akutagawa, T.; Zheng, L.-M., Synthetic-Method-Dependent Magnetic Relaxation in a Cobalt(II) Phosphonate Chain Compound. *Inorganic Chemistry* 2014, 53 (23), 12546-12552.
56. Horsman, G. P.; Zechel, D. L., Phosphonate Biochemistry. *Chemical Reviews* 2017, 117 (8), 5704-5783.

57. Liu, L.; Gong, Z.; Zheng, Y.; Jing, X.; Zhao, H., The effect of preparation conditions on the catalyst $Nd(P_{507})_3/H_2O/Al(i\text{-}Bu)_3$ for the polymerization of styrene. *Macromolecular Chemistry and Physics* 1999, 200 (4), 763-767.
58. Farrokhi, A.; Jafarpour, M.; Najafzade, R., Phosphonate-based Metal Organic Frameworks as Robust Heterogeneous Catalysts for TBHP Oxidation of Benzylic Alcohols. *Catalysis Letters* 2017, 147 (7), 1714-1721.
59. Liu, H.-Y.; Zhang, Z.-J.; Shi, W.; Zhao, B.; Cheng, P.; Liao, D.-Z.; Yan, S.-P., A 3D porous hetero-metal compound with helical channels. *Dalton Transactions* 2009, (23), 4416-4419.
60. Lian, X.; Yan, B., Phosphonate MOFs Composite as Off–On Fluorescent Sensor for Detecting Purine Metabolite Uric Acid and Diagnosing Hyperuricuria. *Inorganic Chemistry* 2017, 56 (12), 6802-6808.
61. Liang, X.; Zhang, F.; Feng, W.; Zou, X.; Zhao, C.; Na, H.; Liu, C.; Sun, F.; Zhu, G., From metal-organic framework (MOF) to MOF-polymer composite membrane: enhancement of low-humidity proton conductivity. *Chemical Science* 2013, 4 (3), 983-992.
62. Itaru, H.; Masanori, Y., Bio-Inspired Membranes for Advanced Polymer Electrolyte Fuel Cells. Anhydrous Proton-Conducting Membrane via Molecular Self-Assembly. *Bulletin of the Chemical Society of Japan* 2007, 80 (11), 2110-2123.
63. Shimizu, G. K. H., Assembly of metal ions and ligands with adaptable coordinative tendencies as a route to functional metal-organic solids. *Journal of Solid State Chemistry* 2005, 178 (8), 2519-2526.
64. Ramaswamy, P.; Wong, N. E.; Gelfand, B. S.; Shimizu, G. K. H., A Water Stable Magnesium MOF That Conducts Protons over 10–2 S cm–1. *Journal of the American Chemical Society* 2015, 137 (24), 7640-7643.
65. Hurd, J. A.; Vaidhyanathan, R.; Thangadurai, V.; Ratcliffe, C. I.; Moudrakovski, I. L.; Shimizu, G. K. H., Anhydrous proton conduction at 150 °C in a crystalline metal–organic framework. *Nature Chemistry* 2009, 1, 705.
66. Shimizu, G. K. H.; Taylor, J. M.; Dawson, K. W., Chapter 15 Metal Organophosphonate Proton Conductors. In *Metal Phosphonate Chemistry: From Synthesis to Applications*, Clearfield, A.; Demadis, K., Ed. The Royal Society of Chemistry: Cambridge, UK, 2012; 493-524.
67. Pramanik, M.; Tsujimoto, Y.; Malgras, V.; Dou, S. X.; Kim, J. H.; Yamauchi, Y., Mesoporous Iron Phosphonate Electrodes with Crystalline Frameworks for Lithium-Ion Batteries. *Chemistry of Materials* 2015, 27 (3), 1082-1089.
68. Pramanik, M.; Malgras, V.; Lin, J.; Alshehri, S. M.; Ahamad, T.; Kim, J. H.; Yamauchi, Y., Electrochemical Property of Mesoporous Crystalline Iron Phosphonate Anode in Li-Ion Rechargeable Battery. *Journal of Nanoscience and Nanotechnology* 2016, 16 (9), 9180-9185.
69. Pramanik, M.; Salunkhe, R. R.; Imura, M.; Yamauchi, Y., Phosphonate-Derived Nanoporous Metal Phosphates and Their Superior Energy Storage Application. *ACS Applied Materials & Interfaces* 2016, 8 (15), 9790-9797.
70. Mei, P.; Pramanik, M.; Lee, J.; Ide, Y.; Alothman, Z. A.; Kim, J. H.; Yamauchi, Y., Highly Ordered Mesostructured Vanadium Phosphonate toward Electrode Materials for Lithium-Ion Batteries. *Chemistry - A European Journal* 2017, 23 (18), 4344-4352.
71. Zhang, F.; Bao, Y.; Ma, S.; Liu, L.; Shi, X., Hierarchical flower-like nickel phenylphosphonate microspheres and their calcined derivatives for supercapacitor electrodes. *Journal of Materials Chemistry A* 2017, 5 (16), 7474-7481.
72. Surendranath, Y.; Dincă, M.; Nocera, D. G., Electrolyte-Dependent Electrosynthesis and Activity of Cobalt-Based Water Oxidation Catalysts. *Journal of the American Chemical Society* 2009, 131 (7), 2615-2620.

73. Shevchenko, D.; Anderlund, M. F.; Thapper, A.; Styring, S., Photochemical water oxidation with visible light using a cobalt containing catalyst. *Energy & Environmental Science* 2011, 4 (4), 1284-1287.
74. Zhou, T.; Wang, D.; Chun-Kiat Goh, S.; Hong, J.; Han, J.; Mao, J.; Xu, R., Bio-inspired organic cobalt(ii) phosphonates toward water oxidation. *Energy & Environmental Science* 2015, 8 (2), 526-534.
75. Saha, J.; Chowdhury, D. R.; Jash, P.; Paul, A., Cobalt Phosphonates as Precatalysts for Water Oxidation: Role of Pore Size in Catalysis. *Chemistry - A European Journal* 2017, 23 (51), 12519-12526.
76. Martin, K. J.; Squattrito, P. J.; Clearfield, A., The Crystal and Molecular-Structure of Zinc Phenylphosphonate. *Inorganica Chimica Acta* 1989, 155 (1), 7-9.
77. Bellitto, C.; Federici, F.; Altomare, A.; Rizzi, R.; Ibrahim, S. A., Synthesis, X-ray Powder Structure, and Magnetic Properties of the New, Weak Ferromagnet Iron(II) Phenylphosphonate. *Inorganic Chemistry* 2000, 39 (8), 1803-1808.
78. Bauer, E. M.; Bellitto, C.; Righini, G.; Colapietro, M.; Portalone, G.; Drillon, M.; Rabu, P., Comparison of the Structure and Magnetic Order in a Series of Layered Ni(II) Organophosphonates, Ni[(RPO_3)(H_2O)] (R = C_6H_5, CH_3, $C_{18}H_{37}$). *Inorganic Chemistry* 2008, 47 (23), 10945-10952.
79. Wong, J.; Lytle, F. W.; Messmer, R. P.; Maylotte, D. H., K-edge absorption spectra of selected vanadium compounds. *Physical Review B* 1984, 30 (10), 5596-5610.
80. Westre, T. E.; Kennepohl, P.; DeWitt, J. G.; Hedman, B.; Hodgson, K. O.; Solomon, E. I., A Multiplet Analysis of Fe K-Edge 1s $\rightarrow$ 3d Pre-Edge Features of Iron Complexes. *Journal of the American Chemical Society* 1997, 119 (27), 6297-6314.
81. Heijboer, W. M.; Glatzel, P.; Sawant, K. R.; Lobo, R. F.; Bergmann, U.; Barrea, R. A.; Koningsberger, D. C.; Weckhuysen, B. M.; de Groot, F. M. F., Kβ-Detected XANES of Framework-Substituted FeZSM-5 Zeolites. *The Journal of Physical Chemistry B* 2004, 108 (28), 10002-10011.
82. Yamamoto, T., Assignment of pre-edge peaks in K-edge x-ray absorption spectra of 3d transition metal compounds: electric dipole or quadrupole? *X-Ray Spectrometry* 2008, 37 (6), 572-584.
83. Farges, F.; Brown, G. E.; Petit, P.-E.; Munoz, M., Transition elements in water-bearing silicate glasses/melts. part I. a high-resolution and anharmonic analysis of Ni coordination environments in crystals, glasses, and melts. *Geochimica et Cosmochimica Acta* 2001, 65 (10), 1665-1678.
84. Wilke, M.; Farges, F.; Petit, P.-E.; Brown Gordon, E.; Martin, F., Oxidation state and coordination of Fe in minerals: An Fe K-XANES spectroscopic study. *American Mineralogist*, 2001; 86(5-6), 714-730.
85. Boubnov, A.; Lichtenberg, H.; Mangold, S.; Grunwaldt, J.-D., Identification of the iron oxidation state and coordination geometry in iron oxide- and zeolite-based catalysts using pre-edge XAS analysis. *Journal of Synchrotron Radiation* 2015, 22 (2), 410-426.
86. Lyons, M. E. G.; Brandon, M. P., The oxygen evolution reaction on passive oxide covered transition metal electrodes in aqueous alkaline solution. Part 1 - Nickel. *International Journal of Electrochemical Science* 2008, (3), 1386-1424.
87. Stern, L.-A.; Feng, L.; Song, F.; Hu, X., Ni_2P as a Janus catalyst for water splitting: the oxygen evolution activity of Ni_2P nanoparticles. *Energy & Environmental Science* 2015, 8 (8), 2347-2351.
88. Xu, K.; Cheng, H.; Liu, L.; Lv, H.; Wu, X.; Wu, C.; Xie, Y., Promoting Active Species Generation by Electrochemical Activation in Alkaline Media for Efficient Electrocatalytic Oxygen Evolution in Neutral Media. *Nano Letters* 2017, 17 (1), 578-583.

89. Chen, W.; Liu, Y.; Li, Y.; Sun, J.; Qiu, Y.; Liu, C.; Zhou, G.; Cui, Y., In Situ Electrochemically Derived Nanoporous Oxides from Transition Metal Dichalcogenides for Active Oxygen Evolution Catalysts. *Nano Letters* 2016, 16 (12), 7588-7596.
90. Li, Y.; Zhao, C., Iron-Doped Nickel Phosphate as Synergistic Electrocatalyst for Water Oxidation. *Chemistry of Materials* 2016, 28 (16), 5659-5666.
91. Maljusch, A.; Ventosa, E.; Rincón, R. A.; Bandarenka, A. S.; Schuhmann, W., Revealing onset potentials using electrochemical microscopy to assess the catalytic activity of gas-evolving electrodes. *Electrochemistry Communications* 2014, 38, 142-145.
92. Subbaraman, R.; Tripkovic, D.; Chang, K.-C.; Strmcnik, D.; Paulikas, A. P.; Hirunsit, P.; Chan, M.; Greeley, J.; Stamenkovic, V.; Markovic, N. M., Trends in activity for the water electrolyser reactions on 3d M(Ni,Co,Fe,Mn) hydr(oxy)oxide catalysts. *Nature Materials* 2012, 11, 550.
93. Zou, S.; Burke, M. S.; Kast, M. G.; Fan, J.; Danilovic, N.; Boettcher, S. W., Fe (Oxy)hydroxide Oxygen Evolution Reaction Electrocatalysis: Intrinsic Activity and the Roles of Electrical Conductivity, Substrate, and Dissolution. *Chemistry of Materials* 2015, 27 (23), 8011-8020.
94. Louie, M. W.; Bell, A. T., An Investigation of Thin-Film Ni–Fe Oxide Catalysts for the Electrochemical Evolution of Oxygen. *Journal of the American Chemical Society* 2013, 135 (33), 12329-12337.
95. Dionigi, F.; Strasser, P., NiFe ‐ Based (Oxy)hydroxide Catalysts for Oxygen Evolution Reaction in Non-Acidic Electrolytes. *Advanced Energy Materials* 2016, 6 (23), 1600621.
96. Fominykh, K.; Chernev, P.; Zaharieva, I.; Sicklinger, J.; Stefanic, G.; Döblinger, M.; Müller, A.; Pokharel, A.; Böcklein, S.; Scheu, C.; Bein, T.; Fattakhova-Rohlfing, D., Iron-Doped Nickel Oxide Nanocrystals as Highly Efficient Electrocatalysts for Alkaline Water Splitting. *ACS Nano* 2015, 9 (5), 5180-5188.
97. Guidelli, R.; Compton Richard, G.; Feliu Juan, M.; Gileadi, E.; Lipkowski, J.; Schmickler, W.; Trasatti, S., Defining the transfer coefficient in electrochemistry: An assessment (IUPAC Technical Report). *Pure and Applied Chemistry*, 2014; 86, 245-258.
98. Wang, D.; Zhou, J.; Hu, Y.; Yang, J.; Han, N.; Li, Y.; Sham, T.-K., In Situ X-ray Absorption Near-Edge Structure Study of Advanced $NiFe(OH)_x$ Electrocatalyst on Carbon Paper for Water Oxidation. *The Journal of Physical Chemistry C* 2015, 119 (34), 19573-19583.
99. Landon, J.; Demeter, E.; İnoğlu, N.; Keturakis, C.; Wachs, I. E.; Vasić, R.; Frenkel, A. I.; Kitchin, J. R., Spectroscopic Characterization of Mixed Fe–Ni Oxide Electrocatalysts for the Oxygen Evolution Reaction in Alkaline Electrolytes. *ACS Catalysis* 2012, 2(8), 1793-1801.
100. Grimaud, A.; Carlton, C. E.; Risch, M.; Hong, W. T.; May, K. J.; Shao-Horn, Y., Oxygen Evolution Activity and Stability of $Ba_6Mn_5O_{16}$, $Sr_4Mn_2CoO_9$, and $Sr_6Co_5O_{15}$: The Influence of Transition Metal Coordination. *The Journal of Physical Chemistry C* 2013, 117 (49), 25926-25932.
101. Kim, H.; Park, J.; Park, I.; Jin, K.; Jerng, S. E.; Kim, S. H.; Nam, K. T.; Kang, K., Coordination tuning of cobalt phosphates towards efficient water oxidation catalyst. *Nature Communications* 2015, 6, 8253.
102. Zhang, C.; Shao, M.; Zhou, L.; Li, Z.; Xiao, K.; Wei, M., Hierarchical NiFe Layered Double Hydroxide Hollow Microspheres with Highly-Efficient Behavior toward Oxygen Evolution Reaction. *ACS Applied Materials & Interfaces* 2016, 8 (49), 33697-33703.
103. Ravel, B.; Newville, M., ATHENA, ARTEMIS, HEPHAESTUS: data analysis for X-ray absorption spectroscopy using IFEFFIT. *Journal of Synchrotron Radiation* 2005, 12 (4), 537-541.

4. Transition-metal phosphides derived from hybrid metal phosphonates for electrocatalytic water splitting

4.1 Introduction

4.1.1 Transition-metal phosphides as electrocatalysts for the hydrogen and oxygen evolution reactions

Electrochemical water splitting is a reaction driven by electricity that separates water into hydrogen (H_2) and oxygen (O_2). As mentioned in the previous chapter, it consists of two half-cell reactions: the hydrogen evolution reaction at the cathode and oxygen evolution reaction at the anode. The anodic half-reaction (OER) has been discussed in detail in the previous chapter and therefore only the HER is thoroughly discussed in this section.

The HER consists of the reduction of protons or water molecules with formation of gaseous hydrogen, according to the following equations:

$$2H(aq)^{+} + 2e^{-} \rightarrow H_2(g) \quad \text{(in acidic medium)} \tag{4.1}$$

$$2H_2O + 2e^{-} \rightarrow H_2(g) + 2OH^{-}(aq) \quad \text{(in alkaline medium)} \tag{4.2}$$

According to the Nernst equation, the thermodynamic potential for the HER against the normal hydrogen electrode (NHE) is

$$E_{HER} = -0.059 \times \text{pH V vs NHE}$$

$$= 0 \text{ V vs RHE} \tag{4.3}$$

which is 0 V against the RHE, regardless of the pH of the electrolyte.

As mentioned previously, electrochemical reactions often do not proceed at the equilibrium potential. In the case of the HER, the reaction only starts when a sufficiently high cathodic potential is applied. Therefore, in practice, the potential at which the HER occurs is given by

$$E = E_{HER} + iR + \eta \tag{4.4}$$

where iR is the ohmic drop and η is the overpotential. Electrocatalysts are necessary to decrease the overpotential and thus increase the energetic efficiency of the process.

The kinetics of the hydrogen evolution reaction depends on its mechanism. It is generally accepted that the HER proceeds through two reaction steps[1]. It is initiated by a hydrogen adsorption reaction, also known as the Volmer reaction:

Volmer reaction:

$$H^+ + e^- \rightarrow H_{ad} \text{ (acidic)} \quad (4.5)$$

$$H_2O + e^- \rightarrow H_{ad} + OH^- \text{ (neutral or alkaline)} \quad (4.6)$$

Subsequently, the reaction may procced in two different ways. The adsorbed hydrogen atom can react with a proton from the solution to form H_2 (Heyrovský reaction):

Heyrovský reaction:

$$H_{ad} + H^+ + e^- \rightarrow H_2(g) \text{ (acidic)} \quad (4.7)$$

$$H_2O + H_{ad} + e^- \rightarrow H_2(g) + OH^- \text{ (neutral or alkaline)} \quad (4.8)$$

Alternatively, two adsorbed hydrogen atoms can react to form H_2 (Tafel reaction):

Tafel reaction:

$$H_{ad} + H_{ad} \rightarrow H_2(g) \text{ (acidic, neutral or alkaline)} \quad (4.9)$$

The Tafel slope of the hydrogen evolution reaction is found to be 118 mV dec^{-1}, 39 mV dec^{-1} and 30 mV dec^{-1} if the rate-determining step is the Volmer, Heyrovský or Tafel reaction, respectively. Therefore, the Tafel slope provides an indication of the HER mechanism. For example, a Tafel slope close to 30 mV dec^{-1} suggests that the HER proceeds through a Volmer reaction followed by a Tafel reaction[2].

The current state-of-the-art catalyst for the hydrogen evolution reaction is platinum, but the scarcity and high cost of this noble metal is one of the factors hindering the large-scale commercialization of water splitting technology. Consequently, intensive research efforts have been dedicated to the development of electrochemically active, stable, and inexpensive catalysts based on earth abundant transition-metals. Recently, several types of materials such as metal sulfides, carbides, phosphides, and selenides including MoS_2[3], CoS_x[4], WC[5], MoP[6], Ni_2P[7], CoP[8], $CoSe_2$[9] have shown HER activity in acidic conditions.

The potential of Ni_2P as an electrocatalyst for HER was first predicted in a theoretical work reported by Liu and Rodriguez in 2005[10], where the Ni_2P (001) facet was found to display superior HER activity than [NiFe] hydrogenase and a Ni-based complex. In 2013, Popczun *et*

al.[7] experimentally demonstrated that nanoparticulated Ni_2P was among the most active non-noble metal HER catalysts in acidic medium reported to date. The nanoparticles were synthesized by thermal decomposition of tri-*n*-octylphosphine (TOP) and Ni acetylacetonate in a 1-octadecene and oleylamine solution. The material was deposited on Ti foil and generated current densities of -20 and -100 mA cm^{-2} at η=130 mV and η=180 mV, respectively. However, the corresponding overpotentials increased by *ca.* 25 and 50 mV after only 500 cyclic voltammetric cycles, indicating long-term instability of the nanoparticles in the acidic conditions. This instability was later attributed to dissolution of the surface of the nickel phosphide materials at pH=0[11]. Feng and co-workers[12] then reported that Ni_2P nanoparticles with size of 10-50 nm was a highly active catalyst in both acidic and basic solutions, requiring overpotentials of only 140 mV and 250 mV to achieve a current density of -20 mA cm^{-2} in 1 M H_2SO_4 and 1 M KOH, respectively.

$Ni_{12}P_5$ is also an active HER electrocatalyst. Menezes *et al.*[13] compared the performances of $Ni_{12}P_5$ and Ni_2P by coating the catalysts on a FTO substrate and testing in 1 M KOH. The $Ni_{12}P_5$ electrode showed lower overpotential than the Ni_2P electrode. The authors argued that the higher concentration of P compared to Ni at the surface plays a prominent role in increasing the catalytic activity, as the P sites were suggested by other authors to act as the proton adsorption centers[14]. Huang *et al.*[15] reported that monodispersed $Ni_{12}P_5$ nanoparticles loaded onto silicon nanowires showed activity in the photoelectrolysis of water. In addition to nickel phosphides, several other transition-metal phosphides including those of Co and Fe have shown HER activity[16-20].

Doping is an efficient approach to optimize the electronic environment of the target materials, and potentially improve the HER performance. Jin *et al.*[21] prepared tungsten-doped Ni_xP microspheres through a solution-phase reaction, which showed overpotentials of 110 mV and 180 mV for achieving current densities of -20 mA cm^{-2} and -100 mA cm^{-2}, respectively. They hypothesized that a partial electron transfer occurred between tungsten and phosphorous, which allowed the P sites to become more efficient proton adsorption centers.

Metal phosphide nanoparticles have also been combined with carbon substrates such as reduced graphene oxide (rGO)[22], carbon nanotubes (CNTs)[23], and carbon spheres[24], to improve the conductivity of the catalysts. Ma *et al.*[22] prepared CoP/rGO composites by phosphorization of a Co_3O_4/rGO precursor using NaH_2PO_2 as phosphorous source. They found that the loading

amount of CoP on rGO had an obvious influence on the HER electrocatalytic activities, which reached a maximum for a CoP: rGO weight ratio of 0.36.

In 2015, several research groups also demonstrated the activity of nickel and cobalt phosphides as OER catalysts in alkaline solution. Characterization of Ni_2P nanoparticles after OER measurements revealed that the Ni_2P nanoparticles were covered with a thin film of nickel oxyhydroxide species forming a core-shell structure[25]. Iron impurities were also detected in the samples after electrocatalysis. Therefore, the activity of nickel phosphide materials in alkaline solution is ascribed to the formation in situ of a $Ni(OH)_2$/NiOOH layer on the surface of the catalysts, as generally occurs for NiO_x materials[13.26,27,28]. Ledendecker *et al.*[26] prepared Ni_5P_4 nanodisks on Ni foil and used it as a bifunctional catalyst for both the HER and OER. The catalyst required a voltage of 1.7 V between the two electrodes to achieve an overall water splitting current density of 10 mA cm^{-2}. Moreover, the metal-rich nickel phosphides exhibit higher OER activity. For example, in the case of the $Ni_{12}P_5$ and Ni_2P phases, the higher amount of Ni on the surface of $Ni_{12}P_5$ particles leads to the formation of more catalytically active NiOOH species promoting the oxygen evolution[13].

4.1.2 Synthesis routes to transition-metal phosphides

Several approaches are described in the literature for the synthesis of metal phosphides, including solid-state reactions[29], chemical vapor deposition[30], and thermal decomposition of metal and phosphorous precursors in solution[31]. However, only a reduced number of synthetic routes are suitable for preparing nanostructured phosphide materials.

Metal phosphides can be easily synthesized by solid state reactions, in which a mixture of the metal and a phosphorous source are reacted at high temperatures under inert atmosphere or under vacuum. Large amounts of bulk metal phosphides with high purity can be produced by using pure metals and elemental phosphorous as precursors[32].

Temperature-programmed reduction (TPR) of metal phosphates is one of the most commonly used methods for producing metal phosphides. It involves the treatment of metal phosphides at high temperatures under H_2 gas flow. Gopalakrishnan and co-workers[33] investigated the reduction of several metal phosphates by H_2 at temperatures up to 1000 °C. They found that this method was not applicable for producing many metal (*e.g.* Mn, V) phosphides and part of phosphorous was lost during the reduction process. Additionally, bulk phosphides are often produced through this procedure due to sintering at high temperatures.

Chemical vapor deposition (CVD) and electrochemical deposition can be applied to synthesize homogeneous metal phosphide thin films on a specific substrate or electrode. In a typical CVD synthesis, the volatile gaseous precursors, such as metal alkyls and metal halides, are decomposed at high temperature over an appropriate substrate[34]. Crystalline metal phosphides can be prepared by CVD, while amorphous Ni-P, Co-P with a wide range of phosphorous contents are obtained through electrochemical deposition methods[34,35].

Another synthetic route for preparing metal phosphides is phosphorization, which consists in a gas-solid reaction between a phosphorous source in the gas phase (e.g. PH_3) and a metal source (e.g. metal, metal salts, metal oxides)[26,36]. The gaseous phosphorization agent (PH_3) can also be produced in situ from the decomposition of hypophosphite (reaction 4.10) under argon flow, which can be mixed with the metal precursor or place upstream from the metal precursor. For example, Ni_2P nanoparticles can be prepared by reacting $Ni(OH)_2$ with solid NaH_2PO_2 in argon at 270 °C for 240 min. This route is very versatile, allowing the synthesis of a wide range of metal phosphides. It also allows the synthesis of nanostructured phosphides by using pre-formed metal oxides with the desired nanostructure, as the morphology of the metal precursor is retained on the final phosphides. The biggest disadvantage of this approach is the employment of the extremely hazardous PH_3 compound and post-synthesis treatment of the gas is necessary[1].

$$2NaH_2PO_2 \rightarrow Na_2HPO_4 + PH_3(g) \qquad (4.10)$$

Nanostructured transition-metal phosphides, especially nanoparticles, can be produced in solution through decomposition of phosphorous sources such as tri-*n*-octylphosphine oxide (TOPO)[37], triphenylphosphine (TPP)[38], trimethyl phosphite [$P(OMe)_3$][39], triethyl phosphite [$P(OEt)_3$][39]. Tri-*n*-octylphosphine (TOP) is widely used in this type of reaction and acts as both the phosphorous source and co-surfactant. Various phosphides such as Fe_2P, FeP, Ni_2P, $Ni_{12}P_5$, Ni_5P_4, Cu_3P, Co_2P, CoP, InP and MnP, as well as several ternary metal phosphides have been successfully synthesized through the TOP route[40,41]. In a typical procedure[42] the metal precursor (*e.g.* nickel acetylacetonate), TOP, and a surfactant (*e.g.* oleylamine) are mixed with an organic solvent (*e.g.* octyl ether) in a Schlenk flask and heated under argon at temperatures of 300-350 °C. Control over the metal phosphide phase is achieved by controlling the synthetic parameters including the P:Ni molar ratio, temperature, time and surfactant quantity. This approach enables the synthesis of monodispersed nanostructures with well-controlled crystal phases and morphologies by optimizing the reaction conditions. However, the high reactivity

and toxicity of the organic phosphorous source and/or of their decomposition products, and the experimental safety requirements, constitutes a drawback that makes the scale up of the process difficult[43].

4.1.3 Nickel phosphides and cobalt phosphides

Metal phosphides exist in a wide range of crystal structures that depend on the composition and type of bonding. With a few exceptions, the coordination in transition-metal phosphides tends to be octahedral, which is generally centered by phosphorous atoms in metal-rich phosphides and by metal atoms in phosphorous-rich phosphides[44]. The electron-rich phosphides with large M:P ratios often exhibit semiconducting behavior and in some cases are even metallic or superconducting materials, due to the presence of M-M bonding[34]. For example, Fe_2P shows metallic behavior[45], whereas GaP is semiconducting[46].

The crystal structures of nickel phosphides are shown in Figure 4.1. Ni_3P, which is the nickel phosphide with the biggest content of nickel, has a tetragonal structure and can be simply synthesized by a solid-state reaction between phosphorous and excess Ni at high temperature[47]. However, Ni_3P decomposes at 300 °C or higher temperatures in air and transforms into metastable $Ni_{12}P_5$ and Ni_2P phases[47]. $Ni_{12}P_5$ is tetragonal, while Ni_2P and Ni_5P_4 have hexagonal structures. These three phases have higher thermodynamic stability than the other nickel phosphides phases. Because of this, and their unique electronic and catalytic properties, they are the most investigated nickel phosphides and have been used in a wide-range of applications such as hydrotreating reaction[48], hydrogen evolution reaction[7] or lithium ion batteries as electrode materials[49]. Pan *et al.*[50] compared the electrocatalytic HER activities of $Ni_{12}P_5$, Ni_2P and Ni_5P_4 nanocrystals synthesized through the TOP route. The Ni:P ratios in the $Ni_{12}P_5$, Ni_2P and Ni_5P_4 materials are 1.54, 0.46 and 0.11, respectively. The Ni_5P_4 phase exhibited superior HER activity compare to $Ni_{12}P_5$ and Ni_2P, which was attributed to the higher positive charge of Ni and the higher amount of P sites. Besides, other research groups investigated the electrocatalytic performances by comparing $Ni_{12}P_5$ and Ni_2P[52], as well as Ni_5P_4 and Ni_2P[53]. The nickel phosphides containing higher amount of P tend to exhibit higher HER activities.

NiP_2 is monoclinic and NiP_3 has cubic structure. The synthesis of phosphorus-rich phosphide structures is challenging because the high nucleation energy of phosphorus-rich phases will cause them to decompose into metal-rich structures[54]. In addition, in these materials the Ni-Ni distances are 3.87 Å and 3.91 Å, respectively, which are much larger than that of Ni_2P (2.61 Å). The absence of Ni-Ni bonding and presence of extensive P-P bonding restricts the conductivity

of these materials and affect the electrocatalytic properties of these metal phosphides. Therefore, NiP_2 and NiP_3 nanoparticles have not yet receive of much attention as electrocatalysts for water splitting. Up to now, the main applications for NiP_2 and NiP_3 in energy conversion and storage are focused on the lithium/sodium ion battery, due to their high theoretical anodic capacity of 1333 and 1591 mA h g^{-1}, respectively[55].

Sun and co-workers[56] prepared NiP_2 nanosheets arrays on carbon cloth substrate (NiP_2 NS/CC) through the hydrothermal synthesis of $Ni(OH)_2$/carbon cloth followed by phosphorization. The NiP_2 NS/CC showed good activity in both acid and alkaline solution for HER, with the overpotential at -10 mA cm^{-2} of 75 mV and 102 mV, respectively. However, it is worth noting that the geometric area which was used to calculate the current density, was increased by the 3D carbon cloth substrate, resulting in an enhancement in HER performance.

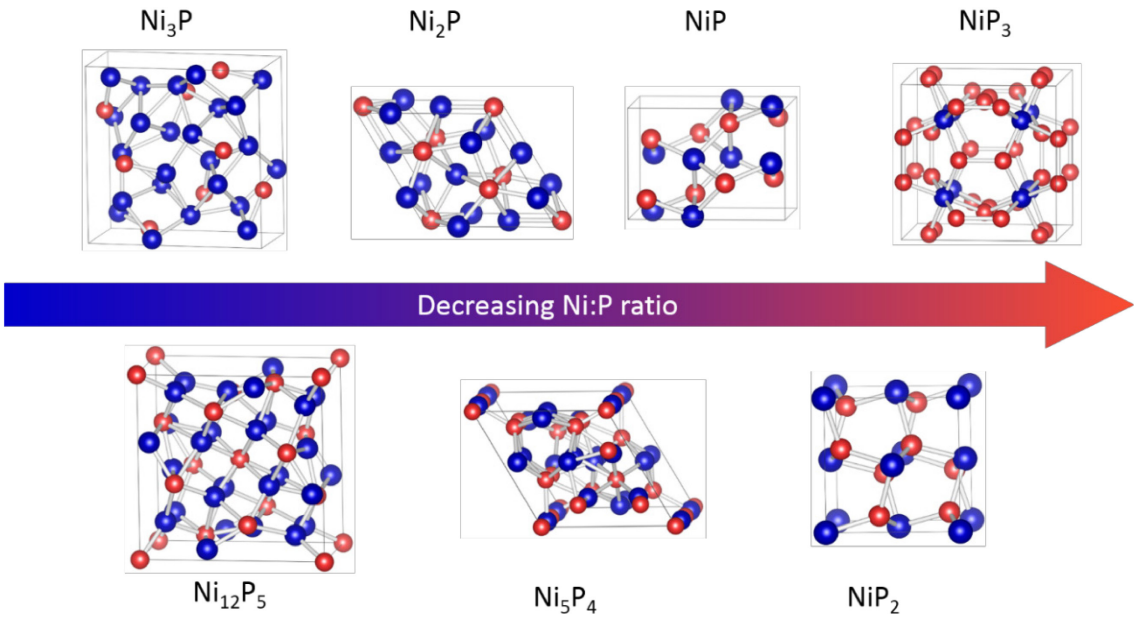

Figure 4.1 Crystal structures of nickel phosphides with various Ni:P ratios (blue: Ni, red: P).

Cobalt phosphides are also known electrolysis catalysts, with the most studied forms being Co_2P and CoP[34] (Figure 4.2). Both Co_2P and CoP have orthorhombic structure with similar Co-P bond lengths. On account of the difference in composition, the crystal structure of Co_2P contains edge-sharing CoP_4 tetrahedra and CoP_5 pentahedra, resulting in nine-coordinate P atoms, while CoP consists of edge-sharing PCo_6 trigonal prisms and face-sharing CoP_6 octahedra[57]. More importantly for heterogeneous catalysis, the low-index surfaces of CoP have larger proportion of exposed P sites compare to Co_2P, due to the lower metal-to-phosphorous ratio[57]. The phosphorous-rich phase CoP_2 is monoclinic.

Cobalt phosphides can be fabricated in various nanostructures. Sun and co-workers[58] prepared three different morphologies of CoP, including 0D nanoparticle, 1D nanowires, and 2D nanosheets, through a two-step reaction, in which the morphology of the phosphide product depends on the morphology of the cobalt oxide (Co_3O_4) precursors produced in the first step. With a similar method, CoP nanowires can be arranged into arrays on carbon cloth, forming a 3D self-stand hydrogen-evolving cathode[59]. Besides, CoP nanoparticles can be combined with carbon nanotubes (CNTs)[14,60], reduced graphene oxide (rGO)[22], and porous carbon[61], to improve the conductivity of the catalysts and the dispersion of the active phases. Hou *et al.*[60] synthesized a CoP-CNT composite using Co_3O_4-CNT as precursor. The catalysts exhibited activity as bifunctional electrocatalyst for both HER and OER in 0.1 M NaOH, achieving an anodic current density of 10 mA cm^{-2} at an overpotential of 330 mV. CoP can also be designed with urchin-like 3D morphology[29]. First, urchin-like $Co(CO_3)_{0.5}(OH)\cdot 0.11H_2O$ was prepared by a hydrothermal reaction, followed by the phosphidation with $Na_2H_2PO_2$. The crystals actively catalyzed the HER and oxygen reduction reaction (ORR). Co_2P@N, P doped CNTs and graphene can be synthesized from the calcination of precursors containing Co, N, P, and corresponding carbon substrates at high temperature under Ar atmosphere[62,63]. For example, Zhuang *et al.*[62] first synthesized N and P functionalized graphene oxide (GO) by anchoring acrylamide monomers and phytic acid molecules onto GO surface under UV irradiation, then calcined the precursor at 900 °C under Ar flow. The dicobalt phosphide nanoparticles are dispersed inside and partially outside the graphene layers with particle size around 30 nm. The N, P-doped hybrid required an overpotential of -129 mV to achieve the current density of -20 mA cm^{-2} in 0.5 M H_2SO_4.

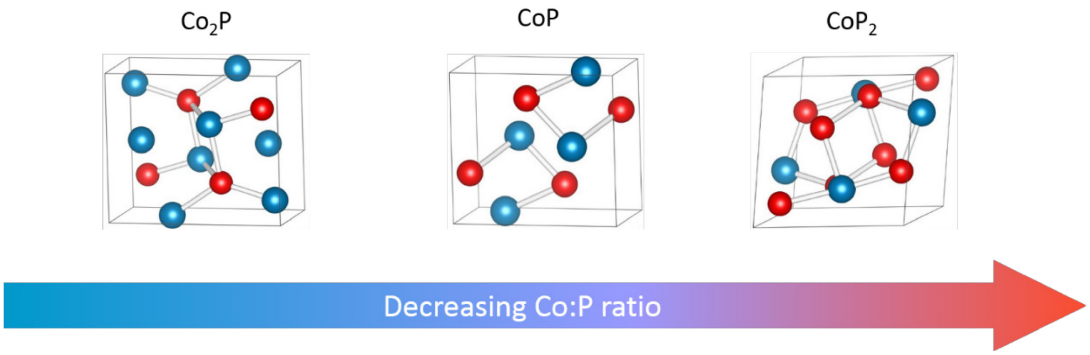

Figure 4.2 Crystal structures of cobalt phosphides with various Co:P ratios (cyan: Co, red: P).

Apart from the syntheses involving solid-state phosphidation, CoP and Co_2P can also be produced in solution[57,64-66]. Hollow Co_2P nanoparticles were synthesized by thermal

decomposition of $Co(acac)_3$ in a solution containing oleylamine, toluene and triphenylphosphine (TPP)[64]. Analogously, hyperbranched Co_2P nanocrystals with sheaf-like structure or hexagonal symmetric structures were synthesized from the decomposition of $Co(OA)_2$ in TOPO at 350 °C[66]. Schaak and co-workers[57] compared the electrocatalytic HER properties of Co_2P and CoP nanoparticles with similar morphology. Phosphide nanoparticles were prepared by the reaction of Co nanoparticles with TOP in 1-octadecene. Both Co_2P and CoP are highly crystalline and have same size dispersity, multifaceted pseudospherical shape, and hollow interiors. The identical morphology facilitated the evaluation of the intrinsic HER catalytic properties. CoP performed slightly better than Co_2P requiring the overpotential of -75 mV to achieve the current density of -10 mA cm^{-2} and yielding the Tafel slop of 50 mV dec^{-1}. The differences in HER activity are consistent with the observations for nickel phosphides that the P sites play an important role in electrocatalytic HER and larger content of P in the catalyst leads to higher activity.

In this chapter, the synthesis of nickel and cobalt phosphides from the corresponding metal organophosphonates is described. The hybrid metal phosphonates act as metal and phosphorous single-source precursors and are transformed into metal phosphide nanoparticles coated with carbon through thermal treatment.

4.2 Results and discussion

4.2.1 Synthesis and characterization of nickel and cobalt phosphides

4.2.1.1 Nickel phosphides

The nickel phenylphosphonate (NiPh) and nickel methylphosphonate (NiMe) used as precursors of the phosphide materials were prepared by reacting Ni(II) acetylacetonate with phenylphosphonic acid or methylphosphonic acid, respectively, in benzyl alcohol at 180 °C under microwave irradiation.

The structure of NiPh was discussed in Section 3.2 of Chapter 3. NiMe ($NiO_3PCH_3 \cdot H_2O$) and NiPh ($NiO_3PC_6H_5 \cdot H_2O$) are isostructural materials[67]. The powder XRD patterns of NiPh and NiMe (Figure 4.3) show intense reflections at low angles, followed by lower intensity reflections corresponding to inter planar distances (d) that are 1/2 and 1/3 of that of the most intense reflection. These diffraction patterns are typical of lamellar structures. In the case of NiPh, the reflections at 2.80, 5.62, and 8.48 ° 2θ correspond to diffraction by the (010), (020), and (030) planes, respectively. For NiMe, broad reflections occur at 3.97 and 7.90° 2θ

corresponding to diffraction by the (010) and (020) planes, suggesting the low crystallinity of this sample. As described in chapter 3, in these structures the metal is coordinated by five oxygens from the phosphonate ligands and one oxygen from a water molecule. The inorganic layers are composed by CPO_3 tetrahedra corner- and edge-shared with four NiO_6 octahedra and the organic groups are located in between the inorganic layers, interacting through van der Waals and dispersion forces. The NiO_6 are corner-shared [67,68]. The interlayer distance, depends on the size of the organic ligand and is given by the d spacing of the most intense reflection (010). It is 1.45 nm and 1.0 nm for NiPh and NiMe, respectively. For NiMe the interlayer distance is slightly larger than previously reported (0.87 nm)[68]. Furthermore, the carbon contents of NiPh and NiMe are 35.8 and 9.4 wt. %, respectively, which are also higher than the values expected based on the formulas $NiO_3PC_6H_5 \cdot H_2O$ (30.9 wt. %) and $NiO_3PCH_3 \cdot H_2O$ (7.0 wt. %) proposed for these materials[67,68]. These differences suggest that some benzyl alcohol (reaction solvent) molecules are trapped in the interlayer space, which has a higher impact on the interlayer distance of NiMe. The presence of a small amount of benzyl alcohol molecules on the phosphonates was confirmed by TG-MS analysis.

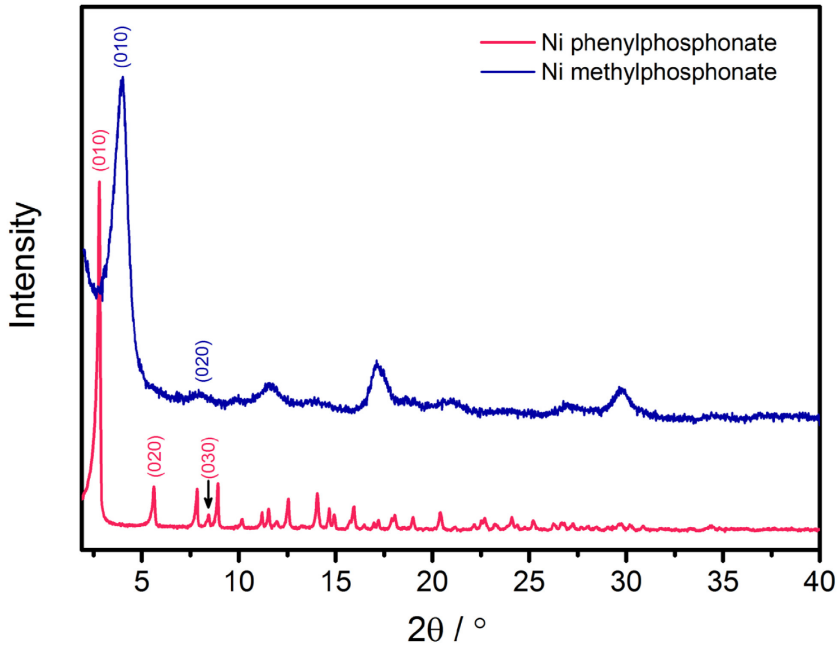

Figure 4.3 Powder X-ray diffraction patterns of the Ni phenylphosphonate (NiPh) and Ni methylphosphonate (NiMe).

NiPh is made of long rectangular particles (Figure 4.4a,b) and NiMe consists of smaller particles of irregular size (Figure 4.4c,d). The layered structure of NiPh is seen on the TEM images, with the darker regions corresponding to the inorganic layer and the lighter to the

organic layer. The interlayer distance measured from TEM matches well the one calculated from the XRD data.

The hybrid metal phosphonates were submitted to thermal treatment at temperatures ranging from 350 to 700 °C under H_2(5%)/Ar. The XRD patterns of the products obtained by thermal treatment of NiPh under H_2(5%)/Ar atmosphere at 400 °C (NiPh-400), 450 °C ($Ni_{12}P_5$-Ph-450), 500 °C ($Ni_{12}P_5$-Ni_2P-Ph-500), 550 °C (Ni_2P-Ph-550) and 700 °C (Ni_2P-Ph-700) are shown in Figure 4.5. The product obtained at 400 °C maintains the layered phosphonate structure and does not show reflections at high 2θ angles indicative of the formation of any crystalline phosphide phases. There is however a loss of crystallinity and a decrease of the d spacing likely due to the loss of structural water and the organic ligands starting to decompose. $Ni_{12}P_5$ is produced at 450 °C and a mixture of $Ni_{12}P_5$ and Ni_2P phases is formed at 500 °C. At 550 °C and 700 °C pure phase Ni_2P is produced, as the Ni_2P phase forms at higher temperatures than $Ni_{12}P_5$[42].

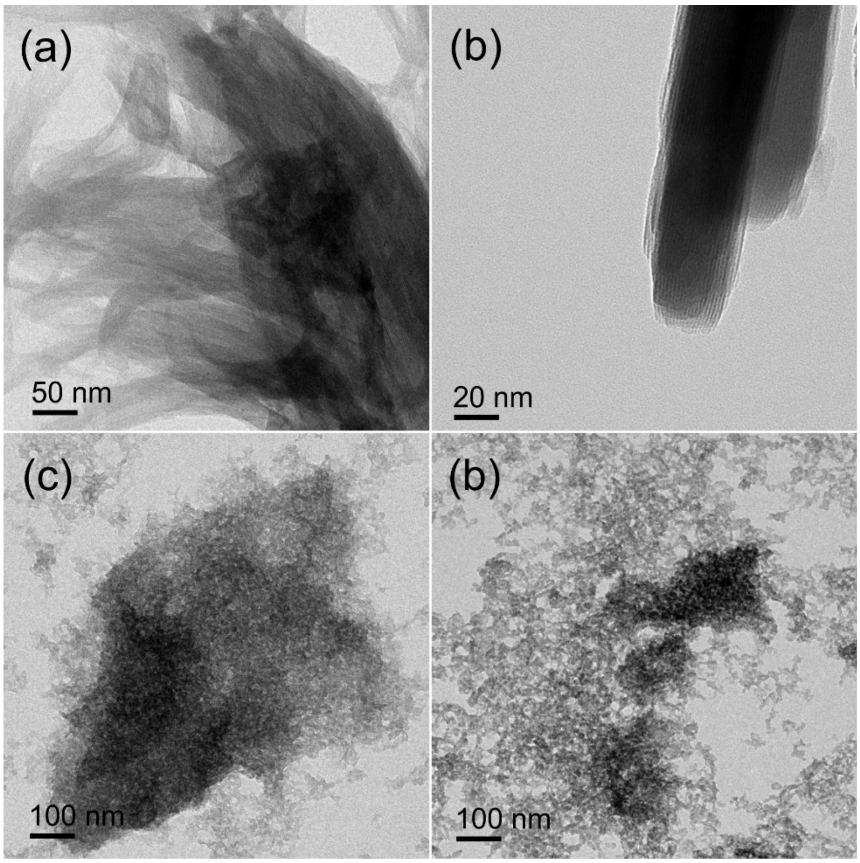

Figure 4.4 TEM images of the (a,b) Ni phenylphosphonate (NiPh) and (c, d) Ni methylphosphonate (NiMe).

The TEM images of $Ni_{12}P_5$-Ph-450 reveal that the product consists of nanoparticles together with incompletely reacted metal phosphonate precursor (Figure 4.6a-f), which likely consists of partially carbonized organic ligand since no intense reflections from the metal phosphonate structure are observed in the XRD pattern of this sample. As the synthesis temperature increases the transformation of the phosphonate precursor is more complete and the amount of carbonaceous material on the final product decreases. At 500 °C and temperatures above the products are nickel phosphide nanoparticles coated with a thin layer of carbon (Figure 4.6f,g).

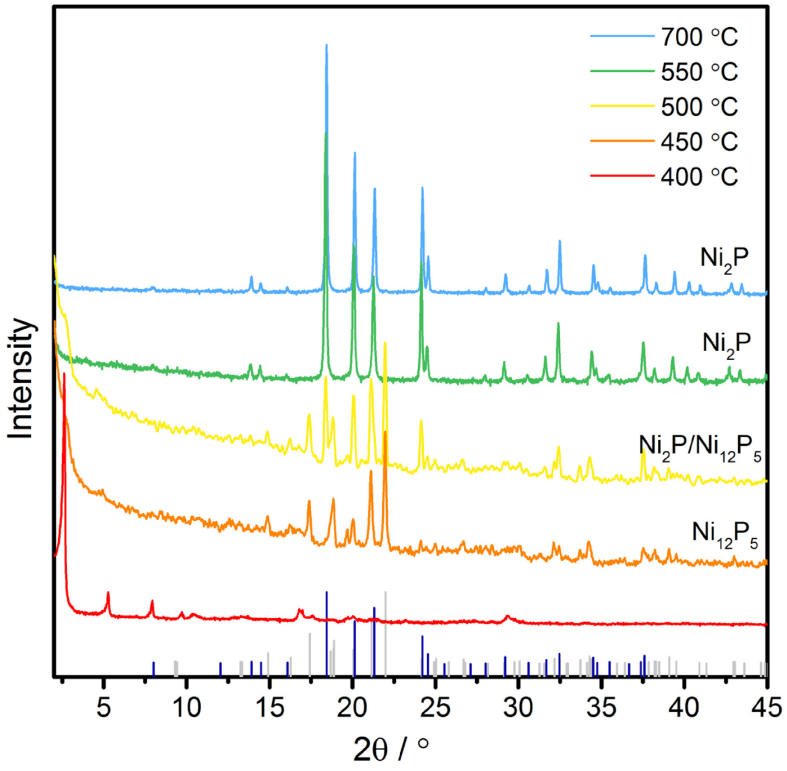

Figure 4.5 Powder X-ray diffraction patterns of the materials produced by thermal treatment of Ni phenylphosphonate under H_2(5%)/Ar atmosphere. Vertical bars represent reference patterns: gray-$Ni_{12}P_5$ (JCPDS card no. 022-1190); dark blue-Ni_2P (JCPDS card no. 074-1385).

Pure phase Ni_2P nanoparticles are produced at 550 °C and higher temperatures, with sizes ranging from *ca.*15 to 45 nm and fairly uniform morphology, considering the high synthesis temperature (Figure 4.6g,h). Further increase of the synthesis temperature to 700 °C did not caused significant changes on the final size of the Ni_2P NPs (Figure 4.6i). Selected area electron diffraction (SAED) measurements were performed to confirm the structure of $Ni_{12}P_5$ and Ni_2P (insets in Figure 4.6b,c,g). The electron diffraction patterns show the (200) and (112) planes of the tetragonal phase $Ni_{12}P_5$ in Figure 4.6b, the (100), (111), (201), (210) and (300) of hexagonal

Ni_2P in Figure 4.6g, and a mixture of $Ni_{12}P_5$ and Ni_2P in Figure 4.6c. A thin layer of carbon material with thickness around 2 - 4.5 nm covers the surface of the phosphide nanoparticles forming a phosphide @carbon core-shell structure (Figure 4.6e,f). The organic ligand likely plays a role on the size and morphology control of the phosphide particles during the synthesis. The small size of the NPs, i.e. the low sintering degree even at temperatures as high as 700 °C, may be attributed to the organic/carbon surrounding the particles during their formation and growth that hinder their coalescence.

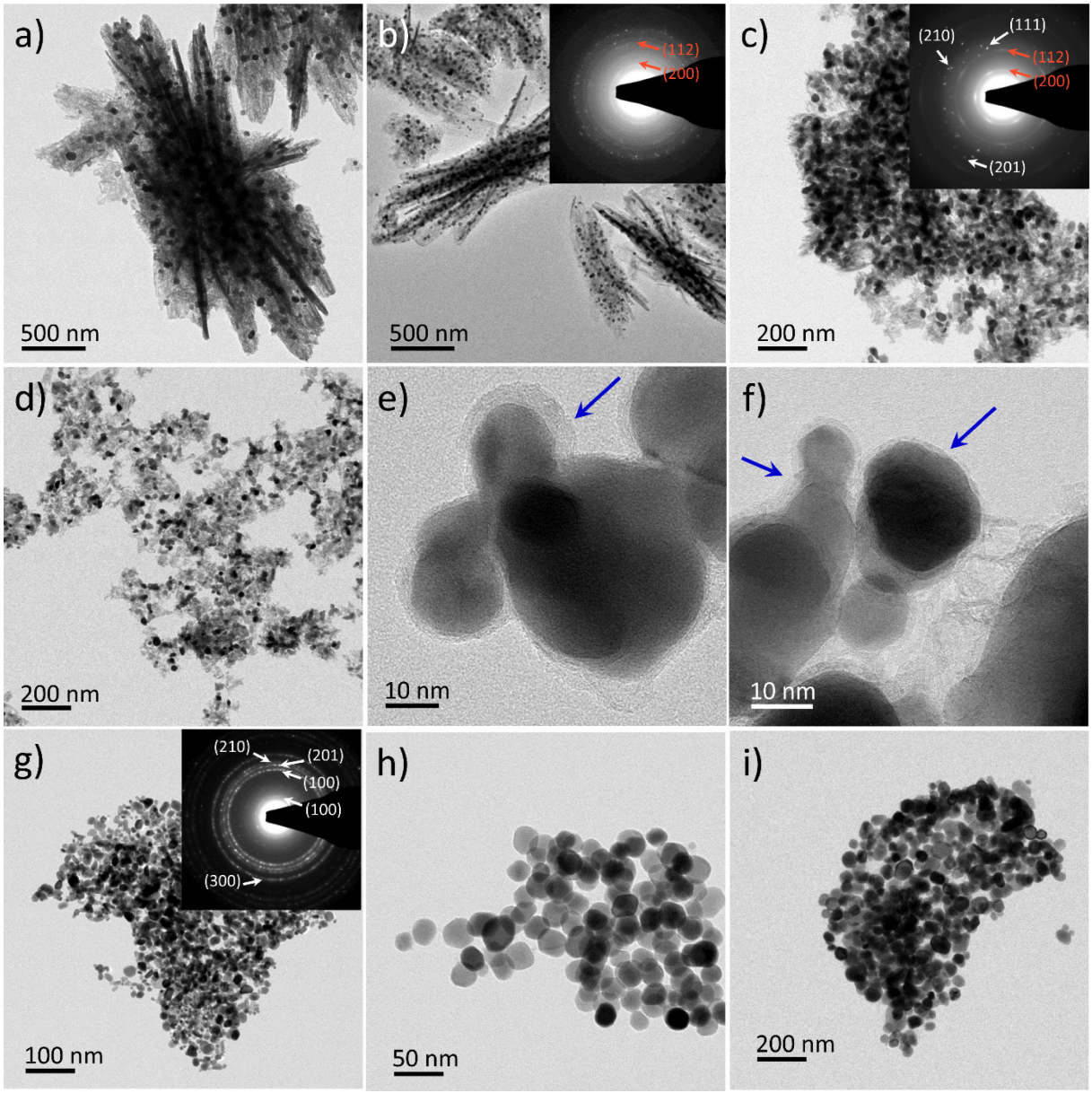

Figure 4.6 TEM images of (a,b) $Ni_{12}P_5$-Ph-450, (c,d,e,f) $Ni_{12}P_5$-Ni_2P-Ph-500, (g,h) Ni_2P-Ph-550 and (i) Ni_2P-Ph-700 synthesized by thermal treatment of nickel phenylphosphonate under H_2(5%)/Ar at 450 °C, 500 °C, 550 °C and 700 °C, respectively. The insets in b, c, and g show the SAED patterns. Blue arrows indicate the carbonaceous shell around the nanoparticles.

When nickel methylphosphonate is used as precursor, the results are similar to those described for NiPh. The XRD patterns in Figure 4.7 show that at 500 °C the product is a mixture of $Ni_{12}P_5$-Ni_2Pphases. The broad reflection at 4°2θ suggests the presence of some unreacted metal phosphonate precursor. TEM images of this sample (Figure 4.8a,b) show that the material consist of irregular particles with ambiguous boundaries, which may indicate there is still organics surrounding the phosphide phases. Pure and well-defined Ni_2P nanoparticles were formed at 550 °C or above. The Ni_2P particles obtained at 600 °C have a thin shell of carbon (Figure 4.8 c, d), which seems to get thinner at 700 °C (Figure 4.8 e, f), as it is not so clearly visible in the TEM images. The spherical nanoparticles trend to coalesce with each other forming irregular and larger particles at 700 °C. This effect is not so pronounced when nickel phenylphosphonate is used as precursor probably owing to the higher of organic/carbon on that precursor that prevents sintering more efficiently.

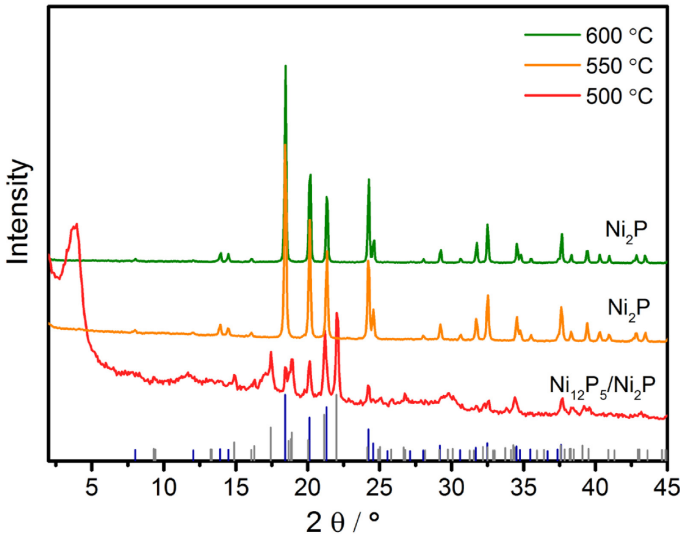

Figure 4.7 Powder XRD patterns of the materials produced by thermal treatment of nickel methylphosphonate. Vertical bars represent reference patterns: gray-$Ni_{12}P_5$ (JCPDS card no. 022-1190); dark blue-Ni_2P (JCPDS card no. 074-1385).

The products synthesized at 450 °C and 500 °C from NiPh and NiMe have carbon contents of *ca.* 4-5 wt. %, and the materials (Ni_2P) synthesized at 550 °C or temperatures above contain 1-2 wt. %. Therefore, most of the organic component of the hybrid precursor decomposes at temperatures below 450 °C. Fourier-Transformed Infrared (FT-IR) spectroscopy analysis of the samples was performed in order to determine the nature of the carbonaceous material that remains on the products after thermal treatment. Figure 4.9 shows the FT-IR spectra of the NiPh precursor and materials synthesized at 350 °C, 400 °C,450 °C, 500 °C, 550 °C, 600 °C and

650 °C. The spectrum of nickel phenylphosphonate shows bands characteristic of the aromatic organic compound, P-O and P-C bonds: the bands between *ca.* 1300 cm^{-1} and 980 cm^{-1} are ascribed to the stretching vibration of P-O bonds; the band at 1438 cm^{-1} is attributed to P-C bonds; the bands in the region between 400 and 800 cm^{-1} are attributed to the aromatic ring, including out-of-plane C-H bending vibrations (750, 719 cm^{-1}) and out-of-plane ring C=C bending (696 cm^{-1}). Bands associated with the C=C skeletal vibrations are found at *ca.* 1600 cm^{-1} and 1488 cm^{-1}. Bands arising from the vibration of O-H groups from adsorbed water are observed at 3000-3600 cm^{-1} and 1600-1650 cm-1 region[68]. Ni-O and Ni-P vibrations occur in the region of the spectra below 400 cm^{-1}. Bands typical of the organic phenyl group (P-C and P-O bonds) are still visible on the spectra of the sample synthesized at 450 °C or lower temperature, indicating that the products at these temperatures still contain unreacted phosphonate. The intensity of these bands significantly decreases or even completely disappears from the spectra of the phosphides synthesized at 500 °C, 550 °C and 600 °C. These samples possess pyrolyzed carbon that forms a thin shell around the nanoparticles and still contains O and P. However, when the temperature increases to 650 °C, there almost no signal is observed in the region belonging to P-O and P-C vibrations in the spectrum, suggesting that most of the phosphorous in carbon shell is eliminated at high temperature.

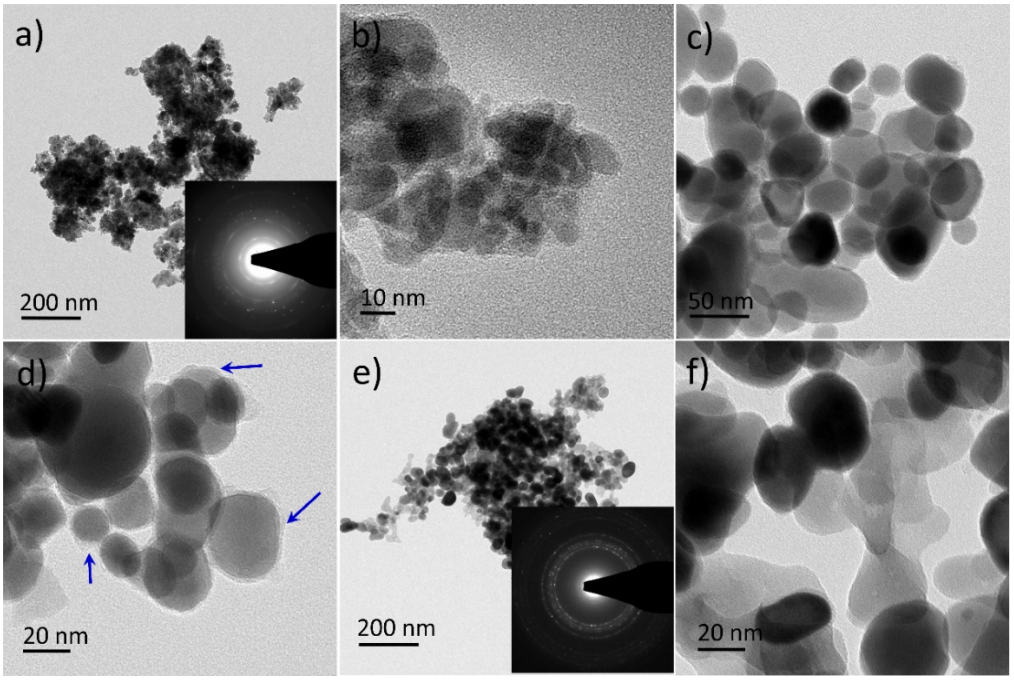

Figure 4.8 TEM images of (a,b) $Ni_{12}P_5$-Ni_2P-Me-500, (c,d) Ni_2P-Me-600, and (e,f) Ni_2P-Me-700 synthesized by thermal treatment of nickel methylphosphonate under H_2(5%)/Ar at 500 °C, 600 °C, and 700 °C, respectively. Inserts in a, e show the SAED patterns. Arrows in blue indicate the carbonaceous shell around the nanoparticles.

The surface composition and valence oxidation state of Ni phosphonate and Ni phosphide nanoparticles were characterized by X-ray photoelectron spectroscopy (XPS). The survey spectra of nickel phenylphosphonate and Ni_2P-Ph-550 obtained at 550 °C (Figure 4.10a) reveal the presence of C, Ni, P and O in both cases (using Mo as substrate in this measurement). Figure 4.10b-e display the Ni 2p and P 2p XPS spectra of NiPh and Ni_2P NPs, which confirm the reduction of the Ni-P species upon thermal treatment of the phosphonate precursor in H_2(5%)/Ar atmosphere. In Figure 4.10a, the C 1s in NiPh is observed at 288.2 eV binding energy (BE). It should be noted that this core level, as well as the Ni and P core levels were observed to shift to higher BE when increasing film thickness. Therefore, the presently measured high binding energy measured for all the elements results from differential charging upon photoionization. To correct for this effect, all the core level spectra were then shifted rigidly by 4.2 eV so that the corrected C 1s level is aligned at 284 eV BE, as expected for C within a phenyl ring[69].

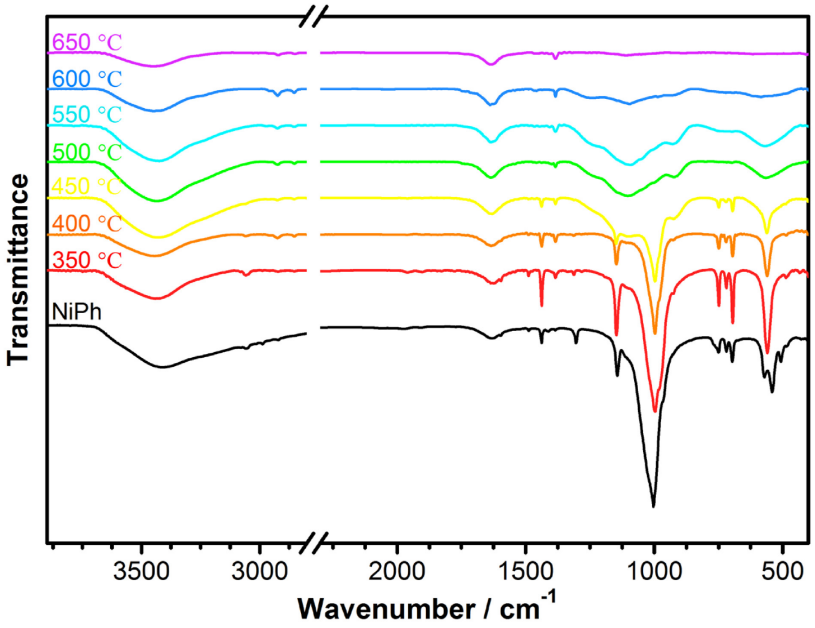

Figure 4.9 FT-IR spectra of nickel phenylphosphonate (NiPh), and the products synthesized by thermal treatment of NiPh under H_2(5%)/Ar at different temperatures.

The corresponding energetically-corrected Ni 2p and P 2p spectra are presented in Figure 4.10 b-e. Changes in the Ni 2p and P 2p regions of the spectra of the phosphonate and phosphide are observed. Contributions at lower binding energies in the Ni 2p and P 2p regions of the Ni_2P spectrum compared to the Ni phosphonate reflect the reduction of Ni-P species. Three contributions are found on the Ni 2p region of the Ni_2P spectrum. The contribution at 853.2 eV

BE results from Ni in Ni phosphide, which is very close to the binding energy of zero valence state Ni. The contribution at 855.9 eV BE indicates the existence of surface oxidized Ni species, while the contribution at 861.1 eV BE is a satellite peak. The P 2p region shows two doublets. The doublet at 129.8 eV BE, which is close to binding energy of elemental P, is attributed to phosphorous in the phosphide material. The doublet at 133.6 eV BE indicates the presence of oxidized P species on the surface of the Ni_2P-Ph nanoparticles, likely phosphates that are formed at the surface by exposure to air[15,70].

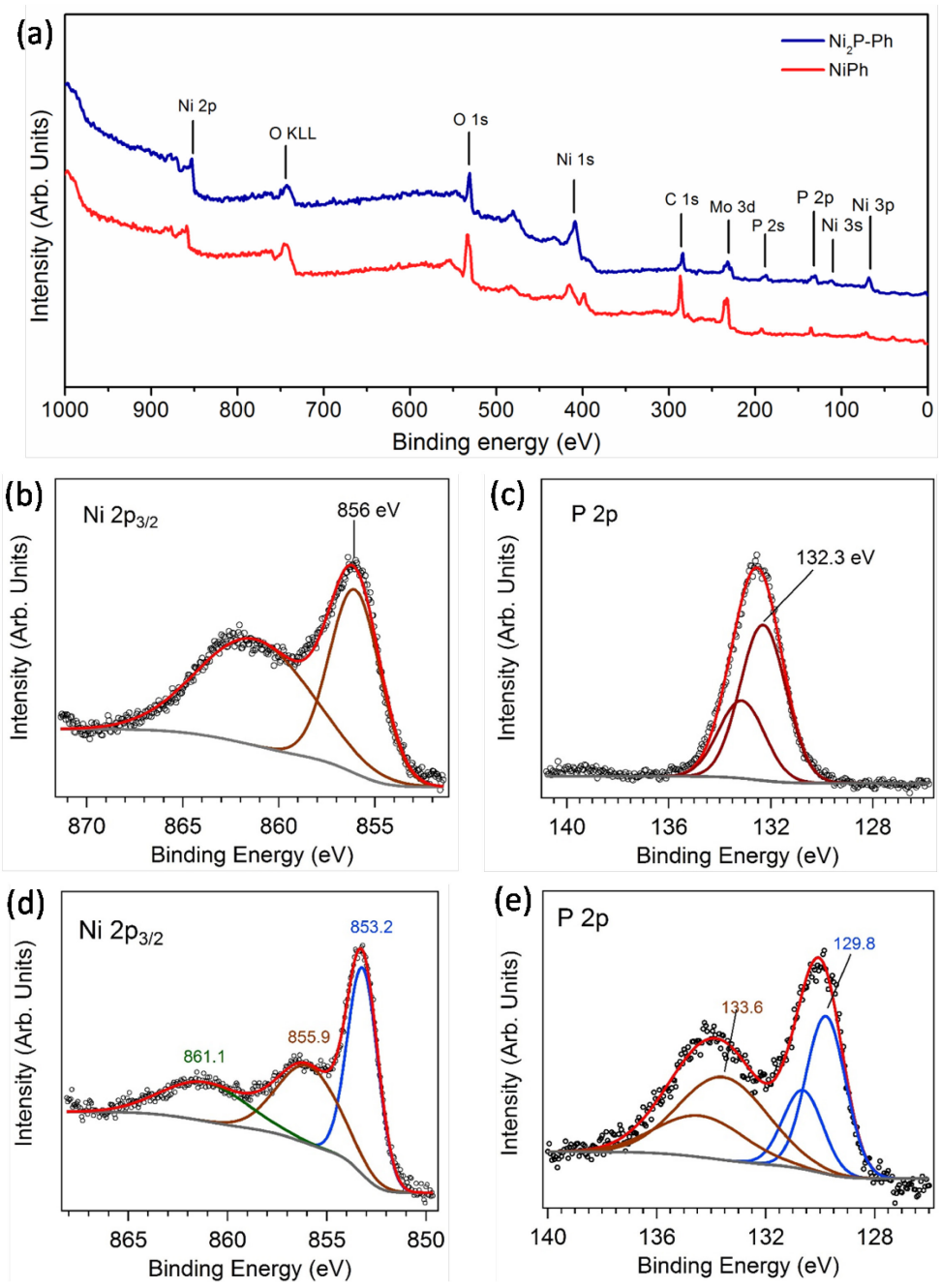

Figure 4.10 (a) Survey X-ray photoelectron spectra of NiPh and Ni_2P-Ph-550. Ni 2p and P 2p XPS spectra of (b, c) nickel phenylphosphonate and (d, e) Ni_2P NPs.

In addition to the treatment under H_2(5%)/Ar flow, the nickel phenylphosphonate was heated at different temperatures under pure argon or under air, for 3 h. The exact composition of the product obtained by heating under Ar depends on the temperature but a nickel phosphide phase is always formed above 550 °C (Figure 4.11). Figure 4.11 a shows that at 500 °C metallic Ni is obtained. A weak and broad reflection at ~4 ° 2θ indicates the existence of organic component in this material. At 550 °C, a mixture of Ni_3P and metallic Ni is synthesized while at 600 °C a pure phase of Ni_3P is produced. A mixture of $Ni_{12}P_5$-Ni_2P and $Ni_2P_2O_7$ are obtained at 800 °C. According to these XRD results, the evolution of nickel phosphide from nickel phenylphosphonate under Ar atmosphere proceeds as described in Scheme 4.1: metallic nickel is first formed from the decomposition of the metal organophosphonate precursor, followed by the reactions with phosphorous species to produce Ni_3P, $Ni_{12}P_5$ and Ni_2P, depending on the temperature.

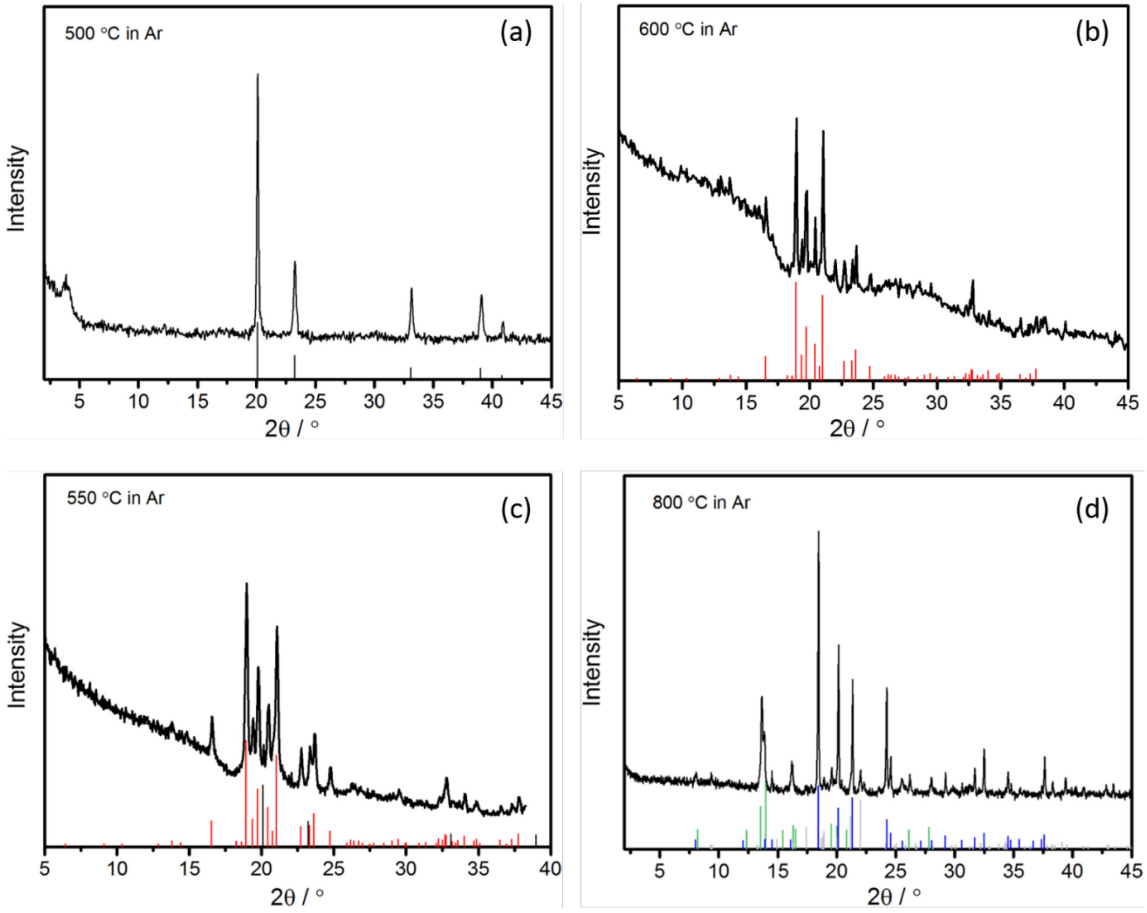

Figure 4.11 X-ray diffraction pattern of the products synthesized by thermal treatment of nickel phenylphosphonate at 500 °C, 550 °C, 600 °C and 700 °C under argon, measured using Mo radiation (λ =0.7093 Å). Vertical bars represent reference patterns: red- Ni_3P (JCPDS card no. 074-1384); gray- $Ni_{12}P_5$ (JCPDS card no. 022-1190); black- Ni (JCPDS card no. 004-0850); blue- Ni_2P (JCPDS card no. 074-1385); green- $Ni_2P_2O_7$ (JCPDS card no. 049-1082).

Mixtures of nickel oxides and phosphides were fabricated at temperatures between 400 and 500 °C under air. Although at sufficiently high temperatures and reaction times only oxides and phosphates are formed, it is somewhat surprising that oxides and phosphates are not always the exclusive products of the reaction performed under oxidizing conditions. The phosphonate precursor is therefore reduced, at least partially, even in the absence of H_2(5%)/Ar gas flow.

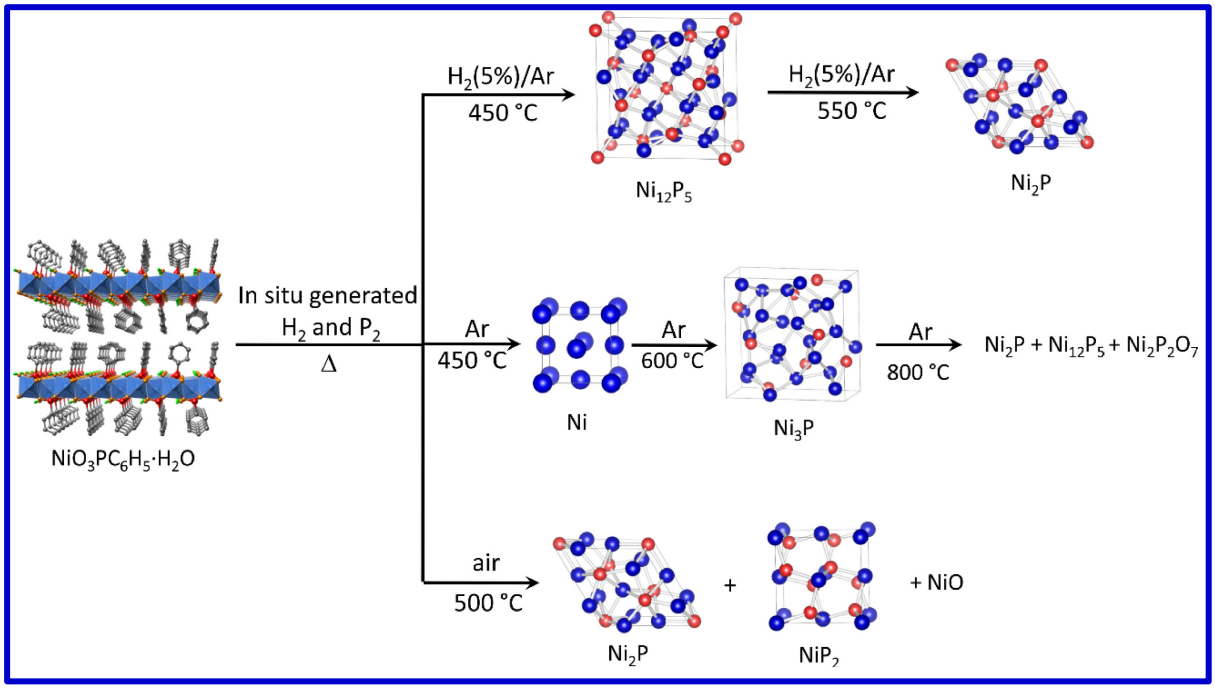

Scheme 4.1 Formation of nickel phosphides with different crystalline phases by thermal treatment of Ni phenylphosphonate. (blue: Ni, red: P, orange: O, green: H, gray: phenyl ring)

4.2.1.2 Cobalt phosphides

The approach used for the synthesis of the Ni phosphides was extended to fabricate cobalt phosphides. Co(II) phenylphosphonate was synthesized from the reaction between Co(II) acetate and phenylphosphonic acid in benzyl alcohol. This procedure is different from the synthesis of Co(II) phenylphosphonate discussed in Section 3.6 Chapter 3 where Co(II) acetylacetonate was used as Co source, resulting in a different particle morphology. Cobalt phosphides, Co_2P and CoP, were prepared from the corresponding metal phenylphosphonate in H_2(5%)/Ar atmosphere.

Similarly to what was observed for the nickel phosphonates, the properties of the final product, such as the phosphide phase, are influenced by the thermal treatment conditions, especially the temperature. XRD patterns in Figure 4.12 show that the Co phenylphosphonate (CoPh) has

well-defined reflections at 2.68, 5.30 and 7.92 °2θ, corresponding to the diffractions by (010), (020) and (030), respectively. The interlayer distance is 1.52 nm, calculated by Bragg's law over the first and most intense reflection (010). A mixed-phase Co_2P-CoP was formed at 550 °C and pure Co_2P can be produced at 600 °C.

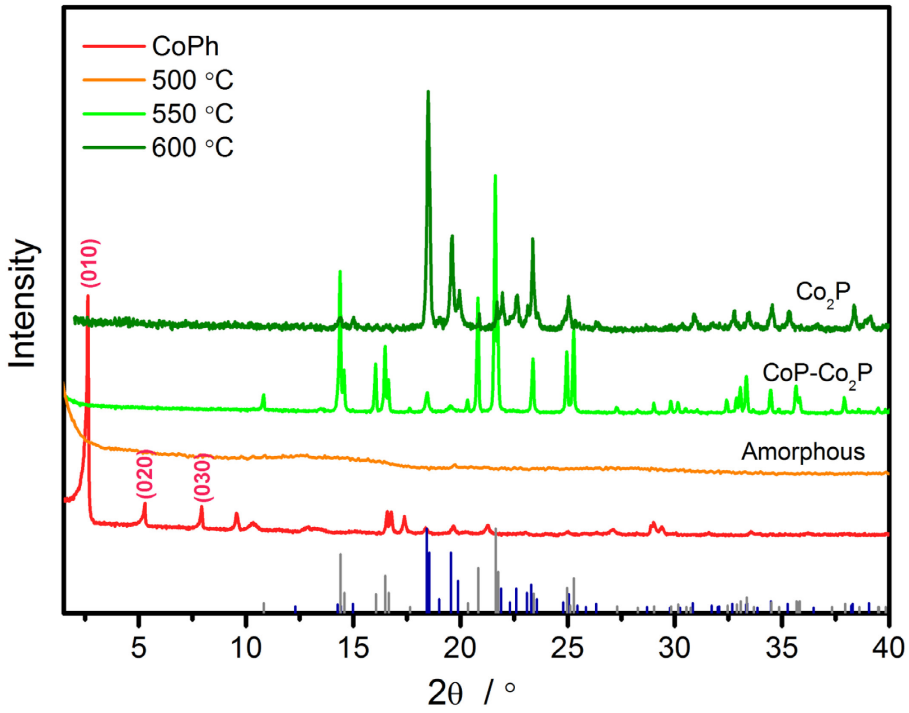

Figure 4.12 XRD patterns of Co phenylphosphonate (CoPh) and the products synthesized by thermal treatment of Co phenylphosphonate at 500 °C, 550 °C, and 600 °C under H_2(5%)/Ar, measured using Mo radiation (λ =0.7093 Å). Vertical bars represent reference patterns: gray-CoP (JCPDS card no. 029-0497); blue-Co_2P (JCPDS card no. 032-0306).

Figure 4.13a,b show that Co phenylphosphonate is composed of thin sheets and the selected area electron diffraction (SAED) pattern in Figure 4.13c indicates the hexagonal structure of these nanocrystals. The hexagonal structure is inherited to the amorphous product synthesized at 500 °C, which has a fixed angle of 120 ° between two adjacent edges. Cobalt phosphide can be obtained at higher temperatures consisting of irregular and polydisperse particles with sizes ranging from *ca.* 10 to 100 nm. Carbonaceous material is also observed surrounding and coating these phosphide nanoparticles, which becomes thinner at 600 °C.

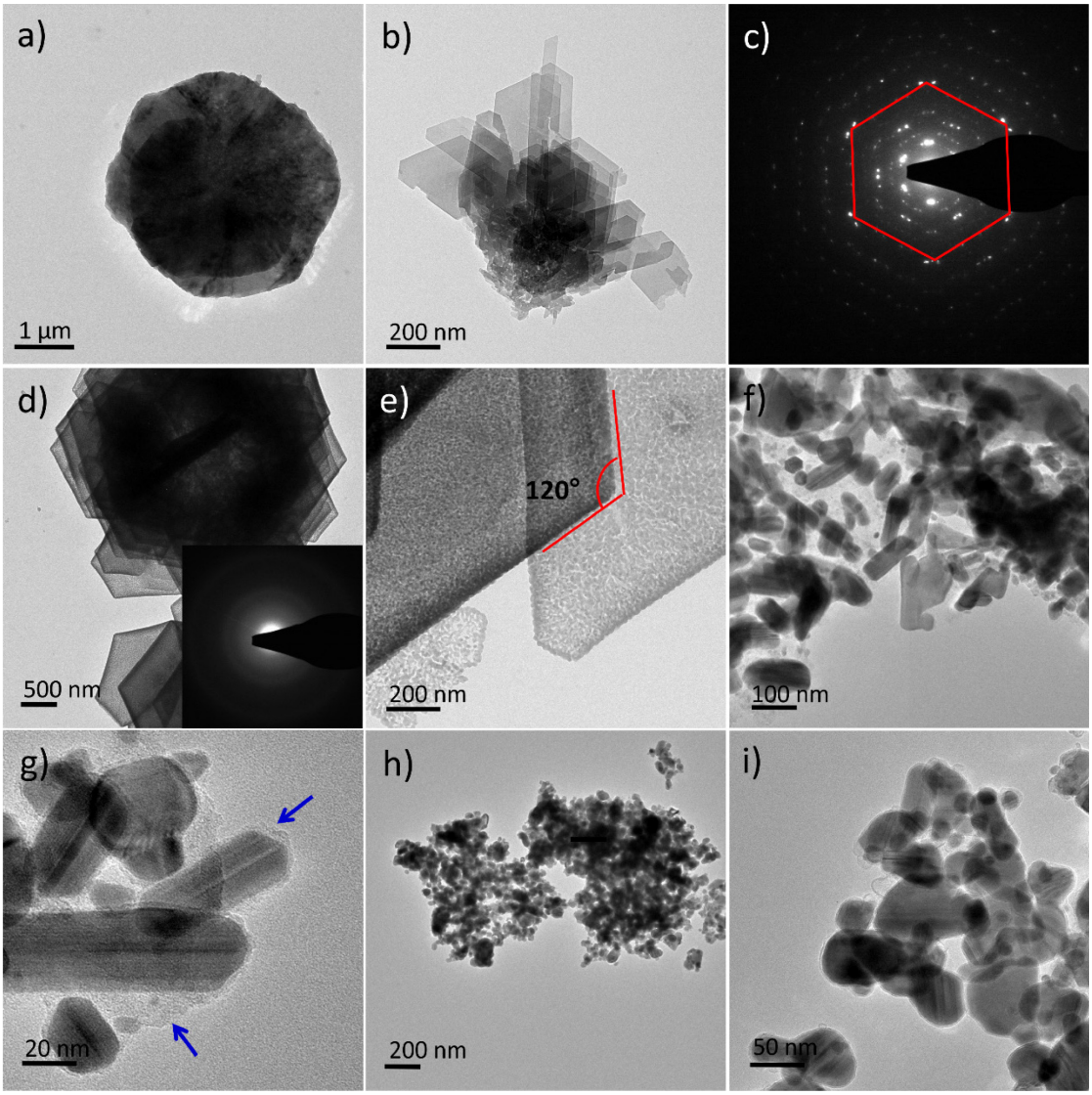

Figure 4.13 TEM images of (a,b) CoPh, (d,e) Co-P-Ph-500, (f,g) Co_2P-CoP-Ph-550, and (h,i) Co_2P-Ph-600 synthesized by thermal treatment of cobalt phenylphosphonate under H_2(5%)/Ar at 500 °C, 550 °C, 600 °C, and 700 °C, respectively. Image (c) and inserts in d show the SAED patterns. Arrows in blue indicate the carbonaceous shell around the nanoparticles. Arrows in blue indicate the carbonaceous shell around the nanoparticles.

4.2.2 Reaction mechanism

Thermogravimetric analysis coupled with mass spectrometry (TG-MS) of the nickel phosphonates was performed in order to determine the species generated during their conversion into phosphides and to get mechanistic insights. The TG curve of nickel phenylphosphonate shown in Figure 4.14 was measured under Ar flow. XRD characterization of the sample after the TG-MS analysis confirmed that nickel phosphide was produced during the measurement. The TG curve shows two pronounced mass losses occurring at temperatures

near 300 °C and 600 °C. MS data reveals that the main species generated during heating have *m/z* of 2, 18, 62 and 77, which are ascribed to the formation of H_2, H_2O, P_2, and C_6H_5, respectively. Additional carbon-containing compounds were detected, *e.g.* methane, which were produced from further decomposition of the organic ligand. Benzyl alcohol was also released during heating. The formation of several phosphorous-containing species including PH_3, organic phosphines and phosphine oxides was monitored, but only P_2 was detected. Furthermore, the amount of P_2 detected is small compared to that of H_2, H_2O and C_6H_5, suggesting that most of the sample phosphorous remains in the solid state during heating.

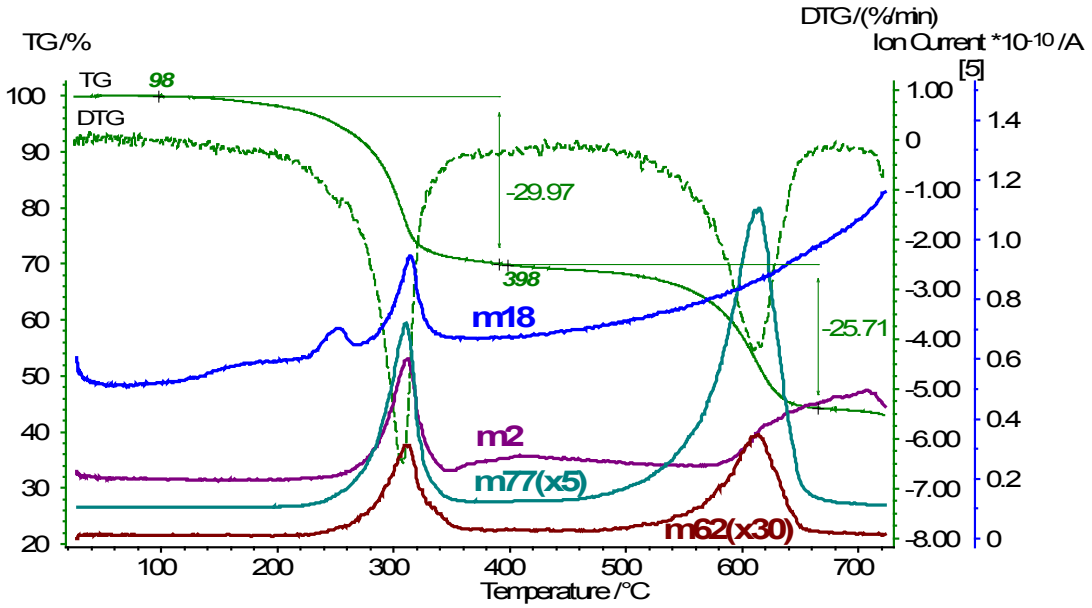

Figure 4.14 TG-MS curves of nickel phenylphosphonate in Ar with the IC curves for the mass numbers *m/z*=2 (H_2^+), 18 (H_2O^+), 62 (P_2^+), and 77 ($C_6H_5^+$). For a better distinction, the IC curves are shifted and the DTA trace is omitted (two weakly expressed endothermal effects).

The water released at *ca.* 250 °C corresponds to structural water, since none of the other species are observed simultaneously at this temperature. The formation of hydrogen likely results from the thermal decomposition of the organic component through a radical mechanism, since the pyrolysis of organic compounds frequently proceed through radical mechanisms,[71] or from the transformation of organic species catalyzed by the metal centers.[15] The production of hydrogen is not exclusive of the phenylphosphonate ligand, as it was also detected during TG-MS analysis of nickel methylphosphonate (Figure 4.15), which exhibits a thermal behavior similar to nickel phenylphosphonate. The H_2 generated likely reacts with the $-PO_3$ groups to form P_2 and H_2O,[72] which accounts for the water and P_2 detected simultaneously with H_2 formation. P_2

subsequently reacts with the metal to produce the phosphide. The production of H_2 in situ during the thermal decomposition of the phosphonate explains why phosphide phases could be produced under Ar or even under air: the phosphonate produces its own reduction agent (Scheme 4.1). However, pure metal phosphide compounds cannot be synthesized under air owing to the presence of O_2 in the system, which reacts with the precursor to produce oxides and phosphates, and because the H_2 generated is only sufficient to partially reduce the precursor.

Furthermore, the fact that no particularly toxic phosphorous-containing compounds are produced during the transformation of the inorganic-organic hybrid into the phosphide makes this a non-hazardous procedure.

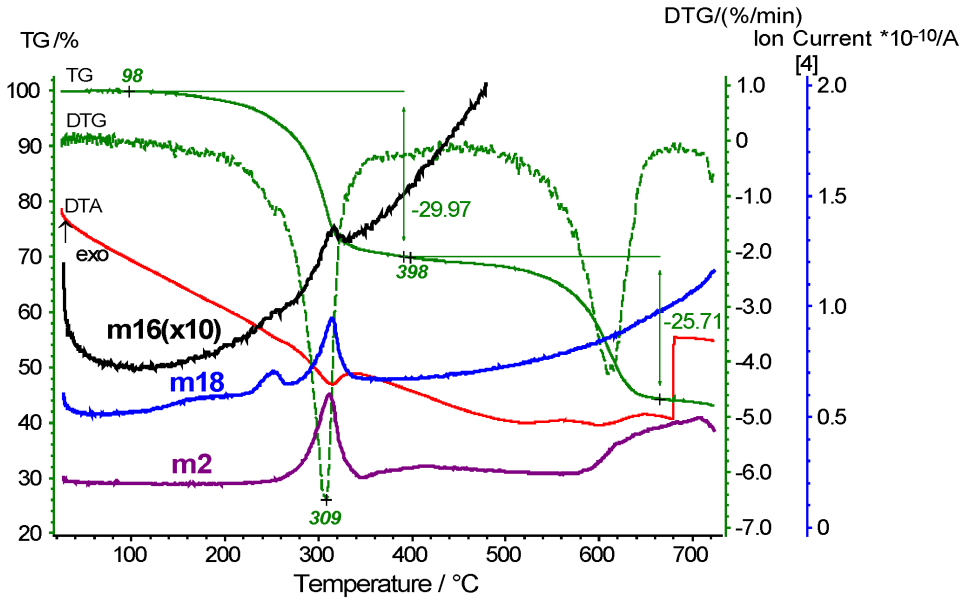

Figure 4.15 TG-MS curves of nickel methylphosphonate in Ar with the IC curvesfor the mass numbers *m/z*=2 (H_2^+), 18 (H_2O^+) and16 (CH_4^+).

4.2.3 Electrocatalytic hydrogen evolution reaction performance in acidic solution

The electrocatalytic activity of the Ni phosphide materials synthesized from the nickel phenylphosphonate precursor under H_2(5%)/Ar at 450 °C ($Ni_{12}P_5$-Ph-450), 500 °C ($Ni_{12}P_5$-Ni_2P-Ph-500) and 550 °C (Ni_2P-Ph-550) was evaluated on the HER in acidic electrolyte. For comparison the catalytic activity of the Ni_2P nanoparticles synthesized using Ni methylphosphonate as precursor (Ni_2P-Me-600) was also investigated. Figure 4.16a shows the HER polarization curves, measured in 0.5 M H_2SO_4 using a three-electrode set-up and a glassy carbon rotating disc electrode as working electrode, rotated at 2000 rpm. The corresponding Tafel plots, η *vs.* logj, are displayed in Figure 4.17a. The performance of a commercial Pt/C (20

wt.% Pt) was examined as a reference. Pt/C shows the best performance; its polarization curve and Tafel slope of 31 mV dec^{-1} agree with the data previously reported.[73,74]

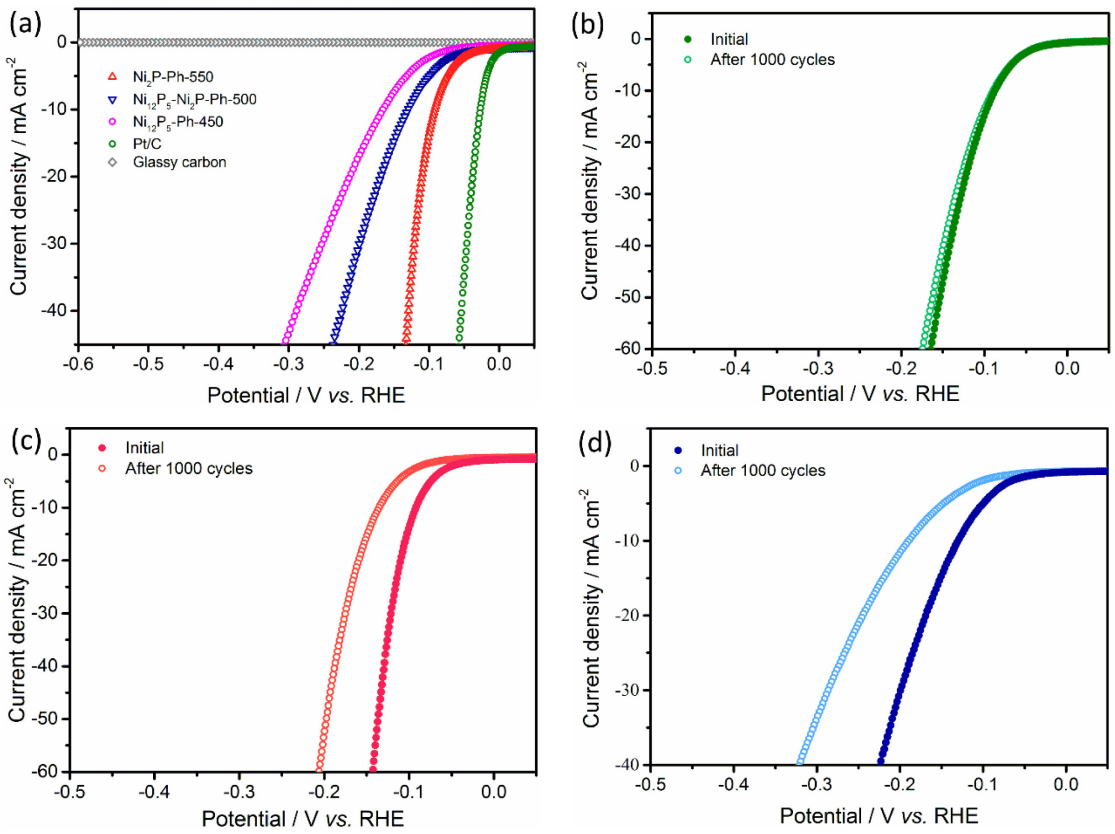

Figure 4.16 (a) Polarization curves of Ni_2P-Ph-550, $Ni_{12}P_5$-Ni_2P-Ph-500, $Ni_{12}P_5$-Ph-450, Pt/C and pristine glassy carbon electrode. Polarization curves of (b) Ni_2P-Me-600, (c) Ni_2P-Ph-550 and (d) $Ni_{12}P_5$-Ni_2P-Ph-500 at initial and after 1000 cycles, respectively. Curves were collected at a scan rate of 10 mV/s in 0.5 M H_2SO_4.

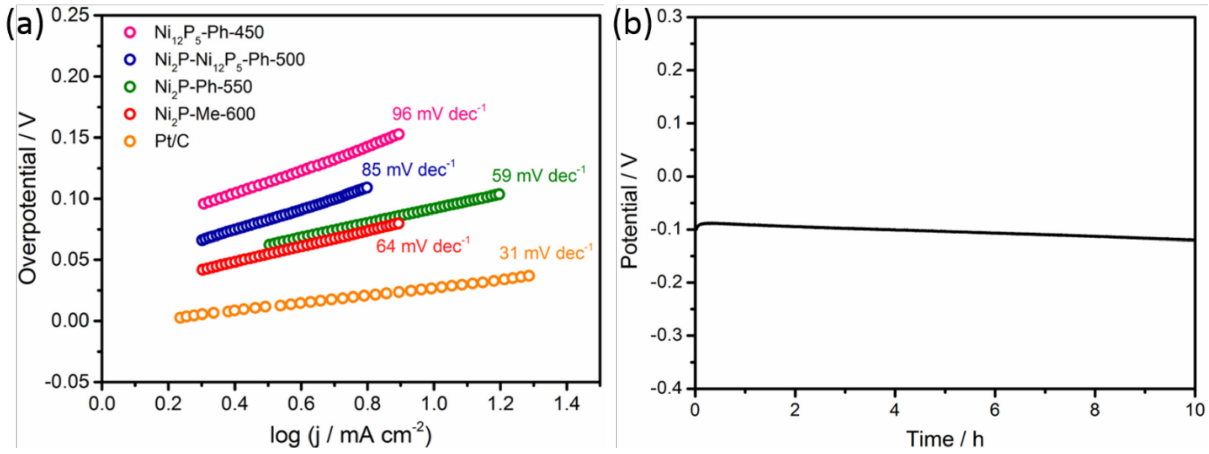

Figure 4.17 (a) Tafel slopes of $Ni_{12}P_5$-Ph-450, $Ni_{12}P_5$-Ni_2P-Ph-500, Ni_2P-Ph-550, Ni_2P-Me-600 and Pt/C, for HER in 0.5 M H_2SO_4. (b) Chronopotentiometric curve with a fixed current density of -10 mA cm^{-2}.

The nickel phosphonates are not active HER catalysts and the performance of $Ni_{12}P_5$-Ph-450 is poor, although $Ni_{12}P_5$ NPs have been found before to be active HER electrocatalysts.[29] On the contrary, $Ni_{12}P_5$-Ni_2P-Ph-500, Ni_2P-Ph-550 are active HER catalysts in acidic medium. $Ni_{12}P_5$-Ni_2P-Ph-500, Ni_2P-Ph-550 catalysts generate a current density of -10 mA cm^{-2} at overpotentials of -132 mV and -92 mV, respectively; overpotentials of -151 and -110 are required to attain a current density of -20 mA cm^{-2}. Ni_2P-Me-600 exhibits similar HER performance as Ni_2P-Ph-550, requiring an overpotential of -87 mV to achieve -10 mA cm^{-2}. These results indicate that Ni_2P is the most active catalyst and the Ni_2P NPs synthesized from both NiPh and NiMe have identical activity, consistent with the similar characterization results of these samples.

The different catalytic activity of the Ni-based catalysts can be explained in the following way. On the one hand, in Ni phosphides the metal has a small partial positive charge, while the phosphorous has a small partial negative charge.[75] This has been confirmed by the XPS data of the Ni_2P-Ph-550 material discussed in section 4.2.1.1: the binding energy of Ni in the phosphide is slightly higher than that of zero valent nickel indicating a partial positive charge on this species; the binding energy of phosphorous is slightly lower, suggesting the phosphorous atoms have a partial negative charge. Therefore, the surface of the catalysts contains metal centers and basic phosphorous centers in their proximity. It has been considered that the metal centers function as hydride-acceptors and the phosphorous as proton-adsorption centers that promote HER.[14] Different nickel phosphide phases exhibit different catalytic activity. Specifically, $Ni_{12}P_5$ was found to be less active than Ni_2P.[50] This can be attributed to the partial positive charge of Ni and atomic percentage of P in Ni_2P being higher than on $Ni_{12}P_5$ that results in a lower intrinsic activity of the latter for the HER. Thus, the presence of the $Ni_{12}P_5$ nanoparticles on the $Ni_{12}P_5$-Ph-450 and $Ni_{12}P_5$-Ni_2P-Ph-500 catalysts contributes to their lower activity compared to the Ni_2P catalysts. On the other hand, the samples $Ni_{12}P_5$-Ph-450 and $Ni_{12}P_5$-Ni_2P-Ph-500 contain precursor or partially carbonized precursor that was not converted into phosphide (Figure 4.6). This is due to the lower synthesis temperatures of these samples, which affects the amount of carbonaceous material as well as its degree of carbonization. $Ni_{12}P_5$-Ph-450 still contains completely non carbonized phosphonate according to the FT-IR data (Figure 4.9). Since the metal phosphonate precursors do not catalyze the hydrogen evolution reaction (Figure 4.18) they have a detrimental effect on the activity of the phosphide catalysts. To demonstrate this detrimental effect, the activity of a physical mixture of Ni_2P NPs and 15 wt. % Ni phosphonate was evaluated. The presence of the phosphonate led to a significant decrease of the HER catalytic performance of the Ni_2P-Me-600 catalyst (Figure 4.18). Thus, the presence

of unreacted or partially carbonized phosphonate on the $Ni_{12}P_5$-Ph-450 and $Ni_{12}P_5$-Ni_2P-Ph-500 samples also contributes to their poorer performance compared to the Ni_2P catalysts.

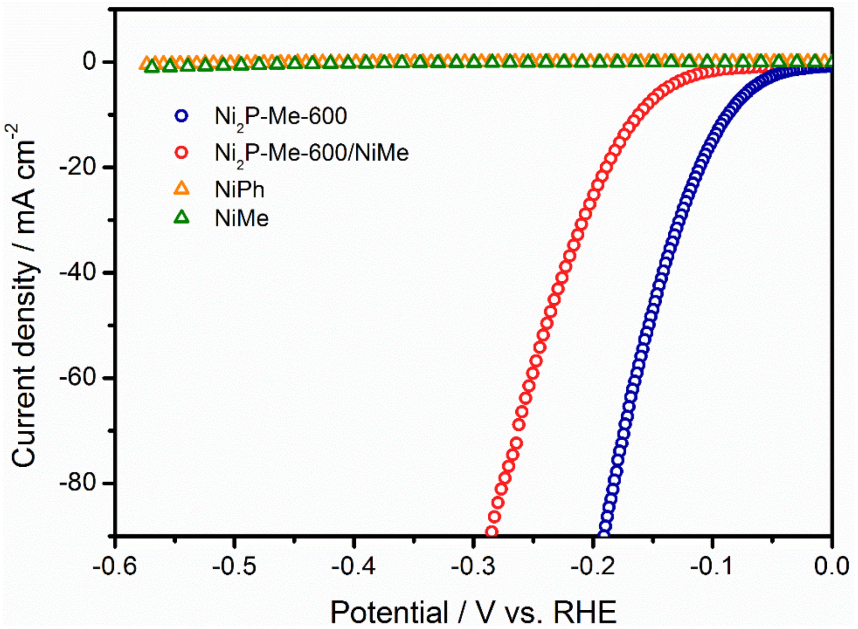

Figure 4.18 Polarization curves of Ni_2P-Me-600, Ni_2P-Me-600 mixed with 15 wt.% nickel methylphosphonate, and the pristine nickel phenylphosphonate and nickel methylphosphonate, for HER in 0.5 M H_2SO_4.

It is generally accepted that the HER is a two-electron process proceeding in two steps. As mentioned in the introduction, the first step is an electrochemical hydrogen adsorption or discharge step (Volmer reaction) which is followed by an electrochemical desorption step (Heyrovský reaction) or by a recombination step (Tafel reaction). Tafel slopes of 116, 38 or 29 mV per decade respectively identify the Volmer, Heyrovský or Tafel reaction as the rate-determining step of the HER.[73] $Ni_{12}P_5$-Ni_2P-Ph-500, Ni_2P-Ph-550 and Ni_2P-Me-600 have Tafel slopes of 85, 59 and 64 mV per decade, respectively, which has been considered indicative that the HER proceeds via a Volmer-Heyrovský mechanism. The smaller Tafel slopes of the Ni_2P electrocatalysts confirm their higher HER activity and suggest faster proton discharge kinetics compared to that of $Ni_{12}P_5$-Ni_2P-Ph-500.[75]

The performance of the Ni_2P electrocatalysts synthesized in this work is superior or comparable to that of most nickel phosphide-based catalysts recently reported.[76-83] Owing to the synthetic method used in this work to fabricate the metal phosphide nanoparticles, the surface of the Ni_2P NPs is in close contact with a thin layer of carbon. Several works have demonstrated that the combination of Ni_2P NPs with carbon materials enhances the HER catalytic activity of the metal

phosphide due in part to the increase of the conductivity of the catalyst that facilitates charge transfer.[24,70,76] Pan *et al.*[70] showed that the HER activity of Ni_2P NPs supported on carbon spheres gradually improved with increasing carbon content until an optimum carbon content was reached. The performance improvement was attributed to the increase of the surface area and electrical conductivity of the catalyst. The beneficial effect of carbon is enhanced by a more intimate and extensive contact between phosphide and carbon material. For example, carbon-encapsulated Ni_2P NPs were found to be considerable more active (η_{10mA} = -87 mV) than uncoated nanoparticles (η_{10mA} ~ -220 mV),[76] and the catalytic activity improvement is larger than that observed for the dispersion of nanoparticles on a carbon support. [24,70,76] Therefore, the intimate contact of the carbon layer surrounding the phosphide nanoparticles in the Ni_2P-Ph-550 and Ni_2P-Me-600 catalysts contributes to the high HER activity of these catalysts. These results demonstrate that the simple and non-hazardous synthesis approach reported here allows the fabrication of highly active nanostructured Ni phosphide HER catalysts.

Stability is an important requirement for an electrocatalyst. Therefore, the stability of the Ni_2P NPs (Ni_2P-Me) was evaluated by potential cycling and chronoamperometry. The potential was swept between -0.20 and 0.20 V vs. RHE at a scan rate of 100 mV s^{-1}. After 1000 continuous cycles the overpotential required to achieve a current density of -10 mA cm^{-2} increased to -97 mV, corresponding to an increase of only -10 mV (Figure 4.16b). The stability of the Ni_2P electrode was further investigated by performing continuous electrolysis at a fixed current density of -10 mA cm^{-2} (Figure 4.17b). The electrode overpotential increases by less than -30 mV after 11 h of continuous operation. Degradation of the activity of some Ni phosphide electrodes with potential cycling or continuous electrolysis has been reported.[7,36] The loss of activity may be attributed to partial dissolution of the Ni phosphide catalyst into the acidic electrolyte. For instance, Wang *et al.*[11] reported that Ni_2P nanorods became blunt and shorter after stability tests probably as a result of partial dissolution and/or aggregation. In addition, the authors reported that most probably structural changes occurred during the stability tests as a consequence of phosphorous loss, leading to the conversion of some Ni_2P into the less active $Ni_{12}P_5$. For evaluating possible structural and morphological changes after the stability tests, TEM and electron diffraction analysis of the Ni_2P catalyst after continuous electrolysis (Figure 4.19) were performed. No significant morphological changes are observed from the TEM images of the Ni_2P-Me-600 catalyst after the stability test. Moreover, the nanoparticles remain coated by the carbon film after electrocatalysis. The diffraction rings in the SAED pattern are indexed to Ni_2P and no other Ni phosphide phase was detected. Therefore, although some loss

of activity occurs during electrolysis, likely due to dissolution at the surface of the catalyst, the degradation is less extensive compared to some other similar catalysts. This is most probably due to the presence of the carbon layer surrounding the nanoparticles that partially hinders the transfer of Ni and P into the electrolyte.

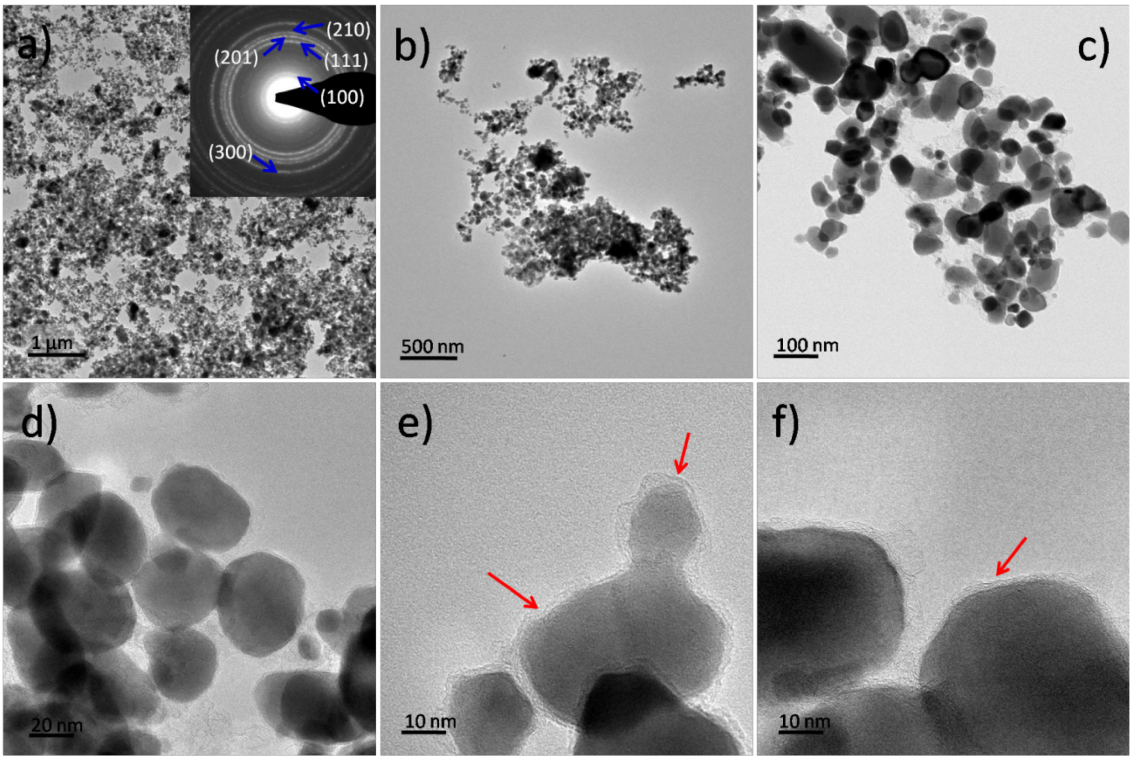

Figure 4.19 TEM images of Ni_2P-Me-600 catalyst after electrolysis at -10 mA cm^{-2} for 30 min. Insert shows the SAED patterns. Arrows in red indicate the carbonaceous shell around the nanoparticles.

The HER catalytic activity in acidic electrolyte of the catalysts derived from cobalt phenylphosphonate was also evaluated; the polarization curves and Tafel plots are shown in Figures 4.20, respectively. The activity of the Co-based catalysts as a function of the synthesis temperature follows a trend similar to that of the Ni phosphide catalysts. Thus, the amorphous material produced at the lowest temperature acts as a very poor HER catalyst, as it consists of partially carbonized Co phosphonate without any metal phosphide phase. A mixture of Co_2P and CoP NPs and pure phase Co_2P NPs were synthesized at 550 °C and 600 °C, respectively. Both these materials are active HER catalysts. Similar to what was observed for the Ni-based electrocatalysts, the single phase Co_2P prepared at higher temperature exhibits the best performance, with an overpotential of -144 mV at j = -10 mA cm^{-2} and a Tafel slope slightly lower than that of Ni_2P (56 mV dec-1), indicative of fast electrode kinetics.

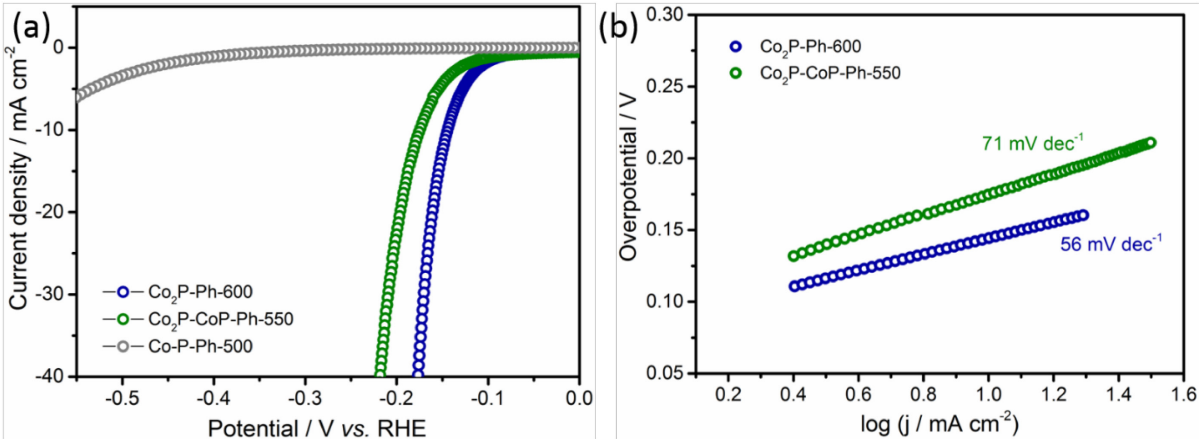

Figure 4.20 (a) Polarization curves of amorphous Co-P (Co-P-Ph-500), Co_2P/CoP (Co_2P-CoP-Ph-550) and pure Co_2P (Co_2P-Ph-600) synthesized by thermal treatment of Co phenylphosphonate. (b) Tafel slopes of Co_2P/CoP and pure Co_2P.

4.2.4 Electrocatalytic oxygen evolution reaction performance in alkaline solution

The OER activity of the Ni phosphide catalysts in alkaline medium was also investigated. The LSV curves measured in 1 M KOH at the scan rate of 10 mV/s are shown in Figure 4.21. All the curves show an oxidation peak prior to the OER onset that is generally observed for Ni-based electrodes in alkaline electrolyte and attributed to the oxidation of nickel.[84] The potential of these oxidation peaks are determined by several factors, such as the composition and structure of the catalysts, and the presence of Fe impurities[85]. All the materials tested, Ni_2P-Ph-550, Ni_2P-$Ni_{12}P_5$-Ph-500, $Ni_{12}P_5$-Ph-450 and Ni_2P-Me-600, exhibit good OER activity, requiring overpotentials of 370, 360, 350 and 360 mV to achieve the anodic current density of 10 mA cm^{-2}. The performance of OER catalyzed by nickel phosphides materials in this work are comparable to that of transition-metal-phosphide-based catalyst recently reported.[86-93] Ni_2P-Ph-550 and Ni_2P-Me-600 have identical catalytic activity, which is consistent with the similar physical and chemical properties of these materials. Although the performances of all the different catalysts are close, the mixture $Ni_{12}P_5$-Ni_2P_5-Ph-500 and $Ni_{12}P_5$-Ph-450 perform slightly better than the pure phase Ni_2P catalysts. $Ni_{12}P_5$ is more active than Ni_2P for the OER owing to the higher Ni atomic percentage of the former,[13] and thus the presence of $Ni_{12}P_5$ NPs enhances the OER activity in comparison with that of the pure phase Ni_2P catalysts. Additionally, as discussed in Chapter 3, the Ni phenylphosphonate is highly active material for OER in alkaline solution (Figure 4.21d), which means that the presence of unreacted or partially carbonized phosphonate on the $Ni_{12}P_5$-Ni_2P_5-Ph-500 and $Ni_{12}P_5$-Ph-450 catalysts has no detrimental effect on their OER activity, contrary to what happens for the HER.

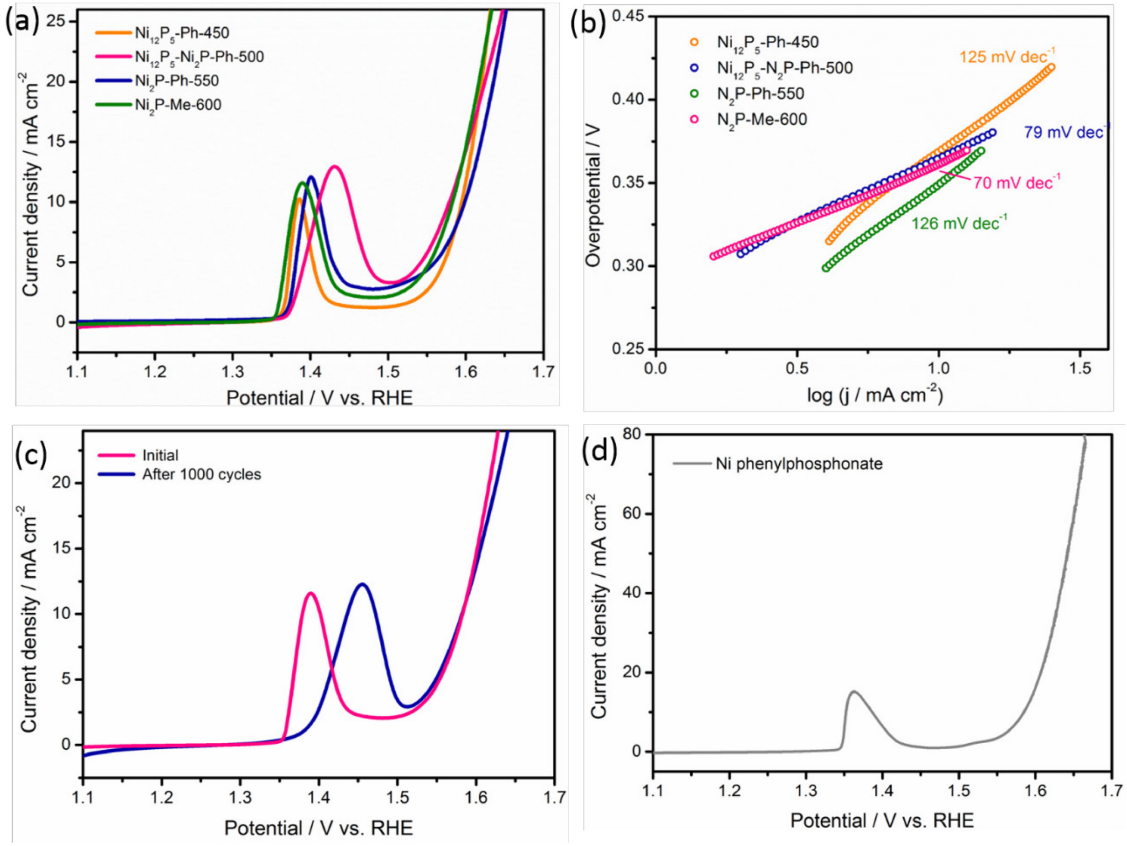

Figure 4.21 (a) LSV curves of Ni_2P-Ph-550, Ni_2P-Me-600, $Ni_{12}P_5$-Ni_2P-Ph-500, and $Ni_{12}P_5$-Ph-450. (b) Tafel plots of Ni_2P-Ph-550, Ni_2P-Me-600, $Ni_{12}P_5$-Ni_2P-Ph-500, and $Ni_{12}P_5$-Ph-450. (c) LSV curves of Ni_2P-Me-600 at the beginning and after 1000 cycles. The potential was scanned in the window of 0 V - 0.6 V vs Ag/AgCl at the scan rate of 100 mV/s. (d) LSV curve of Ni phenylphosphonate. OER performance was tested in 1 M KOH electrolyte at 25 °C.

The Tafel plots of nickel phosphide catalysts are illustrated in Figure 4.21 b revealing the differences in reaction kinetics among these samples. The Ni_2P-Ph-550 and Ni_2P-Me-600 have similar slopes of 79 and 70 mV dec^{-1}, respectively, indicating faster kinetics than the $Ni_{12}P_5$-Ni_2P_5-Ph-500 and $Ni_{12}P_5$-Ph-450 electrocatalysts, which means at high current density the pure Ni_2P materials require lower potentials. This behavior is possibly due to the more deeply carbonized shell that provides improved conductivity and stability for Ni_2P-Ph-550 and Ni_2P-Me-600.

The LSV curve of the Ni_2P-Me electrode was measured at the beginning and after 1000 potential cycles (Figure 4.20 c). An anodic shift of the Ni oxidation peak and a slight improvement of the catalytic activity occurs after 1000 cycles. This is caused by the incorporation of Fe impurities from the KOH electrolyte.[94] The potential cycling data shows that the catalyst exhibits good cycling stability during the oxygen evolution reaction.

Additionally, the cobalt phosphides, Co_2P/CoP and Co_2P, were tested as OER electrocatalysts (Figures 4.22). The pure phase Co_2P catalyst exhibits the highest activity in alkaline electrolyte requiring an overpotential of 340 mV to reach the anodic current density of 10 mA cm^{-2}. Prior to the water oxidation reaction onset, two oxidation peaks are observed in the LSV curve of the Co_2P catalyst, corresponding to Co(II) → Co(III) and Co(III) → Co(IV) oxidation reactions. The overpotential increases to 350 mV after 500 CV cycles, and then the activity is maintained for the next 500 CV cycles, suggesting cycling stability of these materials in alkaline medium.

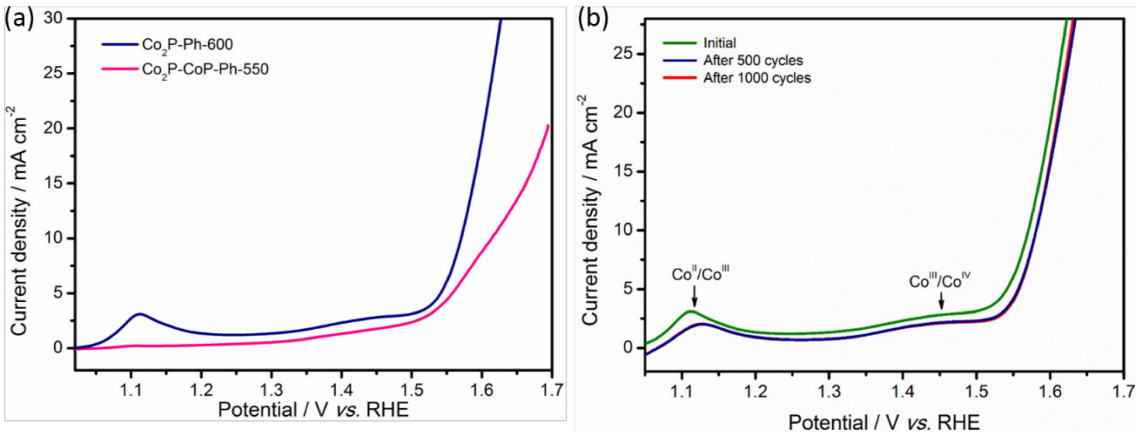

Figure 4.22 (a) LSV curves of Co_2P-Ph-600 and Co_2P-CoP-Ph-550. (c) LSV curves of Co_2P-Ph-600 at the beginning and after 1000 cycles. The potential was scanned in the window of 0 V - 0.6 V vs Ag/AgCl at the scan rate of 100 mV/s.

4.3 Conclusion

In this chapter, a simple, non-hazardous and scalable approach for fabricating transition-metal phosphides@ carbon composite by using metal-organophosphonates as single-source precursors was described. $Ni_{12}P_5$, $Ni_{12}P_5$/Ni_2P and Ni_2P NPs were synthesized from Ni phenyl- and methylphosphonate at temperatures ≥ 450 °C under H_2(5%)/Ar. Co_2P and CoP were synthetized from the corresponding Co phenylphosphonate following the same approach. TG-MS data revealed that H_2, H_2O and P_2 were generated during the thermal transformation of the precursor, suggesting that the H_2 released is able to reduce (at least partially) the phosphonate. No additional phosphorous-containing species were detected. The phosphides were very efficient HER catalysts in acidic medium, with Ni_2P-Me-600 achieving a cathodic current density of -10 mA cm^{-2} at an overpotential of -87 mV. Moreover, the nickel phosphides showed good activity for the OER in alkaline medium, with the overpotential of 360 mV at an anodic current density of 10 mA cm^{-2}. The presence of a carbon shell coating the phosphide

nanoparticles not only hinder the agglomeration during the thermal treatment, but also improve the conductivity of the catalysts and their stability.

The metal-phosphonate chemistry is very rich owing to: i) the strong affinity of the phosphonate group for many metal ions, ii) to the large number of organophosphonic acids available, including bi- and tri-phosphonic acids and those containing additional heteroelements (e.g. S, N), and iii) to the facile synthesis of multimetal phosphonate materials. This approach can be utilized to explore the rich metal phosphonate chemistry for fabricating phosphide-based materials for electrochemical energy conversion and storage applications.

4.4 Experimental section

4.4.1 Materials

Ni (II) acetylacetonate (95 %), Co(II) acetylacetonate (99 %), phenylphosphonic acid (98 %), methylphosphonic acid (98 %), benzyl alcohol (99 %), sulfuric acid (95-98 %), potassium hydroxide (>85 %), Nafion perfluorinated resin solution (5 wt.%) were purchased from Sigma Aldrich. Purified water with resistivity 18.2 MΩ cm^{-1} was used for sample preparation and electrochemical measurements.

4.4.2 Synthesis of catalysts

The metal phosphonates were prepared via a microwave-assisted method using benzyl alcohol as solvent. In a typical synthesis of nickel(II) phenylphosphonate: 0.5 mmol of nickel acetylacetonate, 0.5 mmol of phenylphosphonic acid and 5 mL of benzyl alcohol were mixed in a 10 mL borosilicate glass vial and sealed with a silicon cap. The mixture was stirred for 30 minutes, and then sonicated until a homogenous solution was obtained. The solution was heated in a microwave reactor (Anton Paar Monowave 300) at 180 °C for 30 min with a 5 min heating ramp and subsequently quenched with compressed air. The product was collected by centrifugation, washed three times with ethanol, and dried at 65 °C overnight.

The transition-metal (Ni, Co) phosphides were prepared via a simple heating process using the corresponding metal phosphonate as precursor. In a typical synthesis, 60 mg of metal phosphonate was placed in a combustion boat in a tubular oven (Nabertherm) and purged with 5% H_2 in Ar (99.999%, AirLiquide) for 30 min. Subsequently the sample was heated to a temperature between 350 and 700 °C with a heating ramp of 1 °C/min and maintained at the final temperature for 3 h under H_2(5%)/Ar flow. After cooling to ambient temperature the black

products were collected and grounded in a mortar. The phosphonate precursors were also treated under pure Ar (99.999%, AirLiquide) and under static air (with the tube closed) for 3 h.

4.4.3 Characterization

X-ray powder diffraction patterns were recorded with a STOE MP diffractometer in transmission configuration using Mo Kα radiation (λ=0.07093 nm). TEM images were acquired on a Philips CM 200 microscope at 200 kV. Fourier transformed infrared spectra of the samples were measured on a Thermo Scientific Nicolet iS50 spectrometer in the range of 4000- 400 cm^{-1} (4 cm^{-1} resolution), using pellets of the solid diluted in KBr. Carbon elemental analyses were performed on a HEKAtech Euro EA CHNSO Elemental analyzer. The X-ray photoelectron spectroscopy (XPS) measurements were performed in an analysis chamber (base pressure: 3×10^{-10} mbar) with an overall energy resolution of *ca.* 1.2 eV, using a SPECS Phoibos 100 hemispherical energy analyzer and the Mg Kα radiation (1253.6 eV) generated from a twin anode X-ray source. The thermal behaviour was studied by simultaneously coupled TA-MS measurements. A NETZSCH thermoanalyzer STA 409 C Skimmer®system, equipped with a BALZERS QMG 421, was used to record the thermoanalytical curves (T, DTA, TG, DTG) together with the ionic current (IC) curves in the multiple ion detection (MID) mode. A DTA-TG sample carrier system with platinum crucibles (beaker, 0.8 ml) and Pt/PtRh10 thermocouples was used. A sample of 20.17 mg was measured versus empty reference crucible. A constant purge gas flow of 70 ml/min Argon 5.0 (AirLiquide) and a constant heating rate of 10 K/min were applied. The raw data have been evaluated utilizing the manufacturer's software PROTEUS® (v. 4.3) and QUADSTAR® 422 (v. 6.02) without further data treatment, e.g. such as smoothing. The base line shift of the IC signals at higher temperatures (*e.g.* m/z 18 in Figure 4.14 and 4.15) is characteristic of the *Skimmer®* system where the gas sampling system and the sample holder have the same temperatures, thus avoiding condensation phenomena. Consequently, the MS signal becomes temperature-dependent, and increasing baseline IC intensities at higher temperatures do not indicate generation of gas from the sample, except if intensity maxima sitting on the increasing base line are clearly expressed.

4.4.4 Electrochemical experiments

All electrochemical measurements were performed with a Bio-Logic VMP3 Potentiostat-Galvanostat having a built-in electrochemical impedance spectroscopy analyzer. The electrochemical activity and stability of catalysts were measured in a three-electrode

electrochemical cell using a 3 mm diameter glassy carbon rotating disc electrode (RDE). A platinum wire was used as the counter electrode and an Ag/AgCl (3 M KCl) was used as reference electrode. The catalysts inks were prepared as follow, 5 mg of the sample catalyst was added to 300 μL of H_2O, 290 μL of ethanol and 10 μL of 5 wt.% Nafion solution, and then the mixturewas dispersed by sonication for 30 min to obtain a homogeneous ink. The electrodes were prepared by depositing 3 μL of catalyst ink onto the GC disc and drying at room temperature to achieve a catalyst loading of 0.35 mg cm^2. Prior to catalyst deposition, the GC electrode was polished with 1 μm alumina slurry followed by 0.05 μm alumina slurry, and then rinsed with deionized water, sonicated for 3 min and dried in air. For comparison, a commercial 20 wt. % Pt/C (Johnson Matthey) was deposited on the glassy carbon with the same loading.

The hydrogen evolution reaction (HER) measurements were conducted in 0.5 M H_2SO_4 at 25 °C with the RDE rotated at 2000 rpm. Cyclic voltammetry (CV) experiments were performed in the potential window -0.6 V to 0 V vs. Ag/AgCl with a scan rate of 20 mV s^{-1}. Linear sweep voltammetry (LSV) curves were measured in the same potential window with a slower scan rate of 10 mV s^{-1}. The stability of the catalysts was evaluated by performing 1000 CV sweeps between -0.4 and 0 V vs. Ag/AgCl with a scan rate of 100 mV s^{-1}. The long term stability was evaluated through chronopotentiometry experiments in which the potential was recorded in an 11-hour-electrolysis with the current density maintained at 10 mA cm^{-2}.

The oxygen evolution reaction (OER) measurements were conducted in 1 M KOH electrolyte at 25 °C, with the RDE rotated at 1600 rpm. CVs were measured in the potential window 0 to 0.7 V vs. Ag/AgCl at a scan rate of 20 mV s^{-1}. LSV was measured in the same potential window after CV measurements at a scan rate of 10 mV s^{-1}.

All data was corrected for the ohmic drop. The uncompensated resistance was determined by electrochemical impedance spectroscopy (EIS). The measured potentials of both HER and OER were converted with respect to the reversible hydrogen electrode (RHE).

4.5 Bibliography

1. Shi, Y.; Zhang, B., Recent advances in transition metal phosphide nanomaterials: synthesis and applications in hydrogen evolution reaction. *Chemical Society Reviews* 2016, 45 (6), 1529-1541.
2. Guidelli, R.; Compton Richard, G.; Feliu Juan, M.; Gileadi, E.; Lipkowski, J.; Schmickler, W.; Trasatti, S., Defining the transfer coefficient in electrochemistry: An assessment (IUPAC Technical Report). *Pure and Applied Chemistry*, 2014; Vol. 86(2), 245-258.

3. Li, H.; Tsai, C.; Koh, A. L.; Cai, L.; Contryman, A. W.; Fragapane, A. H.; Zhao, J.; Han, H. S.; Manoharan, H. C.; Abild-Pedersen, F.; Nørskov, J. K.; Zheng, X., Activating and optimizing MoS_2 basal planes for hydrogen evolution through the formation of strained sulphur vacancies. *Nature Materials* 2015, 15, 48.
4. Sun, Y.; Liu, C.; Grauer, D. C.; Yano, J.; Long, J. R.; Yang, P.; Chang, C. J., Electrodeposited Cobalt-Sulfide Catalyst for Electrochemical and Photoelectrochemical Hydrogen Generation from Water. *Journal of the American Chemical Society* 2013, 135 (47), 17699-17702.
5. Fan, X.; Zhou, H.; Guo, X., WC Nanocrystals Grown on Vertically Aligned Carbon Nanotubes: An Efficient and Stable Electrocatalyst for Hydrogen Evolution Reaction. *ACS Nano* 2015, 9 (5), 5125-5134.
6. Kibsgaard, J.; Jaramillo, T. F., Molybdenum Phosphosulfide: An Active, Acid-Stable, Earth-Abundant Catalyst for the Hydrogen Evolution Reaction. *Angewandte Chemie International Edition* 2014, 53 (52), 14433-14437.
7. Popczun, E. J.; McKone, J. R.; Read, C. G.; Biacchi, A. J.; Wiltrout, A. M.; Lewis, N. S.; Schaak, R. E., Nanostructured Nickel Phosphide as an Electrocatalyst for the Hydrogen Evolution Reaction. *Journal of the American Chemical Society* 2013, 135 (25), 9267-9270.
8. Popczun, E. J.; Read, C. G.; Roske, C. W.; Lewis, N. S.; Schaak, R. E., Highly Active Electrocatalysis of the Hydrogen Evolution Reaction by Cobalt Phosphide Nanoparticles. *Angewandte Chemie International Edition* 2014, 53 (21), 5427-5430.
9. Zou, X.; Zhang, Y., Noble metal-free hydrogen evolution catalysts for water splitting. *Chemical Society Reviews* 2015, 44 (15), 5148-5180.
10. Liu, P.; Rodriguez, J. A., Catalysts for Hydrogen Evolution from the [NiFe] Hydrogenase to the $Ni_2P(001)$ Surface: The Importance of Ensemble Effect. *Journal of the American Chemical Society* 2005, 127 (42), 14871-14878.
11. Wang, X.; Kolen'ko, Y. V.; Liu, L., Direct solvothermal phosphorization of nickel foam to fabricate integrated Ni_2P-nanorods/Ni electrodes for efficient electrocatalytic hydrogen evolution. *Chemical Communications* 2015, 51 (31), 6738-6741.
12. Feng, L.; Vrubel, H.; Bensimon, M.; Hu, X., Easily-prepared dinickel phosphide (Ni_2P) nanoparticles as an efficient and robust electrocatalyst for hydrogen evolution. *Physical Chemistry Chemical Physics* 2014, 16 (13), 5917-5921.
13. Menezes, P. W.; Indra, A.; Das, C.; Walter, C.; Göbel, C.; Gutkin, V.; Schmeiβer, D.; Driess, M., Uncovering the Nature of Active Species of Nickel Phosphide Catalysts in High-Performance Electrochemical Overall Water Splitting. *ACS Catalysis* 2017, 7 (1), 103-109.
14. Liu, Q.; Tian, J.; Cui, W.; Jiang, P.; Cheng, N.; Asiri, A. M.; Sun, X., Carbon Nanotubes Decorated with CoP Nanocrystals: A Highly Active Non-Noble-Metal Nanohybrid Electrocatalyst for Hydrogen Evolution. *Angewandte Chemie* 2014, 126 (26), 6828-6832.
15. Huang, Z.; Chen, Z.; Chen, Z.; Lv, C.; Meng, H.; Zhang, C., $Ni_{12}P_5$ Nanoparticles as an Efficient Catalyst for Hydrogen Generation via Electrolysis and Photoelectrolysis. *ACS Nano* 2014, 8 (8), 8121-8129.
16. Huang, Z.; Chen, Z.; Chen, Z.; Lv, C.; Humphrey, M. G.; Zhang, C., Cobalt phosphide nanorods as an efficient electrocatalyst for the hydrogen evolution reaction. *Nano Energy* 2014, 9, 373-382.
17. Son, C. Y.; Kwak, I. H.; Lim, Y. R.; Park, J., FeP and FeP_2 nanowires for efficient electrocatalytic hydrogen evolution reaction. *Chemical Communications* 2016, 52 (13), 2819-2822.
18. Yang, X.; Lu, A.-Y.; Zhu, Y.; Hedhili, M. N.; Min, S.; Huang, K.-W.; Han, Y.; Li, L.-J., CoP nanosheet assembly grown on carbon cloth: A highly efficient electrocatalyst for hydrogen generation. *Nano Energy* **2015,** *15*, 634-641.

19. Yang, J.; Zhang, Y.; Sun, C.; Liu, H.; Li, L.; Si, W.; Huang, W.; Yan, Q.; Dong, X., Graphene and cobalt phosphide nanowire composite as an anode material for high performance lithium-ion batteries. *Nano Research* 2016, 9 (3), 612-621.
20. Mendoza-Garcia, A.; Su, D.; Sun, S., Sea urchin-like cobalt-iron phosphide as an active catalyst for oxygen evolution reaction. *Nanoscale* 2016, 8 (6), 3244-3247.
21. Jin, Z.; Li, P.; Huang, X.; Zeng, G.; Jin, Y.; Zheng, B.; Xiao, D., Three-dimensional amorphous tungsten-doped nickel phosphide microsphere as an efficient electrocatalyst for hydrogen evolution. *Journal of Materials Chemistry A* 2014, 2 (43), 18593-18599.
22. Ma, L.; Shen, X.; Zhou, H.; Zhu, G.; Ji, Z.; Chen, K., CoP nanoparticles deposited on reduced graphene oxide sheets as an active electrocatalyst for the hydrogen evolution reaction. *Journal of Materials Chemistry A* 2015, 3 (10), 5337-5343.
23. Pan, Y.; Lin, Y.; Liu, Y.; Liu, C., A novel CoP/MoS_2-CNTs hybrid catalyst with Pt-like activity for hydrogen evolution. *Catalysis Science & Technology* 2016, 6 (6), 1611-1615.
24. Pan, Y.; Liu, Y.; Liu, C., Nanostructured nickel phosphide supported on carbon nanospheres: Synthesis and application as an efficient electrocatalyst for hydrogen evolution. *Journal of Power Sources* 2015, 285, 169-177.
25. Stern, L.-A.; Feng, L.; Song, F.; Hu, X., Ni_2P as a Janus catalyst for water splitting: the oxygen evolution activity of Ni_2P nanoparticles. *Energy & Environmental Science* 2015, 8 (8), 2347-2351.
26. Ledendecker, M.; Krick Calderón, S.; Papp, C.; Steinrück, H.-P.; Antonietti, M.; Shalom, M., The Synthesis of Nanostructured Ni_5P_4 Films and their Use as a Non-Noble Bifunctional Electrocatalyst for Full Water Splitting. *Angewandte Chemie International Edition* 2015, 54 (42), 12361-12365.
27. Jiang, N.; You, B.; Sheng, M.; Sun, Y., Bifunctionality and Mechanism of Electrodeposited Nickel–Phosphorous Films for Efficient Overall Water Splitting. *ChemCatChem* 2016, 8 (1), 106-112.
28. Wang, X.; Li, W.; Xiong, D.; Petrovykh, D. Y.; Liu, L., Bifunctional Nickel Phosphide Nanocatalysts Supported on Carbon Fiber Paper for Highly Efficient and Stable Overall Water Splitting. *Advanced Functional Materials* 2016, 26, 4067–4077.
29. Yang, H.; Zhang, Y.; Hu, F.; Wang, Q., Urchin-like CoP Nanocrystals as Hydrogen Evolution Reaction and Oxygen Reduction Reaction Dual-Electrocatalyst with Superior Stability. *Nano Letters* 2015, 15 (11), 7616-7620.
30. Panneerselvam, A.; Malik, M. A.; Afzaal, M.; O'Brien, P.; Helliwell, M., The Chemical Vapor Deposition of Nickel Phosphide or Selenide Thin Films from a Single Precursor. *Journal of the American Chemical Society* 2008, 130 (8), 2420-2421.
31. Jiang, J.; Wang, C.; Zhang, J.; Wang, W.; Zhou, X.; Pan, B.; Tang, K.; Zuo, J.; Yang, Q., Synthesis of FeP_2/C nanohybrids and their performance for hydrogen evolution reaction. *Journal of Materials Chemistry A* 2015, 3 (2), 499-503.
32. Stein, B. F.; Walmsley, R. H., Magnetic Susceptibility and Nuclear Magnetic Resonance in Transition-Metal Monophosphides. *Physical Review* 1966, 148 (2), 933-939.
33. Gopalakrishnan, J.; Pandey, S.; Rangan, K. K., Convenient Route for the Synthesis of Transition-Metal Pnictides by Direct Reduction of Phosphate, Arsenate, and Antimonate Precursors. *Chemistry of Materials* 1997, 9 (10), 2113-2116.
34. Callejas, J. F.; Read, C. G.; Roske, C. W.; Lewis, N. S.; Schaak, R. E., Synthesis, Characterization, and Properties of Metal Phosphide Catalysts for the Hydrogen-Evolution Reaction. *Chemistry of Materials* 2016, 28 (17), 6017-6044.
35. Saadi, F. H.; Carim, A. I.; Verlage, E.; Hemminger, J. C.; Lewis, N. S.; Soriaga, M. P., CoP as an Acid-Stable Active Electrocatalyst for the Hydrogen-Evolution Reaction: Electrochemical Synthesis, Interfacial Characterization and Performance Evaluation. The *Journal of Physical Chemistry C* 2014, 118 (50), 29294-29300.

36. Wang, X.; Kolen'ko, Y. V.; Bao, X.-Q.; Kovnir, K.; Liu, L., One-Step Synthesis of Self-Supported Nickel Phosphide Nanosheet Array Cathodes for Efficient Electrocatalytic Hydrogen Generation. *Angewandte Chemie International Edition* 2015, 54 (28), 8188-8192.
37. Hellstern, T. R.; Benck, J. D.; Kibsgaard, J.; Hahn, C.; Jaramillo, T. F., Engineering Cobalt Phosphide (CoP) Thin Film Catalysts for Enhanced Hydrogen Evolution Activity on Silicon Photocathodes. *Advanced Energy Materials* 2016, 6 (4), 1501758-n/a.
38. Pan, Y.; Lin, Y.; Chen, Y.; Liu, Y.; Liu, C., Cobalt phosphide-based electrocatalysts: synthesis and phase catalytic activity comparison for hydrogen evolution. *Journal of Materials Chemistry A* 2016, 4 (13), 4745-4754.
39. Andaraarachchi, H. P.; Thompson, M. J.; White, M. A.; Fan, H.-J.; Vela, J., Phase-Programmed Nanofabrication: Effect of Organophosphite Precursor Reactivity on the Evolution of Nickel and Nickel Phosphide Nanocrystals. *Chemistry of Materials* 2015, 27 (23), 8021-8031.
40. Henkes, A. E.; Vasquez, Y.; Schaak, R. E., Converting Metals into Phosphides: A General Strategy for the Synthesis of Metal Phosphide Nanocrystals. *Journal of the American Chemical Society* 2007, 129 (7), 1896-1897.
41. Henkes, A. E.; Schaak, R. E., Trioctylphosphine: A General Phosphorus Source for the Low-Temperature Conversion of Metals into Metal Phosphides. *Chemistry of Materials* 2007, 19 (17), 4234-4242.
42. Muthuswamy, E.; Savithra, G. H. L.; Brock, S. L., Synthetic Levers Enabling Independent Control of Phase, Size, and Morphology in Nickel Phosphide Nanoparticles. *ACS Nano* 2011, 5 (3), 2402-2411.
43. Xiao, P.; Chen, W.; Wang, X., A Review of Phosphide-Based Materials for Electrocatalytic Hydrogen Evolution. *Advanced Energy Materials* 2015, 5 (24), 1500985-n/a.
44. Pöttgen, R.; Hönle, W.; von Schnering, H. G., *Phosphides: Solid-State Chemistry. In Encyclopedia of Inorganic Chemistry*, John Wiley & Sons, Ltd: 2006.
45. Zhang, Y.; Zhang, H.; Feng, Y.; Liu, L.; Wang, Y., Unique Fe_2P Nanoparticles Enveloped in Sandwichlike Graphited Carbon Sheets as Excellent Hydrogen Evolution Reaction Catalyst and Lithium-Ion Battery Anode. *ACS Applied Materials & Interfaces* 2015, 7 (48), 26684-26690.
46. Hu, S.; Shaner, M. R.; Beardslee, J. A.; Lichterman, M.; Brunschwig, B. S.; Lewis, N. S., Amorphous TiO_2 coatings stabilize Si, GaAs, and GaP photoanodes for efficient water oxidation. *Science* 2014, 344 (6187), 1005-1009.
47. Pfeiffer, H.; Tancret, F.; Brousse, T., Synthesis, characterization and thermal stability of Ni_3P coatings on nickel. *Materials Chemistry and Physics* 2005, 92 (2), 534-539.
48. Layan Savithra, G. H.; Muthuswamy, E.; Bowker, R. H.; Carrillo, B. A.; Bussell, M. E.; Brock, S. L., Rational Design of Nickel Phosphide Hydrodesulfurization Catalysts: Controlling Particle Size and Preventing Sintering. *Chemistry of Materials* 2013, 25 (6), 825-833.
49. Lu, Y.; Tu, J.-P.; Xiong, Q.-Q.; Xiang, J.-Y.; Mai, Y.-J.; Zhang, J.; Qiao, Y.-Q.; Wang, X.-L.; Gu, C.-D.; Mao, S. X., Controllable Synthesis of a Monophase Nickel Phosphide/Carbon (Ni_5P_4/C) Composite Electrode via Wet-Chemistry and a Solid-State Reaction for the Anode in Lithium Secondary Batteries. *Advanced Functional Materials* 2012, 22 (18), 3927-3935.
50. Pan, Y.; Liu, Y.; Zhao, J.; Yang, K.; Liang, J.; Liu, D.; Hu, W.; Liu, D.; Liu, Y.; Liu, C., Monodispersed nickel phosphide nanocrystals with different phases: synthesis, characterization and electrocatalytic properties for hydrogen evolution. *Journal of Materials Chemistry A* 2015, 3 (4), 1656-1665.
51. Li, D.; Senevirathne, K.; Aquilina, L.; Brock, S. L., Effect of Synthetic Levers on Nickel Phosphide Nanoparticle Formation: Ni5P4 and NiP_2. *Inorganic Chemistry* 2015, 54 (16), 7968-7975.

52. Kucernak, A. R. J.; Naranammalpuram Sundaram, V. N., Nickel phosphide: the effect of phosphorus content on hydrogen evolution activity and corrosion resistance in acidic medium. *Journal of Materials Chemistry A* 2014, 2 (41), 17435-17445.
53. Laursen, A. B.; Patraju, K. R.; Whitaker, M. J.; Retuerto, M.; Sarkar, T.; Yao, N.; Ramanujachary, K. V.; Greenblatt, M.; Dismukes, G. C., Nanocrystalline Ni_5P_4: a hydrogen evolution electrocatalyst of exceptional efficiency in both alkaline and acidic media. *Energy & Environmental Science* 2015, 8 (3), 1027-1034.
54. Jiang, P.; Liu, Q.; Sun, X., NiP_2 nanosheet arrays supported on carbon cloth: an efficient 3D hydrogen evolution cathode in both acidic and alkaline solutions. *Nanoscale* 2014, 6 (22), 13440-13445.
55. Carenco, S.; Portehault, D.; Boissière, C.; Mézailles, N.; Sanchez, C., Nanoscaled Metal Borides and Phosphides: Recent Developments and Perspectives. *Chemical Reviews* 2013, 113 (10), 7981-8065.
56. Fullenwarth, J.; Darwiche, A.; Soares, A.; Donnadieu, B.; Monconduit, L., NiP_3: a promising negative electrode for Li- and Na-ion batteries. *Journal of Materials Chemistry A* 2014, 2 (7), 2050-2059.
57. Callejas, J. F.; Read, C. G.; Popczun, E. J.; McEnaney, J. M.; Schaak, R. E., Nanostructured Co_2P Electrocatalyst for the Hydrogen Evolution Reaction and Direct Comparison with Morphologically Equivalent CoP. *Chemistry of Materials* 2015, 27 (10), 3769-3774.
58. Jiang, P.; Liu, Q.; Ge, C.; Cui, W.; Pu, Z.; Asiri, A. M.; Sun, X., CoP nanostructures with different morphologies: synthesis, characterization and a study of their electrocatalytic performance toward the hydrogen evolution reaction. *Journal of Materials Chemistry A* 2014, 2 (35), 14634-14640.
59. Tian, J.; Liu, Q.; Asiri, A. M.; Sun, X., Self-Supported Nanoporous Cobalt Phosphide Nanowire Arrays: An Efficient 3D Hydrogen-Evolving Cathode over the Wide Range of pH 0–14. *Journal of the American Chemical Society* 2014, 136 (21), 7587-7590.
60. Hou, C.-C.; Cao, S.; Fu, W.-F.; Chen, Y., Ultrafine CoP Nanoparticles Supported on Carbon Nanotubes as Highly Active Electrocatalyst for Both Oxygen and Hydrogen Evolution in Basic Media. *ACS Applied Materials & Interfaces* 2015, 7 (51), 28412-28419.
61. Li, M.; Liu, X.; Xiong, Y.; Bo, X.; Zhang, Y.; Han, C.; Guo, L., Facile synthesis of various highly dispersive CoP nanocrystal embedded carbon matrices as efficient electrocatalysts for the hydrogen evolution reaction. *Journal of Materials Chemistry A* 2015, 3 (8), 4255-4265.
62. Zhuang, M.; Ou, X.; Dou, Y.; Zhang, L.; Zhang, Q.; Wu, R.; Ding, Y.; Shao, M.; Luo, Z., Polymer-Embedded Fabrication of Co_2P Nanoparticles Encapsulated in N,P-Doped Graphene for Hydrogen Generation. *Nano Letters* 2016, 16 (7), 4691-4698.
63. Li, X.; Fang, Y.; Li, F.; Tian, M.; Long, X.; Jin, J.; Ma, J., Ultrafine Co_2P nanoparticles encapsulated in nitrogen and phosphorus dual-doped porous carbon nanosheet/carbon nanotube hybrids: high-performance bifunctional electrocatalysts for overall water splitting. *Journal of Materials Chemistry A* 2016, 4 (40), 15501-15510.
64. Cheng, M.; Fan, H.; Xu, Y.; Wang, R.; Zhang, X., Hollow Co_2P nanoflowers assembled from nanorods for ultralong cycle-life supercapacitors. *Nanoscale* 2017, 9 (37), 14162-14171.
65. Chen, X.; Cheng, M.; Chen, D.; Wang, R., Shape-Controlled Synthesis of Co_2P Nanostructures and Their Application in Supercapacitors. *ACS Applied Materials & Interfaces* 2016, 8 (6), 3892-3900.
66. Zhang, H.; Ha, D.-H.; Hovden, R.; Kourkoutis, L. F.; Robinson, R. D., Controlled Synthesis of Uniform Cobalt Phosphide Hyperbranched Nanocrystals Using Tri-n-octylphosphine Oxide as a Phosphorus Source. *Nano Letters* 2011, 11 (1), 188-197.

67. Cao, G.; Lee, H.; Lynch, V. M.; Mallouk, T. E., Synthesis and structural characterization of a homologous series of divalent-metal phosphonates, $M^{II}(O_3PR)\cdot H_2O$ and $M^{II}(HO_3PR)_2$. *Inorganic Chemistry* 1988, 27 (16), 2781-2785.
68. B. Hix, G.; D. M. Harris, K., Synthesis of layered nickel phosphonate materials based on a topotactic approach. *Journal of Materials Chemistry* 1998, 8 (3), 579-584.
69. Schroeder, P. G.; France, C. B.; Parkinson, B. A.; Schlaf, R., Orbital alignment at p-sexiphenyl and coronene/layered materials interfaces measured with photoemission spectroscopy. *Journal of Applied Physics* 2002, 91 (11), 9095-9107.
70. Pan, Y.; Hu, W.; Liu, D.; Liu, Y.; Liu, C., Carbon nanotubes decorated with nickel phosphide nanoparticles as efficient nanohybrid electrocatalysts for the hydrogen evolution reaction. *Journal of Materials Chemistry A* 2015, 3 (24), 13087-13094.
71. Moldoveanu, S. C., *Pyrolysis of Organic Molecules with Applications to Health and Environmental Issues.* 1st ed.; Elsevier: Amsterdam, 2009.
72. Stinner, C.; Tang, Z.; Haouas, M.; Weber, T.; Prins, R., Preparation and ^{31}P NMR Characterization of Nickel Phosphides on Silica. *Journal of Catalysis* 2002, 208 (2), 456-466.
73. Zeng, M.; Li, Y., Recent advances in heterogeneous electrocatalysts for the hydrogen evolution reaction. *Journal of Materials Chemistry A* 2015, 3 (29), 14942-14962.
74. Xiao, P.; Sk, M. A.; Thia, L.; Ge, X.; Lim, R. J.; Wang, J.-Y.; Lim, K. H.; Wang, X., Molybdenum phosphide as an efficient electrocatalyst for the hydrogen evolution reaction. *Energy & Environmental Science* 2014, 7 (8), 2624-2629.
75. Chen, W.-F.; Iyer, S.; Iyer, S.; Sasaki, K.; Wang, C.-H.; Zhu, Y.; Muckerman, J. T.; Fujita, E., Biomass-derived electrocatalytic composites for hydrogen evolution. *Energy & Environmental Science* 2013, 6 (6), 1818-1826.
76. Bai, Y.; Zhang, H.; Li, X.; Liu, L.; Xu, H.; Qiu, H.; Wang, Y., Novel peapod-like Ni_2P nanoparticles with improved electrochemical properties for hydrogen evolution and lithium storage. *Nanoscale* 2015, 7 (4), 1446-1453.
77. Pu, Z.; Liu, Q.; Tang, C.; Asiri, A. M.; Sun, X., Ni_2P nanoparticle films supported on a Ti plate as an efficient hydrogen evolution cathode. *Nanoscale* 2014, 6 (19), 11031-11034.
78. Chang, J.; Li, S.; Li, G.; Ge, J.; Liu, C.; Xing, W., Monocrystalline $Ni_{12}P_5$ hollow spheres with ultrahigh specific surface areas as advanced electrocatalysts for the hydrogen evolution reaction. *Journal of Materials Chemistry A* 2016, 4 (25), 9755-9759.
79. Xu, Y.; Wu, R.; Zhang, J.; Shi, Y.; Zhang, B., Anion-exchange synthesis of nanoporous FeP nanosheets as electrocatalysts for hydrogen evolution reaction. *Chemical Communications* 2013, 49 (59), 6656-6658.
80. Xing, Z.; Liu, Q.; Asiri, A. M.; Sun, X., Closely Interconnected Network of Molybdenum Phosphide Nanoparticles: A Highly Efficient Electrocatalyst for Generating Hydrogen from Water. *Advanced Materials* 2014, 26 (32), 5702-5707.
81. Cabán-Acevedo, M.; Stone, M. L.; Schmidt, J. R.; Thomas, J. G.; Ding, Q.; Chang, H.-C.; Tsai, M.-L.; He, J.-H.; Jin, S., Efficient hydrogen evolution catalysis using ternary pyrite-type cobalt phosphosulphide. *Nature Materials* 2015, 14, 1245.
82. Kibsgaard, J.; Tsai, C.; Chan, K.; Benck, J. D.; Norskov, J. K.; Abild-Pedersen, F.; Jaramillo, T. F., Designing an improved transition metal phosphide catalyst for hydrogen evolution using experimental and theoretical trends. *Energy & Environmental Science* 2015, 8 (10), 3022-3029.
83. Tian, J.; Liu, Q.; Cheng, N.; Asiri, A. M.; Sun, X., Self-Supported Cu_3P Nanowire Arrays as an Integrated High-Performance Three-Dimensional Cathode for Generating Hydrogen from Water. *Angewandte Chemie International Edition* 2014, 53 (36), 9577-9581.

84. Lyons, M. E. G.; Brandon, M. P., The oxygen evolution reaction on passive oxide covered transition metal electrodes in aqueous alkaline solution. Part 1 - Nickel. *International Journal of Electrochemical Science* 2008, (3), 1386-1424.
85. Görlin, M.; Chernev, P.; Ferreira de Araújo, J.; Reier, T.; Dresp, S.; Paul, B.; Krähnert, R.; Dau, H.; Strasser, P., Oxygen Evolution Reaction Dynamics, Faradaic Charge Efficiency, and the Active Metal Redox States of Ni–Fe Oxide Water Splitting Electrocatalysts. *Journal of the American Chemical Society* 2016, 138 (17), 5603-5614.
86. You, B.; Jiang, N.; Sheng, M.; Bhushan, M. W.; Sun, Y., Hierarchically Porous Urchin-Like Ni_2P Superstructures Supported on Nickel Foam as Efficient Bifunctional Electrocatalysts for Overall Water Splitting. *ACS Catalysis* 2016, 6 (2), 714-721.
87. Wang, C.; Jiang, J.; Ding, T.; Chen, G.; Xu, W.; Yang, Q., Monodisperse Ternary NiCoP Nanostructures as a Bifunctional Electrocatalyst for Both Hydrogen and Oxygen Evolution Reactions with Excellent Performance. *Advanced Materials Interfaces* 2016, 3 (4), 1500454.
88. Li, D.; Baydoun, H.; Verani, C. N.; Brock, S. L., Efficient Water Oxidation Using CoMnP Nanoparticles. *Journal of the American Chemical Society* 2016, 138 (12), 4006-4009.
89. Wang, J.; Yang, W.; Liu, J., CoP_2 nanoparticles on reduced graphene oxide sheets as a super-efficient bifunctional electrocatalyst for full water splitting. *Journal of Materials Chemistry A* 2016, 4 (13), 4686-4690.
90. Chang, J.; Xiao, Y.; Xiao, M.; Ge, J.; Liu, C.; Xing, W., Surface Oxidized Cobalt-Phosphide Nanorods As an Advanced Oxygen Evolution Catalyst in Alkaline Solution. *ACS Catalysis* 2015, 5 (11), 6874-6878.
91. Zhu, Y.-P.; Liu, Y.-P.; Ren, T.-Z.; Yuan, Z.-Y., Self-Supported Cobalt Phosphide Mesoporous Nanorod Arrays: A Flexible and Bifunctional Electrode for Highly Active Electrocatalytic Water Reduction and Oxidation. *Advanced Functional Materials* 2015, 25 (47), 7337-7347.
92. Wang, P.; Song, F.; Amal, R.; Ng, Y. H.; Hu, X., Efficient Water Splitting Catalyzed by Cobalt Phosphide-Based Nanoneedle Arrays Supported on Carbon Cloth. *ChemSusChem* 2016, 9 (5), 472-477.
93. Niu, S.; Jiang, W.-J.; Tang, T.; Zhang, Y.; Li, J.-H.; Hu, J.-S., Facile and Scalable Synthesis of Robust $Ni(OH)_2$ Nanoplate Arrays on NiAl Foil as Hierarchical Active Scaffold for Highly Efficient Overall Water Splitting. *Advanced Science* 2017, 4 (8), 1800084.
94. Trotochaud, L.; Young, S. L.; Ranney, J. K.; Boettcher, S. W., Nickel–Iron Oxyhydroxide Oxygen-Evolution Electrocatalysts: The Role of Intentional and Incidental Iron Incorporation. *Journal of the American Chemical Society* 2014, 136 (18), 6744-6753.

5. Conclusions

This thesis reported the study of the physical-chemical properties and their correlation with the catalytic properties of three types of nanomaterials: TiO_2@carbon composites, hybrid transition-metal organic-inorganic phosphonate compounds, and metal phosphide nanoparticles.

Composites consisting of titanium dioxide nanoparticles deposited on reduced graphene oxide (TiO_2/rGO) or amorphous carbon (TiO_2/AC) were synthesized by a non-aqueous sol-gel route in benzyl alcohol using microwave and conventional heating methods, in order to investigate the effect of the heating conditions (e.g. heating rate) and heating mechanisms on the structural/morphological characteristics of the TiO_2 NPs, on the strength of the TiO_2-carbon interactions, and on the photocatalytic activity of the composites. It was found that, compared to the conventional autoclave syntheses, the high heating rates achieved with microwave irradiation leads to a more homogeneous and extensive coating of the carbon surfaces with TiO_2 NPs, and to the formation of TiO_2 nanoparticles with smaller sizes and narrower particle size distributions. The strength of the TiO_2-carbon interactions (specifically the extent of covalent bonding) was enhanced by fast heating rates. Moreover, by using MW-shielding SiC vials for reproducing with conventional heating the MW-assisted heating profiles, it was found that specific interactions of the carbon materials with the electromagnetic microwave, causing "overheating" of the carbon surface, further promoted the strong binding of the nanoparticles to the carbons. The stronger binding and more extensive contact between TiO_2 and the carbons resulted in more stable nanocomposites and enhancement of the photocatalytic activity.

A series of layered organic-inorganic hybrid NiFe-phenylphosphonate compounds ($Ni_xFe_{1-x}O_3PC_6H_5.H_2O$), with Fe atomic percentages ranging from 0 to 100, were produced by microwave-assisted synthesis in benzyl alcohol. The hybrids consist of inorganic layers containing the metal cations separated by two organic layers. Due to the 1:1 metal:phenylphosphonate ratio and presence of coordinating water molecules, the metals have a distorted octahedral coordination. For this reason, the compounds were investigated as oxygen evolution catalysts in alkaline medium. The hybrid materials act as precursors of NiFe hydroxide nanosheets that are formed in situ during OER. The catalyst with an iron atomic percentage of 16 % delivered a geometric current density of 10 mA cm^{-2} at an overpotential of 240 mV and was stable for 160 h, outperforming NiFe oxides and hydroxides used as reference catalysts. X-ray absorption spectroscopy measurements suggested that the distorted octahedral coordination partly remains in the hydroxide formed in situ. The high activity was attributed to

the synergistic effects between Ni and Fe and to the irregular octahedral geometry of the metal sites. The rich chemistry of the family of organic-inorganic transition-metal phosphonate compounds can be used to design specific structural motifs by carefully selecting the organophosphonate ligands composition and structure, and the synthesis conditions. This allows the optimization of the local electronic environment of the metal sites for electrocatalytic reactions. Moreover, these materials can be used for in situ studies (such as in situ X-ray absorption studies) to get insights into the relationship between the structure of the metal catalytic sites and the electrocatalytic activity.

This thesis also described a novel route to synthesize carbon coated transition-metal phosphide nanoparticles using the corresponding metal phosphonate that act as a single-source precursor. The method does not involve the production of significant amounts of hazardous P-containing compounds. In particular, $Ni_{12}P_5$, $Ni_{12}P_5/Ni_2P$ and Ni_2P NPs were synthesized from Ni phenyl- or methylphosphonate at temperatures ≥ 450 °C under H_2(5%)/Ar flow. Co_2P and CoP NPs were also synthesized through this route from cobalt phenylphosphonate precursor. The morphology, crystalline phase, and electrochemical properties of the final products are determined by the composition of the precursor, and the parameters of the heat treatment (heating ramp, temperature, time, and atmosphere). The metal phosphide NPs were active electrocatalysts for HER in acidic solution and OER in alkaline solution. Particularly, Ni_2P exhibits high activity in HER; the carbon coating improves the conductivity and protects the surface of the Ni_2P against degradation. This synthesis approach is promising for the preparation of other transition-metal phosphides nanostructures and composites, and multi-metal phosphides.

List of figures

Figure 4.3 Powder X-ray diffraction patterns of the Ni phenylphosphonate (NiPh) and Ni methylphosphonate (NiMe).

Figure 4.4 TEM images of the (a,b) Ni phenylphosphonate (NiPh) and (c, d) Ni methylphosphonate (NiMe).

Figure 4.5 Powder X-ray diffraction patterns of the materials produced by thermal treatment of Ni phenylphosphonate under H_2(5%)/Ar atmosphere. Vertical bars represent reference patterns: gray-$Ni_{12}P_5$ (JCPDS card no. 022-1190); dark blue-Ni_2P (JCPDS card no. 074-1385).

Figure 4.6 TEM images of (a,b) $Ni_{12}P_5$-Ph-450, (c,d,e,f) $Ni_{12}P_5$-Ni_2P-Ph-500, (g,h) Ni_2P-Ph-550 and (i) Ni_2P-Ph-700 synthesized by thermal treatment of nickel phenylphosphonate under H_2(5%)/Ar at 450 °C, 500 °C, 550 °C and 700 °C, respectively. The insets in b, c, and g show the SAED patterns. Blue arrows indicate the carbonaceous shell around the nanoparticles.

Figure 4.7 Powder XRD patterns of the materials produced by thermal treatment of nickel methylphosphonate. Vertical bars represent reference patterns: gray-$Ni_{12}P_5$ (JCPDS card no. 022-1190); dark blue-Ni_2P (JCPDS card no. 074-1385).

Figure 4.8 TEM images of (a,b) $Ni_{12}P_5$-Ni_2P-Me-500, (c,d) Ni_2P-Me-600, and (e,f) Ni_2P-Me-700 synthesized by thermal treatment of nickel methylphosphonate under H_2(5%)/Ar at 500 °C, 600 °C, and 700 °C, respectively. Inserts in a, e show the SAED patterns. Arrows in blue indicate the carbonaceous shell around the nanoparticles.

Figure 4.9 FT-IR spectra of nickel phenylphosphonate (NiPh), and the products synthesized by thermal treatment of NiPh under H_2(5%)/Ar at different temperatures.

Figure 4.10 (a) Survey X-ray photoelectron spectra of NiPh and Ni_2P-Ph-550. Ni 2p and P 2p XPS spectra of (b, c) nickel phenylphosphonate and (d, e) Ni_2P NPs.

Figure 4.11 X-ray diffraction pattern of the products synthesized by thermal treatment of nickel phenylphosphonate at 500 °C, 550 °C, 600 °C and 700 °C under argon, measured using Mo radiation (λ =0.7093 Å). Vertical bars represent reference patterns: red- Ni_3P (JCPDS card no. 074-1384); gray-$Ni_{12}P_5$ (JCPDS card no. 022-1190); black- Ni (JCPDS card no. 004-0850); blue- Ni_2P (JCPDS card no. 074-1385); green- $Ni_2P_2O_7$ (JCPDS card no. 049-1082).

Figure 4.12 XRD patterns of Co phenylphosphonate (CoPh) and the products synthesized by thermal treatment of Co phenylphosphonate at 500 °C, 550 °C, and 600 °C under H_2(5%)/Ar, measured using Mo radiation (λ =0.7093 Å). Vertical bars represent reference patterns: gray-CoP (JCPDS card no. 029-0497); blue-Co_2P (JCPDS card no. 032-0306).

Figure 4.13 TEM images of (a,b) CoPh, (d,e) Co-P-Ph-500, (f,g) Co_2P-CoP-Ph-550, and (h,i) Co_2P-Ph-600 synthesized by thermal treatment of cobalt phenylphosphonate under H_2(5%)/Ar at 500 °C, 550 °C, 600 °C, and 700 °C, respectively. Image (c) and inserts in d show the SAED patterns. Arrows in blue indicate the carbonaceous shell around the nanoparticles. Arrows in blue indicate the carbonaceous shell around the nanoparticles.

Figure 4.14 TG-MS curves of nickel phenylphosphonate in Ar with the IC curves for the mass numbers *m/z*=2 (H_2^+), 18 (H_2O^+), 62 (P_2^+), and 77 ($C_6H_5^+$). For a better distinction, the IC curves are shifted and the DTA trace is omitted (two weakly expressed endothermal effects).

Figure 4.15 TG-MS curves of nickel methylphosphonate in Ar with the IC curvesfor the mass numbers *m/z*=2 (H_2^+), 18 (H_2O^+) and16 (CH_4^+).

Figure 4.16 (a) Polarization curves of Ni_2P-Ph-550, $Ni_{12}P_5$-Ni_2P-Ph-500, $Ni_{12}P_5$-Ph-450, Pt/C and pristine glassy carbon electrode. Polarization curves of (b) Ni_2P-Me-600, (c) Ni_2P-Ph-550 and (d) $Ni_{12}P_5$-Ni_2P-Ph-500 at initial and after 1000 cycles, respectively. Curves were collected at a scan rate of 10 mV/s in 0.5 M H_2SO_4.

Figure 4.17 (a) Tafel slopes of $Ni_{12}P_5$-Ph-450, $Ni_{12}P_5$-Ni_2P-Ph-500, Ni_2P-Ph-550, Ni_2P-Me-600 and Pt/C, for HER in 0.5 M H_2SO_4. (b) Chronopotentiometric curve with a fixed current density of -10 mA cm^{-2}.

Figure 4.18 Polarization curves of Ni_2P-Me-600, Ni_2P-Me-600 mixed with 15 wt.% nickel methylphosphonate, and the pristine nickel phenylphosphonate and nickel methylphosphonate, for HER in 0.5 M H_2SO_4.

Figure 4.19 TEM images of Ni_2P-Me-600 catalyst after electrolysis at -10 mA cm^{-2} for 30 min. Insert shows the SAED patterns. Arrows in red indicate the carbonaceous shell around the nanoparticles.

Figure 4.20 (a) Polarization curves of amorphous Co-P (Co-P-Ph-500), Co_2P/CoP (Co_2P-CoP-Ph-550) and pure Co_2P (Co_2P-Ph-600) synthesized by thermal treatment of Co phenylphosphonate. (b) Tafel slopes of Co_2P/CoP and pure Co_2P.

Figure 4.21 (a) LSV curves of Ni_2P-Ph, Ni_2P-Me, $Ni_{12}P_5$-Ni_2P-Ph, and $Ni_{12}P_5$-Ph. (b) Tafel plots of Ni_2P-Ph, Ni_2P-Me, $Ni_{12}P_5$-Ni_2P-Ph, and $Ni_{12}P_5$-Ph. (c) LSV curves of Ni_2P-Me at the beginning and after 1000 cycles. The potential was scanned in the window of 0 V - 0.6 V vs Ag/AgCl at the scan rate of 100 mV/s. (d) LSV curve of Ni phenylphosphonate. OER performance was tested in 1 M KOH electrolyte at 25 °C.

Figure 4.22 (a) LSV curves of Co_2P-Ph and Co_2P-CoP-Ph. (c) LSV curves of Co_2P-Ph at the beginning and after 1000 cycles. The potential was scanned in the window of 0 V - 0.6 V vs Ag/AgCl at the scan rate of 100 mV/s.

List of Tables

List of schemes

Acknowledgement

I acknowledge the fellowship from the China Scholarship Council (CSC) and my reference Prof. Dr. Yihe Zhang at China University of Geosciences (Beijing).

I am eternally grateful to my supervisor, Prof. Dr. Nicola Pinna, for the opportunity in working on this interesting and challenging topic under his supervision, for the freedoms he gives to me to practice different ideas, and for providing the internship and conference opportunities in other institutes. Special thanks to my co-supervisor, Dr. Patrícia A. Russo, for pushing me to do and learn more than I ever thought I could, and for her rigorous academic attitude and patient perseverance to shape me into a chemist that I am today.

I thank all of my fantastic colleagues in AK Pinna; I am especially grateful to those who helped me to start the work in this lab. Special thanks to Christoph Erdmann for passing countless TEM images and organizing the coffee group, to Dr. Matthias Karg for the help in XRD measurements and language translation, to Sebastian Wahl, Yafei Fan and Andréa Martin for answering countless and rambling questions about electrochemistry. Meanwhile, thanks to Dr. Nicolas Goubard, Dr. Yanlin Wu, Dr. Yu Wang, Alexander Birnbaum, Sayed M. El-Refaei, Xianying Han, Hamid Raza, Kai Skrodczky, Dr. Guylhaine Clavel, Dr. Gianvito Caputo, Dr. Donato E. Conte, Dr. Lidia Di Carlo, Dr. Ricardo Silva, Dr. Valentina Rebuttini, Dr. Xiaofeng Lu, and Dr. Jun Zhang.

Special mention goes to the collaborators who make important contributions to this thesis, including Dr. Michael Feist (Institut für Chemie, HU), Prof. Dr. Norbert Koch and Dr. Patrick Amsalem (Institut für Physik, HU), Prof. Dr. Saveria Santangelo (Università “Mediterranea”, Italy), Dr. Massimiliano D’Arienzo and Prof. Dr. Franca Morazzoni (Università di Milano-Bicocca, Italy), Dr. Enza Fazio and Prof. Dr. Fortunato Neri (Università di Messina, Italy), Dr. Taeyeol Jeon (Pohang Accelerator Laboratory, South Korea), and Dr. Ana G. Buzanich (Federal Institute for Materials Research and Testing, Germany). Thanks to Prof. Dr. Dan Wang (Institute of Process Engineering, CAS, Beijing) and the group members in his lab for the intense and interesting work in IPE.

Finally, I would like to thank my family and friends, for the continuous, unselfish and unbelievable support during the last years. Special thanks to my wife, Lijun, for taking care of our children and the family.

Selbstständigkeitserklärung

Hiermit erkläre ich, die vorliegende Arbeit selbstständig geschrieben und erarbeitet zu haben. Alle im Text beschriebenen von anderen erarbeiteten wissenschaftlichen Inhalte und verwendeten Methoden sind als solche explizit gekennzeichnet und mit den richtigen bibliographischen Angaben im Literaturverzeichnis zitiert.

Weiterhin erkläre ich, diese Arbeit nicht an anderer Stelle eingereicht zu haben.

Declaration of independent work

Here, I declare that the present doctoral thesis was independently written and the described scientific contents were independently elaborated. All the used methods and knowledge firstly developed by others have been explicitly cited in the written text and the proper bibliographic references were reported in a dedicated section.

Furthermore, I declare that this thesis has not been submitted elsewhere before.